Preparation and control of electronic wave packets in neutral molecules via an attosecond X-Ray pulse

Dissertation

zur Erlangung des Doktorgrades an der Fakultät
für Mathematik, Informatik und Naturwissenschaften
Fachbereich Physik
der Universität Hamburg

vorgelegt von
ROSSI EMANUELE

Hamburg
2025

Eidesstattliche Versicherung
Hiermit versichere ich an Eides statt, die vorliegende Dissertationsschrift selbst verfasst und keine anderen als die angegebenen Hilfsmittel und Quellen benutzt zu haben. Sofern im Zuge der Erstellung der vorliegenden Dissertationsschrift generative Künstliche Intelligenz (gKI) basierte elektronische Hilfsmittel verwendet wurden, versichere ich, dass meine eigene Leistung im Vordergrund stand und dass eine vollständige Dokumentation aller verwendeten Hilfsmittel gemäß der Guten wissenschaftlichen Praxis vorliegt. Ich trage die Verantwortung für eventuell durch die gKI generierte fehlerhafte oder verzerrte Inhalte, fehlerhafte Referenzen, Verstöße gegen das Datenschutz- und Urheberrecht oder Plagiate.

Hamburg, March 12, 2025

Emanuele Rossi

Gutachter der Dissertation:	Prof. Dr. Nina Rohringer Prof. Dr. Robin Santra
Zusammensetzung der Prüfungskommission:	Prof. Dr. Michael Potthoff Prof. Dr. Nina Rohringer Prof. Dr. Robin Santra Prof. Dr. Daniela Pfannkuche Prof. Dr. Markus Gühr
Vorsitzender der Prüfungskommission:	Prof. Dr. Michael Potthoff
Datum der Disputation:	12/06/2025
Vorsitzender des Fach-Promotionsausschusses Physik:	Prof. Dr. Markus Drescher
Leiter des Fachbereichs Physik:	Prof. Dr. Wolfgang J. Parak
Dekan der Fakultät MIN:	Prof. Dr.-Ing. Norbert Ritter

"se tu âs lidrîs ben saldis, tu tegnis dûr pardut"
Ai mei gjenitôrs

Abstract

The goal of attochemistry is to use the properties of electronic wave packets excited by an attosecond pulse to manipulate the electronic distribution within a molecule and control its chemical reactivity. This work focuses on studying the preparation of an electronic wave packet in a neutral molecule by means of an attosecond X-Ray pulse. The electronic wave packet is expanded in terms of the core- and valence-excited states of the molecule, which are coherently populated respectively via a one-photon X-Ray absorption and a two-photons impulsive stimulated X-Ray Raman process. The goal of this work is to analyse the characteristics of the electronic excitation and their dependence on the pulse polarisation and the X-Ray excitation edge. Particular attention is posed on the atom-specific properties of the X-Ray excitation, a goal being the unequivocal demonstration of the possibility of initially localising the valence wave packet (excited by the X-Ray Raman process) on the specifically pumped atom. The excitation is described within time-dependent perturbation theory, modelling the X-Ray absorption as a first-order process and the X-Ray Raman as a second-order process. The electronic structure of the considered molecules, i.e. Carbonyl sulfide and Oxazole, is described at the equation-of-motion coupled-cluster level of theory, including an accurate description of the X-Ray Raman process which avoids the customary truncation of the sum-over-states characterising second-order perturbative contributions. The evolution of the intramolecular electronic distribution due to the preparation and propagation of the electronic wave packet are analysed in terms of the time-dependent electronic density. In particular, the 'excited' part of the electronic density is decomposed in terms of the main perturbative components of the excitation, separating the contributions related to the core-excited and the valence-excited states. In the initial stages of the time-evolution the contributions relative to the core-excited states, which are characterised by an atom-specific localised character, play the dominant role. The atom-specific localisation of the core-excitation can be transferred to the manifold of valence-excited states via the X-Ray Raman process, provided a sufficiently large number of valence-excited states are included in the wave packet. This is the case of Oxazole, wherein the possibility of localising the initial 'source' of the valence electronic migration around a specific atom of the molecule is shown. This conditions the subsequent electronic migration, whose spatial distribution depends also on the pulse polarisation, which controls the symmetry of the states included in the wave packet. Owing to the ultrafast decay of the core-excited states, on a long timescale, when the nuclear motion starts to have a sizeable influence, the electronic dynamics are dominated by the component associated with the valence excitation. This makes the impulsive stimulated X-Ray Raman technique a valuable tool to control the chemical reactivity in a neutral molecule.

Zusammenfassung

Das Ziel der Attochemie ist es, die Eigenschaften elektronischer Wellenpakete, die durch einen Attosekundenpuls angeregt werden, zu nutzen, um die elektronische Verteilung in einem Molekül zu manipulieren und dessen chemische Reaktivität zu steuern. Diese Arbeit konzentriert sich auf der Vorbereitung eines elektronischen Wellenpakets in einem neutralen Molekül mittels eines Attosekunden-Röntgenpulses. Das elektronische Wellenpaket wird in Bezug auf die angeregten Kern- und Valenzzustände des Moleküls dargestellt, die jeweils kohärent durch eine Ein-Photon-Röntgenabsorption und einen Zwei-Photonen-impulsiven stimulierten Röntgen-Raman-Prozess besetzt werden. Ziel dieser Arbeit ist es, die Eigenschaften der elektronischen Anregung und ihre Abhängigkeit von der Polarisierung des Pulses und der Röntgenanregungskante zu analysieren. Besonderes Augenmerk wird auf die atomspezifischen Eigenschaften der Röntgenanregung gelegt. Das Ziel ist eine eindeutige Demonstration der Möglichkeit, das Valenzwellenpaket (das durch den Röntgen-Raman-Prozess angeregt wird) anfänglich auf dem speziell angeregten Atom zu lokalisieren. Die Anregung wird im Rahmen der zeitabhängigen Störungstheorie beschrieben, wobei die Röntgenabsorption als ein Prozess erster Ordnung und der Röntgen-Raman-Prozess als ein Prozess zweiter Ordnung simuliert wird. Die elektronische Struktur der betrachteten Moleküle, d.h. Carbonylsulfid und Oxazol, wird auf dem Niveau der 'equation-of-motion coupled cluster'-Theorie beschrieben, einschließlich einer genauen Beschreibung des Röntgen-Raman-Prozesses. Dabei wird das übliche Abschneiden der Summen über Zustände, die die zweiten Störungsordnung charakterisiert, vermieden. Die zeitabhängige Elektronendichte aufgrund der Vorbereitung und Propagation des elektronischen Wellenpakets wird analysiert. Insbesondere wird der „angeregte“ Teil der Elektronendichte in Bezug auf die Hauptstörungkomponenten der Anregung zerlegt, wobei die Beiträge zu den kernangeregten und den valenzangeregten Zuständen getrennt werden. In den Anfangsstadien der Zeitentwicklung dominieren die Beiträge zu den kernangeregten Zuständen, die sich durch einen atomspezifischen lokalisierten Charakter auszeichnen. Die atomspezifische Lokalisierung der Kernanregung kann durch den Röntgen-Raman-Prozess auf das Ensemble der valenzangeregten Zustände übertragen werden, vorausgesetzt, dass eine ausreichend große Anzahl von valenzangeregten Zuständen im Wellenpaket enthalten ist. Im Fall von Oxazol wird gezeigt, dass die Möglichkeit besteht, den anfänglichen „Ursprung“ der Valenzelektronenmigration um ein spezifisches Atom des Moleküls zu lokalisieren. Dies beeinflusst die anschließende elektronische Migration, deren räumliche Verteilung auch von der Polarisation des Pulses abhängt, die die Symmetrie der im Wellenpaket enthaltenen Zustände steuert. Aufgrund des ultraschnellen Zerfalls der kernangeregten Zustände, wird auf langen Zeitskalen, wenn die Kernbewegung beginnt einen beträchtlichen Einfluss zu haben, die elektronische Dynamik von der Valenzanregungskomponente dominiert. Dies macht die impulsive stimulierte Röntgen-Raman-Technik zu einem wertvollen Werkzeug, um die chemische Reaktivität in einem neutralen Molekül zu steuern.

Contents

Units, constants and notation

The system of atomic units (a.u.) is used throughout the derivations presented in the following, unless otherwise stated. The value of the fundamental constants and the definition of fundamental quantities used in this work is presented in the following table:

Fundamental constants			
Name	Value in a.u.	Value in SI	Symbol
electron rest mass	1	9.11×10^{-31} kg	m_e
elementary charge	1	1.60×10^{-19} C	e
reduced Planck constant	1	1.05×10^{-34} J s	$\hbar$
Coulomb's constant	1	8.99×10^{9} $\mathrm{F}^{-1}\,\mathrm{m}$	$1/4\pi\epsilon_0$
fine-structure constant	$\approx 7.30 \times 10^{-3}$	7.30×10^{-3}	α
speed of light in vacuum	$1/\alpha \approx 137$	$3.00 \times 10^{8}\mathrm{m\,s}^{-1}$	c
vacuum permittivity	$1/4\pi$	8.85×10^{-12} $\mathrm{F\,m}^{-1}$	ϵ_0

Derived atomic units			
Name	Definition	Value in SI	Symbol
length	$4\pi\epsilon_0\hbar^2/(e^2 m_e)$	5.30×10^{-11} m	a_0
energy	$\hbar^2/a_0^2 m_e$	4.36×10^{-18}J ≈ 27.2eV	E_h
time	$\hbar/E_h$	24.2×10^{-18}s	
irradiance	$E_h^2/\hbar a_0^2$	6.44×10^{19} $\mathrm{W\,m}^{-2}$	I

As a general guideline, in the following the bold-typesetting is used to indicate vectorial quantities in $\mathbb{R}^3$, such as the position vector $\boldsymbol{r}$. On the other hand, a 'hat' notation is employed to indicate quantum-mechanical operators, for example, $\hat{\boldsymbol{p}}$ indicates the momentum operator or $\hat{H}$ indicates the Hamiltonian operator. Throughout this work, the angular frequency ω will often be indicated simply as 'frequency'. Additionally, the angular frequency may also be designated as 'energy', given that $E = \hbar\omega$ with $\hbar = 1$ in a.u..

Glossary of Abbreviations

1PDM	one-particle reduced density matrix
ADC	algebraic diagrammatic construction
AM	Auger-Meitner
CBH	Cambell-Baker-Hausdorff
CC	coupled-cluster
CCSD	coupled-cluster singles doubles
CI	configuration interaction
CISD	configuration interaction singles doubles
DOF	degrees of freedom
DOFs	degrees of freedom
EOM-CC	equation of motion coupled-cluster
FWHM	Full width at half maximum
HF	Hartree-Fock
HHG	high harmonic generation
HOMO	Highest Occupied Molecular Orbital
IR	infrared
ISRIXS	Impulsive Stimulated Resonant Inelastic X-Ray Scattering
LUMO	Lowest Unoccupied Molecular Orbital
MCTDH	multiconfigurational time-dependent Hartree
MCTDHF	multiconfigurational time-dependent Hartree Fock
MO	molecular orbital
OCS	carbonyl sulphide
QED	Quantum Electrodynamics
RIXS	Resonant Inelastic X-Ray Scattering
SD	Slater determinant
SOS	sum over intermediate states
SRIXS	Stimulated Resonant Inelastic X-Ray Scattering
STIRAP	Stimulated Raman Adiabatic Passage
TD-CASSCF	time-dependent complete-active-space self-consistent-field
TD-CC	time-dependent coupled-cluster
TD-CI	time-dependent configuration interaction
TD-DFT	time-dependent density functional theory
TD-EOM-CC	time-dependent equation of motion coupled-cluster
TD-RASSCF	time-dependent restricted-active-space self-consistent-field
TDM	transition dipole moment
TDPT	time-dependent perturbation theory
TDSE	time-dependent Schrödinger equation
TISE	time-independent Schrödinger equation
UCC	unitary coupled cluster
UV	ultraviolet
WP	wave packet
XANES	X-Ray absorption near-edge spectroscopy
XFEL	X-Ray Free Electron Laser

CHAPTER 1

Introduction

The fundamental interest of chemistry lies in the understanding and control of a chemical reaction, which can be schematised as a series of steps connecting the reagents to the products. Each of these steps can be considered as a frame of the reaction 'movie', in which the nuclei and electrons play the part of the main actors. Their motion determines the rupture and formation of the chemical bonds, transforming reagents into products. In the context of this 'movie', light can play different roles. Light can be a 'camera', by means of which the motion of the electrons and nuclei can be captured, thereby reconstructing the dynamical path followed by the chemical reaction. The development of ever shorter light pulses has allowed to 'film' chemical reactions at an increasingly higher frame rate, which has progressively reached the characteristic natural timescales of the nuclear and electronic motions, i.e. the femtosecond (*fs*) and the attosecond (*as*), respectively. Light can also play the role of the 'director', which starts a chemical reaction and directs it to the desired products. This role is of fundamental importance in Nature, where it plays a pivotal function in fundamental processes such as vision and the photosynthesis [1], and for the field of photochemistry. This work focuses on contributing to the understanding of the mechanisms underlying the 'director' role of light in a chemical reaction. An overview of the progresses in the study and control of the light-induced chemical dynamics is presented in section 1.1, following the path traced by the progresses in the generation of ever shorter light pulses towards the *as* timescale. This work focuses in particular on studying the excitation of the electronic degrees of freedom (DOF) in a neutral molecule via an *as* X-Ray pulse. The X-Ray spectroscopic processes considered in this work and the characteristics of the electronic excitation they create in a neutral molecule are discussed in section 1.2. The description of the electronic excitation and the subsequent electronic dynamics requires an accurate modelling of the molecule's electronic structure. In section 1.3 a review of the theoretical tools available for the description of the ultrafast molecular electronic dynamics will be presented, contextualising the method used in this work. Finally, in section 1.4 the research questions guiding the investigation will be formulated and an outline of the dissertation will be presented.

1.1 Controlling chemistry with light

1.1.1 Wave packets, short pulses and control

The broad bandwidth of an ultra short light pulse allows the generation of a coherent superposition of eigenstates of a quantum system, i.e. a wave packet (WP), which leads to the spatial redistribution of the system's DOF. A seminal example of this process is represented by the preparation and detection of a WP of Rydberg electronic states in an atomic system [2, 3]. The broad bandwidth of a picosecond laser pulse enables the coherent excitation of several Rydberg eigenstates, leading to the formation of a (radially) localised electronic WP. The localisation provides a bridge towards a 'classical' description of the WP's motion, which is understood as that of a classical particle travelling along a trajectory. As observed experimentally in [3], the 'classical' description of the WP's motion is not always possible. In fact, due to the differences in the energy spacing of the Rydberg states, the localisation of the WP during its radial motion collapses and revives periodically, showing the alternation of the quantum-mechanical and 'classical' descriptions. As the pulse duration progressed to the *fs* limit [4] it became possible to access the timescale of nuclear motion. In the pioneering studies by Zewail *et al.* [5, 6], a *fs* resolved pump-probe experiment was performed to study the dynamics of a unimolecular dissociation reaction. Here, the broad bandwidth of the *fs* pulse allowed to excite a WP including multiple vibrational levels and to monitor the dissociation reaction as it proceeded through the transition states connecting the reagents to the products. The resulting progresses in the understanding of chemical reactions were accompanied by efforts aimed at controlling the yield and distribution of their products. An active control method consists in the manipulation of the initial coherent superposition state through the modulation of the amplitudes and phases of the spectral components of the pulse [7, 8]. The resulting regulation of the reaction channels' interference can lead to the control of the yield and distribution of the reaction's products [9]. The possibility of studying and controlling the chemical reactions at the *fs* timescale shed light on the dynamics of the chemical bond connected with the nuclear motions, establishing the field of femtochemistry [10].

1.1.2 The way towards attochemistry

A new perspective on the control of chemical reactivity was stimulated by Weinkauf and Schlag's experiment [11], which demonstrated the role of the electronic dynamics in the control of a peptide's fragmentation. In the experiment, an UV laser pulse ionised the peptide creating a hole specifically localised in correspondence to an aromatic amino acid at the C-terminal end. The observation of ions related to the N-terminal end in the subsequent photofragmentation of the peptide was interpreted as the result of an efficient migration of the positive charge from the chromophore at the C-terminal end to the N-terminal end. The charge migration process is a purely electronic mechanism, which relocates the charge before the motion of the nuclei can have a significant impact on the dynamics. The nature of this process was explained by Cederbaum and Zobeley [12], who demonstrated how the initially localised charge migrates as a consequence of the correlation between the electrons. Successive theoretical works by Remacle and Levine [13, 14] showed how it is the localisation of the positive charge along the peptide chain which determines which

bond will break, demonstrating the possibility of a 'charge directed chemistry' where the electronic dynamics play a crucial 'director' role. This introduced an electronic timescale to the study of chemical reactions [15] which, owing to the introduction of *as* pulses [16, 17], pushed the study of chemical dynamics to the natural timescale of the electronic motion. The extremely short duration of the *as* pulses corresponds to a broad spectral bandwidth, which can be used to coherently populate several electronic states in a molecule. This allows to manipulate the electronic dynamics which are relevant for chemical processes in chemical and biological systems. The first studies of the electronic dynamics in molecular systems by means of *as* pulses considered the simplest molecule, i.e. H_2. In a study by Sansone *et al.* [18], the dissociative ionisation of H_2 was studied by means of a pulse sequence formed by an *as* ultraviolet (UV) pump pulse and an intense infrared (IR) probe pulse. Based on the results of a previous work by Kling *et al.* [19], the experiment measured the intramolecular localisation of the electronic charge distribution as a function of the *as* pump-probe delay. On one hand, this established a starting point for the investigation of the intramolecular electronic dynamics in a molecule by means of *as* pulses. On the other hand, both [19] and [18] demonstrate the possibility of controlling the molecular dynamics via the manipulation of the electronic DOF. The experimental observation of sub-*fs* electronic dynamics in a larger molecular system was achieved by Calegari *et al.* [20], who used an *as* extreme-UV pulse to launch an electronic WP in phenylalanine upon its prompt ionisation. The intramolecular electronic dynamics were reconstructed by monitoring the oscillation of the fragmentation yields, recorded as a function of the delay with respect to a *fs* visible/near-IR probe pulse. This work established the possibility of using *as* pulses to excite complex molecules, manipulating their intramolecular electronic distribution before the nuclear relaxation takes place. The link connecting the electronic distribution to the chemical dynamics is the coupling between the electronic and nuclear DOF of the molecule [21], which creates the possibility of using the initial, purely electronic process to influence the nuclear dynamics taking place at a later time [22]. The advent of the *as* pulses endowed the researchers with the possibility of manipulating the initial electronic dynamics within a molecule [23], thus offering a platform for the control of its chemical reactivity. Based on this idea, intense theoretical [24, 25] and experimental [26] developments advanced the comprehension of charge migration, electron-nuclei coupling and their influence on chemical reactivity. This established the field of 'attochemistry', which bears the potential of providing deeper insights on chemical reactions [27] and on the nature of the chemical bond [28].

1.1.3 Attochemistry in neutral molecules

Building on the groundbreaking studies on charge migration, the field of attochemistry is also advancing towards the study of the electronic dynamics in neutral molecules [29], which is relevant for the understanding of fundamental natural processes like the photosynthesis [22]. The excitation and control of an electronic WP in neutral molecules could provide a more gentle way to manipulate the electrons, affording control of the molecular dynamics while avoiding photofragmentation [27]. A first step in this direction was provided by Matselyukh *et al.*, who performed an *as* X-Ray transient absorption experiment to study the migration of the electrons in neutral Silane (SiH_4) [30]. In this work, an IR pump pulse launched an

electronic WP of valence and Rydberg excited states of neutral SiH_4 while an *as* probe pulse was used to reconstruct the subsequent electronic migration. This experiment not only showed the possibility of studying the migration of electrons in neutral molecules on the *as* timescale, but also highlighted the consequences of the electron-nuclei couplings, confirming the possibility of using the electrons as a tool for the manipulation of the chemical dynamics. This dissertation aims at contributing to this new direction of attochemistry, by theoretically studying the electronic dynamics launched in a neutral molecule by an *as* X-Ray pulse. In the next section, two X-Ray spectroscopic processes, which can be used to excite a WP in a neutral molecule, will be described, focusing in particular on the properties of the excitation they create in the molecular system.

1.2 X-Ray excitation in a neutral molecule

Attosecond pulses in the X-Ray regime can be routinely generated by means of high harmonic generation (HHG) sources [31] or at an X-Ray Free Electron Laser (XFEL) [32]. In this work, the excitation of a neutral molecule with an *as* X-Ray pulse is considered to be mediated by two spectroscopic processes: an X-Ray one-photon absorption and a two-photon stimulated Resonant Inelastic X-Ray Scattering (RIXS) process.

1.2.1 Core-excited states and X-Ray absorption spectroscopy

The X-Ray one-photon absorption process entails the excitation of the molecular system from the ground state to the manifold of core-excited states. A one-particle representation of this process is depicted in panel a) of fig. 1.1, where the example case of the CO molecule is considered. The absorption of an X-Ray photon promotes an electron from a core molecular orbital (MO) to an unoccupied MO, determining the formation of a core-hole. As shown by the red and purple arrows, photons of different energy promote the core electrons to different unoccupied MOs (the Lowest Unoccupied Molecular Orbital (LUMO) and the LUMO+1, respectively) below the ionisation threshold (indicated by the blue line). These transitions can be (approximately) mapped to resonances in the pre-edge region of the X-Ray absorption spectrum [33], which is characterised by an atom-specific energy range. This specificity can be understood by considering that the core MOs lie in an energetically deep region of the molecular potential which retains its atomic character. This translates into an atom-specific excitation energy which allows, by appropriately tuning the X-Ray pulse, to excite the system to C-specific or O-specific core-excited states. This can be generalised to any molecule, wherein different atoms can be targeted exploiting the differences in their elemental identity and chemical environment. The atomic specificity of the X-Ray excitation (and in turn of the core-excited states) is the foundation of techniques like X-Ray absorption near-edge spectroscopy (XANES), which provides atom-specific information on the unoccupied MOs and more in general on the molecule's electronic structure and reactivity [33]. The XANES technique is routinely applied at synchrotrons, where the narrow bandwidth of the X-Ray radiation allows to precisely target core-excited states with atomic specificity. Such a precise selectivity is not possible when the molecule interacts with an *as* X-Ray pulse, which allows, on the other hand, to coherently populate multiple core-excited

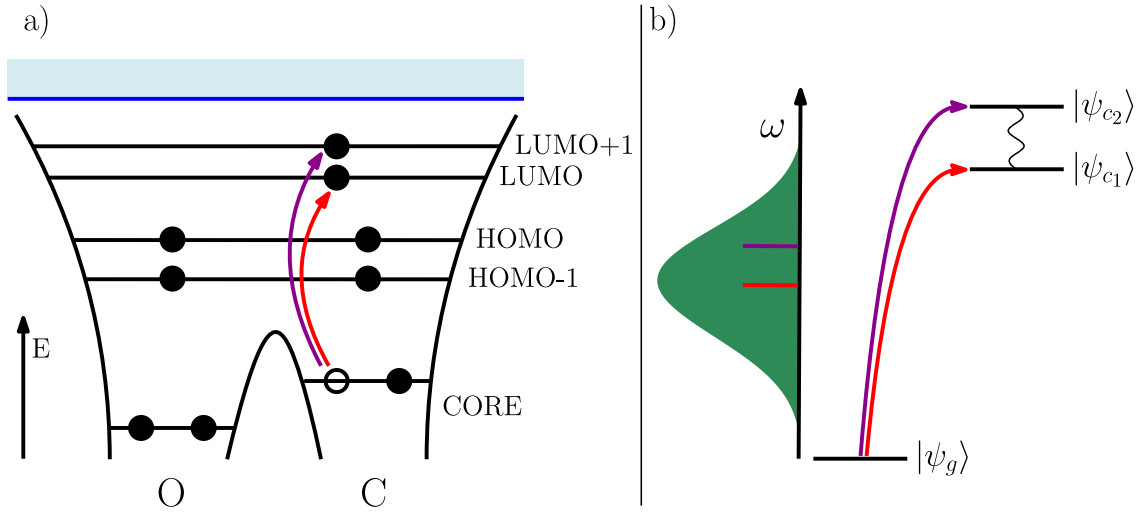

Figure 1.1: *Schematic representations of the one-photon X-Ray absorption process. The representation of the process in the one-particle picture is shown in panel a), where the electronic structure of carbon monoxide (CO) is represented in terms of MOs of increasing energy within the molecular potential. The electrons are indicated as full circle, the holes as hollow circles. The one-photon absorption of two photons of different energy is represented by the red and purple arrows. The blue line and azure-shaded area represent the ionisation threshold and the continuum, respectively. The representation of the one-photon X-Ray absorption process performed with a broad bandwidth* as *pulse is shown in panel b). The pulse in the frequency domain is represented by the green Gaussian, with the red and purple bars corresponding to the frequencies resonant to the excitations from the ground state* $|\psi_g\rangle$ *to the core-excited states* $|\psi_{c_1}\rangle$ *and* $|\psi_{c_2}\rangle$*, respectively. The sinusoidal line connecting* $|\psi_{c_1}\rangle$ *and* $|\psi_{c_2}\rangle$ *represents their coherent superposition.*

states. This is shown in the schematic example in panel b) of fig. 1.1, where the coherent excitation is represented in the context of a three-level system. Here, owing to the frequencies of both the absorbed photons (purple and red bars within the green Gaussian pulse bandwidth) being included within the pulse bandwidth, the system is excited from the ground state $|\psi_g\rangle$ to a superposition of core-excited states $|\psi_{c_1}\rangle$ and $|\psi_{c_2}\rangle$. This can be extended to a general system with several core-excited states, which can be included in the WP exploiting the broad bandwidth of the *as* X-Ray pulse. After the core-hole is created, the electronic structure tends to relax by means of spontaneous processes. While in heavier atoms the radiative decay is predominant [34], in lighter atoms (such as those constituting the organic molecules present in biological systems) the decay of the core-holes is dominated by Auger-Meitner (AM) processes [35, 36], which limits the lifetimes of the core-excited states to a few *fs* (e.g. ≈ 4 *fs* for O [37, 38] or ≈ 6.5 *fs* for C [39]). This restricts the time-window available for time-resolved experiments and the manipulation of the electronic distribution in a neutral molecule. Conversely, the valence-excited states are characterised by much longer lifetimes (typically in the order of ps to ns [40]) and lower excitation energies, which allows them to be directly involved in naturally-occurring photochemical processes.

1.2.2 Valence-excited states and stimulated RIXS

The population of the valence-excited states in the X-Ray regime relies on a resonant Raman scattering process. This process lies at the heart of the RIXS technique [41], which is a well-established tool for the study of the electronic structure in a variety of systems in the gas- [42], liquid- [43] and solid-phase [44]. The RIXS process can be schematised as a sequence of two steps, represented in panel a) of fig. 1.2 in the context of a simplified, one-particle picture of the electronic structure. The first

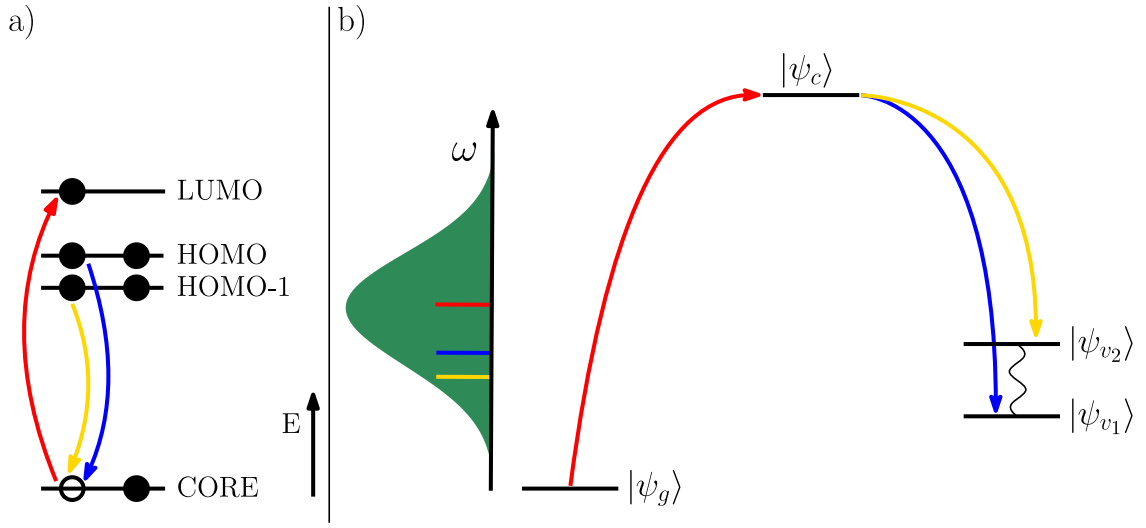

Figure 1.2: *Schematic representation of the RIXS and ISRIXS processes. Panel a) contains a representation in the one-particle picture. The system relaxes to its valence-excited states as the core-hole generated by the absorption is refilled during a radiative de-excitation of the electrons from the occupied MOs. The ISRIXS process is represented in panel b). The green Gaussian represents the pulse in the frequency domain, the red bar representing the absorbed frequency, the blue and yellow bars the emitted, Stokes frequencies. During the absorption step (red arrow) the system is excited from the ground state $|\psi_g\rangle$ to the core-excited state $|\psi_c\rangle$. In the stimulated emission step the system radiatively relaxes into a WP (indicated by the sinusoidal line) of valence-excited states $|\psi_{v_1}\rangle$ (blue arrow) and $|\psi_{v_2}\rangle$ (yellow arrow).*

step, indicated by the red arrow, corresponds to the absorption of a 'pump' photon, which excites a core-electron to the LUMO orbital. The second step corresponds to a spontaneous radiative de-excitation of the system, during which Stokes photons are emitted as the core-hole is refilled by electrons e.g. from the Highest Occupied Molecular Orbital (HOMO) (i.e. blue arrow) or the HOMO-1 (i.e. yellow arrow) orbitals. A typical RIXS measurement relies on narrowband X-Ray radiation (e.g. from a synchrotron) to pump the system, which subsequently relaxes via the incoherent radiation of Stokes photons. The coherent population of the valence-excited states relies on the nonlinear counterpart of RIXS, i.e. stimulated RIXS [45], wherein the radiative de-excitation step corresponds to a stimulated emission of Stokes photons. The practical application of the stimulated RIXS technique has been enabled by the development of the XFELs, which are capable of delivering short, intense and coherent X-Ray pulses [46, 47]. The first experimental demonstration of stimulated RIXS was provided by Weninger *et al.* [48], who showed evidence of the effect in a gaseous neon target excited by *fs* XFEL pulses. Similar experiments on carbon monoxide [49] paved the way to the demonstration of stimulated RIXS in molecules

by O'Neal *et al.* [50], who detected the population transfer to the valence-excited states of gaseous nitric oxide mediated by stimulated RIXS. This experiment was recently extended to the liquid phase by Alexander *et al.* [51], who reported the measurement of stimulated RIXS in liquid water. In both [50] and [51], the stimulated RIXS process was driven by an *as* XFEL pulse [32], which allowed to push the process to the impulsive limit. The Impulsive Stimulated Resonant Inelastic X-Ray Scattering (ISRIXS) process is schematised in terms of four stationary states of a molecule in panel b) of fig. 1.2. Here, the absorption, 'pump' step (red arrow) excites the system from the ground state $|\psi_g\rangle$ to a core-excited state $|\psi_c\rangle$, while the stimulated-emission step (i.e. the 'dump' step corresponding to the coherent emission of Stokes photons) leads to the radiative de-excitation from $|\psi_c\rangle$ to the manifold of valence-excited states $|\psi_{v_1}\rangle$ (i.e. blue arrow) and $|\psi_{v_2}\rangle$ (i.e yellow arrow). The energy difference between the pump and Stokes photons corresponds to optical excitation energies associated with the valence-excited states. As shown by the coloured bars within the pulse, both the pump and Stokes photon energies are contained within the coherent bandwidth of a single *as* X-Ray pulse, leading to the coherent population of the manifold of valence-excited states in a neutral molecule. The impulsive limit is reached as the excitation takes place within the few hundreds of *as* of the pulse duration, which is shorter than the timescale of the dynamics within the manifold of valence-excited states (corresponding to the inverse of their energy separation). This is a key factor in the study of ultrafast dynamics in molecules, as the dynamics following the excitation are determined solely by the prepared WP and are not influenced by external fields.

1.2.3 Characteristics of the ISRIXS wave packet

The characteristics of the WP launched by ISRIXS can be controlled through the properties of the *as* X-Ray pulse. For example, tuning the bandwidth of the pulse allows to regulate how many states are included in the WP, while changing the pulse polarisation enables the selection of the states according to their symmetry. A peculiarity of the WP launched by ISRIXS is related to the involvement of electrons from the core-shells in the excitation process. In fact, by tuning the *as* X-Ray pulse to be resonant with the core-excited states associated to different atoms, it is possible to coherently populate the valence-excited states with atomic specificity [52]. This corresponds to an accordingly atom-specific dynamical redistribution of the valence-electrons across the molecule, which should, in principle, be characterised by an initial localisation on the specific atom interested by the X-Ray excitation. This property and its applications have been explored in a number of publications by Mukamel *et al.* [53, 54, 55]. A pump-probe experiment is simulated in [53], where a WP of valence-excited states in 5-quinolinol is both pumped and probed via an ISRIXS process. The 5-quinolinol molecule is formed by two heteroaromatic rings, with a N and an O located on different rings. Pumping the molecule at the N K-Edge/O K-Edge results in the excitation of element-specific WPs, which are initially localised prevalently on the N-bearing/O-bearing ring. The atom-specific character of ISRIXS as a pump process can also be used to probe the time-evolution of the WP. That is, the atom-specificity can be used to choose the molecular regions where the WP is created and probed, consequently providing a temporally and spatially resolved reconstruction of the intramolecular electronic migration. A work

by Healion *et al.* [54] studies the preparation of a WP of valence particle-hole pairs via ISRIXS in cysteine, focusing on the initial, atom-specific localisation of the WP and the characteristics of the highly correlated motion of the valence particle-hole pairs. The WPs corresponding to excitations at the O, N and S K-Edge do not show clear evidence of an initial localisation around the excited atoms, with only the hole components of the WPs showing more convincing signs of this property. The atom-specific character is rather related to the initial distribution of the WP across the whole molecule and its dynamics, which clearly change depending on the K-Edge selected for the excitation. More recently Yong *et al.* [55] simulated an experiment where the valence-electron dynamics triggered by ISRIXS are monitored by ultrafast X-Ray diffraction in Oxazole. The Oxazole molecule is a heteroaromatic, 5-membered ring containing N and O. By exciting the molecule at the O K-Edge or at the N K-Edge with an *as* X-Ray pulse, an element-specific initial redistribution of the valence electrons is predicted which is however not clearly localised on the excited atom. This lack of localisation is attributed to the small dimensions of the molecule. A recent study by Balbi *et al.* [56] simulates a WP including both core-excited and valence-excited states. While the coherent population of the core-excited states is due to a one-photon X-Ray absorption process, the valence-excited states are coherently populated via ISRIXS. The study shows the dependence of the WP's properties on the level of theory (e.g. basis set, number of included core-excited states) and on the pulse properties (e.g. polarisation, K-Edge of the excitation). In particular, the initial localisation is discussed in the context of *p*-aminophenol excited at the O K-Edge. Snapshots of the time-dependent difference density, obtained by subtracting the ground state density from the time-dependent electronic density, show an initial electronic accumulation on O and more generally the localisation of the excitation in the region centred on O, which is followed by long-range electronic migration across the molecule. This work clearly shows the atom-specific localised characteristics of the X-Ray excitation, but does not discuss the particular contributions to the localisation coming from the core-excited and the valence-excited states (i.e. from the ISRIXS process). In conclusion, this brief review indicates that, especially in smaller systems, the atom-specific initial localisation of the WP excited via ISRIXS process is yet to be clearly demonstrated. The investigation of this aspect of the ISRIXS process is one of the goals of this work. The pursue of this objective relies on a theoretical platform which enables the accurate description of the time-dependent electronic structure of the molecule. In the next section, a brief review of various families of time-dependent electronic structure methods will be presented, providing the context for the theoretical methods used in this work.

1.3 Time-dependent electronic structure methods

The experimental studies of the electronic dynamics on the *as* timescale have been supported and enabled by the development of a variety of theoretical methods, which afford an accurate description of the time-dependent electronic structure of atoms and molecules. The objective of theory is the solution of the time-dependent Schrödinger equation (TDSE) for many-electron systems interacting with ultrashort and intense light pulses. Since the exact solution of the TDSE is limited to systems formed by few electrons (e.g. He or H_2), several approximate methods have been developed, which describe the electronic correlation within atomic and molecular systems in an increasingly accurate way. A computationally affordable approach is represented by the time-dependent density functional theory (TD-DFT) [57], within which the time-dependent many-body wavefunction is mapped to the time-dependent density. This reduces a many-particle problem to a one-particle problem, where the electronic correlation is accounted for (mostly in a semiempirical way) via the exchange and correlation functional. Exemplary applications of this method come from Véniard *et al.* [58], who applied it to the theoretical study of the response of atomic clusters of atoms to a strong field, or from Bruner *et al.* [59], who demonstrated the capability of TD-DFT to adequately describe the charge migration process in relatively large molecular systems. Despite its low computational cost, which allows its application to large systems, TD-DFT delivers the time-dependent electronic density and not the wave function, posing difficulties in the definition of the observables. Moreover, it is difficult to estimate the accuracy of the exchange and correlation functional and to systematically improve the description of the electronic correlation. This is allowed by wave function-based methods such as the time-dependent configuration interaction (TD-CI) approach. Within TD-CI, the wave function is expanded in terms of Slater determinants (SDs), with the time-dependence lying in the CI expansion coefficients. The full TD-CI theory stands as a benchmark capable of providing an exact solution of the TDSE. In practice, due to the combinatorial growth of the computational effort with the number of electrons and basis functions, the full TD-CI approach can be applied only to small systems with a moderate number of electrons and basis functions. The application of the TD-CI approach to larger systems relies on the truncation of the CI expansion [60]. The first (and most affordable) of the truncated TD-CI approaches is the TD-CI singles, within which the wave function is expanded in a basis of SDs formed by the reference determinant (usually corresponding to the Hartree-Fock (HF) ground state determinant) and singly excited determinants generated from the reference. This method was applied, for example, to the treatment of strong-field processes in atomic systems by Greenman *et al.* [61], to the study of strong-field ionisation in small molecular systems by Carlström *et al.* [62] or to the study of the ultrafast many-electron dynamics in a polyatomic molecule by Klamroth [63]. Starting from the TD-CI singles, the accuracy of the wave function ansatz can be improved systematically towards the full TD-CI limit by explicitly including doubly, triply, etc. excited SDs in the CI expansion [64, 65] or by describing the effects of their inclusion by means of perturbation theory [65, 66]. A step ahead with respect to the TD-CI approaches is represented by the family of methods collectively known as multiconfigurational time-dependent Hartree (MCTDH) [67]. As shown in [68] and references therein, the MCTDH approach provides an excel-

lent framework for the solution of the TDSE, which can flexibly adapt to systems formed by bosons, fermions or both type of indistinguishable particles. Based on the MCTDH method, the multiconfigurational time-dependent Hartree Fock (MCTDHF) approach [69] has been developed to describe the dynamics of many-electron systems. The MCTDHF expansion of the wave function extends the TD-CI ansatz by considering time-dependent SDs, which inherit their time-dependence from the one-particle orbitals forming them. This confers great flexibility to the MCTDHF method, which provides an accurate representation of the wave function with a reduced number of SDs compared to TD-CI [70]. Being based on a full-CI expansion, the great accuracy of MCTDHF is associated with a computational cost which scales exponentially with the number of electrons, thus limiting its application to small systems. To obviate to this problem, methods such as the time-dependent complete-active-space self-consistent-field (TD-CASSCF) [71] or the time-dependent restricted-active-space self-consistent-field (TD-RASSCF) [72] have been developed, allowing to extend the computational applicability to larger systems, while delivering a reasonably accurate description. Alternatively, approaches like the time-dependent multiconfiguration self-consistent field method [73] rely on the truncation of MCTDHF's CI expansion, allowing to systematically improve the quality of the wave function from the limiting case comprising a single time-dependent SD, corresponding to the time-dependent Hartree Fock method [74], to the exact MCTDHF solution. Another valid framework for the calculation of the correlated electronic dynamics is based on the excitation-class-based algebraic diagrammatic construction (ADC) and coupled-cluster (CC) methods. The ADC approach [75] provides a series of methods to accurately calculate excited states in large molecular systems. Examples of the application of ADC-based methods to time-dependent problems come from Kuleff *et al.* [76], who showed its application to the description of multielectron WP dynamics in large molecules, or from Ruberti *et al.* [77], who proposed a time-dependent ADC approach for the *Ab Initio* simulation of *as* pump-probe experiments. Within the CC approach [78], the many-body wave function is parametrized according to an exponential excitation operator acting on the reference SD. This ansatz makes the CC methods size-extensive (and size-consistent) at any level of truncation, which is a quality lacking in analogously truncated-configuration interaction (CI) approaches [79]. In addition to that, the accurate description of the electronic correlation provided by CC is accompanied by a favourable polynomial scaling of the computational costs with the system's size. The time-dependent coupled-cluster (TD-CC) approach is based on the introduction of a time-dependent excitation operator in the CC ansatz [80], which leads to the formulation of equations of motion for the time-dependent wave function and expressions for the expectation values of the relevant observables. The TD-CC method can effectively be used for the study of the valence electron dynamics in molecules as recently showed by Skeidsvoll *et al.* [81], who simulated a pump-probe transient absorption experiment involving lithium fluoride. Following the basic idea of the MCTDHF method, Kvaal proposed the orbital-adaptive TD-CC approach [82], which extends the TD-CC method by considering time-dependent one-particle orbitals. Based on Kvaal's work, Sato *et al.* [83] proposed the time-dependent optimised CC method applying it to the simulation of intense laser-driven correlated electron dynamics in atoms. Compared to results obtained via the TD-CASSCF approach, Sato *et al.* showed the accuracy and cost-effectiveness of CC-based methods by producing results of comparable quality

at a lower computational cost [84]. An alternative strategy to the solution of the TDSE is based on the expansion of the time-dependent wave function in terms of the eigenstates of the time-independent field-free Hamiltonian, which correspond to the ground and excited stationary states of the system. Based on this ansatz, the TDSE reduces to a set of coupled differential equations for the time-dependent coefficients of the expansion. A suitable approach for the accurate calculation of the stationary excited states and their properties is the equation of motion coupled-cluster (EOM-CC) method [85, 86], within which the stationary excited states are obtained by applying a linear excitation operator to the CC ground state. The expansion of the time-dependent wave function in terms of the EOM-CC states lies at the heart of the time-dependent equation of motion coupled-cluster (TD-EOM-CC) method [87], which has been applied to a variety of problems. For example, Sonk *et al.* [87] applied a TD-EOM-CC approach to the simulation of butadiene's response to the interaction with short and intense laser pulses. Similarly, Luppi *et al.* [88] used this method to calculate HHG spectra of H_2 and N_2. More recently, Skeidsvoll *et al.* [89] presented an application to the simulation of *as* valence pump-core probe spectra in small molecules, while Balbi *et al.* [56] studied the electronic dynamics triggered by an *as* X-Ray pulse, including a description of the ISRIXS process. The main drawback of the TD-EOM-CC approach lies in the necessity to perform the full diagonalization of the time-independent Hamiltonian, which poses a computational limit to the number of excited states included in the wave function ansatz. The theoretical platform in this work is based on the TD-EOM-CC ansatz of the time-dependent wave function. Differently from TD-EOM-CC, the time-dependent expansion coefficients (i.e. the probability amplitudes) associated to the core-excited and valence-excited states are here obtained via time-dependent perturbation theory (TDPT). The reason behind this choice is related to the calculation of the probability amplitudes associated to the valence-excited states, which are approximated as second-order perturbative contributions. Within TDPT the calculation of the second-order perturbative contributions involves the evaluation of a sum over intermediate states (SOS), which characterises also the RIXS transition moments. The conventional approach to the calculation of the SOS resorts to its truncation to a manifold of presumably dominant terms. Despite its computational advantages, the effects of the truncation on the accuracy of the transition moment are difficult to assess *a priori*. This problem was addressed by Nanda *et al.* [90, 91], who presented a formally exact reformulation of the RIXS transition moments which avoids the truncation of the SOS. This allows to avoid the truncation-related inaccuracies and circumvent the computational challenges related to the diagonalization of a large Hamiltonian, which might arise from the inclusion of numerous intermediate states in an accurate, 'truncated' calculation. In this work, the non-truncated implementation from Nanda *et al.* is applied to the calculation of the probability amplitudes associated to the valence-excited states. This choice is motivated by the formal exactness of the non-truncated approach and accuracy of the EOM-CC method, which should translate into a precise description of the valence-excitation and the intramolecular electronic dynamics. In this sense, the goal of this effort is to offer a very accurate computational platform for the simulation of the coherent population of the valence-excited electronic states via ISRIXS in the perturbative regime.

1.4 Outline of the dissertation

A pivotal moment of a photochemical reaction is the initial interaction of the system with the light pulse, during which the necessary energy for the chemical reaction is deposited into the molecule. It is relatively to this moment that one of the fundamental questions of chemical reaction dynamics is asked, which Ahmed Zewail, in his Nobel Prize feature article [92], formulated as:

> *How does the energy put into a reactant molecule redistribute among the different degrees of freedom, and how fast does this happen?*

The investigation presented in this work departs from this question, aiming at understanding how the energy deposited by an *as* X-Ray pulse in a neutral molecule distributes among its electronic DOF (represented in terms of the ground, valence-excited and core-excited states) during the excitation of an electronic WP. In particular, based on the ideas underlying the field of attochemistry, the goal is to understand how the excitation of the WP modifies the intramolecular electronic distribution during and within a few *fs* after the pulse. Based on these objectives, the first questions guiding the investigation are formulated as:

> *Q1: How does the energy distribute among the considered excited states? How does the excitation modify the electronic distribution within the molecule during and after a few fs after the pulse?*

The answers to Q1 are based on the analysis of the time-dependent difference electronic density (i.e. obtained by subtracting the ground state density to the time-dependent electronic density), whose distribution reflects the properties of the excitation and the energy distribution across the electronic states of the molecule. In particular, the analysis is based on the decomposition of the difference density in terms of the components of the density matrix, which allows separating the properties of the excitation related to the core-excited and valence-excited states. The control of a chemical reaction through the electrons is based on the possibility of using the properties of the *as* pulse to manipulate the dynamical electronic distribution within the molecule. This is the basis for the next step in the investigation, which is concerned with understanding how the pulse polarisation and the atomic-specificity of the X-Ray excitation influence the dynamical electronic distribution within the molecule. This goal corresponds to answering the following questions:

> *Q2: How do the properties of the excitation depend on the pulse polarisation and the core-excited states the X-Ray pulse is resonant to? How is the dynamical electronic distribution within the molecule conditioned by these pulse parameters?*

The answers to Q2 are based on a systematic study of the dynamics within the difference density and its components as they vary according to the chosen edge for the X-Ray excitation and the pulse polarisation. In particular, the dependence on the former is considered in order to investigate the atom-specific properties of the WP, with special attention posed on the observation of the initial, atom-specific localisation of the valence electronic density due to the ISRIXS process. The dissertation is structured as follows: the theoretical tools used to conduct the investigation and the details of their computational implementation are presented in chapters 2

and 3. The investigation guided by Q1 and Q2 is conducted in the context of two molecules, carbonyl sulphide (OCS) and Oxazole, which are considered as they are examples of linear and ring-shaped molecular systems. The results relative to OCS are presented in chapter 4 while those relative to Oxazole are presented in chapter 5, with separate discussion sections being attached to each chapter. The results obtained for OCS and Oxazole will be discussed in a more general framework in chapter 6, where the potential application of each component of the excitation as a 'platform' for the manipulation of the electronic dynamics in a neutral molecule will be assessed, indicating a set of possible outlooks for the project.

CHAPTER 2

Theory

This chapter is dedicated to the presentation of the theoretical background necessary for the simulation of the electronic dynamics in a neutral molecule. The theory revolves around the solution of the TDSE,

$$i\frac{\partial}{\partial t}\left|\Psi(t)\right\rangle = \hat{H}\left|\Psi(t)\right\rangle, \tag{2.1}$$

and the study of the properties of the time-dependent state $|\Psi(t)\rangle$. In section 2.1, the fundamentals of the semiclassical theory of light-matter interaction are discussed, leading to the explicit formulation of the Hamiltonian operator appearing in eq. (2.1). The focus moves to the description of the molecular electronic structure in section 2.2, where the fundamentals of the EOM-CC theory are presented, setting the stage for the practical computation of the molecular properties. The description of the quantum dynamics of $|\Psi(t)\rangle$ is presented in section 2.3, where the discussion is developed in the context of TDPT. The chapter ends with section 2.4, where the time-dependent electronic density and its perturbative decomposition are discussed, defining the tools used in the analysis performed in the results' chapters.

2.1 Theory of light-matter interaction

2.1.1 The minimal-coupling principle

The description of the combined system formed by the molecule and the radiation field starts at the classical level. The molecule can be considered as a system of N *nonrelativistic* particles, each characterised by a charge q_ζ, a mass m_ζ, a canonical momentum $\boldsymbol{p}_\zeta$ and a position $\boldsymbol{r}_\zeta$ (defined with respect to a three-dimensional coordinate system). The electromagnetic field established by the charged particles and the radiation is defined by a vector potential $\boldsymbol{A}(\boldsymbol{r},t)$ and a scalar potential $\phi(\boldsymbol{r},t)$, which describe both the inter-particle and the particle-radiation interactions. According to the *principle of minimal coupling* [93, 94], the interacting Hamiltonian for each particle can be obtained by applying the substitution

$$\boldsymbol{p}_\zeta \to \boldsymbol{p}_\zeta - q_\zeta \boldsymbol{A}(\boldsymbol{r}_\zeta, t) \tag{2.2}$$

in the free-particle Hamiltonian $h_\zeta = {}^{\boldsymbol{p}_\zeta^2}/_{2m_\zeta}$, which replaces the canonical momentum with the kinematic momentum [93, 95]. This substitution is accompanied by the transformation

$$h_\zeta \to h_\zeta + q_\zeta \phi(\boldsymbol{r}_\zeta, t), \tag{2.3}$$

which leads to the minimal coupling Hamiltonian for a single particle

$$h_\zeta = \frac{[\boldsymbol{p}_\zeta - q_\zeta \boldsymbol{A}(\boldsymbol{r}_\zeta, t)]^2}{2m_\zeta} + q_\zeta \phi(\boldsymbol{r}_\zeta, t). \tag{2.4}$$

Here, it can be seen that the particle's coupling with the electromagnetic fields relies entirely on the particle's electric charge and not on its higher multipole moments, hence the 'minimal' definition of the coupling.

2.1.2 Electromagnetic potentials and the Coulomb Gauge

The classical behaviour of the electric field, $\boldsymbol{E}(\boldsymbol{r},t)$, the magnetic field, $\boldsymbol{B}(\boldsymbol{r},t)$, and their interaction with charged particles and currents is described completely by the Maxwell equations. According to the homogeneous Maxwell equations[I], the electric and magnetic fields are completely determined by the scalar and vector potentials as specified by

$$\boldsymbol{E}(\boldsymbol{r},t) = -\frac{\partial \boldsymbol{A}(\boldsymbol{r},t)}{\partial t} - \boldsymbol{\nabla}\phi(\boldsymbol{r},t), \tag{2.6a}$$

$$\boldsymbol{B}(\boldsymbol{r},t) = \boldsymbol{\nabla} \times \boldsymbol{A}(\boldsymbol{r},t). \tag{2.6b}$$

The fields $\boldsymbol{E}(\boldsymbol{r},t)$ and $\boldsymbol{B}(\boldsymbol{r},t)$ are experimentally measurable physical observables, which are uniquely determined. The same is not true for the potentials $\boldsymbol{A}(\boldsymbol{r},t)$ and

[I] In atomic units, the homogeneous Maxwell equations read

$$\boldsymbol{\nabla} \times \boldsymbol{E}(\boldsymbol{r},t) - \frac{\partial \boldsymbol{B}(\boldsymbol{r},t)}{\partial t} = 0 \qquad \boldsymbol{\nabla} \cdot \boldsymbol{B}(\boldsymbol{r},t) = 0. \tag{2.5}$$

$\phi(\boldsymbol{r},t)$, which bear a certain degree of arbitrariness. In fact, the potentials can be transformed according to the so-called *gauge transformations* [96]

$$\phi(\boldsymbol{r},t) \to \phi(\boldsymbol{r},t) - \frac{\partial f(\boldsymbol{r},t)}{\partial t}, \tag{2.7a}$$

$$\boldsymbol{A}(\boldsymbol{r},t) \to \boldsymbol{A}(\boldsymbol{r},t) + \boldsymbol{\nabla} f(\boldsymbol{r},t). \tag{2.7b}$$

Here, $f(\boldsymbol{r},t)$ is a smooth and real-valued gauge function. The gauge transformations do not affect $\boldsymbol{E}(\boldsymbol{r},t)$ and $\boldsymbol{B}(\boldsymbol{r},t)$, which, being physical observables, are gauge invariant. A suitable gauge choice at the nonrelativistic limit is given by the *Coulomb gauge*, which is defined by the condition [93]

$$\boldsymbol{\nabla} \cdot \boldsymbol{A}(\boldsymbol{r},t) = 0. \tag{2.8}$$

Being vector fields, the electric and magnetic fields can be decomposed into sums of a zero-curl, longitudinal component (indicated by $^{||}$) and a zero-divergence, transverse component (indicated by $^{\perp}$). Within the Coulomb gauge, the contributions of $\boldsymbol{A}(\boldsymbol{r},t)$ and $\phi(\boldsymbol{r},t)$ to the transverse and longitudinal components of $\boldsymbol{E}(\boldsymbol{r},t)$ and $\boldsymbol{B}(\boldsymbol{r},t)$ separate [93]. This entails writing the components of the electric field as

$$\boldsymbol{E}^{||}(\boldsymbol{r},t) = -\boldsymbol{\nabla}\phi(\boldsymbol{r},t) \qquad \text{and} \qquad \boldsymbol{E}^{\perp}(\boldsymbol{r},t) = -\frac{\partial \boldsymbol{A}(\boldsymbol{r},t)}{\partial t}, \tag{2.9}$$

while the magnetic field, being purely transverse according to eq. (2.5), is simply given by eq. (2.6b). The dynamical behaviour of the potentials is determined by the *inhomogeneous* Maxwell equations[II]. Expressed in terms of the potentials in the Coulomb gauge, these read [93]

$$\Delta\phi(\boldsymbol{r},t) = -4\pi \sum_{\zeta}^{N} q_\zeta \delta(\boldsymbol{r} - \boldsymbol{r}_\zeta(t)), \tag{2.11}$$

$$(\Delta - \alpha^2 \frac{\partial^2}{\partial t^2})\boldsymbol{A}(\boldsymbol{r},t) = -4\pi\alpha^2 \sum_{\zeta}^{N} \boldsymbol{j}_\zeta^{\perp}(\boldsymbol{r},t), \tag{2.12}$$

where $\boldsymbol{j}_\zeta^{\perp}(\boldsymbol{r},t)$ is the transverse current due to the ζ^{th} particle. With the choice of the Coulomb gauge, the scalar potential corresponds to the *instantaneous* Coulomb potential, which is given by the solution of Poisson's eq. (2.11), i.e.

$$\phi(\boldsymbol{r},t) = \sum_{\zeta}^{N} \frac{q_\zeta}{|\boldsymbol{r} - \boldsymbol{r}_\zeta(t)|}. \tag{2.13}$$

[II] In atomic units, the inhomogeneous Maxwell equations read

$$\boldsymbol{\nabla} \cdot \boldsymbol{E}(\boldsymbol{r},t) = 4\pi \sum_{\zeta}^{N} q_\zeta \delta(\boldsymbol{r} - \boldsymbol{r}_\zeta(t)), \tag{2.10a}$$

$$\boldsymbol{\nabla} \times \boldsymbol{B}(\boldsymbol{r},t) = \alpha^2 \frac{\partial \boldsymbol{E}(\boldsymbol{r},t)}{\partial t} + 4\pi\alpha^2 \sum_{\zeta}^{N} \boldsymbol{j}_\zeta(\boldsymbol{r},t). \tag{2.10b}$$

2.1.3 The semiclassical method

The passage to a quantized description of the molecule-field system entails the conversion of the classical dynamical variables to quantum operators, which are subject to the canonical commutation rules [93, 97]. The quantization of both the molecular and radiation field degrees of freedom (DOFs) leads to the Quantum Electrodynamics (QED) theory. Its rigorousness is counteracted by its computational expense, which makes the solution of the complete QED problem unfeasible in most cases. Within QED, all the DOFs are treated at the same level, implying a symmetric energy exchange between them. If the radiation field is very intense this 'symmetry' breaks, since any influence of the molecule on the radiation field becomes negligibly small. The number of photons associated with the quantized radiation field are so numerous that the radiation field can be treated as a classical, fixed, external agent acting on the quantized molecular DOFs. This semiclassical treatment affects the scalar and the vector potential differently in the context of the Coulomb gauge. The scalar potential, which mediates the intramolecular interactions, takes the form of the Coulomb operator

$$\hat{\phi}(\hat{\boldsymbol{r}}) = \sum_{\zeta}^{N} \frac{q_\zeta}{|\hat{\boldsymbol{r}} - \hat{\boldsymbol{r}}_\zeta|}, \tag{2.14}$$

while the vector potential, which describes the radiation field, is treated classically. The application of the semiclassical treatment is limited by the impossibility of describing spontaneous decay processes such as fluorescence [93]. Furthermore, the theory is restricted to a 'microscopic' level, with its extrapolation limited to a diluted gas of molecules (i.e. at a pressure of $\approx 0.1\,\mathrm{mmHg}$) [98].

2.1.4 The semiclassical Hamiltonian operator

The semiclassical many-particle Hamiltonian operator is obtained by applying the considerations discussed in sections 2.1.2 and 2.1.3 to the minimal-coupling Hamiltonian in eq. (2.4) and by summing the contributions from all the charged particles of the system. The resulting operator has the form

$$\hat{H}(t) = \sum_{\zeta}^{N} \left\{ \frac{[\hat{\boldsymbol{p}}_\zeta - q_\zeta \boldsymbol{A}(\boldsymbol{r}_\zeta, t)]^2}{2m_\zeta} + q_\zeta \hat{\phi}(\hat{\boldsymbol{r}}_\zeta) \right\}, \tag{2.15}$$

where the position and momentum have become first quantized operators in the Schrödinger picture and the vector potential is a classical complex-valued field. Inserting the definition of the Coulomb operator from eq. (2.14) into eq. (2.15) leads to

$$\hat{H}(t) = \sum_{\zeta}^{N} \Big[\underbrace{\frac{\hat{\boldsymbol{p}}_\zeta^2}{2m_\zeta} + q_\zeta \sum_{\zeta' \neq \zeta}^{N} \frac{q_{\zeta'}}{|\hat{\boldsymbol{r}}_\zeta - \hat{\boldsymbol{r}}_{\zeta'}|}}_{\hat{H}_{\mathrm{mol}}} - \underbrace{\frac{q_\zeta \hat{\boldsymbol{p}}_\zeta \cdot \boldsymbol{A}(\boldsymbol{r}_\zeta, t)}{m_\zeta} + \frac{q_\zeta^2 \boldsymbol{A}^2(\boldsymbol{r}_\zeta, t)}{2m_\zeta}}_{\hat{H}_{\mathrm{int}}(t)} \Big], \tag{2.16}$$

where $\hat{H}_{\mathrm{mol}}$ is the *molecular* Hamiltonian operator, while $\hat{H}_{\mathrm{int}}(t)$ is the *interaction* Hamiltonian operator. The explicit time-dependence of $\hat{H}_{\mathrm{int}}(t)$ is related to $\boldsymbol{A}(\boldsymbol{r}, t)$, whose instantaneous value defines a new, effective $\hat{H}_{\mathrm{int}}(t)$ at each instant t. In

general, $\hat{H}_{\text{int}}(t')$ and $\hat{H}_{\text{int}}(t'')$ do not commute at two different instants of time t' and t''. This makes the time-ordering of t' and t'' important in the development of the perturbative theory [95]. In eq. (2.16), no additional terms related to the electronic spin are included, which entails neglecting effects like the level splitting due to spin-orbit coupling. This is acceptable for the organic molecules considered in this work, as they contain only light atoms [99].

Molecular Hamiltonian operator

The molecular Hamiltonian operator describes the isolated molecule, which is formed by N_{n} nuclei and N_{e} electrons (with $N = N_{\text{n}} + N_{\text{e}}$). The generic indexes ξ, ζ used in eqs. (2.15) and (2.16) contain both the electronic indexes $\{i, j, ...\}$ and the nuclear indexes $\{I, J, ...\}$. According to the new indexing convention, $\hat{H}_{\text{mol}}$ can be written as

$$\hat{H}_{\text{mol}} = \underbrace{\sum_{i}^{N_{\text{e}}} \frac{\hat{\boldsymbol{p}}_i^2}{2}}_{\hat{T}_e} + \underbrace{\sum_{j<i}^{N_{\text{e}}} \frac{1}{|\hat{\boldsymbol{r}}_i - \hat{\boldsymbol{r}}_j|}}_{\hat{V}_{ee}} - \underbrace{\sum_{i}^{N_{\text{e}}} \sum_{J}^{N_{\text{n}}} \frac{Z_J}{|\hat{\boldsymbol{r}}_i - \hat{\boldsymbol{r}}_J|}}_{\hat{V}_{eN}} + \underbrace{\sum_{I}^{N_{\text{n}}} \frac{\hat{\boldsymbol{p}}_I^2}{2m_I}}_{\hat{T}_N} + \underbrace{\sum_{J<I}^{N_{\text{n}}} \frac{Z_J Z_I}{|\hat{\boldsymbol{r}}_I - \hat{\boldsymbol{r}}_J|}}_{\hat{V}_{NN}}. \tag{2.17}$$

Here, according to the a.u. system, $q_i = -1$ and $m_i = 1$, while Z_I and m_I represent, the nuclear charge to e ratio (i.e. the atomic number Z) and the nuclear mass to m_e ratio, respectively. The $\hat{T}_e$ term in eq. (2.17) represents the electronic kinetic energy operator, while the term $\hat{T}_N$ represents the nuclear kinetic energy operator. The operator $\hat{V}_{eN}$ describes the electron-nucleus attraction, while the operators $\hat{V}_{NN}$ and $\hat{V}_{ee}$ describe the nucleus-nucleus and the electron-electron repulsion, respectively.

Interaction Hamiltonian operator and dipole approximation

The interaction Hamiltonian operator describes the interaction of the molecule with the radiation field. The radiation field considered here spans an interval of frequencies characteristic of the X-Ray region of the electromagnetic spectrum. Since the nuclei are too heavy to undergo substantial oscillation in response to the field [94], the sum in eq. (2.16) can be limited to the electrons alone. As a consequence, $\hat{H}_{\text{int}}(t)$ assumes the form

$$\hat{H}_{\text{int}}(t) = \sum_{i}^{N_{\text{e}}} \Big[\hat{\boldsymbol{p}}_i \cdot \boldsymbol{A}(\boldsymbol{r}_i, t) + \frac{\boldsymbol{A}^2(\boldsymbol{r}_i, t)}{2} \Big]. \tag{2.18}$$

The X-Ray field interacts particularly with the core-electrons of the molecule, whose wave functions extend over a region of space much smaller than the X-Ray wavelength [33]. Thus, at their length scale, the core-electrons effectively 'see' the radiation field as spatially-uniform. This allows to apply the dipole approximation. To this end, $\boldsymbol{A}(\boldsymbol{r}, t)$ is expanded around the molecule's centre of mass, $\boldsymbol{r}_{cm}$, retaining only the lowest-order term, i.e. $\boldsymbol{A}(\boldsymbol{r}_{cm}, t)$ [100]. By setting the centre of mass coincident with the origin of the coordinate system, i.e. $\boldsymbol{A}(\boldsymbol{r}_{cm}, t) \equiv \boldsymbol{A}(\boldsymbol{0}, t)$, the $\hat{H}_{\text{int}}(t)$ in the dipole approximation can be written as

$$\hat{H}_{\text{int}}(t) = \sum_{i}^{N_{\text{e}}} \Big[\hat{\boldsymbol{p}}_i \cdot \boldsymbol{A}(t) + \frac{\boldsymbol{A}^2(t)}{2} \Big]. \tag{2.19}$$

Here, $\boldsymbol{r}_{cm} \equiv \mathbf{0}$ has been omitted to simplify the notation. In addition, the dipole approximation implies that $\boldsymbol{\nabla} \times \boldsymbol{A}(t) = 0$ determining $\boldsymbol{B}(\boldsymbol{r}, t) = 0$.

2.1.5 Length frame of light-matter interaction

The semiclassical description of light-matter interaction is not unique; instead there exist different, equivalent 'frames', which are related by unitary transformations [95]. These can be defined using the operator $\hat{U}$ as

$$|\Psi(t)\rangle \to \hat{U}\,|\Psi(t)\rangle \qquad\qquad \hat{H}(t) \to \hat{U}\hat{H}(t)\hat{U}^{\dagger}, \tag{2.20}$$

with the transformed $|\Psi(t)\rangle$ and transformed Hamiltonian operator equally satisfying the TDSE. A particular choice for $\hat{U}$ corresponds to the Göppert-Mayer transformation [101]

$$\hat{U}^{L} = e^{-i\boldsymbol{A}(t)\cdot\hat{\boldsymbol{r}}}, \tag{2.21}$$

which leads to the *length frame* of light-matter interaction

$$|\Psi(t)\rangle^{L} = \hat{U}^{L}\,|\Psi(t)\rangle \qquad\qquad \hat{H}^{L}(t) = \hat{H}_{\mathrm{mol}} - \boldsymbol{E}^{\perp}(t)\cdot\hat{\boldsymbol{\mu}}. \tag{2.22}$$

Here, $\hat{H}^{L}_{\mathrm{int}}(t) = \boldsymbol{E}^{\perp}(t)\cdot\hat{\boldsymbol{\mu}}$, and $\hat{\boldsymbol{\mu}} = \sum_i -\hat{\boldsymbol{r}}_i$ is the electric dipole operator. In the following, the theory will be developed in the length frame, since it allows a more straightforward computational implementation. In order to have a simpler notation, hereinafter $|\Psi\rangle \equiv |\Psi(t)\rangle^{L}$ and $\hat{H}(t) \equiv \hat{H}^{L}(t)$, with the transverse electric field being indicated simply as $\boldsymbol{E}(t)$.

2.2 Molecular electronic structure

In this section, the discussion will focus on the description of the stationary states of the molecule. The stationary states correspond to the energy eigenstates of $\hat{H}_{\mathrm{mol}}$, which are obtained as solutions of the time-independent Schrödinger equation (TISE),

$$\hat{H}_{\mathrm{mol}} |\psi_n\rangle = E_n |\psi_n\rangle . \tag{2.23}$$

The set of all eigenstates corresponds to an orthonormal basis, which can be used to represent $|\Psi(t)\rangle$ and the operators [95]. In the following, the theoretical tools and approximations involved in the description of the molecular electronic structure are presented, preparing the ground for the description of the computational implementation in chapter 3.

2.2.1 Particles in a molecule: focusing on the electrons

The description of a molecular system generally includes both the nuclei and the electrons, with the electrons being 'kept captive' in the field generated by the nuclei and the nuclei being bound to each other by the electrons' field. Since the electrons are much lighter than the nuclei, they move much faster when submitted to comparable forces. It follows that, to a good degree of approximation, the motion of the nuclei can be considered to exert an 'adiabatic' [102] perturbation to the motion of the electrons. This allows to apply the *clamped nuclei approximation*, according to which the electrons in a molecule are considered to be moving in the field of a fixed nuclear configuration [103]. Within this approximation, the $\hat{T}_N$ term of $\hat{H}_{\mathrm{mol}}$ can be neglected and the $\hat{V}_{NN}$ term becomes a constant, leading to the electronic Hamiltonian

$$\hat{H}_{\mathrm{e}} = \hat{T}_e + \hat{V}_{ee} + \hat{V}_{eN}. \tag{2.24}$$

Here, the $\hat{V}_{NN}$ term is omitted since the addition a constant to $\hat{H}_{\mathrm{e}}$ does not modify its eigenstates, but merely adds a constant offset to its eigenvalues. Considering $\hat{H}_{\mathrm{e}}$ in eq. (2.23) leads to the electronic TISE,

$$\hat{H}_e |\psi_n\rangle_e = E_n^e |\psi_n\rangle_e . \tag{2.25}$$

The solutions of eq. (2.25) correspond to the electronic eigenstates of the molecule, $|\psi_n\rangle_e$, which form a complete orthonormal set at a given nuclear configuration [104][III]. This work focuses specifically on the study of the purely electronic dynamics, solving eq. (2.25) at a fixed nuclear configuration corresponding to the equilibrium nuclear geometry of the electronic ground state. By considering a single, fixed nuclear geometry, the model neglects the effects of the distribution of nuclear positions (in particular for the light hydrogen atoms) in the ground-state and subsequent nuclear motion upon electronic excitation which can lead to fast decoherence of the electronic wave packet [105, 106]. Since only $|\psi_n\rangle_e$ and E_n^e are considered in this work, in the following sections the notation will be simplified by considering $|\psi_n\rangle \equiv |\psi_n\rangle_e$ and $E_n \equiv E_n^e$.

[III] This corresponds, in the position-space representation, to electronic wave functions depending on the position of the electrons and only *parametrically* on the positions of the nuclei.

2.2.2 The many-electron state and its properties

The solution of eq. (2.25) and its computational implementation rely on the definition of the many-electron states, $|\psi_n\rangle$, whose construction and relevant properties can be elucidated by taking as an example the simple case of a two-electron system. The construction of a two-electron state starts from the consideration of a generic system of two identical but distinguishable particles. Each particle is defined within a one-particle Hilbert space, $\mathcal{H}^1$, spanned by a one-particle basis, $\{|\chi_p\rangle\,|p \in [1, v]\}$. The states of the two-particle system are defined in a two-particle Hilbert space

$$\mathcal{H}^2 = \mathcal{H}^1 \otimes \mathcal{H}^1, \tag{2.26}$$

where $\otimes$ denotes a tensor product operation. Following eq. (2.26), a basis for $\mathcal{H}^2$ can be constructed from product states

$$|\chi_p\rangle \otimes |\chi_q\rangle \equiv |\chi_p, \chi_q\rangle\,, \tag{2.27}$$

with the dimension of $\mathcal{H}^2$ being equal to v^2. In the description provided by eq. (2.27), particle 1 is in state $|\chi_p\rangle$ while particle 2 is in state $|\chi_q\rangle$. On the other hand, the interchange of the particles according to the action of the transposition operator $\hat{P}_{12}$, i.e.

$$\hat{P}_{12}\,|\chi_p, \chi_q\rangle = |\chi_q, \chi_p\rangle\,, \tag{2.28}$$

leads to a new state $|\chi_q, \chi_p\rangle$, distinct from $|\chi_p, \chi_q\rangle$ for $p \neq q$, where particle 1 is in state $|\chi_q\rangle$ and particle 2 is in state $|\chi_p\rangle$. This description is not suitable for quantum mechanics, wherein identical particles are *indistinguishable*. This implies that, upon action of $\hat{P}_{12}$, the state of a two-particle system remains the same up to a phase factor, which is equal to minus one in the case of the electrons, owing to their fermionic nature. Accordingly, a state of a two-electron system takes the form [95]

$$|\Phi\rangle = \frac{1}{\sqrt{2}}(|\chi_p, \chi_q\rangle - |\chi_q, \chi_p\rangle). \tag{2.29}$$

This follows the antisymmetric prescription of the *Pauli exclusion principle* [107], which ensures that no two electrons can occupy the same state. These concepts can be extended to a N_e-electron system by constructing the N_e-particle Hilbert space, $\mathcal{H}^{N_e}$, and extending the definitions for the two-particle case in eqs. (2.26) and (2.27) to the N_e-particle case. The transposition operator $\hat{P}_{12}$, referring to particles 1 and 2 in the two-particle case, is defined in $\mathcal{H}^{N_e}$ as $\hat{P}_2$, with the subscript referring to all possible couples of particles. A permutation operator $\hat{P}_n$, defining the permutation of any set of $n \leq N_e$ particles, is constructed as an associative product of $\hat{P}_2$ operators, with its parity corresponding to the odd/even number of $\hat{P}_2$ operators used for its construction. All the $N_e!$ permutation operators for the N_e particles form a permutation group $\mathcal{S}_{N_e}$, also called symmetric group [108]. The set of all $\hat{P}_n \in \mathcal{S}_{N_e}$ is used to build the antisymmetrization operator

$$\hat{\mathcal{A}} = \frac{1}{N_e!} \sum_{\hat{P}_n \in \mathcal{S}_{N_e}} \mathrm{sgn}(\hat{P}_n)\hat{P}_n, \tag{2.30}$$

where the sign function $\mathrm{sgn}(\hat{P}_n)$ assumes a minus/plus one value depending on the odd/even parity of $\hat{P}_n$. The operator $\hat{\mathcal{A}}$ projects the elements of $\mathcal{H}^{N_e}$ into its antisymmetrized subspace $\mathcal{H}^{N_e}_{\mathcal{A}}$, within which the many-electron states are defined. In

particular, the action of $\hat{\mathcal{A}}$ on the elements of $\mathcal{H}^{N_e}$'s basis defines the basis elements of $\mathcal{H}^{N_e}_{\mathcal{A}}$ as

$$|\Phi\rangle = \frac{1}{\sqrt{N_e!}}\hat{\mathcal{A}}\,|\chi_p, \chi_q, \ldots, \chi_r\rangle \equiv |pq\ldots r\rangle\,, \tag{2.31}$$

with the prefactor introduced for normalisation purposes. Since the signs of the different terms in eq. (2.31) are determined in the same way as those of a determinant, $|\Phi\rangle$ is commonly called *Slater determinant (SD)* [60]. It follows that the basis of SDs can be used for the expansion of an electronic state

$$|\psi_n\rangle = \sum_a \alpha_a\,|\Phi\rangle_a\,, \tag{2.32}$$

where the sum runs over the $\binom{v}{N_e}$ elements of the basis.

Second quantization formalism

The second quantization formalism offers the opportunity to represent the many-electrons states and operators in a compact notation, providing a more efficient way for their manipulation. The formalism depends on the orthonormal one-electron basis $\{|\chi_p\rangle\,|p \in [1, v]\}$, which is used to construct $\mathcal{H}^n_{\mathcal{A}}$ spaces for $n = 0, 1, \ldots, v$ electrons. The ensemble of the so-constructed many-electrons Hilbert spaces can be used to build the Fock space $\mathcal{F}_{\mathcal{A}}$ as

$$\mathcal{F}_{\mathcal{A}} = \bigoplus_{n=0}^{v} \mathcal{H}^n_{\mathcal{A}}, \tag{2.33}$$

where $\oplus$ represents the direct sum operation. The second quantization formalism is defined within $\mathcal{F}_{\mathcal{A}}$, hence offering a flexible representation of the many-electron states and operators with respect to the number of electrons in the system [94, 109]. The SDs and the operators are represented in terms of the *creation and annihilation operators*, $\hat{c}^\dagger_p$ and $\hat{c}_p$. These operators are defined in terms of their action on the SDs as

$$\hat{c}^\dagger_p\,|q\ldots r\rangle = |pq\ldots r\rangle\,, \tag{2.34a}$$

$$\hat{c}_p\,|pq\ldots r\rangle = |q\ldots r\rangle\,, \tag{2.34b}$$

and by their anticommutation relations

$$\{c^\dagger_p, c^\dagger_q\} = \{c_p, c_q\} = 0, \qquad \{c^\dagger_p, c_q\} = \hat{\delta}_{pq}, \tag{2.35}$$

which contain all the antisymmetry properties of the electronic states [60]. In particular, by applying a sequence of creation operators to the vacuum state, $|\rangle$, it is possible to construct an arbitrary SD [60, 109], i.e.

$$c^\dagger_p c^\dagger_q \ldots c^\dagger_r\,|\rangle = |pq\ldots r\rangle\,. \tag{2.36}$$

The bra state corresponding to the ket in eq. (2.36) is built from the vacuum bra, $\langle|$, which is defined according to $\langle|\rangle = 1$. That is,

$$\langle|\,c_r \ldots c_q c_p = \langle pq\ldots r|\,, \tag{2.37}$$

where the adjoint relation of the creation and annihilation operators was used [109]. Within the second quantization formalism, also the operators can be represented in terms of creation and annihilation operators; the electronic Hamiltonian operator takes the form [109]

$$\hat{H}_e = \sum_{pq} \langle p| \hat{h} |q\rangle \, \hat{c}_p^\dagger \hat{c}_q + \frac{1}{2} \sum_{pqrs} \langle pq| \hat{v} |rs\rangle \, \hat{c}_p^\dagger \hat{c}_q^\dagger \hat{c}_s \hat{c}_r. \tag{2.38}$$

Here, the first term represents the one-electron interactions, with $\hat{h} = \hat{T}_e + \hat{V}_{eN}$, and the second term represents the two-electron interactions, with $\hat{v} = \hat{V}_{ee}$. The formulation of $\hat{H}_e$ in second quantization is very useful, since a single Hamiltonian can be used to describe systems containing an arbitrary number of electrons [94].

2.2.3 The first approximation: Hartree-Fock theory

The first approximated solution of the many-electron problem is afforded by the *Hartree-Fock (HF)* method. Within HF, the electronic ground state of the molecule, $|\psi_g\rangle$, is approximated as a single, variationally optimized Slater determinant, $|\Phi_0\rangle$, of energy E_{HF} [60]. This corresponds to a description of the many-electron system in which the electrons with parallel spin are correlated, while those of antiparallel spin 'see' the others as a mean field [60]. The E_{HF} represents an upper limit to the exact nonrelativistic energy of the electronic ground state, E_g, with $E_g - E_{HF}$ corresponding to the correlation energy E_{corr}. The task assigned to post-HF methods, such as the *coupled-cluster (CC)* method, is to obtain E_{corr} by improving the description of $|\psi_g\rangle$. A common approach relies on the expansion of $|\psi_g\rangle$ in the basis of SDs. For this purpose, it is convenient to change the reference state for the construction of the SDs from the physical vacuum $|\rangle$ to $|\Phi_0\rangle$, which becomes the *Fermi vacuum* of the system [109]. The elements of the one-particle basis spanning $|\Phi_0\rangle$ (generically indicated by the indices $p, q, r, \dots$) are then divided in two groups: the *hole states* (indicated by indices $i, j, k, \dots$), which correspond to the occupied one-particle states in $|\Phi_0\rangle$, and the *particle states* (indicated by the indices $a, b, c, \dots$) which correspond to the unoccupied one-particle states in $|\Phi_0\rangle$. A basis of SDs for the N_e-electron system can be generated in terms of hole-particle excitations from $|\Phi_0\rangle$, i.e.

$$|\Phi_i^a\rangle \equiv c_a^\dagger c_i \, |\Phi_0\rangle \qquad \text{(single excitation)}, \tag{2.39a}$$

$$|\Phi_{ij}^{ab}\rangle \equiv c_a^\dagger c_b^\dagger c_j c_i \, |\Phi_0\rangle \qquad \text{(double excitation)}, \tag{2.39b}$$

and so on for triply, quadruply, etc. excited determinants. The change of the reference state affects also $\hat{H}_e$, which assumes the form [109]

$$\begin{aligned} \hat{H}_e = \Big[\sum_{pq} \langle p| \hat{h} |q\rangle + \sum_{ipq} (\langle i,p| \hat{v} |i,q\rangle - \langle i,p| \hat{v} |q,i\rangle) \Big] \{\hat{c}_p^\dagger \hat{c}_q\} \\ + \frac{1}{2} \sum_{pqrs} \langle pq| \hat{v} |rs\rangle \, \{\hat{c}_p^\dagger \hat{c}_q^\dagger \hat{c}_s \hat{c}_r\} + E_{HF}. \end{aligned} \tag{2.40}$$

Here, the curly braces indicate that the creation and annihilation operators are in normal order with respect to $|\Phi_0\rangle$, i.e. all the $\hat{c}_i^\dagger$ and $\hat{c}_a$ stand to the right of all $\hat{c}_a^\dagger$ and $\hat{c}_i$. The terms highlighted in green in eq. (2.40) form the *normal-ordered Hamiltonian*, $\hat{H}_N$, which corresponds to a 'correlation operator' adding E_{corr} to E_{HF}.

2.2.4 A correlated ground state: coupled-cluster theory

The CC theory provides an accurate description of the electronic correlation in the ground state of the electronic system. The theory is based on an exponential ansatz for the ground state [110], i.e.

$$|\psi_g\rangle = e^{\hat{T}} |\Phi_0\rangle \,, \tag{2.41}$$

where $\hat{T}$ corresponds to the cluster operator. The cluster operator is expanded as

$$\hat{T} = \hat{T}_1 + \hat{T}_2 + \hat{T}_3 + \dots \,, \tag{2.42}$$

where $\hat{T}_n$ (for $n = 1, 2, 3, \dots$) is a general excitation operator of the form

$$\hat{T}_n = \left(\frac{1}{n!}\right)^2 \sum_{ij\dots ab\dots}^{n} t_{ij\dots}^{ab\dots} c_a^\dagger c_b^\dagger \dots c_j c_i, \tag{2.43}$$

with $[\hat{T}_n, \hat{T}_m] = 0$ [111]. For $n = 1, 2, 3, \dots$ $\hat{T}_n$ introduces singly-, doubly-, triply-,... excited SDs in the expansion of $|\psi_g\rangle$ [79]. The various coupled cluster methods are distinguished by the level of truncation of $\hat{T}$, with e.g. the coupled-cluster singles doubles (CCSD) method being characterised by $\hat{T} = \hat{T}_1 + \hat{T}_2$. The CCSD excitation operator, $e^{\hat{T}_1 + \hat{T}_2}$, can be written as its Taylor expansion, i.e.

$$e^{\hat{T}_1 + \hat{T}_2} = 1 + \hat{T}_1 + \hat{T}_2 + \frac{\hat{T}_1^2}{2} + \hat{T}_1\hat{T}_2 + \frac{\hat{T}_2^2}{2} + \dots \tag{2.44}$$

where the blue terms are referred to as *connected*, while the red terms as *disconnected* [110]. The expansion in eq. (2.44) can be compared with that of the configuration interaction singles doubles (CISD) method, where a linear ansatz is obtained by applying $\hat{T} = 1 + \hat{T}_1 + \hat{T}_2$ to $|\Phi_0\rangle$. The difference between CISD and CCSD lies in the presence of the disconnected terms, which are responsible for the size-extensivity of CCSD [79] and allow to 'fold in' the effects of higher excitations in the CCSD expansion [85]. The CC approach to the solution of the TISE entails writing [110]

$$e^{-\hat{T}} \hat{H}_N e^{\hat{T}} |\Phi_0\rangle = \hat{\bar{H}} |\Phi_0\rangle = E_{corr} |\Phi_0\rangle \tag{2.45}$$

with $\hat{\bar{H}} = e^{-\hat{T}} \hat{H}_N e^{\hat{T}}$ being the non-hermitian, similarity transformed Hamiltonian. The E_{corr} is obtained by projecting eq. (2.45) onto $|\Phi_0\rangle$, i.e.

$$\langle\Phi_0| \hat{\bar{H}} |\Phi_0\rangle = E_{corr}, \tag{2.46}$$

while the cluster amplitudes, $t_{ij\dots}^{ab\dots}$, are obtained by projection onto the excited SDs, i.e.

$$\langle\Phi_{ij\dots}^{ab\dots}| \hat{\bar{H}} |\Phi_0\rangle = 0. \tag{2.47}$$

The evaluation of eqs. (2.46) and (2.47) is performed by writing $\hat{\bar{H}}$ in terms of the Cambell-Baker-Hausdorff (CBH) formula

$$\begin{aligned} \hat{\bar{H}} = \hat{H}_N + \left[\hat{H}_N, \hat{T}\right] + \frac{1}{2!}\left[\left[\hat{H}_N, \hat{T}\right], \hat{T}\right] + \\ + \frac{1}{3!}\left[\left[\left[\hat{H}_N, \hat{T}\right], \hat{T}\right], \hat{T}\right] + \frac{1}{4!}\left[\left[\left[\left[\hat{H}_N, \hat{T}\right], \hat{T}\right], \hat{T}\right], \hat{T}\right] + \dots \end{aligned} \tag{2.48}$$

Since the $\hat{T}_n$ operators commute and $\hat{H}_N$ contains at most two-electron operators, the expansion in eq. (2.48) terminates automatically after the quadruple nested commutator [79]. This causes the CC equations to always have a finite number of terms, regardless of the level of truncation considered in the expansion of $\hat{T}$ [79]. This advantage is counteracted by the resulting expression for E_{corr} being non-variational and by $\hat{\bar{H}}$ being non-hermitian. Approaches such as the unitary coupled cluster (UCC) [112, 113] theory tackle this problem by defining the cluster operator as $\hat{S} = \hat{T} - \hat{T}^\dagger$ and the similarity transformed Hamiltonian as $\hat{\bar{H}} = e^{\hat{S}^\dagger} \hat{H}_N e^{\hat{S}}$. On one hand, this leads to a variational energy expression and a hermitian $\hat{\bar{H}}$. On the other hand, the CBH expansion of $\hat{\bar{H}}$ doesn't terminate naturally, and it must be approximately truncated to a determined number of terms.

2.2.5 Excited states: equation of motion coupled-cluster

Based on the accurate description of the ground state within CC theory, the EOM-CC theory offers a valid platform for the description of the excited electronic states of the molecule. Within the EOM-CC theory [85, 86] an electronic eigenstate is defined as

$$|\psi_n^R\rangle = \hat{R}^n e^{\hat{T}} |\Phi_0\rangle . \tag{2.49}$$

Here, $\hat{R}^n$ is an excitation operator associated to $|\psi_n^R\rangle$, whose generic form is

$$\hat{R} = \hat{R}_0 + \hat{R}_1 + \hat{R}_2 + \hat{R}_3 + \dots , \tag{2.50a}$$

where

$$\hat{R}_x = \left(\frac{1}{x!}\right)^2 \sum_{ij\dots ab\dots}^{x} r_{ij\dots}^{ab\dots} c_a^\dagger c_b^\dagger \dots c_j c_i. \tag{2.50b}$$

Just like the cluster operators in section 2.2.4, also the operators $\hat{R}$ and $\hat{T}$ commute [111]. The ansatz in eq. (2.49) leads to a TISE of the form

$$\hat{\bar{H}} \hat{R}^n |\Phi_0\rangle = E_n \hat{R}^n |\Phi_0\rangle , \tag{2.51}$$

which reduces to the CC case in eq. (2.45) when $n = g$ (with $\hat{R}^g = \hat{R}_0 = 1$). The non-hermiticity of $\hat{\bar{H}}$ entails the association of the same eigenvalue E_n with both right, $|\psi_n^R\rangle$, and left, $\langle\psi_n^L|$, eigenvectors, with $\langle\psi_n^L|$ being defined as

$$\langle\psi_n^L| = \langle\Phi_0| \hat{L}^n e^{-\hat{T}}. \tag{2.52}$$

Here, $\hat{L}^n$ is a de-excitation operator, whose general form is given by

$$\hat{L} = \hat{L}_0 + \hat{L}_1 + \hat{L}_2 + \hat{L}_3 + \dots , \tag{2.53a}$$

with

$$\hat{L}_x = \left(\frac{1}{x!}\right)^2 \sum_{ab\dots ij\dots}^{x} l_{ij\dots}^{ab\dots} c_i^\dagger c_j^\dagger \dots c_b c_a. \tag{2.53b}$$

The two sets of left and right eigenvectors are not orthogonal among themselves but rather they satisfy the property of biorthogonality, i.e. $\langle\psi_n^L|\psi_{n'}^R\rangle = \delta_{nn'}$, which allows to define an expression for the energy of the form [85]

$$E_n = \langle\psi_n^L| \hat{H} |\psi_n^R\rangle . \tag{2.54}$$

2.3 Wave-packet preparation and dynamics

2.3.1 Quantum dynamics and the interaction picture

The evolution of a state vector from an initial time t_0 to a final time t is governed by the time-evolution operator $\hat{U}(t, t_0)$ according to [95]

$$|\Psi(t)\rangle = \hat{U}(t, t_0)\,|\Psi(t_0)\rangle\,. \tag{2.55}$$

Investigating the system's time-evolution is strictly connected with the derivation of an explicit form of $\hat{U}(t, t_0)$, which can be obtained by solving the TDSE

$$i\frac{\partial}{\partial t}\hat{U}(t, t_0) = \hat{H}(t)\hat{U}(t, t_0), \tag{2.56}$$

where $\hat{H}(t) = \hat{H}_e + \hat{H}^L_{\text{int}}$. The first step towards the solution of eq. (2.56) corresponds to the expansion of $|\Psi(t_0)\rangle$ in terms of the eigenstates of $\hat{H}_e$, i.e.

$$|\Psi(t_0)\rangle = \sum_n a_n(t_0)\,|\psi_n\rangle\,, \tag{2.57}$$

where $a_n(t_0)$ is the probability amplitude related to an eigenstate $|\psi_n\rangle$ at t_0. The characteristics of the solution of eq. (2.56) vary according to the properties of the electric field $\boldsymbol{E}(t)$, which is considered to have the form of a (short) pulse of light. In correspondence to the pulse being 'off' or 'on', two cases are considered [95]:

1) $\boldsymbol{E}(t) = 0$, which makes $\hat{H}(t) \equiv \hat{H}_e$ and $\hat{U}(t, t_0) = e^{-i\hat{H}_e(t-t_0)}$. In such case

$$|\Psi(t)\rangle = \sum_n a_n(t_0)e^{-iE_n(t-t_0)}\,|\psi_n\rangle\,, \tag{2.58}$$

with the time-evolution corresponding solely to a phase modulation.

2) $\boldsymbol{E}(t) \neq 0$, with the $\hat{H}(t)$'s not commuting at different times. In this case, the form of $\hat{U}(t, t_0)$ is not trivial and

$$|\Psi(t)\rangle = \sum_n a_n(t)e^{-iE_n(t-t_0)}\,|\psi_n\rangle\,. \tag{2.59}$$

Here, the time-dependence associated with $\hat{H}_e$ (i.e. the phase modulation) is accompanied by the time-dependence of the probability amplitudes.

By comparing eqs. (2.58) and (2.59) it appears evident that the time-evolution given by $a_n(t)$ is due solely to the interaction with the radiation field, which enables the transitions between the stationary states of the system [97]. The specific study of this time-dependence is facilitated by switching from the *Schrödinger picture* to the *interaction picture*, which is defined according to the transformation

$$|\Psi(t)\rangle_I = e^{i\hat{H}_e t}\,|\Psi(t)\rangle\,, \tag{2.60}$$

where the subscript I indicates the interaction picture. In applying the interaction picture to eq. (2.59), it is convenient to choose an initial phase shift, $e^{-iE_n t_0}$, for each $|\psi_n\rangle$ in the Schrödinger picture [95], such that

$$|\Psi(t)\rangle_I = \sum_n a_n(t)\,|\psi_n\rangle\,. \tag{2.61}$$

Switching to the interaction picture leads also to a different form of the TDSE, i.e.

$$i\frac{\partial}{\partial t}\hat{U}_I(t,t_0) = \hat{H}^L_{\text{int},I}(t)\hat{U}_I(t,t_0), \tag{2.62}$$

where $\hat{H}^L_{\text{int},I}(t) = e^{i\hat{H}_e t}\hat{H}^L_{\text{int}}(t)e^{-i\hat{H}_e t}$ and $\hat{U}_I(t,t_0) = e^{i\hat{H}_e t}\hat{U}(t,t_0)e^{-i\hat{H}_e t}$. From the comparison between eq. (2.62) and eq. (2.56), it is evident how in the interaction picture the system's time-evolution is solely due to the interaction Hamiltonian operator.

2.3.2 Characteristics of the processes and states involved

A schematic representation of the excitation processes considered in this work is shown in fig. 2.1, which serves as a 'visual guide' the reader can refer to while going through the equations presented in the following sections. The one-photon X-Ray absorption process is represented in panel a), while the two-photon ISRIXS process is represented in panel b). The consideration of these processes limits the basis of

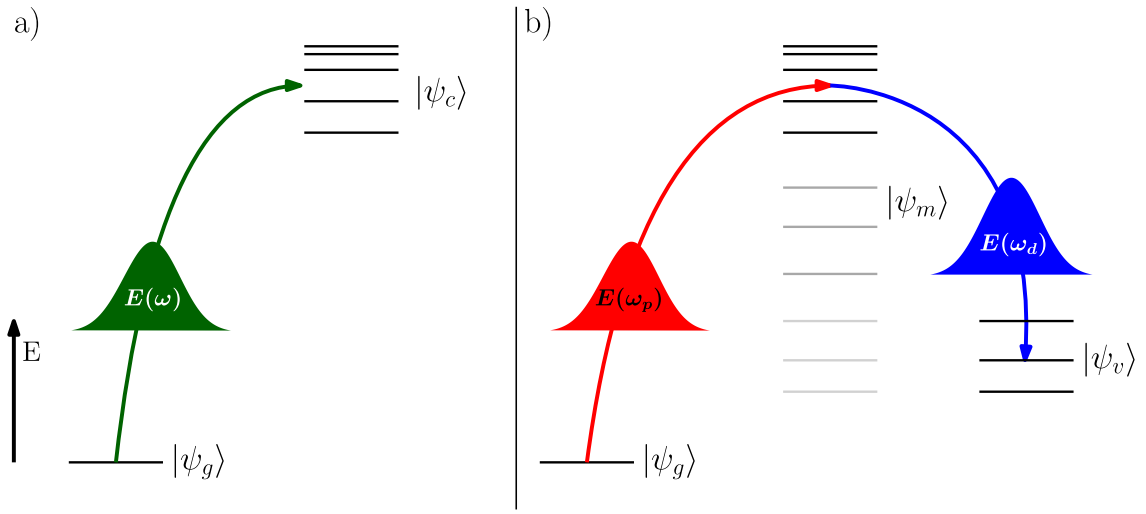

Figure 2.1: *Schematic representation of the considered resonant excitation processes. Panel a) refers to a resonant one-photon absorption process, with the ground state indicated by $|\psi_g\rangle$, the core-excited states by $|\psi_c\rangle$ and the pulse in the frequency domain by $E(\omega)$. Panel b) refers to the two-photon Stimulated Resonant Inelastic X-Ray Scattering (SRIXS) process, where $|\psi_v\rangle$ corresponds to the valence-excited states while $E(\omega_p)$ and $E(\omega_d)$ refer to the 'pump' and 'dump' interactions with the pulse, respectively. The states $|\psi_m\rangle$ correspond to the complete set of eigenstates of $\hat{H}_e$, with the different shading (less pronounced in correspondence to the $|\psi_c\rangle$ manifold) indicating the relative contribution of the intermediate states to the two-photon process.*

eigenstates of $\hat{H}_e$, used for the expansion of $|\Psi(t)\rangle$, to the following set of bound states: the ground state $|\psi_g\rangle$, the valence-excited states $|\psi_v\rangle$ (populated through SRIXS) and the core-excited states $|\psi_c\rangle$ (populated through a one-photon X-Ray absorption process). The focus on the resonant excitation processes leaves out photoionisation processes involving the valence- and core-electrons, which can likewise take place when the molecule interacts with an intense X-Ray pulse. In particular, the core-shell photoionisation plays a prominent role at X-Ray frequencies. In fact, while the central frequency of the pulse might be below the ionisation edge of the

selected element, the same frequency might correspond to the above-edge region of another element (e.g. the energy region below the O K-Edge is still above the C K-Edge). Neglecting the photoionisation processes is approximately justified by the resonant enhancement, which should make the resonant excitation competitive with the photoionisation. The relaxation of the electronic structure following the excitation – associated with spontaneous processes like X-Ray fluorescence or the AM decay – is not treated explicitly in this work, but rather phenomenologically by applying the transformation

$$E_n \to E_n - i\frac{\Gamma_n}{2}. \tag{2.63}$$

Here, Γ_n corresponds to the decay rate of the generic state $|\psi_n\rangle$, which is inversely proportional to its lifetime $\tau_n \simeq \hbar/\Gamma_n$. The application of the transformation in eq. (2.63) makes the time-evolution of the system non-unitary.

2.3.3 Perturbative theory

The perturbative ansatz assumes that the interaction with the pulse determines only a small perturbation of the system [97]. Accordingly, the excitation is represented in terms of perturbative 'corrections' to a time-independent zero order, which corresponds to the unperturbed system. In this context, upon consideration of the initial condition $\hat{U}_I(t,t_0)|_{t=t_0} = 1$, the perturbative solution of eq. (2.62) is given by a series expansion of $\hat{U}_I(t,t_0)$, i.e.

$$\hat{U}_I(t,t_0) \approx \hat{\mathbb{1}} - i\int_{t_0}^{t} dt' \hat{H}^L_{\mathrm{int},I}(t') + (-i)^2 \int_{t_0}^{t} dt' \int_{t_0}^{t'} dt'' \hat{H}^L_{\mathrm{int},I}(t')\hat{H}^L_{\mathrm{int},I}(t'') + \ldots, \tag{2.64}$$

which is commonly known as Dyson series. Here, the time-ordering $t > t' > t'' > \cdots > t_0$ applies. Considering the system in its ground state $|\psi_g\rangle$ at t_0 (i.e. $|\Psi(t_0)\rangle_I \equiv |\psi_g\rangle$ with $a_n(t_0) = \delta_{ng}$), allows to write

$$|\Psi(t)\rangle_I = \hat{U}_I(t,t_0)\,|\psi_g\rangle = \sum_n |\psi_n\rangle\,\langle\psi_n|\,\hat{U}_I(t,t_0)\,|\psi_g\rangle\,. \tag{2.65}$$

The comparison between eq. (2.61) and eq. (2.65) indicates that $\langle\psi_n|\,\hat{U}_I(t,t_0)\,|\psi_g\rangle$ corresponds to the probability amplitude $a_n(t)$. Following the perturbative ansatz, the probability amplitudes are approximated in terms of an expansion of the form

$$a_n(t) \approx \delta_{ng} + a_n^{(1)}(t) + a_n^{(2)}(t) + \ldots, \tag{2.66}$$

where the superscripts indicate amplitudes of the first order, second order and so on. Combining the expansion of $\hat{U}_I(t,t_0)$ in eq. (2.64) with eqs. (2.65) and (2.66), the explicit form of the perturbative corrections in eq. (2.66) can be obtained. In particular,

$$a_n^{(1)}(t) = -i\int_{t_0}^{t} dt'\,\langle\psi_n|\,\hat{H}^L_{\mathrm{int},I}(t')\,|\psi_g\rangle \tag{2.67a}$$

and

$$a_n^{(2)}(t) = (-i)^2 \sum_m \int_{t_0}^{t} dt' \int_{t_0}^{t'} dt''\,\langle\psi_n|\,\hat{H}^L_{\mathrm{int},I}(t')\,|\psi_m\rangle\,\langle\psi_m|\,\hat{H}^L_{\mathrm{int},I}(t'')\,|\psi_g\rangle\,, \tag{2.67b}$$

with the index m in eq. (2.67b) running over the whole spectrum of $\hat{H}_e$.

Core-excited states

The one-photon processes are associated to the first order contribution in eq. (2.67a), which corresponds to considering $a_c(t) \approx a_c^{(1)}(t)$. The derivation of the final form[IV] of $a_c^{(1)}(t)$ starts from eq. (2.67a) and leads to

$$a_c^{(1)}(t) = i \int_{t_0}^{t} dt' e^{i(\omega_{cg} - i\frac{\Gamma_c}{2})t'} E(t') \boldsymbol{\epsilon} \cdot \langle \psi_c | \, \hat{\boldsymbol{\mu}} \, | \psi_g \rangle \, . \tag{2.68}$$

Here, $\omega_{cg} = \omega_c - \omega_g = E_n - E_g$[V], $\boldsymbol{\epsilon}$ is the pulse polarisation and $E(t)$ its amplitude. Γ_c corresponds to the decay rate associated to the core-excited states, with Γ_g being set to zero according to the non-decaying nature of the ground state. The electric field $E(t)$ in eq. (2.68) is substituted with its Fourier transform,

$$E(t) = \frac{1}{\sqrt{2\pi}} \int_0^{\infty} d\omega (E(\omega) e^{i\omega t} + E^*(\omega) e^{-i\omega t}), \tag{2.69}$$

leading to the expression

$$a_c^{(1)}(t) = i \int_{t_0}^{t} \frac{dt'}{\sqrt{2\pi}} \int_0^{\infty} d\omega \Big(E(\omega) e^{i(\omega_{cg} + \omega - i\frac{\Gamma_c}{2})t'} + E^*(\omega) e^{i(\omega_{cg} - \omega - i\frac{\Gamma_c}{2})t'} \Big) \boldsymbol{\epsilon} \cdot \boldsymbol{\mu}_{cg}. \tag{2.70}$$

Here, $E(\omega) = |E(\omega)| e^{i\phi(\omega)}$ (with $\phi(\omega)$ being the spectral phase of each frequency component) and $\boldsymbol{\mu}_{cg} = \langle \psi_c | \, \hat{\boldsymbol{\mu}} \, | \psi_g \rangle$. The time-integral in eq. (2.70) is evaluated in the limit of $t_0 \to -\infty$, which allows to remove the t_0-dependence and simplify the final expression. The convergence of the integral is ensured by the transformation in eq. (2.63), which effectively introduces a $e^{\Gamma_c t}$ factor, ensuring that the integrand equals to 0 in the limit $t_0 \to -\infty$ [114]. Performing the time-integral leads to

$$a_c^{(1)}(t) = \frac{1}{\sqrt{2\pi}} \int_0^{\infty} d\omega \Big(\underbrace{E(\omega) \frac{e^{i(\omega_{cg} + \omega - i\frac{\Gamma_c}{2})t}}{\omega_{cg} + \omega - i\frac{\Gamma_c}{2}}}_{\text{one-photon emission}} + \underbrace{E^*(\omega) \frac{e^{i(\omega_{cg} - \omega - i\frac{\Gamma_c}{2})t}}{\omega_{cg} - \omega - i\frac{\Gamma_c}{2}}}_{\text{one-photon absorption}} \Big) \boldsymbol{\epsilon} \cdot \boldsymbol{\mu}_{cg}, \tag{2.71}$$

where the two addends are associated with the one-photon emission and one-photon absorption processes, respectively. Since no excited state is initially populated, the one-photon emission term can be neglected, leading to the final expression

$$a_c^{(1)}(t) = \frac{1}{\sqrt{2\pi}} \int_0^{\infty} d\omega \frac{e^{i(\omega_{cg} - \omega - i\frac{\Gamma_c}{2})t}}{\omega_{cg} - \omega - i\frac{\Gamma_c}{2}} E^*(\omega) \boldsymbol{\epsilon} \cdot \boldsymbol{\mu}_{cg}. \tag{2.72}$$

[IV] Only the most relevant passages are reported here, with the complete derivation being available in section A.1

[V] The switch of notation to the angular frequency is done to have a more compact notation, and it's justified by $E_n = \omega_n$ in a.u.

Valence-excited states

A Raman process like ISRIXS is associated to a second order contribution in eq. (2.66), which corresponds to considering $a_v(t) \approx a_v^{(2)}(t)$. The derivation of the final expression for $a_v^{(2)}(t)$ (presented in its full version in section A.2) starts from eq. (2.67b), leading to the intermediate expression

$$\begin{aligned} a_v^{(2)}(t) = \frac{1}{2\pi}\sum_m \int_0^\infty d\omega' \int_0^\infty d\omega''(\boldsymbol{\epsilon}'\cdot\boldsymbol{\mu}_{vm})(\boldsymbol{\epsilon}''\cdot\boldsymbol{\mu}_{mg})\times \\ \times\Bigg[\underbrace{\frac{E(\omega')E(\omega'')e^{i(\omega_{vg}+\omega'+\omega''-i\frac{\Gamma_v}{2})t}}{(\omega_{mg}+\omega''-i\frac{\Gamma_m}{2})(\omega_{vg}+\omega'+\omega''-i\frac{\Gamma_v}{2})}}_{\text{two-photon emission}}+ \\ +\underbrace{\frac{E^*(\omega')E^*(\omega'')e^{i(\omega_{vg}-\omega'-\omega''-i\frac{\Gamma_v}{2})t}}{(\omega_{mg}-\omega''-i\frac{\Gamma_m}{2})(\omega_{vg}-\omega'-\omega''-i\frac{\Gamma_v}{2})}}_{\text{two-photon absorption}}+ \\ +\underbrace{\frac{E^*(\omega')E(\omega'')e^{i(\omega_{vg}-\omega'+\omega''-i\frac{\Gamma_v}{2})t}}{(\omega_{mg}+\omega''-i\frac{\Gamma_m}{2})(\omega_{vg}-\omega'+\omega''-i\frac{\Gamma_v}{2})}}_{\text{Raman}}+ \\ +\underbrace{\frac{E(\omega')E^*(\omega'')e^{i(\omega_{vg}+\omega'-\omega''-i\frac{\Gamma_v}{2})t}}{(\omega_{mg}-\omega''-i\frac{\Gamma_m}{2})(\omega_{vg}+\omega'-\omega''-i\frac{\Gamma_v}{2})}}_{\text{Raman}}\Bigg]. \end{aligned} \tag{2.73}$$

Here, the two-photon emission term is neglected according to the same reason justifying the exclusion of the one-photon emission term in eq. (2.71). The two-photon absorption term can also be neglected, considering that ω_{vg} lies in the UV-Vis region of the electromagnetic spectrum in a generic organic molecule. Since both ω' and ω'' correspond to X-Ray frequencies, the denominator of the two-photon absorption term will always be very large. This allows to neglect the contribution of this term in eq. (2.73). A change of notation is performed in the Raman terms by renaming the 'absorbed' frequencies (i.e. ω' or ω'' preceded by a '$-$' sign) as 'pump' (ω_p) and the 'emitted' frequencies (i.e. ω' or ω'' preceded by '$+$' sign) as 'dump' (ω_d). This leads to the final expression

$$\begin{aligned} a_v^{(2)}(t) = \frac{1}{2\pi}\int_0^\infty d\omega_p \int_0^\infty d\omega_d \frac{e^{i(\omega_{vg}-\omega_p+\omega_d-i\frac{\Gamma_v}{2})t}}{\omega_{vg}-\omega_p+\omega_d-i\frac{\Gamma_v}{2}} E^*(\omega_p)E(\omega_d)\times \\ \times\sum_m\left(\frac{(\boldsymbol{\epsilon}_p\cdot\boldsymbol{\mu}_{vm})(\boldsymbol{\epsilon}_d\cdot\boldsymbol{\mu}_{mg})}{\omega_{mg}+\omega_d-i\frac{\Gamma_m}{2}}+\frac{(\boldsymbol{\epsilon}_d\cdot\boldsymbol{\mu}_{vm})(\boldsymbol{\epsilon}_p\cdot\boldsymbol{\mu}_{mg})}{\omega_{mg}-\omega_p-i\frac{\Gamma_n}{2}}\right). \end{aligned} \tag{2.74}$$

The term highlighted in green establishes the resonance condition $\omega_{vg} = \omega_p - \omega_d$, which involves the ground and the valence-excited states, but not the intermediate states. This suggests that the excitation (i.e. 'pump') and de-excitation (i.e. 'dump') are not separate processes, but rather they are part of a single, non-separable scattering event [41]. The virtual nature of the intermediate state is also reflected by the structure of the transition moment (highlighted in blue). This is expressed in terms of a SOS, which formally includes the whole spectrum of $\hat{H}_e$. The denominator within the SOS determines a resonant enhancement of the transition moment at

particular frequencies. In the present case, these frequencies cover a range characteristic of the X-Ray absorption spectrum at a given edge of the molecule.

Ground state

The ground state's probability amplitude up to second order is given by

$$a_g(t) \approx 1 + a_g^{(2)}(t), \tag{2.75}$$

where the first contribution corresponds to the zeroth perturbative order while $a_g^{(2)}(t)$ is given by

$$\begin{aligned} a_g^{(2)}(t) = \frac{1}{2\pi} \int_0^\infty d\omega_p \int_0^\infty d\omega_d \frac{e^{i(\omega_d - \omega_p)t}}{\omega_d - \omega_p} E^*(\omega_p) E(\omega_d) \times \\ \times \sum_m \left(\frac{(\boldsymbol{\epsilon}_p \cdot \boldsymbol{\mu}_{gm})(\boldsymbol{\epsilon}_d \cdot \boldsymbol{\mu}_{mg})}{\omega_{mg} + \omega_d - i\frac{\Gamma_m}{2}} + \frac{(\boldsymbol{\epsilon}_d \cdot \boldsymbol{\mu}_{gm})(\boldsymbol{\epsilon}_p \cdot \boldsymbol{\mu}_{mg})}{\omega_{mg} - \omega_p - i\frac{\Gamma_m}{2}} \right). \end{aligned} \tag{2.76}$$

The resonance condition $\omega_p = \omega_d$ (imposed by the 'green' prefactor) indicates the relation of $a_g^{(2)}(t)$ with an 'elastic' process, with the excitation and de-excitation starting from and leading back to the ground state. This is also shown in the transition moment (indicated in blue) where both the initial and final states of the Raman process coincide with the ground state.

2.3.4 Perturbative representation of the density operator

Having obtained the perturbative expressions for the probability amplitudes in the interaction picture, it is now possible to perturbatively expand $|\Psi(t)\rangle$ in the Schrödinger picture as

$$\begin{aligned} |\Psi(t)\rangle \approx (1 + a_g^{(2)}(t)) |\psi_g\rangle + \sum_c a_c^{(1)}(t) e^{-i(\omega_c - i\frac{\Gamma_c}{2})t} |\psi_c\rangle \\ + \sum_v a_v^{(2)}(t) e^{-i(\omega_v - i\frac{\Gamma_v}{2})t} |\psi_v\rangle . \end{aligned} \tag{2.77}$$

The substitution of eq. (2.77) in the definition of density operator,

$$\hat{\rho}(t) = |\Psi(t)\rangle \langle\Psi(t)| , \tag{2.78}$$

yields the perturbative expansion of the matrix elements, $\rho_{nn'}(t)$, of $\hat{\rho}(t)$, i.e.

$$\rho_{nn'}(t) \approx \delta_{nn'}\delta_{n'g} + \rho_{nn'}^{(1)}(t) + \rho_{nn'}^{(2)}(t) + \dots . \tag{2.79}$$

Here, the perturbative order of each term is given by the sum of the orders of the probability amplitudes used to construct them. For example,

$$\rho_{gg}(t) \approx 1 + 2\,\mathrm{Re}\{a_g^{(2)}(t)\} + a_g^{(2)}(t) a_g^{(2)}(t)^* = 1 + \rho_{gg}^{(2)}(t) + \rho_{gg}^{(4)}(t). \tag{2.80}$$

Since the probability amplitudes have been approximated considering terms up to second order, the perturbative expansion in eq. (2.79) contains all the terms only

up to second order. Accordingly, the populations of the ground state, $\rho_{gg}(t)$, and of the core-excited states, $\rho_{cc}(t)$, are approximated as

$$\rho_{gg}(t) \approx 1 + \rho_{gg}^{(2)}(t) = 1 + 2\,\mathrm{Re}\big\{a_g^{(2)}(t)\big\}, \tag{2.81a}$$

$$\rho_{cc}(t) \approx \rho_{cc}^{(2)}(t) = a_c^{(1)}(t) a_c^{(1)}(t)^* e^{-\Gamma_c t}. \tag{2.81b}$$

The populations of the valence-excited states, $\rho_{vv}(t)$, are neglected since their leading perturbative contribution is of fourth order. Similar considerations apply also to the coherences. In fact, only the coherences between the ground state and the excited states, i.e. $\rho_{cg}(t)$ and $\rho_{vg}(t)$, and between the core-excited states, $\rho_{cc'}(t)$, contain contributions up to second order. Their perturbative expansions are given by

$$\rho_{cg}(t) \approx \rho_{cg}^{(1)}(t) = a_c^{(1)}(t) e^{-i\omega_{cg}t} e^{-\frac{\Gamma_c}{2}t}, \tag{2.82a}$$

$$\rho_{vg}(t) \approx \rho_{vg}^{(2)}(t) = a_v^{(2)}(t) e^{-i\omega_{vg}t} e^{-\frac{\Gamma_v}{2}t}, \tag{2.82b}$$

$$\rho_{cc'}(t) \approx \rho_{cc'}^{(2)}(t) = a_c^{(1)}(t) a_{c'}^{(1)}(t)^* e^{-i\omega_{cc'}t} e^{-\frac{\Gamma_c+\Gamma_{c'}}{2}t}. \tag{2.82c}$$

These expressions show how the coherences oscillate at a frequency proportional to the energy separation of the states and, just like the populations in eq. (2.81b), decay as an effect of spontaneous decay processes (with a rate depending on the type of excited states involved).

2.4 The time-dependent electronic density

The time-evolution of the electronic density is strictly related to the characteristics of the WP. The changes of the intramolecular distribution of the electronic density over time provide fundamental information on the changes in the molecule's structure and reactivity. This section aims at presenting the expression for the time-dependent difference electronic density, its decomposition in terms of perturbative components and their physical interpretation. This will serve as a basis for the analysis performed in the results chapters.

2.4.1 Position-spin representation

The study of the electronic density requires the representation of the density operator in a suitable basis. Here, this basis is constructed in terms of the orthonormal bases of eigenstates of two compatible operators: the position operator, $\hat{\boldsymbol{r}}$, and the operator $\hat{\mathcal{S}}_z$, which represents the projection of the electron's spin along the z-axis [95]. The basis of $\hat{\boldsymbol{r}}$ corresponds to the infinite set of position eigenstates $|\boldsymbol{r}\rangle$, with the corresponding eigenvalue being the position vector $\boldsymbol{r}$. It must be noted that the introduction of the position representation defines also the algebraic form of the momentum operator as $\hat{\boldsymbol{p}} = -i\nabla$. The basis of $\hat{\mathcal{S}}_z$ for a single electron is formed by two eigenstates, $|1/2\rangle$ and $|-1/2\rangle$, corresponding to the eigenvalues $s_z = \frac{1}{2}$ and $s_z = -\frac{1}{2}$, respectively. Starting from the bases of $\hat{\boldsymbol{r}}$ and $\hat{\mathcal{S}}_z$, the position-spin basis can be constructed as

$$|\boldsymbol{r}\rangle \otimes |s_z\rangle \equiv |\boldsymbol{r}, s_z\rangle \equiv |\boldsymbol{x}\rangle \,, \tag{2.83}$$

where $\boldsymbol{x} = \{\boldsymbol{r}, s_z\}$. The position-spin basis can be used to expand e.g. a one-electron state $|\chi\rangle$, leading to its *position-spin representation*

$$|\chi\rangle = \int d\boldsymbol{x}\, |\boldsymbol{x}\rangle \langle \boldsymbol{x}|\chi\rangle \,, \tag{2.84}$$

where $\langle \boldsymbol{x}|\chi\rangle = \chi(\boldsymbol{x})$ is the one-electron wave function (i.e. the *spin orbital*) and $\int d\boldsymbol{x} \equiv \sum_{s_z} \int d\boldsymbol{r}$.

2.4.2 Time-dependent electronic density in real space

The expansion of the density operator in the basis of eigenstates of $\hat{H}_e$ reads

$$\hat{\rho}(t) = \sum_{nn'} \rho_{nn'}(t)\, |\psi_n\rangle \langle \psi_{n'}| \,. \tag{2.85}$$

The density operator can be represented in the position-spin basis relative to a N_e-electron system, leading to the time-dependent N_e-electron density matrix

$$\begin{aligned} \rho(\boldsymbol{x}_1, \boldsymbol{x}_2, \ldots, \boldsymbol{x}_{N_e}; \boldsymbol{x}'_1, \boldsymbol{x}'_2, \ldots, \boldsymbol{x}'_{N_e}; t) = \\ = \sum_{nn'} \rho_{nn'}(t)\, \langle \boldsymbol{x}_1, \boldsymbol{x}_2, \ldots, \boldsymbol{x}_{N_e}|\psi_n\rangle \left\langle \psi_{n'}\middle|\boldsymbol{x}'_1, \boldsymbol{x}'_2, \ldots, \boldsymbol{x}'_{N_e}\right\rangle . \end{aligned} \tag{2.86}$$

The diagonal elements of eq. (2.86) correspond to the time-dependent N_e-electron spin-electronic density. This density contains information on the time-dependent

probability of finding an electron in the space-spin volume element $d\boldsymbol{x}_1$ at $\boldsymbol{x}_1$, while another electron is located in $d\boldsymbol{x}_2$ at $\boldsymbol{x}_2$ and so on. This provides the full information on the time-evolution of the correlated electronic system. For the purposes of a three-dimensional spatial visualisation, this study relies on the time-dependent one-electron reduced density matrix, $\rho(\boldsymbol{x}_1;\boldsymbol{x}_1';t)$, whose explicit expression can be obtained by taking the trace of eq. (2.86) with respect to the space-spin coordinates of N-1 electrons, i.e.

$$\begin{aligned}\rho(\boldsymbol{x}_1;\boldsymbol{x}_1';t) &= \\ &= \sum_{nn'} \rho_{nn'}(t) \underbrace{N_e \int d\boldsymbol{x}_2 \dots d\boldsymbol{x}_{N_e} \langle \boldsymbol{x}_1, \boldsymbol{x}_2, \dots, \boldsymbol{x}_{N_e}|\psi_n\rangle \langle \psi_{n'}|\boldsymbol{x}_1', \boldsymbol{x}_2, \dots, \boldsymbol{x}_{N_e}\rangle}_{\gamma^{nn'}(\boldsymbol{x}_1;\boldsymbol{x}_1')} .\end{aligned} \tag{2.87}$$

Here, $\gamma^{nn'}(\boldsymbol{x}_1;\boldsymbol{x}_1')$ is the time-independent one-electron reduced density matrix, commonly referred to as 1PDM, relative to the eigenstates of $\hat{H}_e$ corresponding to the n and n' indexes. The 1PDM can be expanded in the basis of one-electron spin orbitals, $\{|\chi_p\rangle\}$, leading to the more compact expression

$$\rho(\boldsymbol{x};\boldsymbol{x}';t) = \sum_{nn'} \rho_{nn'}(t) \sum_{pq} \gamma_{pq}^{nn'} \chi_p(\boldsymbol{x}) \chi_q^*(\boldsymbol{x}'). \tag{2.88}$$

Here, $\gamma_{pq}^{nn'}$ corresponds to the 1PDM in the spin orbitals basis[VI] and the subscripts of the space-spin coordinates have been removed to simplify the notation. The diagonal elements of $\rho(\boldsymbol{x};\boldsymbol{x}';t)$, i.e. $\rho(\boldsymbol{x};\boldsymbol{x},t) \equiv \rho(\boldsymbol{x},t)$, correspond to the time-dependent one-electron spin-electronic density. This density contains information on the time-dependent probability of finding an electron in $d\boldsymbol{x}_1$ at $\boldsymbol{x}_1$, independently of where the other electrons are. For the purpose of the three-dimensional visualisation, it is necessary to average $\rho(\boldsymbol{x},t)$ over the spin coordinates. This leads to the time-dependent one-electron spin-less electronic density (i.e. the time-dependent electronic density)

$$\rho(\boldsymbol{r},t) = \sum_{\mathcal{S}_z} \rho(\boldsymbol{x}) = \sum_{nn'} \rho_{nn'}(t) \sum_{pq} \gamma_{pq}^{nn'} \phi_p(\boldsymbol{r}) \phi_q^*(\boldsymbol{r}), \tag{2.90}$$

where $\phi_p(\boldsymbol{r})$ corresponds to the spatial component of $\chi_p(\boldsymbol{x})$.

2.4.3 Populations, coherences and corresponding densities

In order to make the notation more compact and intuitive, the expression for the time-dependent electronic density in eq. (2.90) is written as

$$\rho(\boldsymbol{r},t) = \sum_{nn'} \rho_{nn'}(t) \rho_{nn'}(\boldsymbol{r}), \tag{2.91}$$

with $\rho_{nn'}(\boldsymbol{r}) = \sum_{pq} \gamma_{pq}^{nn'} \phi_p(\boldsymbol{r}) \phi_q^*(\boldsymbol{r})$. The expression in eq. (2.91) shows a direct connection between the populations and the state densities ($\rho_{nn}(t)$ and $\rho_{nn}(\boldsymbol{r})$, respectively) and between the coherences and the transition densities ($\rho_{nn'}(t)$ and

[VI] The notation of $\gamma_{pq}^{nn'}$ follows the same convention as $\rho_{nn'}(t) = a_n(t)a_{n'}^*(t)$, as it is shown more detail in section 2.3.4, with its expression in second quantization being given by

$$\gamma_{pq}^{nn'} = \langle \psi_{n'}| \hat{c}_q^\dagger \hat{c}_p |\psi_n\rangle . \tag{2.89}$$

$\rho_{nn'}(\boldsymbol{r})$, respectively). The state density allows to visualise the electronic probability distribution characteristic of each eigenstate of H_e. At every point in space $\rho_{nn}(\boldsymbol{r}) \geq 0$ and the integral over all space must be equal to the number of electrons N_e [115], i.e.

$$\int d\boldsymbol{r}\rho_{nn}(\boldsymbol{r}) = N_e. \tag{2.92}$$

The transition density describes the changes in the electronic density due to the transition between two eigenstates of H_e. It can be both positively- and negatively-valued, with its spatial integral

$$\int d\boldsymbol{r}\rho_{nn'}(\boldsymbol{r}) = 0. \tag{2.93}$$

Within a transition density, the electronic transition is visualised as the migration of the electronic density from regions where $\rho_{nn'}(\boldsymbol{r}) < 0$ to regions where $\rho_{nn'}(\boldsymbol{r}) > 0$.

2.4.4 The difference density and its perturbative components

The perturbative treatment of the excitation imposes the populations of the excited states to be negligibly small compared to that of the ground state, which is approximately equal to one at all times. Correspondingly, the contribution of the ground state density to $\rho(\boldsymbol{r}, t)$ plays a dominant role, such that $\rho(\boldsymbol{r}, t) \approx \rho_{gg}(\boldsymbol{r})$. This effectively 'hides' the changes in $\rho(\boldsymbol{r}, t)$ caused by the excitation, whose study is the main focus of this work. For this reason, the time-dependent difference density,

$$\rho_\Delta(\boldsymbol{r}, t) = \rho(\boldsymbol{r}, t) - \rho_{gg}(\boldsymbol{r}), \tag{2.94}$$

is considered in the following. The construction of $\rho_\Delta(\boldsymbol{r}, t)$ is based on eq. (2.91), where the populations and the coherences act as time-dependent 'weights' for the corresponding state and transition densities. According to the perturbative expansion of the density operator presented in section 2.3.4, only few populations and coherences 'survive' the truncation of the expansion up to second order. This allows to decompose $\rho_\Delta(\boldsymbol{r}, t)$ in terms of four components, i.e.

$$\rho_\Delta(\boldsymbol{r}, t) = \rho_{cg}(\boldsymbol{r}, t) + \rho_{vg}(\boldsymbol{r}, t) + \rho_{cc'}(\boldsymbol{r}, t) + \Delta_{cg}(\boldsymbol{r}, t), \tag{2.95}$$

each containing different information on the excitation and the electronic dynamics. The $\rho_{cg}(\boldsymbol{r}, t)$ component corresponds to the coherences established between the ground state and the core-excited states, which modulate the contributions of the corresponding transition densities to $\rho_\Delta(\boldsymbol{r}, t)$ according to

$$\rho_{cg}(\boldsymbol{r}, t) = \sum_c 2\,\mathrm{Re}\big\{\rho_{cg}^{(1)}(t)\big\}\rho_{cg}(\boldsymbol{r}). \tag{2.96}$$

The $\rho_{vg}(\boldsymbol{r}, t)$ component corresponds to the coherences established between the ground state and the valence-excited states. Its expression is similar to that for $\rho_{cg}(\boldsymbol{r}, t)$ in eq. (2.96), i.e.

$$\rho_{vg}(\boldsymbol{r}, t) = \sum_v 2\,\mathrm{Re}\big\{\rho_{vg}^{(2)}(t)\big\}\rho_{vg}(\boldsymbol{r}). \tag{2.97}$$

On the other hand, the $\rho_{cc'}(\boldsymbol{r},t)$ component is characterised by the expression

$$\rho_{cc'}(\boldsymbol{r},t) = \sum_{c'>c} \mathrm{Re}\Big\{\rho^{(2)}_{cc'}(t)\Big\}\rho_{cc'}(\boldsymbol{r}), \tag{2.98}$$

which shows its relation to the coherences established between the core-excited states. The contribution to $\rho_{\Delta}(\boldsymbol{r},t)$ corresponding to the populations is given by $\Delta_{gc}(\boldsymbol{r},t)$, which is constructed according to

$$\Delta_{gc}(\boldsymbol{r},t) = \sum_{c} \rho_{cc}(\boldsymbol{r},t) + \rho^{(2)}_{gg}(\boldsymbol{r},t) = \sum_{c} \rho^{(2)}_{cc}(t)\rho_{cc}(\boldsymbol{r}) + \rho^{(2)}_{gg}(t)\rho_{gg}(\boldsymbol{r}). \tag{2.99}$$

Here, the first term (in the following referred to as $\rho^{s}_{cc}(\boldsymbol{r},t)$) corresponds to the total population of the core-excited states. The second term corresponds to the depopulation of the ground state, with $\rho^{(2)}_{gg}(t)$ being accordingly characterised by a negative sign.

CHAPTER 3

Implementation

3.1 Implementation within EOM-CC theory

The expressions presented in sections 2.3 and 2.4, defining the probability amplitudes of the WP and the time-dependent electronic density, depend on molecular properties such as the (dipole and RIXS) transition moments and the 1PDMs. Evaluating these expressions requires the approximation of the molecular properties within a quantum chemical framework, which in this work corresponds to the EOM-CC theory. The implementation within EOM-CC theory entails the substitution of the bras and kets in the expressions in sections 2.3 and 2.4, with the corresponding left bras and right kets from EOM-CC theory, i.e.

$$\langle\psi_n| \rightarrow \langle\psi_n^L| \qquad\qquad |\psi_{n'}\rangle \rightarrow |\psi_{n'}^R\rangle\,, \tag{3.1}$$

with $\langle\psi_n^L|$ and $|\psi_{n'}^R\rangle$ satisfying the biorthonormality condition,

$$\langle\psi_n^L|\psi_{n'}^R\rangle = \delta_{nn'}. \tag{3.2}$$

The non-hermitian nature of EOM-CC theory creates challenges in the unambiguous definition of the molecular properties, which are related to the normalisation of the EOM-CC bras and kets. These aspects of the implementation are discussed in sections 3.1.1–3.1.3. The discussion in section 3.1.4 proposes a procedure to obtain unambiguously defined transition properties from the EOM-CC transition properties. In section 3.1.5 the procedure outlined in section 3.1.4 is applied to the specific cases of the transition dipole moments, RIXS moments and 1PDMs. Finally, the protocol followed by the quantum chemical calculation is described in section 3.1.6.

3.1.1 Relation between EOM-CC bras and kets

The biorthonormality condition in eq. (3.2) is accompanied by the lack of orthonormality between the right bras and kets and between the left bras and kets, i.e.

$$\langle\psi_n^R|\psi_n^R\rangle \neq 1 \qquad\qquad \langle\psi_n^L|\psi_n^L\rangle \neq 1. \tag{3.3}$$

From the comparison of eq. (3.2) and eq. (3.3) follows that $\langle\psi_n^L|$ and $\langle\psi_n^R|$ can be linked as

$$\langle\psi_n^L| = \langle\psi_n^R| N_n, \tag{3.4}$$

where N_n represents a normalisation constant. Projecting both sides of eq. (3.4) on $|\psi_n^R\rangle$, while considering eq. (3.2), leads to

$$\langle\psi_n^L|\psi_n^R\rangle = N_n \langle\psi_n^R|\psi_n^R\rangle = 1, \tag{3.5}$$

from which it follows that

$$N_n = \frac{1}{\langle\psi_n^R|\psi_n^R\rangle}. \tag{3.6}$$

Plugging eq. (3.6) into eq. (3.4) yields

$$\langle\psi_n^L| = \frac{\langle\psi_n^R|}{\langle\psi_n^R|\psi_n^R\rangle}, \tag{3.7}$$

which explicitly defines the relation between $\langle\psi_n^L|$ and $\langle\psi_n^R|$.

3.1.2 EOM-CC definition of state properties

The expectation value of an arbitrary linear operator, $\hat{\mathcal{O}}$, relative to a given eigenstate – here called 'state property' – is defined within EOM-CC [85] as

$$\mathcal{O}_{nn} = \langle\psi_n^L| \hat{\mathcal{O}} |\psi_n^R\rangle . \tag{3.8}$$

The definition in eq. (3.8) contains both the right ket and the left bra relative to the same eigenstate. This ensures the correct normalisation and the unambiguous definition of state properties within EOM-CC. In fact, substituting $\langle\psi_n^L|$ in eq. (3.8) with its definition from eq. (3.7) results into

$$\mathcal{O}_{nn} = \frac{\langle\psi_n^R|}{\langle\psi_n^R|\psi_n^R\rangle} \hat{\mathcal{O}} |\psi_n^R\rangle = \frac{\langle\psi_n^R|}{\sqrt{\langle\psi_n^R|\psi_n^R\rangle}} \hat{\mathcal{O}} \frac{|\psi_n^R\rangle}{\sqrt{\langle\psi_n^R|\psi_n^R\rangle}}, \tag{3.9}$$

where both the bra and ket sides of the expression are correctly normalised.

3.1.3 EOM-CC definition of transition properties

The matrix element of $\hat{\mathcal{O}}$ relative to two different eigenstates of index n and n' – here called 'transition property' – can be defined within EOM-CC [85] either as

$$\mathcal{O}_{n\leftarrow n'} = \langle\psi_n^L| \hat{\mathcal{O}} |\psi_{n'}^R\rangle \qquad \text{or} \qquad \mathcal{O}_{n'\leftarrow n} = \langle\psi_{n'}^L| \hat{\mathcal{O}}^\dagger |\psi_n^R\rangle . \tag{3.10}$$

The substitution of the left bras in eq. (3.10) with their respective definitions according to eq. (3.7) leads to

$$\mathcal{O}_{n\leftarrow n'} = \frac{\langle \psi_n^R |}{\sqrt{\langle \psi_n^R | \psi_n^R \rangle}} \hat{\mathcal{O}} \frac{| \psi_{n'}^R \rangle}{\sqrt{\langle \psi_n^R | \psi_n^R \rangle}}, \tag{3.11a}$$

$$\mathcal{O}_{n'\leftarrow n} = \frac{\langle \psi_{n'}^R |}{\sqrt{\langle \psi_{n'}^R | \psi_{n'}^R \rangle}} \hat{\mathcal{O}}^\dagger \frac{| \psi_n^R \rangle}{\sqrt{\langle \psi_{n'}^R | \psi_{n'}^R \rangle}}. \tag{3.11b}$$

The comparison between eqs. (3.11a) and (3.11b) shows how the bras and kets are normalised differently in the two expressions, generally making $\mathcal{O}_{n\leftarrow n'} \neq \mathcal{O}^*_{n'\leftarrow n}$. This indicates that the definition of the transition properties as in eq. (3.10) is ambiguous within EOM-CC theory. On the other hand, the definition of 'squared' transition properties [85], i.e.

$$|\mathcal{O}_{nn'}|^2 = \mathcal{O}_{n\leftarrow n'} \mathcal{O}_{n'\leftarrow n}, \tag{3.12}$$

is unambiguous within the EOM-CC framework. In fact, substituting eqs. (3.11a) and (3.11b) in eq. (3.12), while aptly redistributing the normalisation factors, leads to

$$|\mathcal{O}_{nn'}|^2 = \frac{\langle \psi_n^R |}{\sqrt{\langle \psi_n^R | \psi_n^R \rangle}} \hat{\mathcal{O}} \frac{| \psi_{n'}^R \rangle}{\sqrt{\langle \psi_{n'}^R | \psi_{n'}^R \rangle}} \frac{\langle \psi_{n'}^R |}{\sqrt{\langle \psi_{n'}^R | \psi_{n'}^R \rangle}} \hat{\mathcal{O}}^\dagger \frac{| \psi_n^R \rangle}{\sqrt{\langle \psi_n^R | \psi_n^R \rangle}}, \tag{3.13}$$

where all the bras and kets are correctly normalised.

3.1.4 Transition properties from EOM-CC properties

The definition of $\mathcal{O}_{nn'}$ in terms of the corresponding EOM-CC transition properties starts from its definition as a generic complex object, i.e.

$$\mathcal{O}_{nn'} = \langle \psi_n | \hat{\mathcal{O}} | \psi_{n'} \rangle = |\mathcal{O}_{nn'}| e^{i\phi_{nn'}}. \tag{3.14}$$

Here, $|\mathcal{O}_{nn'}|$ can be obtained straightforwardly by taking the square root of $|\mathcal{O}_{nn'}|^2$ which, as shown in the previous section, is well-defined within EOM-CC theory. The phase factor $e^{i\phi_{nn'}}$ can be obtained by considering that the orthonormal $\langle \psi_n |$ and $| \psi_{n'} \rangle$ can be written in terms of EOM-CC eigenkets as

$$\mathcal{O}_{nn'} = \langle \psi_n | \hat{\mathcal{O}} | \psi_{n'} \rangle = \frac{\langle \psi_n^R |}{\sqrt{\langle \psi_n^R | \psi_n^R \rangle}} \hat{\mathcal{O}} \frac{| \psi_{n'}^R \rangle}{\sqrt{\langle \psi_{n'}^R | \psi_{n'}^R \rangle}}. \tag{3.15}$$

Considering the definition in eq. (3.7), eq. (3.15) can be rewritten as

$$\mathcal{O}_{nn'} = \langle \psi_n^L | \hat{\mathcal{O}} | \psi_{n'}^R \rangle \frac{\sqrt{\langle \psi_n^R | \psi_n^R \rangle}}{\sqrt{\langle \psi_{n'}^R | \psi_{n'}^R \rangle}}, \tag{3.16}$$

where the factor highlighted in blue corresponds to a positive, real number. It follows that the phase factor $e^{i\phi_{nn'}}$ associated to $\mathcal{O}_{nn'}$ corresponds to the phase factor $e^{i\phi_{n\leftarrow n'}}$ associated to $\mathcal{O}_{n\leftarrow n'}$, i.e.

$$e^{i\phi_{nn'}} = e^{i\phi_{n\leftarrow n'}} = \frac{\mathcal{O}_{n\leftarrow n'}}{|\mathcal{O}_{n\leftarrow n'}|}. \tag{3.17}$$

3.1.5 Transition moments and 1PDMs

The following subsections outline the computational procedures followed to obtain $\mathcal{O}_{nn'}$ in the specific cases of the transition dipole moments, RIXS moments and 1PDMs.

Transition dipole moments

The transition dipole moments (TDMs) $\boldsymbol{\mu}_{n\leftarrow n'}$ and $\boldsymbol{\mu}_{n'\leftarrow n}$ are defined within EOM-CC by considering $\hat{\mathcal{O}} \equiv \hat{\boldsymbol{\mu}}$ in eq. (3.10). The quantum chemical calculation returns both $\boldsymbol{\mu}_{n\leftarrow n'}$ and $\boldsymbol{\mu}_{n'\leftarrow n}$ as real-valued, three-dimensional vectors. Each component of $|\boldsymbol{\mu}_{nn'}|$ is obtained by taking the square root of the component-wise product of $\boldsymbol{\mu}_{n\leftarrow n'}$ and $\boldsymbol{\mu}_{n'\leftarrow n}$, i.e.

$$|\mu_a^{nn'}| = \sqrt{|\mu_a^{nn'}|^2} = \sqrt{\mu_a^{n\leftarrow n'} * \mu_a^{n'\leftarrow n}}, \tag{3.18}$$

where the index a runs over the x, y and z components of the vectors. The vector of phase factors, $e^{i\boldsymbol{\phi}_{nn'}}$, is obtained via eq. (3.17) by performing an element-wise quotient of the vectors $\boldsymbol{\mu}_{n\leftarrow n'}$ and $|\boldsymbol{\mu}_{n\leftarrow n'}|$. The components of $e^{i\boldsymbol{\phi}_{nn'}}$ can be either plus/minus one – owing to the real-valued nature of $\boldsymbol{\mu}_{n\leftarrow n'}$ – or zero, when the corresponding components of $\boldsymbol{\mu}_{n\leftarrow n'}$ are zero. Each component of $\boldsymbol{\mu}_{nn'}$ is calculated by multiplying the corresponding components of $|\boldsymbol{\mu}_{nn'}|$ and $e^{i\boldsymbol{\phi}_{nn'}}$, i.e.

$$\mu_a^{nn'} = |\mu_a^{nn'}| * e^{i\phi_a^{nn'}}, \tag{3.19}$$

with $\boldsymbol{\mu}_{n'n} = \boldsymbol{\mu}_{nn'}$.

State and transition 1PDMs

A state 1PDM, γ_{pq}^{nn}, is defined according to eq. (3.8) by considering $\hat{\mathcal{O}} \equiv \hat{c}_q^\dagger \hat{c}_p$. Being a state property, a state 1PDM is well-defined within EOM-CC theory and is returned by the quantum chemical calculation as a real-valued, symmetric matrix (in accordance with the properties of state 1PDMs discussed in chapter B). The transition 1PDMs returned by the EOM-CC quantum chemical calculation correspond to

$$\gamma_{pq}^{n\leftarrow n'} = \left\langle \psi_{n'}^L \right| \hat{c}_q^\dagger \hat{c}_p \left| \psi_n^R \right\rangle \qquad \text{and} \qquad \gamma_{pq}^{n'\leftarrow n} = \left\langle \psi_n^L \right| \hat{c}_q^\dagger \hat{c}_p \left| \psi_{n'}^R \right\rangle. \tag{3.20}$$

Here, the same notational convention introduced for $\gamma_{pq}^{nn'}$ in section 2.4 is followed. Both $\gamma_{pq}^{n\leftarrow n'}$ and $\gamma_{pq}^{n'\leftarrow n}$ are returned as real-valued, squared matrices and used to obtain $|\gamma_{pq}^{nn'}|$ according to

$$|\gamma_{pq}^{nn'}| = \sqrt{|\gamma_{pq}^{nn'}|^2} = \sqrt{\gamma_{pq}^{n\leftarrow n'} * \gamma_{qp}^{n'\leftarrow n}}. \tag{3.21}$$

The phase factor in eq. (3.14), $e^{i\phi_{pq}^{nn'}}$, is also represented as a matrix, which has the same dimension of $\gamma_{pq}^{n\leftarrow n'}$ and $\gamma_{pq}^{n'\leftarrow n}$. Each element of $e^{i\phi_{pq}^{nn'}}$ is calculated according to eq. (3.17) as an element-wise quotient of $\gamma_{pq}^{n\leftarrow n'}$ and $|\gamma_{pq}^{n\leftarrow n'}|$. The quotient can be either plus/minus one – owing to $\gamma_{pq}^{n\leftarrow n'}$ being real-valued – or zero, if the corresponding element of $\gamma_{pq}^{n\leftarrow n'}$ equals zero. The transition 1PDM $\gamma_{pq}^{nn'}$ can thereby be obtained as

$$\gamma_{pq}^{nn'} = |\gamma_{pq}^{nn'}| * e^{i\phi_{pq}^{nn'}}. \tag{3.22}$$

The $\gamma_{pq}^{n'n}$ is obtained from $\gamma_{pq}^{nn'}$ based on the properties of the 1PDMs (discussed more in detail in chapter B), according to which $(\gamma_{pq}^{nn'})^\dagger = \gamma_{qp}^{n'n}$. Both $\gamma_{pq}^{nn'}$ and $\gamma_{pq}^{n'n}$ are utilised together with the canonical HF MOs – returned as real-valued volume data by the quantum chemical calculation – in the spatial rendering of $\rho(\boldsymbol{r}, t)$ according to eq. (2.90).

'Non-truncated' RIXS transition moments

The RIXS transition moments correspond to tensors of the form

$$M_{ab}^{kg}(\omega_p, \omega_d) = \sum_n \Big(\frac{\langle \psi_k | \hat{\mu}_a | \psi_n \rangle \langle \psi_n | \hat{\mu}_b | \psi_g \rangle}{\omega_{ng} - \omega_p - i\frac{\Gamma_n}{2}} + \frac{\langle \psi_k | \hat{\mu}_b | \psi_n \rangle \langle \psi_n | \hat{\mu}_a | \psi_g \rangle}{\omega_{ng} + \omega_d - i\frac{\Gamma_n}{2}} \Big), \quad (3.23)$$

where $k \in \{v, g\}$ and the indices a, b run over the x, y and z components of the dipole operator. A 'truncated' approach to the calculation of eq. (3.23) curtails the sum-over-states to a manifold of presumably dominant terms, which are evaluated by calculating all the TDMs involving the considered intermediate states. This approach is often exploited in the simulation of RIXS spectra, see e.g. [116, 117]. While the 'truncated' method is computationally convenient, it is difficult to evaluate *a priori* the loss of accuracy connected with the truncation. The methods described in [90, 91] used in this work reformulate $M_{ab}^{kg}(\omega_p, \omega_d)$ in a closed form using damped response theory [118, 119] and EOM-CC theory. This avoids the explicit specification of the intermediate states, formally including all their contributions and avoiding the accuracy losses connected with the truncation [91]. Drawbacks of this solution include a more complicated implementation and the impossibility of choosing state-specific decay rates, $\frac{\Gamma_n}{2}$, which are substituted by the non-state-specific damping term γ. The definition of eq. (3.23) within EOM-CC theory can be divided in two cases: whenever k=g, $M_{ab}^{kg}(\omega_p, \omega_d)$ becomes

$$M_{ab}^{gg}(\omega_p, \omega_d) = \sum_n \Big(\frac{\langle \psi_g^L | \hat{\mu}_a | \psi_n^R \rangle \langle \psi_n^L | \hat{\mu}_b | \psi_g^R \rangle}{\omega_{ng} - \omega_p - i\gamma} + \frac{\langle \psi_g^L | \hat{\mu}_b | \psi_n^R \rangle \langle \psi_n^L | \hat{\mu}_a | \psi_g^R \rangle}{\omega_{ng} + \omega_d + i\gamma} \Big). \quad (3.24)$$

Here, both the right ket and left bra relative to the ground state and all the intermediate states are present, ensuring – similarly to the case of the state properties discussed in section 3.1.2 – the correct normalisation of all the bras and kets involved. Whenever k=v, $M_{ab}^{kg}(\omega_p, \omega_d)$ becomes a transition property and is accordingly defined within EOM-CC either as

$$M_{ab}^{v\leftarrow g}(\omega_p, \omega_d) = \sum_n \Big(\frac{\langle \psi_v^L | \hat{\mu}_a | \psi_n^R \rangle \langle \psi_n^L | \hat{\mu}_b | \psi_g^R \rangle}{\omega_{ng} - \omega_p - i\gamma} + \frac{\langle \psi_v^L | \hat{\mu}_b | \psi_n^R \rangle \langle \psi_n^L | \hat{\mu}_a | \psi_g^R \rangle}{\omega_{ng} + \omega_d + i\gamma} \Big) \quad (3.25)$$

or

$$M_{ba}^{g\leftarrow v}(\omega_p, \omega_d) = \sum_n \Big(\frac{\langle \psi_g^L | \hat{\mu}_b | \psi_n^R \rangle \langle \psi_n^L | \hat{\mu}_a | \psi_v^R \rangle}{\omega_{ng} - \omega_p + i\gamma} + \frac{\langle \psi_g^L | \hat{\mu}_a | \psi_n^R \rangle \langle \psi_n^L | \hat{\mu}_b | \psi_v^R \rangle}{\omega_{ng} + \omega_d - i\gamma} \Big). \quad (3.26)$$

In eqs. (3.25) and (3.26), the correct normalisation is solely limited to the bras and kets of the intermediate states, but not to those relative to the ground and valence-excited states. $M_{ab}^{gg}(\omega_p, \omega_d)$, $M_{ab}^{v\leftarrow g}(\omega_p, \omega_d)$ and $M_{ba}^{g\leftarrow v}(\omega_p, \omega_d)$ are returned by the

quantum chemical calculation as 3x3 matrices evaluated at each point of the (same) frequency grid defined by ω_p and ω_d. The absolute value of the RIXS moment, $|M_{ab}^{vg}(\omega_p, \omega_d)|$, is calculated as

$$|M_{ab}^{vg}(\omega_p, \omega_d)| = \sqrt{|M_{ab}^{vg}(\omega_p, \omega_d)|^2} = \sqrt{M_{ab}^{v\leftarrow g}(\omega_p, \omega_d) * M_{ba}^{g\leftarrow v}(\omega_p, \omega_d)}. \tag{3.27}$$

Based on the definition in eq. (3.17), the phase factor, $e^{i\phi_{ab}^{vg}}(\omega_p, \omega_d)$, is defined as a 3x3 matrix at each point of the frequency grid. The elements of $e^{i\phi_{ab}^{vg}}(\omega_p, \omega_d)$ are defined according to eq. (3.17), setting them to zero should the corresponding elements of $|M_{ab}^{v\leftarrow g}(\omega_p, \omega_d)|$ be zero. Finally, $M_{ab}^{vg}(\omega_p, \omega_d)$ is obtained as

$$M_{ab}^{vg}(\omega_p, \omega_d) = |M_{ab}^{vg}(\omega_p, \omega_d)| * e^{i\phi_{ab}^{vg}}(\omega_p, \omega_d), \tag{3.28}$$

with $M_{ab}^{gv}(\omega_p, \omega_d) = M_{ab}^{vg^*}(\omega_p, \omega_d)$.

3.1.6 Computational details

All the quantum chemical calculations are performed using a developer version of the Q-Chem 6.1 software package [120], modified to output both $\gamma_{pq}^{n'\leftarrow n}$ and $\gamma_{pq}^{n\leftarrow n'}$. The ground state equilibrium geometries of OCS and Oxazole are optimised at the CCSD/aug-cc-pvdz level of theory. The calculations of the respective electronic structures are performed at the fc-CVS-EOM-EE-CCSD/6-311+G* level of theory. The electronic structure calculation follows a 3-step protocol: a restricted HF calculation is followed by a ground-state CCSD calculation (i.e. $\hat{T} = \hat{T}_1 + \hat{T}_2$), with the final step being a fc-CVS-EOM-EE-CCSD calculation [121]. In order to assemble the time-dependent electronic density correctly it is necessary to obtain all the necessary quantities from a single calculation. This is needed since each HF molecular orbital and EOM-CC state is determined up to a ± 1 factor, which changes arbitrarily between different instances of the same calculation. Assembling the electronic density with the output of a single calculation instance ensures the consistent compensation of the ± 1 factors and the reproducibility of the results. A detailed description of the calculation parameters can be found at [122], where sample Qchem input files are available.

3.2 Numerical implementation

3.2.1 Description of the light pulse

The electric field amplitude $E(\omega) = |E(\omega)|e^{i\phi(\omega)}$ is implemented considering the phase $\phi(\omega) = 0$ for every value of ω and

$$|E(\omega)| = E_0 e^{-\frac{(\omega-\omega_f)^2}{4\beta}}. \tag{3.29}$$

Here, $|E(\omega)|$ corresponds to the Fourier transform of the time-domain Gaussian pulse

$$|E(t)| = E_0 \sqrt{\frac{\beta}{\pi}} e^{-\beta t^2} \cos(\omega_f t). \tag{3.30}$$

Here, ω_f is the carrier frequency, the parameter β is related to the pulse bandwidth $\Delta\nu$ (i.e. Full width at half maximum (FWHM) of $|E(\omega)|^2$) and the pulse duration Δt (i.e. FWHM of $|E(t)|^2$) according to

$$\Delta\nu = \frac{\Delta\omega}{2\pi} = \frac{\sqrt{2\beta \ln 2}}{\pi} \qquad \text{and} \qquad \Delta t = \sqrt{\frac{2\ln 2}{\beta}}, \tag{3.31}$$

respectively. In this work, a bandwidth $\Delta\omega = {}^{8\ eV}/_{\hbar}$ (corresponding to a pulse duration $\Delta t \approx 230$ as) has been considered. This follows from the need to include a large number of excited states in the WP prepared in OCS and Oxazole. Pulses of similar duration/bandwidth in the water window might soon become available at HHG-based [31, 123] and XFEL facilities [32]. The parameter E_0 in eq. (3.30) is related to the pulse irradiance, I, according to

$$E_0 = \sqrt{2I\alpha/\epsilon_0}. \tag{3.32}$$

For all the calculations performed in this work, I was limited to $10^{16}\ {}^{W}/_{cm^2}$. This value for I is easily achievable at XFEL facilities and allows to safely remain in the perturbative regime, fitting the requirements of the theory. The polarisation vectors are expressed according to the Jones formalism [124]. The linear polarisation options tested in this thesis correspond to the following vectors:

$$\boldsymbol{\epsilon}^{x} = \begin{bmatrix} 1 \\ 0 \\ 0 \end{bmatrix}, \qquad \boldsymbol{\epsilon}^{z} = \begin{bmatrix} 0 \\ 0 \\ 1 \end{bmatrix}, \qquad \boldsymbol{\epsilon}^{xz} = \frac{1}{\sqrt{2}} \begin{bmatrix} 1 \\ 0 \\ 1 \end{bmatrix}. \tag{3.33}$$

The circularly polarised options are defined in the xy-plane as

$$\boldsymbol{\epsilon}^{R_{xy}} = \frac{1}{\sqrt{2}} \begin{bmatrix} 1 \\ i \\ 0 \end{bmatrix}, \qquad \boldsymbol{\epsilon}^{L_{xy}} = \frac{1}{\sqrt{2}} \begin{bmatrix} 1 \\ -i \\ 0 \end{bmatrix}, \tag{3.34}$$

where $\boldsymbol{\epsilon}^{R_{xy}}$ represents the right-handed circular polarisation while $\boldsymbol{\epsilon}^{L_{xy}}$ the left-handed circular polarisation.

3.2.2 Numerical integration

The computation of the integrals in the expressions for $a_c^{(1)}(t)$ in eq. (2.72), $a_v^{(2)}(t)$ in eq. (2.74) and $a_g^{(2)}(t)$ in eq. (2.76) poses some challenges when performed numerically on a frequency grid. The calculation of the integral for $a_c^{(1)}(t)$ in eq. (2.72) is computationally defined on a one-dimensional frequency array. The convergence of the integral is ensured by the ${}^{\Gamma_c}/_2$-dependent term in the denominator, which makes the integrand finite especially in the frequency region where $\omega \approx \omega_{cg}$. In this region, the integrand undergoes a fast oscillation, whose width is inversely proportional to Γ_c. The adequate sampling of this oscillation requires the grid step size, $\Delta\omega$, to be small enough to satisfy $\Delta\omega \approx {}^{\Gamma_c}/_2$, potentially making the integration computationally challenging. In the calculation of eq. (2.72), the values of $\Delta\omega$ corresponding to the considered Γ_c allow a computationally affordable numerical integration. The following values of Γ_c (the same for all the core-excited states at a given edge) are considered in this work: 0.005 a.u. (0.140 eV) at the Oxygen K-Edge [37], 0.0049

a.u. (0.132 eV) at the Nitrogen K-Edge [39] and 0.0039 a.u. (0.105 eV) at the Sulfur L1-Edge [125] [I]. Challenges similar to those faced in the one-dimensional integral in eq. (2.72) are present in the solution of the two-dimensional integrals associated with $a_v^{(2)}(t)$ in eq. (2.74) and $a_g^{(2)}(t)$ in eq. (2.76). The respective double integrals are numerically defined on a two-dimensional frequency grid, which is schematically represented in fig. 3.1. Here, the red line represents the points of the grid at which the resonance condition $\omega_{kg} - \omega_p + \omega_d = 0$ is satisfied, with $k \in \{v, g\}$. On the other hand, the blue strip corresponds to the points of the frequency grid where the size of the grid steps $\Delta\omega_p$ and $\Delta\omega_d$ should be small enough to capture the rapid oscillation of the integrand. It is at this point that computational challenges arise in the numerical calculation of the double integrals. In fact, in the case of $a_v^{(2)}(t)$

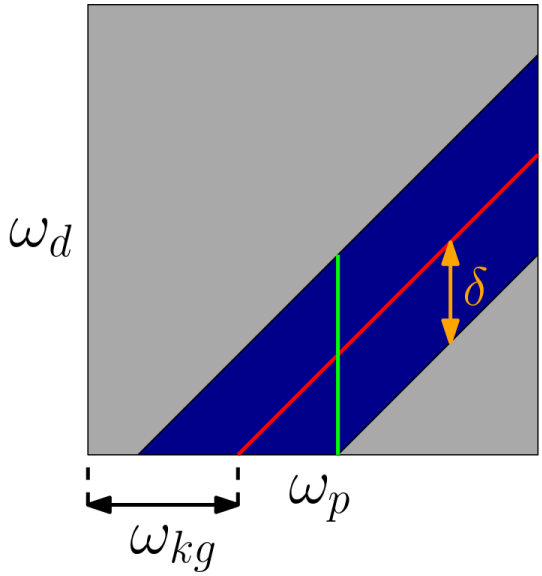

Figure 3.1: *Frequency grid partitioning for numerical integration. In the grey areas the integration is performed numerically, while in the blue strip the analytical formulation is applied. The red line corresponds to points where $\omega_{kg} = \omega_p - \omega_d$ is satisfied. The green line corresponds to the 'strip element', the orange double arrow to the strip's half width δ.*

in eq. (2.74), satisfying the condition $\Delta\omega_p = \Delta\omega_d \approx {}^{\Gamma_v}/_2$ – with $\Gamma_v \ll \Gamma_c$, owing to the longer lifetime of the valence-excited states compared to the core-excited states – requires a very dense frequency grid. The dimension of this grid quickly makes the numerical integration very demanding from a computational standpoint. The problem is even bigger in the case of $a_g^{(2)}(t)$ in eq. (2.76). In fact, due to $\Gamma_g = 0$, the integrand diverges for values of ω_p and ω_d such that $\omega_d - \omega_p \approx 0$, which correspond to the blue strip in fig. 3.1 A possible solution to this problem relies on the approximated calculation of

$$a_k^{(2)}(t) = \lim_{\Gamma \to 0} \frac{1}{2\pi} \int_0^\infty d\omega_p \int_0^\infty d\omega_d \frac{e^{i(\omega_{kg} - \omega_p + \omega_d - i\frac{\Gamma}{2})t}}{\omega_{kg} - \omega_p + \omega_d - i\frac{\Gamma}{2}} f_{kg}(\omega_p, \omega_d). \tag{3.35}$$

Here, $f_{kg}(\omega_p, \omega_d) = E^*(\omega_p)E(\omega_d)\boldsymbol{\epsilon}_p\boldsymbol{\epsilon}_d \cdot \boldsymbol{M}_{kg}(\omega_p, \omega_d)$, with $k \in \{v, g\}$, and Γ corresponds to a generic decay rate. The proposed solution entails solving the integral in

[I] Here, the value of Γ_c at the Sulfur L2-Edge has been adopted, in relation to the difficulty of finding the L1-Edge value in the literature

eq. (3.35) in a different way in the two regions of the frequency grid represented by the grey areas and the blue strip in fig. 3.1. This corresponds to the formulation of $a_k^{(2)}(t)$ in terms of two contributions, i.e.

$$a_k^{(2)}(t) = a_k^N(t) + a_k^S(t). \tag{3.36}$$

The $a_k^N(t)$ contribution derives from the grey areas of the frequency grid, which correspond to values of ω_p and ω_d such that $\omega_{kg} - \omega_p + \omega_d \ll 0$ or $\gg 0$. In these areas, the integrand in eq. (3.35) is slowly oscillating, which allows the numerical calculation of the double integral on a computationally affordable grid. On the other hand, the $a_k^S(t)$ contribution corresponds to the blue strip of the frequency grid, where the numerical integration of eq. (3.35) is very demanding/unfeasible. Here, the numerical implementation relies on an analytical approximation based on the division of the strip into discrete 'strip elements' of length 2δ. An example of strip element is pictorially represented by the green vertical segment in fig. 3.1. Each strip element corresponds to a one-dimensional frequency domain, along which the integral in eq. (3.35) is approximated in terms of a truncated Taylor expansion as

$$a_k^{S_e}(t) = \lim_{\Gamma\to 0} \int_{\omega_0-\delta}^{\omega_0+\delta} d\omega_s \frac{e^{i(\omega_s-\omega_0-i\frac{\Gamma}{2})t}}{\omega_s - \omega_0 - i\frac{\Gamma}{2}} f(\omega_s) \approx$$
$$\approx f(\omega_0)\Big(i\pi + 2i\mathrm{Si}(\delta t)\Big) + f'(\omega_0)\frac{2\sin\delta t}{t}. \tag{3.37}$$

Here, $a_k^{S_e}(t)$ corresponds to the contribution of each strip element to $a_k^S(t)$. In eq. (3.37), ω_0 represents the centre of the strip element, ω_s the points of the frequency grid belonging to the strip element, while $f(\omega_s)$ corresponds to the values of $f_{kg}(\omega_p, \omega_d)$ evaluated on the strip element. The summation of the $a_k^{S_e}(t)$ contributions from all the strip elements leads to an approximate value of $a_k^S(t)$. Finally, the summation of $a_k^S(t)$ to $a_k^N(t)$ affords an approximate value of $a_k^{(2)}(t)$. An in-depth discussion and the complete derivation[II] of the solution for $a_k^{S_e}(t)$ in eq. (3.37) is contained in chapter C, while more details on its practical implementation can be found at [122] [III].

[II] Developed in close collaboration with Stasis Chuchurka, whose contribution has been fundamental in the conception of the idea and its theoretical development.

[III] The great help from Dr. Mads Jakobsen with the optimisation and parallelisation of the implementation is gratefully acknowledged.

CHAPTER 4

Wave packet in OCS

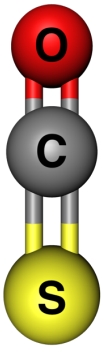

The OCS molecule is characterised by the linear structure shown in the inset, where O, C and S are bound through double bonds. The cylindrical symmetry of the molecule is described by the $C_{\infty v}$ point group, with the C_∞ axis coinciding with the molecular axis containing O, C and S [I]. The first seven valence-excited states of OCS, together with the corresponding transition energies ω_{vg}, are listed on the left side of table 4.1. The energy range spanned by the ω_{vg}'s is comparable with the 8 eV of the pulse bandwidth, thereby allowing the coherent population of several valence-excited states. Each valence-excited state is labelled according to an irreducible representation of the $C_{\infty v}$ point group, whose character table is shown on the right side of table 4.1. In accordance with the (dipole and Raman) selection rules, each irreducible representation is associated with one or more of the considered pulse polarisations. This suggests the possibility of using the pulse polarisation to control the symmetry and number of the valence-excited states included in the WP. The presence of atoms of three different elements allows investigating how the element-specific X-Ray excitation affects the WP preparation and dynamics. The flexibility of the computational implementation allows simulating the excitation at any edge of O, C or S. This study focuses on excitations at the O K-Edge and at the S L1-Edge, considering the central frequency of the pulse, ω_0, resonant to the $1s \rightarrow \pi^*$ transition. At the considered level of theory, ω_0 is equal to 535.63 eV at the O K-Edge and to 229.74 eV at the S L1-Edge. The considered core-excited states are listed in table 4.2. To give a measure of the number of core-excited states included within the bandwidth, the transition energies $\delta\omega_O$ and $\delta\omega_S$ are calculated relatively to the $1s \rightarrow \pi^*$ transition (which corresponds to the $1\Sigma^+ \rightarrow 1^c\Pi_x/1^c\Pi_y$ transition). The comparison between the $\delta\omega_S$ and $\delta\omega_O$ columns shows that more core-excited states are potentially included when the excitation at the S L1-Edge is considered. Just like for the valence-excited states, the variation of

[I] In this work, the C_∞ rotation axis coincides with the z-axis of the three-dimensional Cartesian system.

$\|\psi_v\rangle$	ω_{vg} (eV)
$1\Sigma^-$	5.72
$1\Delta_{x^2-y^2}$	5.75
$1\Pi_x$	7.21
$2\Sigma^+$	8.22
$2\Pi_x$	8.43
$2\Delta_{x^2-y^2}$	9.10
$3\Pi_x$	9.18

$C_{\infty v}$	E	$2C_\infty^\Phi$	...	$\infty\sigma_v$	ϵ
Σ^+	1	1	...	1	$x^\dagger$, $z^{*\dagger}$, $Cxy^\dagger$, $xz^{*\dagger}$
Σ^-	1	1	...	-1	$Cxy^\dagger$
Π	2	$2\cos\Phi$	...	0	x^*, Cxy^*, $xz^{*\dagger}$
Δ	2	$2\cos 2\Phi$	...	0	$x^\dagger$, $xz^\dagger$

Table 4.1: *Transition energies of the considered valence-excited states (left) and character table of the $C_{\infty v}$ point group (right). The transition energies are referred to the ground state $1\Sigma^+$. Each irreducible representation in the character table is associated with a pulse polarisation, in accordance with the selection rules associated with the $C_{\infty v}$ point group. The * superscript indicates dipole-allowed transitions, the † superscript indicates Raman-allowed transitions. Both the right-handed and left-handed circular polarisations are indicated as Cxy.*

$\|\psi_c\rangle$	$\delta\omega_S$ (eV)	$\delta\omega_O$ (eV)	$\|\psi_c\rangle$	$\delta\omega_S$ (eV)	$\delta\omega_O$ (eV)
$1^c\Sigma^+$	0.99	2.87	$1^c\Pi_x$, $1^c\Pi_y$	0	0
$2^c\Sigma^+$	2.33	4.98	$2^c\Pi_x$, $2^c\Pi_y$	3.76	5.21
$3^c\Sigma^+$	2.68	5.69	$3^c\Pi_x$, $3^c\Pi_y$	5.24	6.79
$4^c\Sigma^+$	5.26	6.26	$4^c\Pi_x$, $4^c\Pi_y$	10.01	10.00
$5^c\Sigma^+$	6.80	8.34	$5^c\Pi_x$, $5^c\Pi_y$	10.74	13.57

Table 4.2: *Detuning of the core-excited states' transition energies from the $1s \rightarrow \pi^*$ transition at the S L1-Edge ('$\delta\omega_S$' column) and at the O K-Edge ('$\delta\omega_O$' column). The core-excited states are labelled according to the irreducible representations of the $C_{\infty v}$ point group, with the superscript ^{c} standing for core-excited.*

the pulse polarisation allows – by means of the dipole selection rules – to select the symmetry of the core-excited states included in the WP. Since the Σ^+-symmetric states distribute over a smaller energy range than the Π-symmetric states, also the number of core-excited states included in the WP can be tuned via the polarisation. In the following, the electronic WP launched in neutral OCS by an *as* X-Ray pulse is studied, with the aim of answering the questions formulated in section 1.4. The properties of the WP are studied in terms of the electronic difference density and the decomposition into its components presented in section 2.4. In particular, the structure of each density component will be discussed more in-depth, connecting it with the characteristics of the excitation. The variation of each density component with respect to the pulse polarisation and resonant frequency (i.e. S L1-Edge vs O K-Edge) is furthermore examined.

4.1 Difference density $\rho_\Delta(\boldsymbol{r}, t)$

4.1.1 x polarisation

Snapshots of $\rho_\Delta(\boldsymbol{r}, t)$, relative to a pulse linearly polarised along the x-axis, are shown in fig. 4.1. At 400 *as*, as the pulse has almost completely faded, $\rho_\Delta(\boldsymbol{r}, t)$ ap-

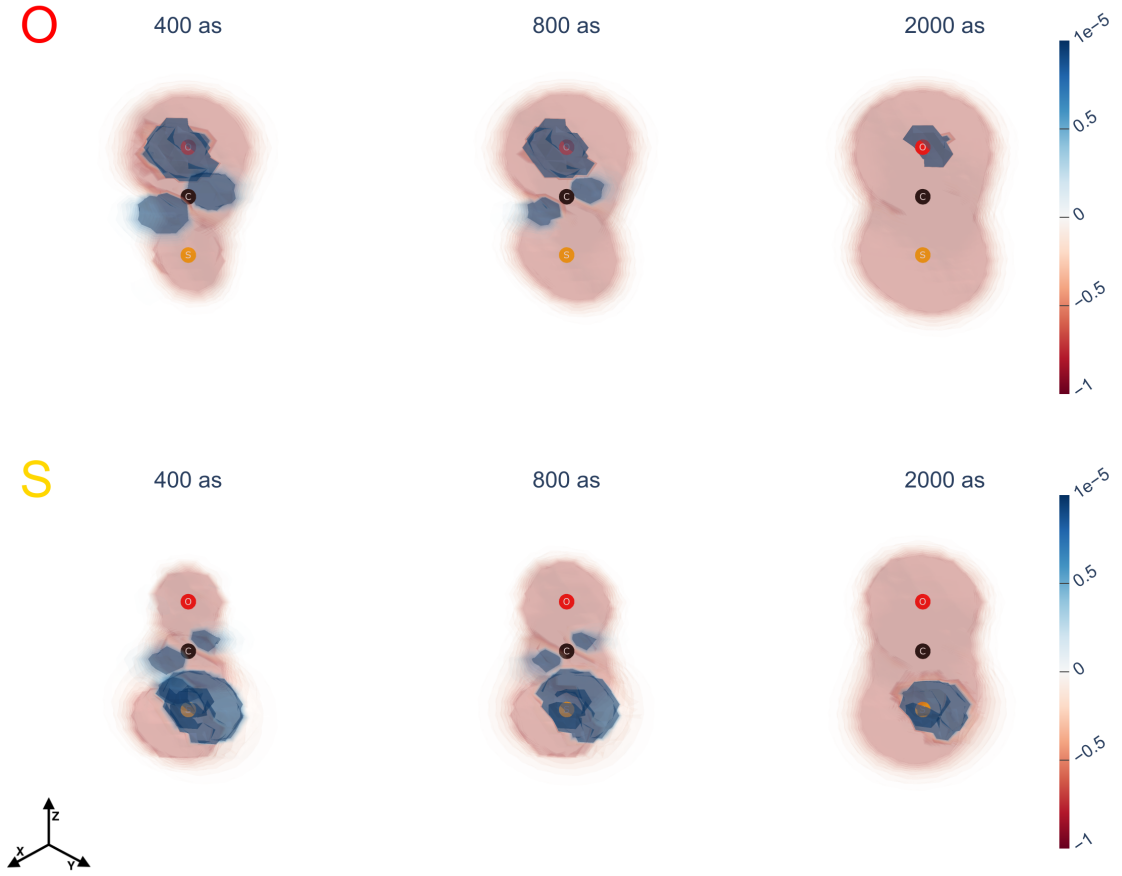

Figure 4.1: *Snapshots of $\rho_\Delta(\boldsymbol{r}, t)$ relative to the excitation considering a pulse linearly polarised along the x-axis. The upper panel is relative to the excitation at the O K-Edge, the lower panel to the excitation at the S L1-Edge. The axes orientation is illustrated in the lower left corner.*

pears polarised towards O or S (i.e. the pumped atoms) depending on the molecule being pumped at the O K-Edge or S L1-Edge, respectively. In particular, positively-valued regions of $\rho_\Delta(\boldsymbol{r}, t)$ are localised around O, S and C. $\rho_\Delta(\boldsymbol{r}, t)$ appears symmetric with respect to the σ_{xz} plane but not with respect to the σ_{yz} plane. The snapshots at 800 *as* and 2000 *as* show the evolution of $\rho_\Delta(\boldsymbol{r}, t)$ in time, which is characterized by progressive disappearance of the positively-valued regions in favour of the negatively-valued ones.

4.1.2 z polarisation

Snapshots of $\rho_\Delta(\boldsymbol{r}, t)$, relative to a pulse linearly polarised along the z-axis, are shown in fig. 4.2. Similarly to the x-polarised case, $\rho_\Delta(\boldsymbol{r}, t)$ is positively-valued

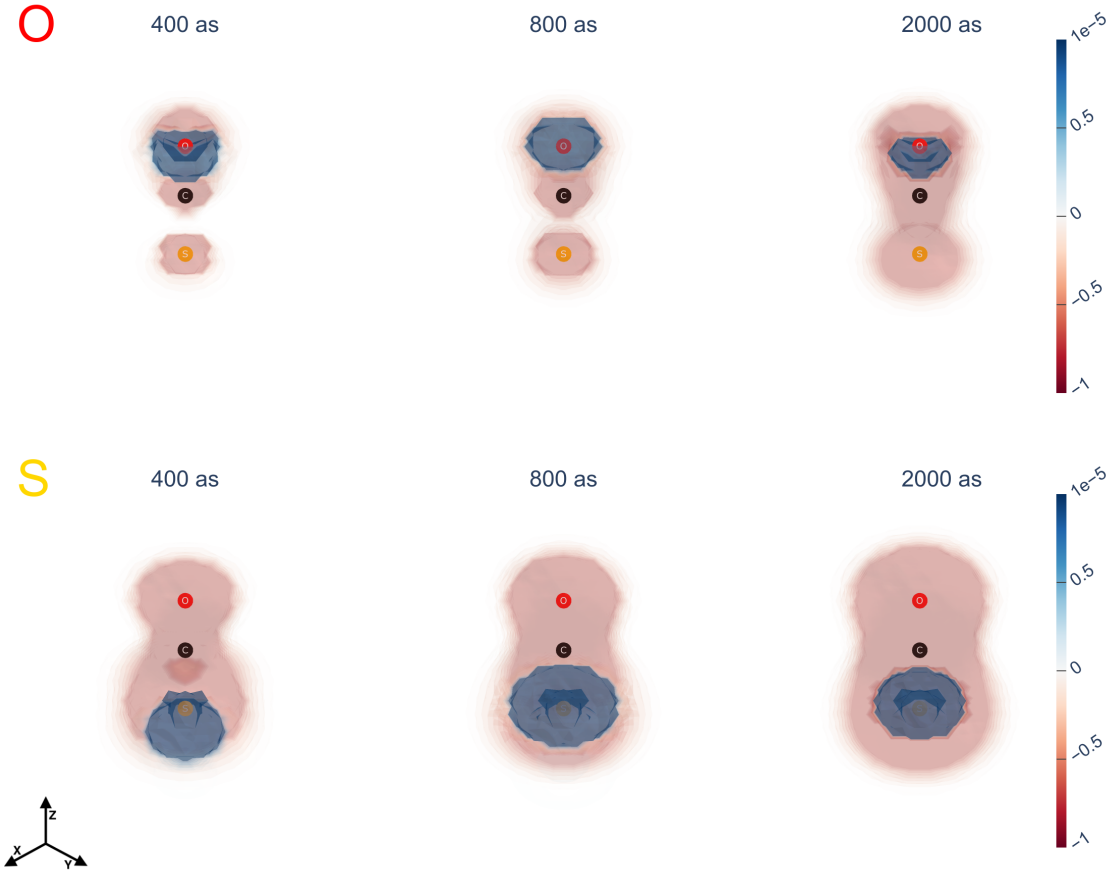

Figure 4.2: *Snapshots of $\rho_\Delta(\boldsymbol{r}, t)$ relative to the excitation considering a pulse linearly polarised along the z-axis. The upper panel is relative to the excitation at the O K-Edge, the lower panel to the excitation at the S L1-Edge. The axes orientation is illustrated in the lower left corner.*

around the pumped atoms. The negatively-valued regions grow with time, reaching eventually – especially for the excitation at the S L1-Edge – a distribution similar to that found at 2000 *as* in the x-polarised case. The comparison of the upper and lower panels shows a smaller spatial extent of the negative regions of $\rho_\Delta(\boldsymbol{r}, t)$ at the O K-Edge compared to the S L1-Edge. Unlike the x-polarised case, $\rho_\Delta(\boldsymbol{r}, t)$ is characterised by a cylindrical symmetry around the z-axis, consistently with the Σ^+ symmetry of the states involved in the WP (c.f. tables 4.1 and 4.2).

4.1.3 xz polarisation

Snapshots of $\rho_\Delta(\boldsymbol{r}, t)$, relative to a pulse linearly polarised at a 45 degrees angle in the σ_{xz} plane, are shown in fig. 4.3. As in the x- and z-polarised cases, the positively-

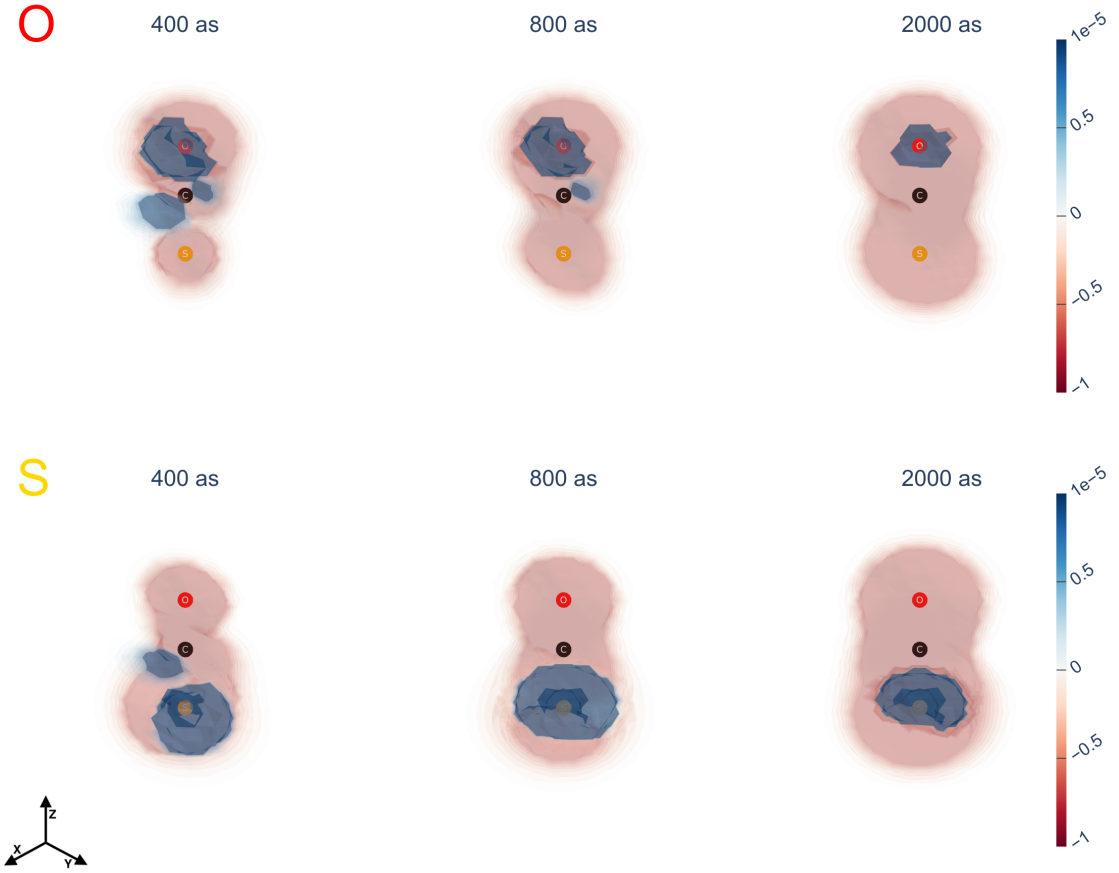

Figure 4.3: *Snapshots of $\rho_\Delta(\boldsymbol{r}, t)$ relative to the excitation considering a pulse linearly polarised at a 45 degrees angle in the σ_{xz} plane. The upper panel is relative to the excitation at the O K-Edge, the lower panel to the excitation at the S L1-Edge. The axes orientation is illustrated in the lower left corner.*

valued parts of $\rho_\Delta(\boldsymbol{r}, t)$, except those around the pumped atoms, are progressively offset by the negatively-valued parts. The symmetry properties of $\rho_\Delta(\boldsymbol{r}, t)$ at the O K-Edge resemble closely those obtained in the x-polarised case (c.f. fig. 4.1-upper panel). On the other hand, at the S L1-Edge, particularly at 400 *as*, $\rho_\Delta(\boldsymbol{r}, t)$ presents symmetry properties lying in between those of the x-polarised and z-polarised cases, with the characteristics proper of the z-polarised case prevailing at 800 *as* and 2000 *as*.

4.1.4 Rxy and Lxy polarisations

Snapshots of $\rho_\Delta(\boldsymbol{r}, t)$, relative to the excitation with a right-handed (Rxy) and a left-handed (Lxy) circularly polarised pulse are shown in figs. 4.4 and 4.5, respectively. The properties of $\rho_\Delta(\boldsymbol{r}, t)$'s structure and time evolution appears very similar in

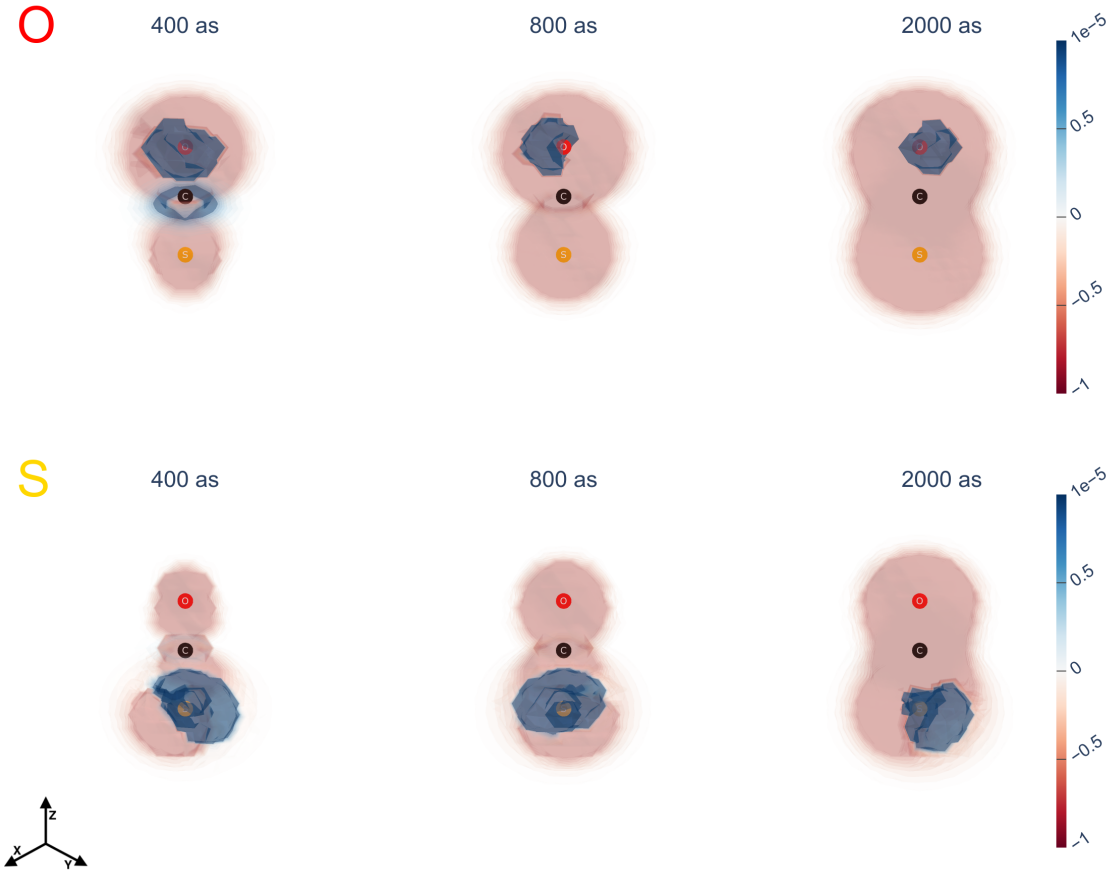

Figure 4.4: *Snapshots of $\rho_\Delta(\boldsymbol{r}, t)$ relative to the excitation with a right-handed, circularly polarised pulse in the σ_{xy} plane. The upper panel is relative to the excitation at the O K-Edge, the lower panel to the excitation at the S L1-Edge. The axes orientation is illustrated in the lower left corner.*

the two cases. Similarly to other polarisation cases, $\rho_\Delta(\boldsymbol{r}, t)$ is positively-valued in correspondence to the pumped atom, with the positively-valued region on C gradually disappearing in favour of negatively-valued regions. With the exclusion of the region localised on the pumped atom, $\rho_\Delta(\boldsymbol{r}, t)$ shows a cylindrical symmetry with respect to the C_∞ axis. This is evident in the negatively-valued regions and the positively-valued regions at C where, especially in the 400 *as* snapshot at the O K-Edge, the positively-valued region presents a ring-like shape.

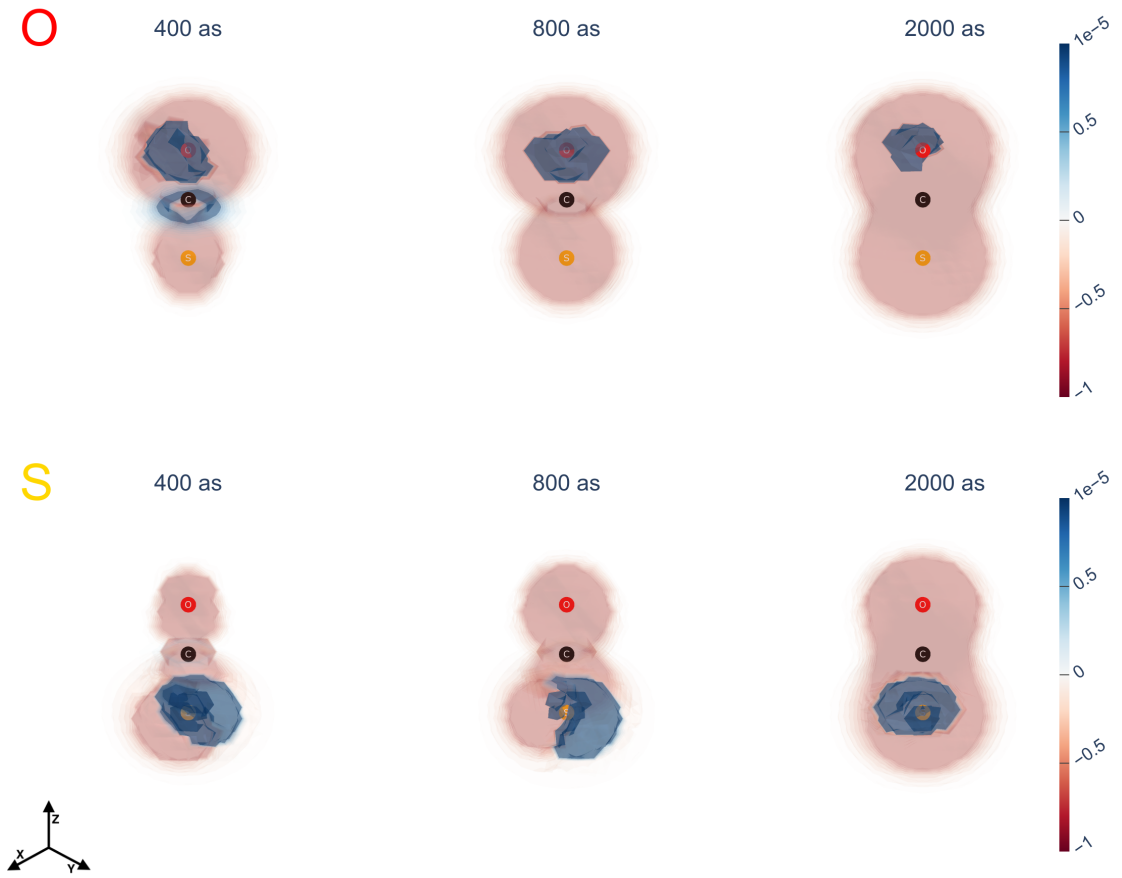

Figure 4.5: *Snapshots of $\rho_\Delta(\boldsymbol{r}, t)$ relative to the excitation with a left-handed, circularly polarised pulse in the σ_{xy} plane. The upper panel is relative to the excitation at the O K-Edge, the lower panel to the excitation at the S L1-Edge. The axes orientation is illustrated in the lower left corner.*

4.2 $\rho_{cg}(\boldsymbol{r}, t)$ component

The characteristics of $\rho_{cg}(\boldsymbol{r}, t)$'s spatial distribution are directly connected to the properties of the transition density $\rho_{cg}(\boldsymbol{r})$, i.e.

$$\rho_{cg}(\boldsymbol{r}) = \sum_{pq} \gamma_{pq}^{cg} \phi_p(\boldsymbol{r}) \phi_q(\boldsymbol{r}), \tag{4.1}$$

and in particular to the structure of the transition 1PDM, $\gamma_{pq}^{cg} = \langle \psi_g | \hat{c}_q^\dagger \hat{c}_p | \psi_c \rangle$. Two

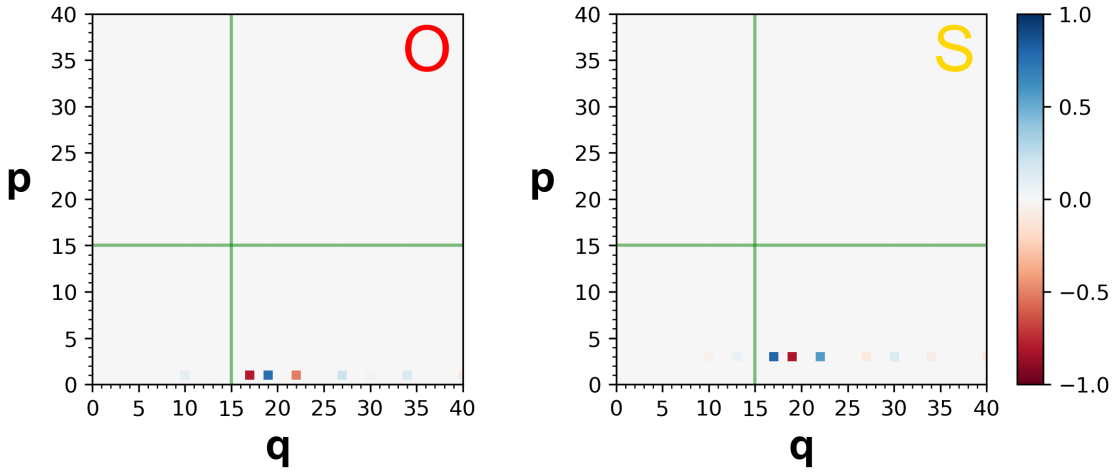

Figure 4.6: *Transition 1PDM γ_{pq}^{cg}, relative to $c \equiv 1^c\Pi_x$, expanded in the basis of canonical MOs. The left panel corresponds to the O K-Edge excitation, the right panel to the S L1-Edge excitation. The range p, q=0-15 represents the hole MOs while the range p, q=0-40 the particle MOs (limited to 40 from the 74 generated through the 6-311+G* basis). The green lines divide the matrices in hole-hole, particle-hole and particle-particle subspaces.*

examples of γ_{pq}^{cg} are shown in fig. 4.6, where the excitations at the O K-Edge and S L1-Edge relative to $c \equiv 1^c\Pi_x$ are compared. Here, γ_{pq}^{cg} are represented in the basis of canonical MOs, which are grouped in terms of their hole or particle nature by the green lines. The main non-zero matrix elements are found in the particle-hole subspace in the lower-right quadrants, with the 'p' rows representing the hole MOs while the 'q' columns the particle MOs. In both cases, only a single 'p' row contains non-zero elements: at the O K-Edge (left) p=1, corresponding to an electron being annihilated in the O 1s MO, while at the S L1-Edge (right) p=3, corresponding to an electron being annihilated in the S 2s MO. On the other hand, multiple 'q' columns show non-zero elements, in correspondence to the particle MOs in which the electron is 'created'. In the construction of $\rho_{cg}(\boldsymbol{r})$ via eq. (4.1), γ_{pq}^{cg} acts as a 'filter' which allows only certain MOs to participate in the $\phi_p(\boldsymbol{r})\phi_q(\boldsymbol{r})$ products. In this particular case, the $\phi_p(\boldsymbol{r})$s correspond to the core MOs, which are characterised by a very tight atom-specific spatial localisation; the $\phi_q(\boldsymbol{r})$s correspond to MOs from the valence-shells of the electronic structure, which are generally delocalised over the whole molecule and characterised by a specific symmetry (which depends on the irreducible representation they are basis for). The inclusion of the core MOs in the $\phi_p(\boldsymbol{r})\phi_q(\boldsymbol{r})$ products determines the atom-specific localisation properties of $\rho_{cg}(\boldsymbol{r})$. Conversely, owing to the total symmetric nature of the $\phi_p(\boldsymbol{r})$s, the $\phi_q(\boldsymbol{r})$s determine the symmetry of the $\phi_p(\boldsymbol{r})\phi_q(\boldsymbol{r})$ products, which is directly inherited by

$\rho_{cg}(\boldsymbol{r})$. Therefore, the properties of the pulse (i.e. the edge selected for the excitation and polarisation) control directly the localisation and symmetry characteristics of the $\rho_{cg}(\boldsymbol{r})$s which, through the mediation of the $\rho_{cg}^{(1)}(t)$ coherences, participate in the construction of the $\rho_{cg}(\boldsymbol{r}, t)$ component.

4.2.1 x polarisation

The time-evolution of $\rho_{cg}(\boldsymbol{r}, t)$, relative to an excitation with a pulse linearly polarised along the x-axis, is illustrated in fig. 4.7. In line with the high oscillation

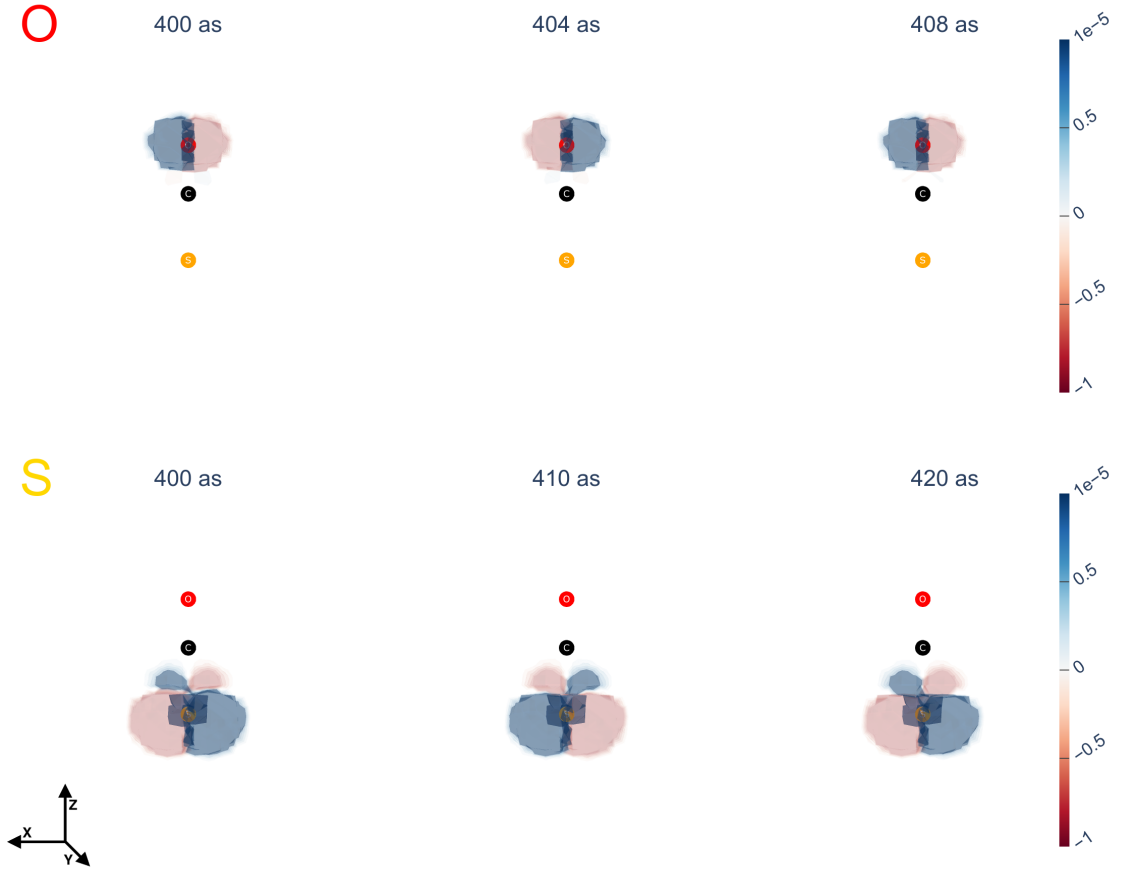

Figure 4.7: *Snapshots of $\rho_{cg}(\boldsymbol{r}, t)$ relative to the excitation considering a pulse linearly polarised along the x-axis. The upper panel is relative to the excitation at the O K-Edge, the lower panel to the excitation at the S L1-Edge. The axes orientation is illustrated in the lower left corner.*

frequency of $\rho_{cg}^{(1)}(t)$, due to ω_{cg} being in the X-Ray domain, $\rho_{cg}(\boldsymbol{r}, t)$ oscillates with a period of ≈ 8 *as* at the O K-Edge and ≈ 20 *as* at the S L1-Edge. Consistently with the polarisation alignment, $\rho_{cg}(\boldsymbol{r}, t)$ oscillates along the x-axis in both cases. The shape of $\rho_{cg}(\boldsymbol{r}, t)$ differs between the two edges, resembling that of a p_x atomic orbital at the O K-Edge and that of a d_{xz} atomic orbital at the S L1-Edge. This is consistent with the Π_x symmetry (c.f. table 4.2) of the core-excited states selected via the pulse polarisation.

4.2.2 z polarisation

The time-evolution of $\rho_{cg}(\boldsymbol{r}, t)$, relative to an excitation with a pulse linearly polarised along the z-axis, is shown in fig. 4.8. The properties of $\rho_{cg}(\boldsymbol{r}, t)$ reflect the

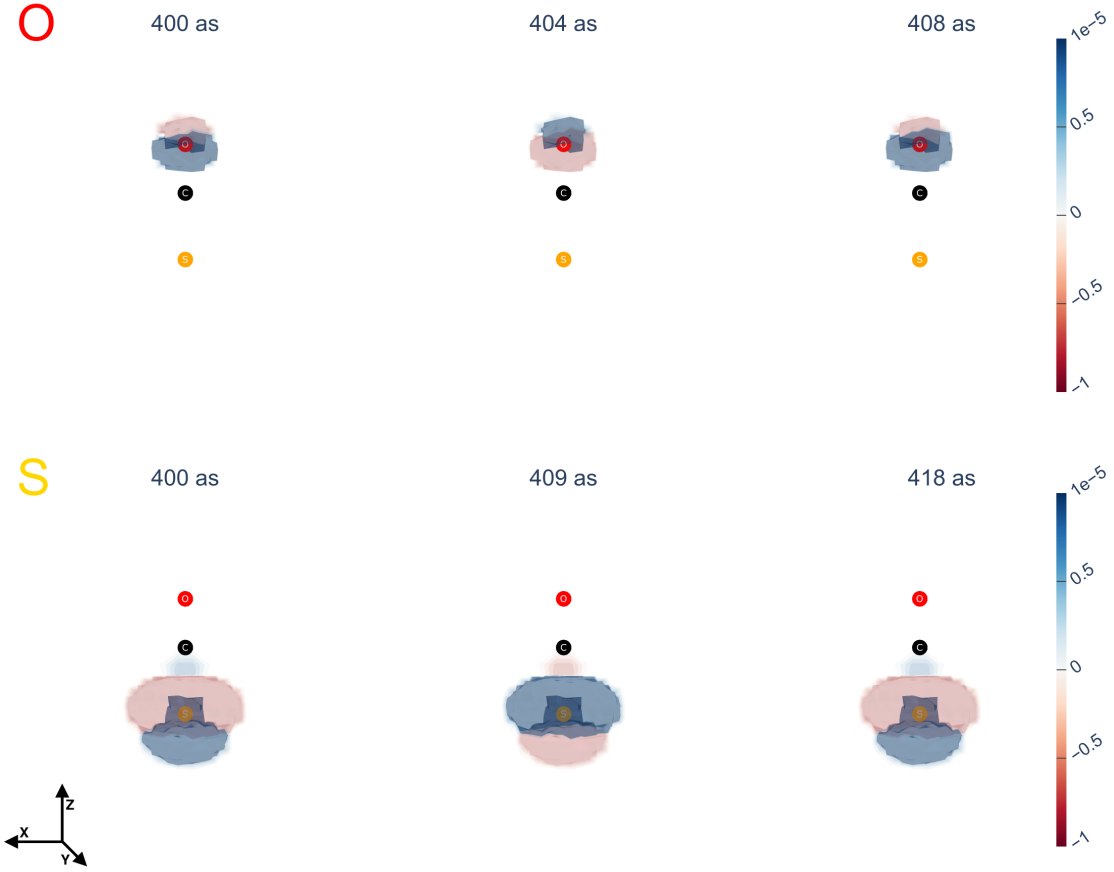

Figure 4.8: *Snapshots of $\rho_{cg}(\boldsymbol{r}, t)$ relative to the excitation considering a pulse linearly polarised along the z-axis. The upper panel is relative to the excitation at the O K-Edge, the lower panel to the excitation at the S L1-Edge. The axes orientation is illustrated in the lower left corner.*

Σ^+ symmetry of the core-excited states selected via the z-polarised pulse. Accordingly, $\rho_{cg}(\boldsymbol{r}, t)$ is symmetric with respect to the z-axis, resembling the shape of a p_z atomic orbital at the O K-Edge and that of a d_{z^2} atomic orbital at the S L1-Edge. Also the oscillation direction is related to the polarization choice, with $\rho_{cg}(\boldsymbol{r}, t)$ oscillating along the z-axis with a period of ≈ 8 *as* at the O K-Edge and ≈ 18 *as* at the S L1-Edge.

4.2.3 xz polarisation

The time-evolution of $\rho_{cg}(\boldsymbol{r}, t)$, relative to the excitation with a pulse linearly polarised at 45 degrees in the σ_{xz} plane, is shown in fig. 4.9. At the O K-Edge, the

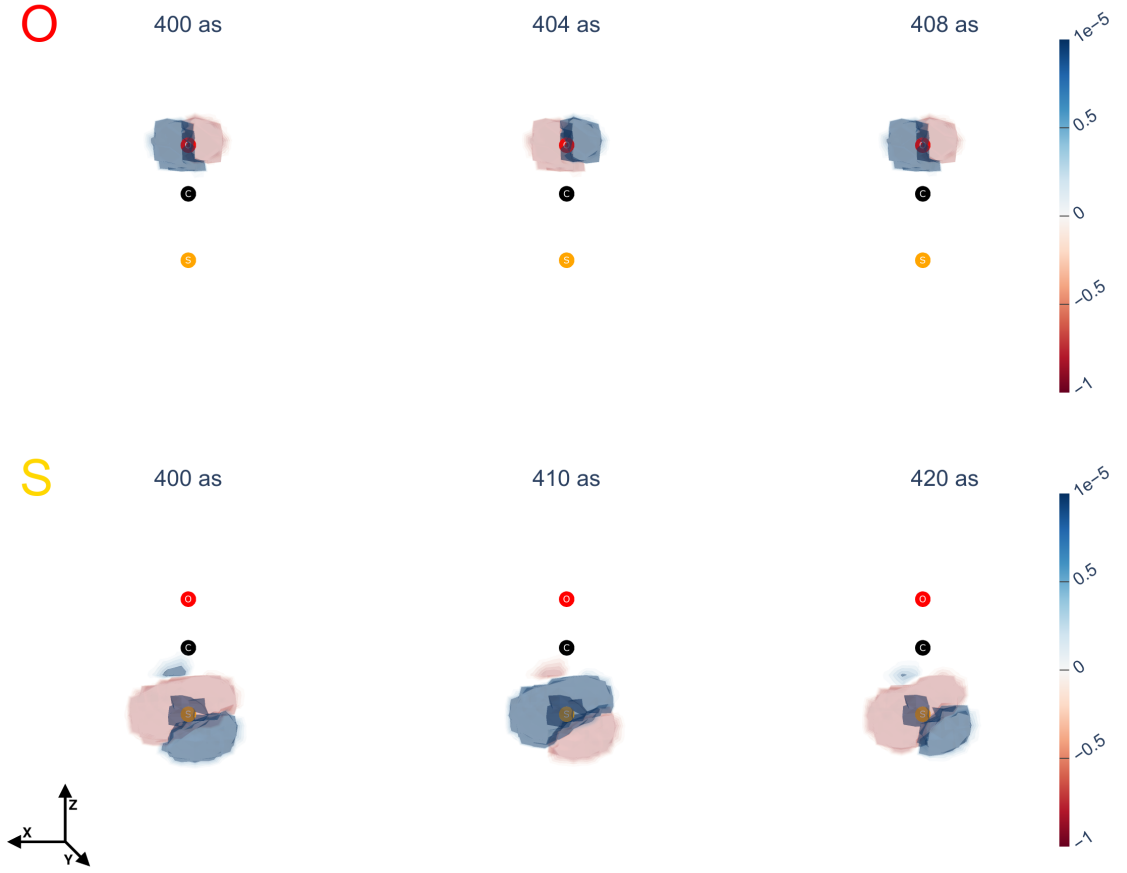

Figure 4.9: *Snapshots of $\rho_{cg}(\boldsymbol{r}, t)$ relative to the excitation considering a pulse linearly polarised at a 45 degrees angle in the σ_{xz} plane. The upper panel is relative to the excitation at the O K-Edge, the lower panel to the excitation at the S L1-Edge. The axes orientation is illustrated in the lower left corner.*

oscillation of $\rho_{cg}(\boldsymbol{r}, t)$ is very similar to the x-polarised case in fig. 4.7. This indicates a substantial contribution of the Π_x-symmetric states, which outweighs that from the Σ^+-symmetric states. At the S L1-Edge, the characteristics of $\rho_{cg}(\boldsymbol{r}, t)$ are similar, symmetry-wise, to the z-polarised case in fig. 4.8. However, unlike the z-polarised case, the oscillation of $\rho_{cg}(\boldsymbol{r}, t)$ unfolds along an axis 'tilted' in the σ_{xz} plane. This is indicative of a more balanced ratio of contributions to $\rho_{cg}(\boldsymbol{r}, t)$ from the Π_x and Σ^+ core-excited states compared to the excitation at the O K-Edge.

4.2.4 Rxy and Lxy polarisations

The time-evolution of $\rho_{cg}(\boldsymbol{r}, t)$, relative to the excitation with a right-handed and left-handed circularly polarised pulse, is illustrated in figs. 4.10 and 4.11. The former

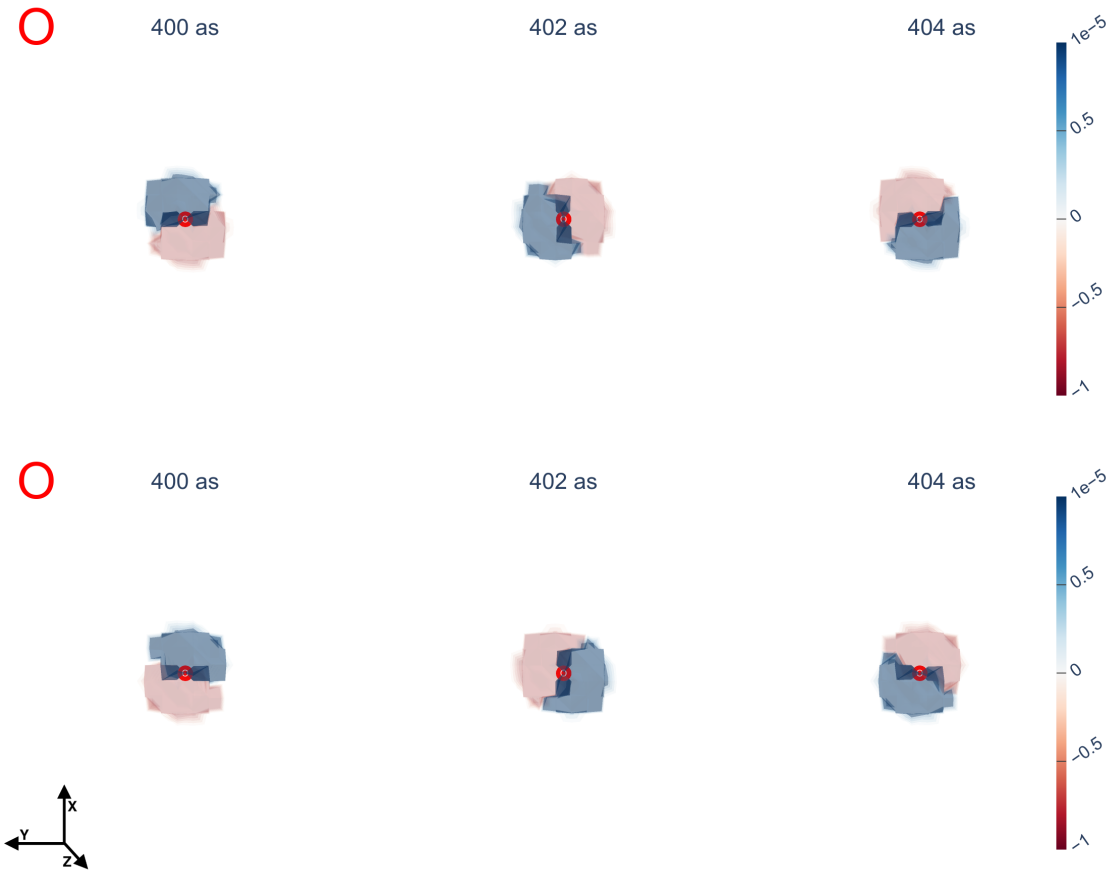

Figure 4.10: *Snapshots of $\rho_{cg}(\boldsymbol{r}, t)$ relative to the O K-Edge excitation, considering a right-handed (upper panel) and left-handed (lower panel) circularly polarised pulse in the σ_{xy} plane. The axes orientation is illustrated in the lower left corner.*

is relative to the excitation at the O K-Edge while the latter to the excitation at the S L1-Edge. In both cases, $\rho_{cg}(\boldsymbol{r}, t)$ has the form of a p orbital revolving around the z-axis in the σ_{xy} plane. The switch from the excitation at the O K-Edge to that at the S L1-Edge, simply changes the localisation of $\rho_{cg}(\boldsymbol{r}, t)$ from O to S. The different handedness of the polarisation is reflected in the opposite rotation direction of $\rho_{cg}(\boldsymbol{r}, t)$, which can be intuitively seen by comparing the upper and lower panels of figs. 4.10 and 4.11.

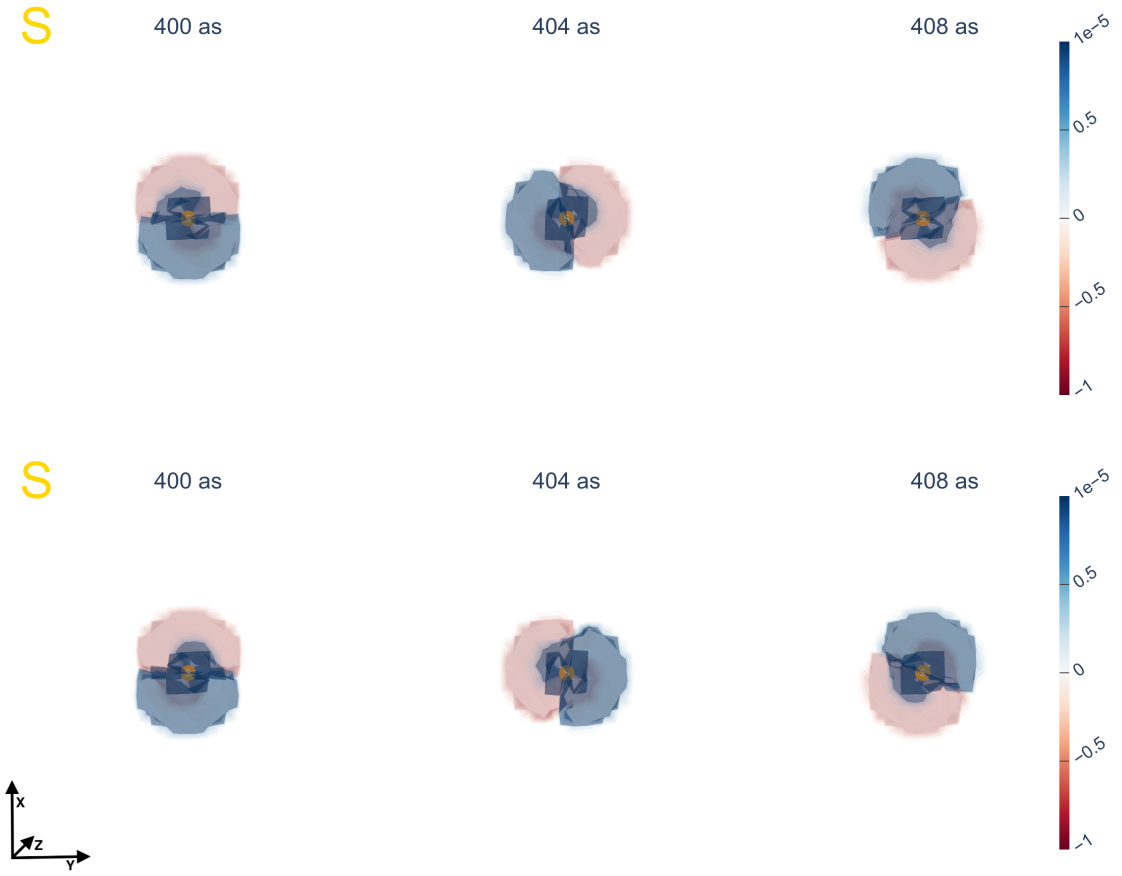

Figure 4.11: *Snapshots of $\rho_{cg}(\boldsymbol{r}, t)$ relative to the S L1-Edge excitation, considering a right-handed (upper panel) and left-handed (lower panel) circularly polarised pulse in the σ_{xy} plane. The axes orientation is illustrated in the lower left corner.*

4.3 $\Delta_{cg}(\boldsymbol{r}, t)$ component

The time-evolution of the $\Delta_{cg}(\boldsymbol{r}, t)$ component is directly related to the relative importance of the $\rho^{s}_{cc}(\boldsymbol{r}, t)$ and $\rho^{(2)}_{gg}(\boldsymbol{r}, t)$ terms in eq. (2.99). As the populations of the core-excited states exponentially decay over time, the $\rho^{(2)}_{gg}(\boldsymbol{r}, t)$ term becomes progressively dominant over the $\rho^{s}_{cc}(\boldsymbol{r}, t)$ term. This is directly reflected in the time-evolution of $\Delta_{cg}(\boldsymbol{r}, t)$, which progressively assumes the distribution of the (negatively-valued) ground state density $\rho_{gg}(\boldsymbol{r})$. When the magnitudes of $\rho^{s}_{cc}(\boldsymbol{r}, t)$ and $\rho^{(2)}_{gg}(\boldsymbol{r}, t)$ are comparable at the beginning of the time-evolution, the spatial distribution of $\Delta_{cg}(\boldsymbol{r}, t)$ assumes characteristics related to the structure of the difference 1PDM, $\Delta^{cg}_{pq} = \gamma^{cc}_{pq} - \gamma^{gg}_{pq}$. Two examples of Δ^{cg}_{pq} are shown in fig. 4.12, where

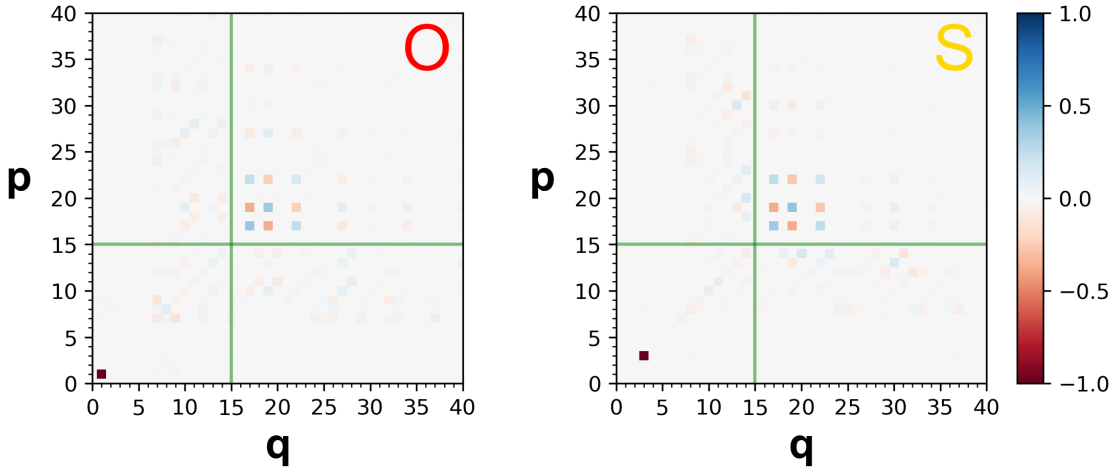

Figure 4.12: *Difference density matrices, Δ^{cg}_{pq} for $c \equiv 1^{c}\Pi_{x}$, expanded in the basis of canonical MOs. The left panel corresponds to an excitation at the O K-edge, the right panel to an excitation at the S L1-Edge. The division of the molecular orbitals in terms of the particle-hole formalism is indicated by the green lines, as in fig. 4.6.*

the left matrix is relative to an excitation at the O K-Edge, while the right matrix to an excitation at the S L1-Edge. In correspondence to p=q=1 at the O K-Edge and p=q=3 at the S L1-Edge, the matrices present coefficients equal to -1. These coefficients correspond to the O 1s MO at the O K-Edge and to the S 2s MO at the S L1-Edge, which translates into 'core-holes' being present in the corresponding difference density $\Delta_{cg}(\boldsymbol{r}) = \rho_{cc}(\boldsymbol{r}) - \rho_{gg}(\boldsymbol{r})$[II]. The positive coefficients in the upper-right quadrant of Δ^{cg}_{pq} (i.e. the particle-particle quadrant), correspond to the positively-valued parts of $\Delta_{cg}(\boldsymbol{r})$, which represent the spatial region the core-electron is excited to. Therefore, when the contributions from the two terms forming $\Delta_{cg}(\boldsymbol{r}, t)$ are of comparable magnitude at the beginning of the time-evolution, the distribution of $\Delta_{cg}(\boldsymbol{r}, t)$ provides a spatial visualisation of the incoherent part of the core-excitation. On the other hand, the time-evolution of $\Delta_{cg}(\boldsymbol{r}, t)$ provides a spatial visualisation of the core-excited states' decay.

[II]The core-hole cannot be seen in the snapshots of $\Delta_{cg}(\boldsymbol{r}, t)$ shown in the following. This is due to the choice of volume grid which has been geared towards the rendering of the density over the whole molecule, and it's too coarse to show the tightly localised core-hole.

4.3.1 x polarisation

The time-evolution of the populations, relative to the excitation with a pulse linearly polarised along the x-axis, is shown in fig. 4.13. The comparison of the populations

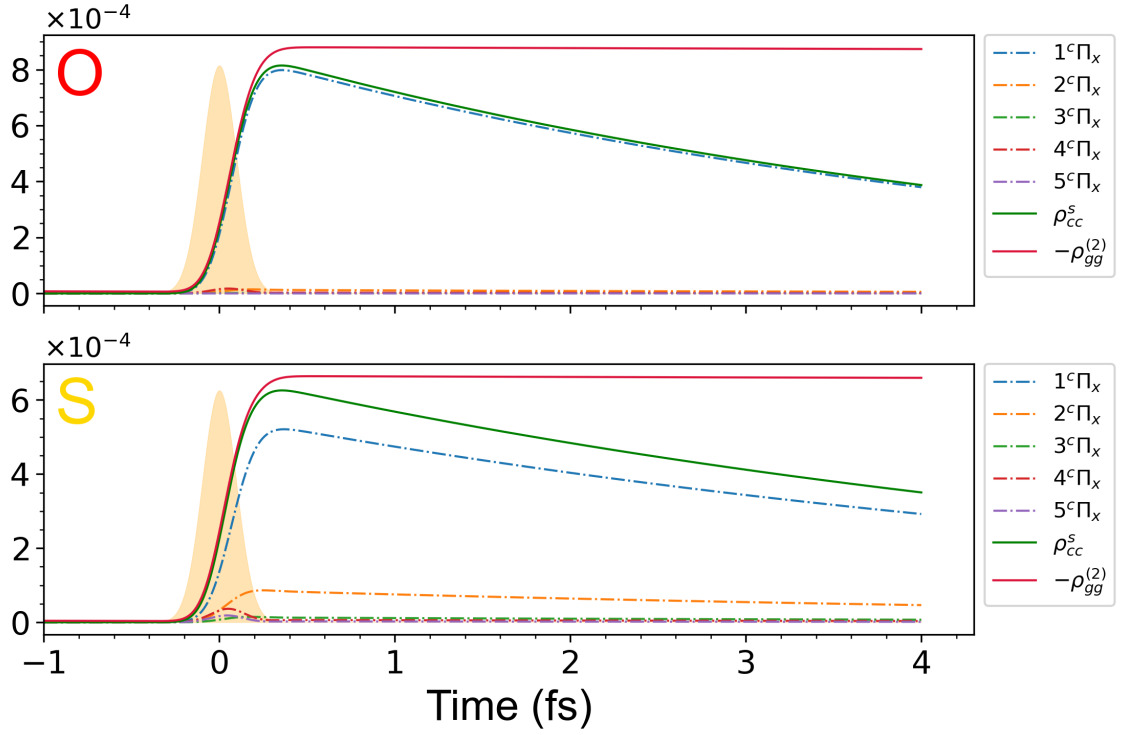

Figure 4.13: *Populations of the density matrix as a function of time relative to the excitation with a pulse linearly polarised along the x-axis. The upper panel is relative to the O K-Edge excitation, the lower panel to the S L1-Edge excitation.*

of the core-excited states shows that, both at the O K-Edge and the S L1-Edge, the main contribution to $\rho^s_{cc}(t)$ (i.e. the sum of the core-excited states' populations) comes from the $1^c\Pi_x$ state. This is due to the pulse central frequency being resonant to the $1\Sigma^+ \rightarrow 1^c\Pi_x$ transition; this makes it detuned relative to higher $^c\Pi_x$ states, the detuning being more pronounced at the O K-Edge than at the S L1-Edge (vide table 4.2). The comparison between $\rho^s_{cc}(t)$ and $\rho^{(2)}_{gg}(t)$ (shown as $-\rho^{(2)}_{gg}(t)$ for an easier comparison) shows the former decaying at a rate Γ_c, while the latter remains constant. Accordingly, as time progresses, $\rho^{(2)}_{gg}(\boldsymbol{r},t)$ gradually 'outweighs' $\rho^s_{cc}(\boldsymbol{r},t)$ in the contribution to $\Delta_{cg}(\boldsymbol{r},t)$. This is directly reflected in the time-evolution of $\Delta_{cg}(\boldsymbol{r},t)$, snapshots of which are shown in fig. 4.14. At 400 *as* the contributions from the $\rho^s_{cc}(\boldsymbol{r},t)$ and $\rho^{(2)}_{gg}(\boldsymbol{r},t)$ terms are comparable, with $\Delta_{cg}(\boldsymbol{r},t)$ showing both positively-valued and negatively-valued regions. During the subsequent time-evolution, represented by the 1000 *as* and 2000 *as* snapshots, the $\rho^s_{cc}(\boldsymbol{r},t)$ term decays, leaving way to the gradual prevalence of the $\rho^{(2)}_{gg}(\boldsymbol{r},t)$ term. This translates into $\Delta_{cg}(\boldsymbol{r},t)$ progressively assuming the shape of the negatively valued ground state density. Comparing the 400 *as* snapshots relative to the excitation at different edges (i.e. upper and lower panel of fig. 4.14) a certain degree of atomic specificity emerges, with the positively-valued regions of $\Delta_{cg}(\boldsymbol{r},t)$ being polarised towards the CO moiety at the O K-Edge and towards the CS moiety at the S L1-Edge. The symmetry of $\Delta_{cg}(\boldsymbol{r},t)$ reflects that of both the ground state $1\Sigma^+$ and the

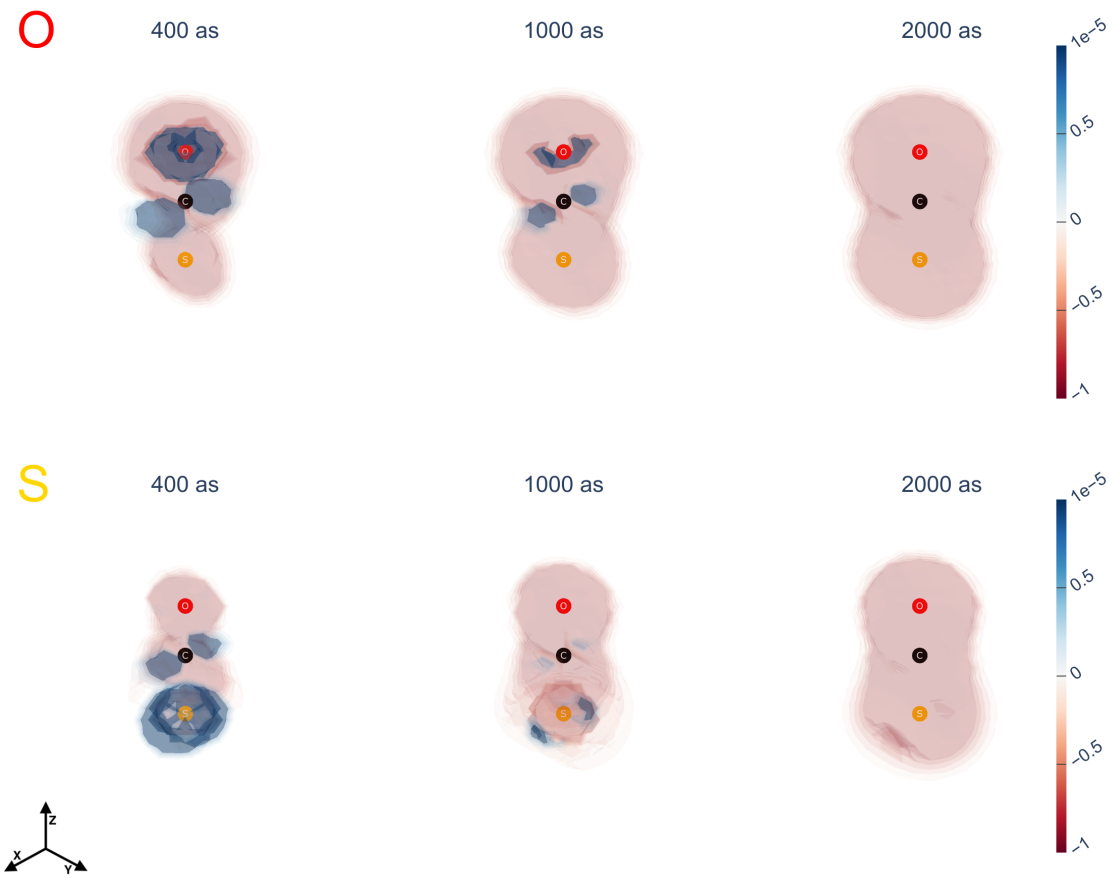

Figure 4.14: *Snapshots of $\Delta_{cg}(\boldsymbol{r}, t)$ relative to the excitation with a pulse linearly polarised along the x-axis. The upper panel is relative to the excitation at the O K-Edge, the lower panel to the excitation at the S L1-Edge. The axes orientation is illustrated in the lower left corner.*

Π_x-symmetric core-excited states. In particular, in the 400 *as* snapshots, due the positively-valued regions, $\Delta_{cg}(\boldsymbol{r}, t)$ results polarised along the x-axis and symmetric with respect to a C_2 rotation about the z-axis, as typical of the Π_x-symmetric state densities. On the other hand, as the contribution from the ground state prevails, the symmetry of $\Delta_{cg}(\boldsymbol{r}, t)$ becomes coincident with the Σ^+ symmetry of the ground state density.

4.3.2 z polarisation

The time-evolution of the populations, relative to the excitation with a pulse linearly polarised along the z-axis, is shown in fig. 4.15. From the comparison between the

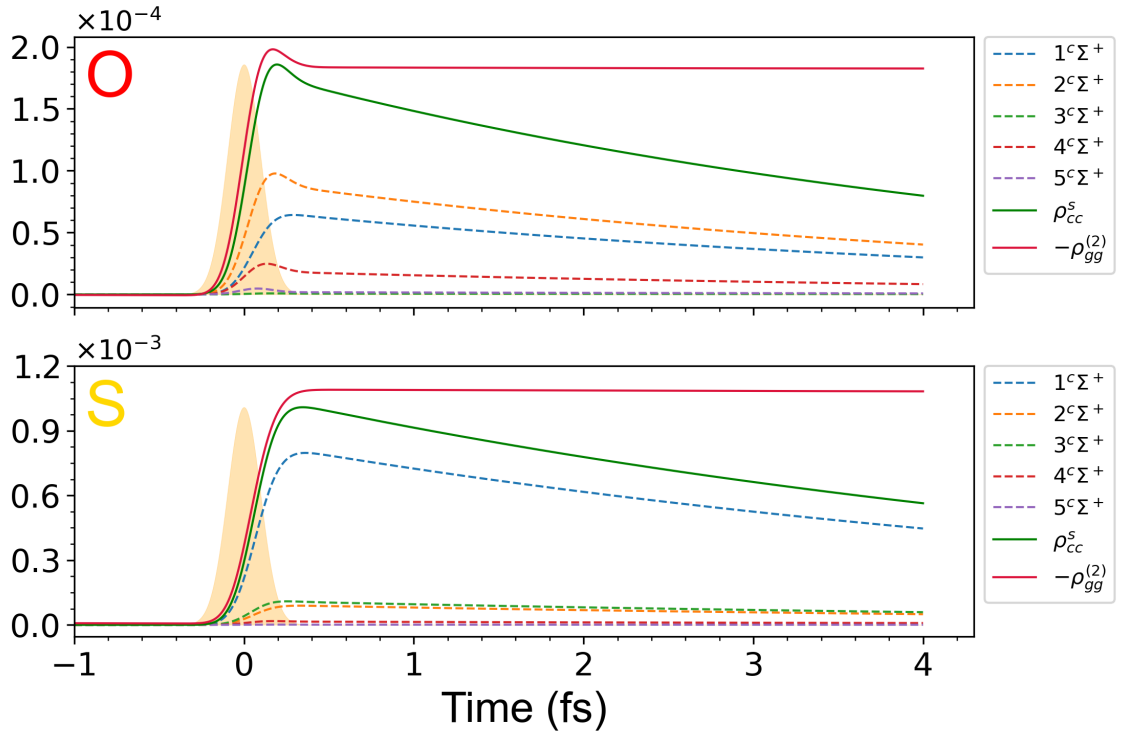

Figure 4.15: *Populations of the density matrix as a function of time relative to the excitation considering a pulse polarised along the z-axis. The upper panel is relative to the O K-Edge excitation, the lower panel to the S L1-Edge excitation.*

two panels, it emerges how the populations at the S L1-Edge are about one order of magnitude bigger than at the O K-Edge. The main cause of this can be traced to the detuning shown in table 4.2, which, being larger at the O K-Edge than at the S L1-Edge, determine smaller populations of the ${}^c\Sigma^+$ states in the former case than in the latter. The time-evolution of $\Delta_{cg}(\boldsymbol{r}, t)$ is shown in fig. 4.16, where a behaviour similar to the x-polarised case is found. The smaller spatial extension of $\Delta_{cg}(\boldsymbol{r}, t)$ at the O K-Edge compared to the S L1-Edge, reflects the relative magnitude of the populations shown in fig. 4.15. The atom-specific localisation of $\Delta_{cg}(\boldsymbol{r}, t)$ is evident particularly in the 400 *as* snapshot, where positively-valued regions of $\Delta_{cg}(\boldsymbol{r}, t)$ are present in correspondence to the pumped atom. The Σ^+ symmetry of the core-excited states is reflected in the spatial distribution of $\Delta_{cg}(\boldsymbol{r}, t)$, which is symmetric with respect to the z-axis.

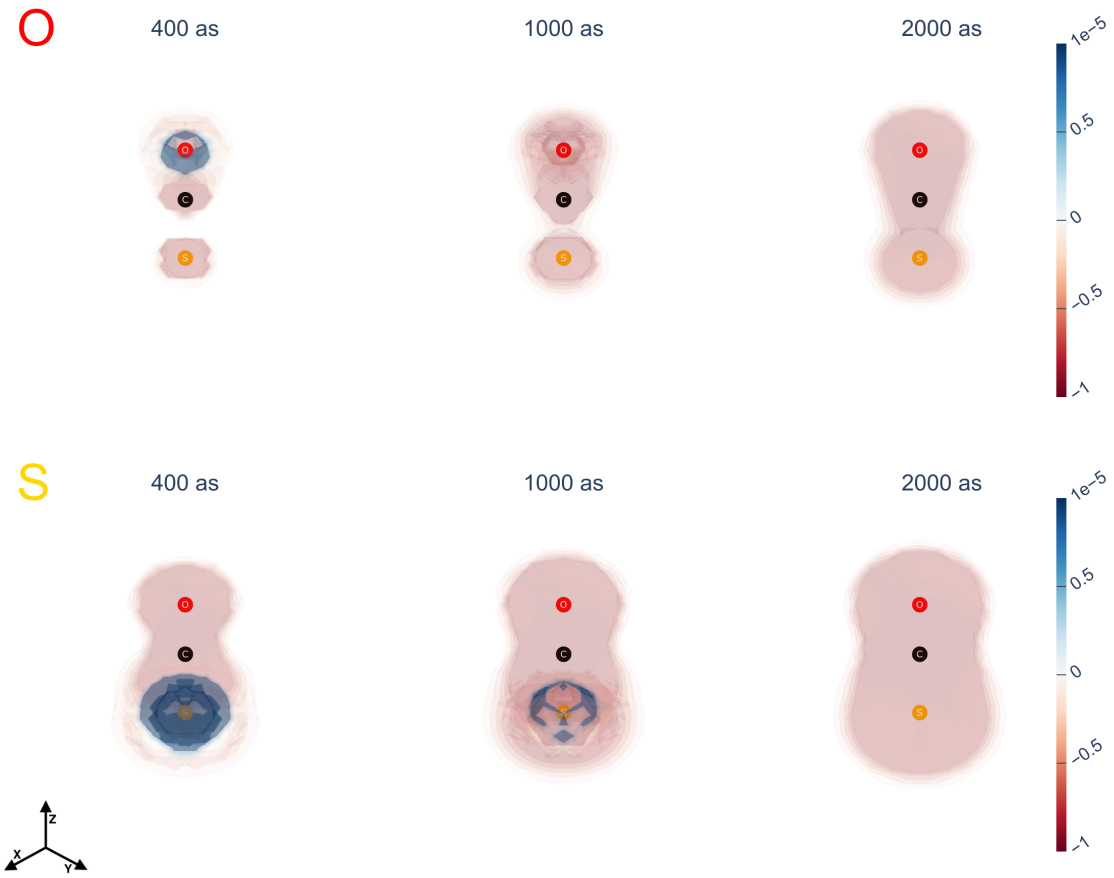

Figure 4.16: *Snapshots of $\Delta_{cg}(\boldsymbol{r}, t)$ relative to the excitation considering a pulse linearly polarised along the z-axis. The upper panel is relative to the excitation at the O K-Edge, the lower panel to the excitation at the S L1-Edge. The axes orientation is illustrated in the lower left corner.*

4.3.3 xz polarisation

The time-evolution of the populations, relative to the excitation with a pulse linearly polarised at 45 degrees in the σ_{xz} plane, is shown in fig. 4.17. Since the polarisation

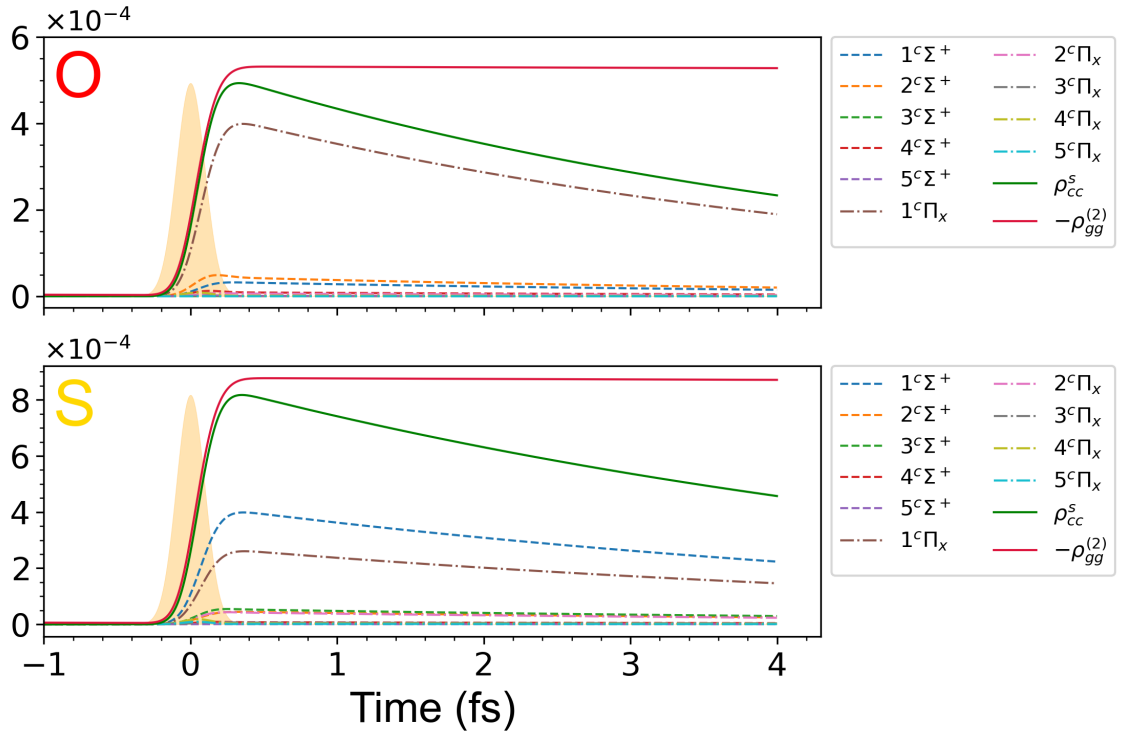

Figure 4.17: *Populations of the density matrix as a function of time, relative to the excitation considering a pulse linearly polarised at a 45 degrees angle in the σ_{xz} plane. The upper panel is relative to the O K-Edge excitation, the lower panel to the S L1-Edge excitation.*

vector has components along both the x-axis and z-axis, both Σ^+-symmetric and Π_x-symmetric states are populated in the excitation. At the O K-Edge, $\rho^s_{cc}(t)$ is dominated by the population of the $1^c\Pi_x$ state; at the S L1-Edge, the dominant populations of the $1^c\Sigma^+$ and $1^c\Pi_x$ are of comparable magnitude, although with a bigger contribution from the former. The distribution of the populations is reflected in the properties of $\Delta_{cg}(\boldsymbol{r}, t)$, snapshots of which are shown in fig. 4.18. In the 400 *as* snapshot at the O K-Edge, the domination of the $1^c\Pi_x$ state population is reflected in the close similarity to the x-polarised case shown in the upper panel of fig. 4.14. The distribution of the populations at the S L1-Edge is reflected in the relative 400 *as* snapshot, where the positively-valued regions of $\Delta_{cg}(\boldsymbol{r}, t)$ are characterised by a distribution very similar to the z-polarised case shown in the lower panel of fig. 4.16. Additionally, the positively-valued regions are slightly elongated along the x-axis (similar to the x-polarised case in the lower panel of fig. 4.14), which is indicative of the contribution from the Π_x-symmetric states.

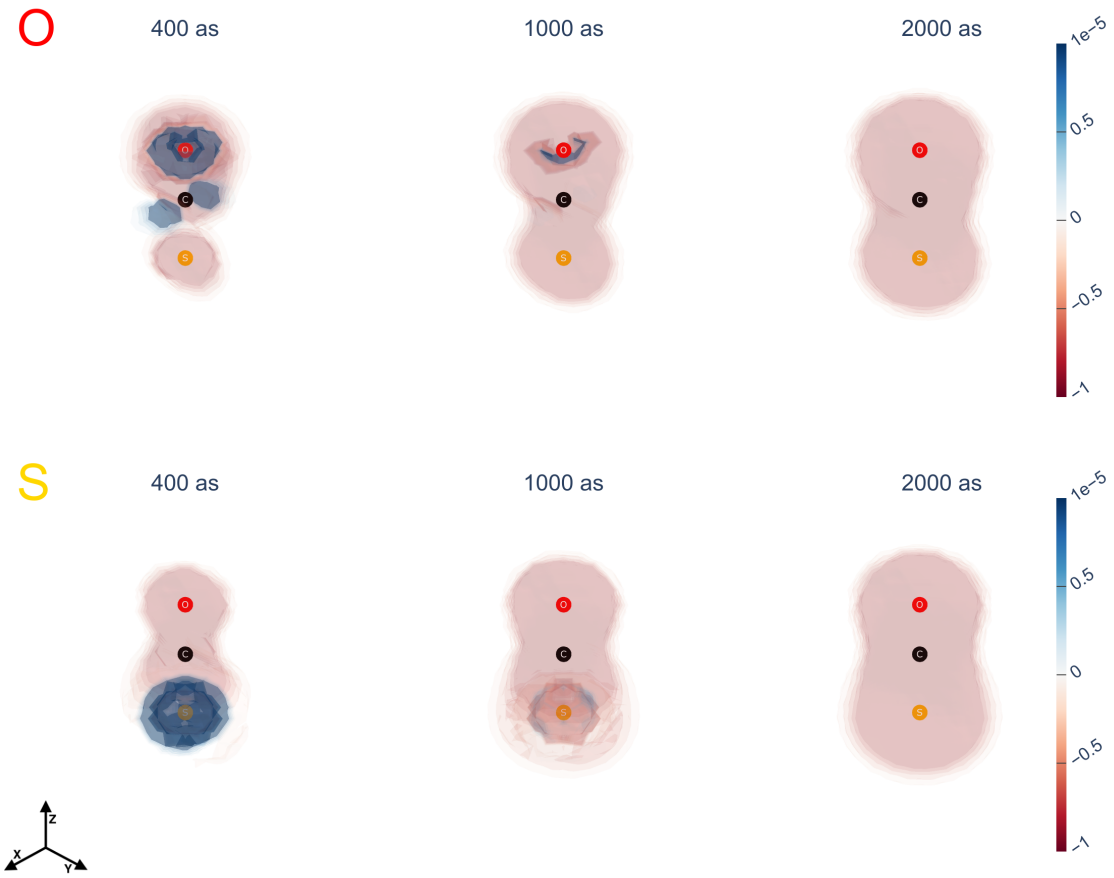

Figure 4.18: *Snapshots of $\Delta_{cg}(\boldsymbol{r}, t)$ relative to the excitation considering a pulse linearly polarised at a 45 degrees angle in the σ_{xz} plane. The upper panel is relative to the excitation at the O K-Edge, the lower panel to the excitation at the S L1-Edge. The axes orientation is illustrated in the lower left corner.*

4.3.4 Rxy and Lxy polarisations

The populations and $\Delta_{cg}(\boldsymbol{r}, t)$ obtained considering a Rxy-polarised pulse are equivalent to those obtained considering a Lxy-polarised pulse. Therefore, only the results relative to the Rxy polarisation will be discussed here. As shown in fig. 4.19, states of both Π_x and Π_y symmetry are populated. Given their energy degeneracy, the

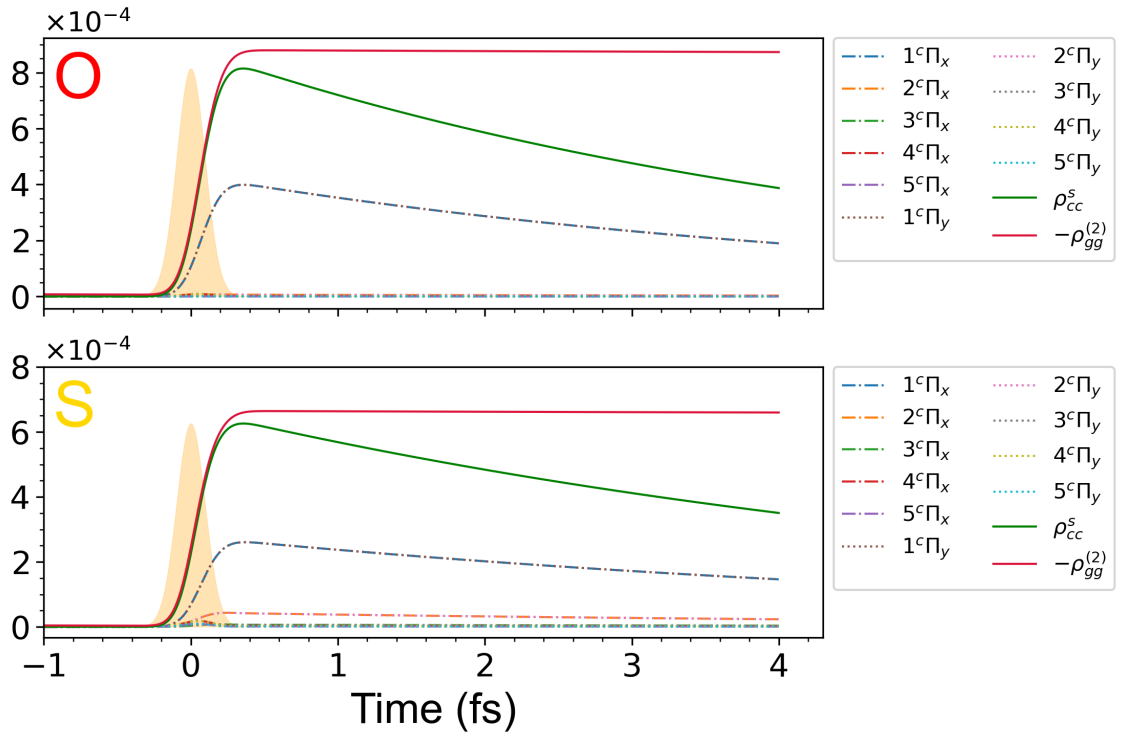

Figure 4.19: *Populations of the density matrix as a function of time, relative to the excitation with a right-handed, circularly polarised pulse. The upper panel is relative to the O K-Edge excitation, the lower panel to the S L1-Edge excitation.*

populations of the Π_x-symmetric and Π_y-symmetric states coincide, with a distribution among the manifold of core-excited states corresponding to that obtained in the x-polarised case (c.f. fig. 4.13). The characteristics of $\Delta_{cg}(\boldsymbol{r}, t)$ can be understood as resulting from the sum of those obtained in the x-polarised case (c.f. fig. 4.14) and those obtained in the y-polarised case, which corresponds to the x-polarised case rotated by 90 degrees. This makes $\Delta_{cg}(\boldsymbol{r}, t)$ symmetric with respect to the z-axis, as shown in particular in the 400 *as* snapshot of fig. 4.20.

Figure 4.20: *Snapshots of $\Delta_{cg}(\boldsymbol{r}, t)$ relative to the excitation considering a right-handed, circularly polarised pulse. The upper panel is relative to the excitation at the O K-Edge, the lower panel to the excitation at the S L1-Edge. The axes orientation is illustrated in the lower left corner.*

4.4 $\rho_{vg}(\boldsymbol{r}, t)$ component

The spatial characteristics of the $\rho_{vg}(\boldsymbol{r}, t)$ component are encoded in the properties of the transition 1PDM, $\gamma^{vg}_{pq} = \langle \psi_g | \hat{c}^\dagger_q \hat{c}_p | \psi_v \rangle$, an example of which (relative to the valence-excited state $1\Delta_{x^2-y^2}$) is shown in fig. 4.21. Similarly to γ^{cg}_{pq} shown in

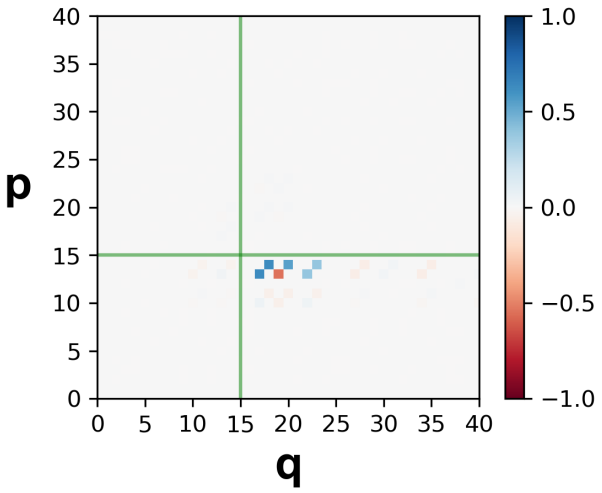

Figure 4.21: *Transition density matrix γ^{vg}_{pq} for $v \equiv 1\Delta_{x^2-y^2}$, expanded in the basis of canonical MOs. The green lines divide the molecular orbitals according to the particle-hole formalism, as in fig. 4.6.*

fig. 4.6, the non-zero elements of γ^{vg}_{pq} are found in the particle-hole subspace in the lower right corner. Unlike in γ^{cg}_{pq}, both the hole MOs (indicated by the 'p' index) and the particle MOs (indicated by the 'q' index) are 'located' in the valence shells of the electronic structure, which are atom-unspecific and generally delocalised over the whole molecule. Therefore, differently from the $\rho_{cg}(\boldsymbol{r}, t)$ component, the transition densities used to build $\rho_{vg}(\boldsymbol{r}, t)$ don't carry the atom-specific properties typical of an X-Ray excitation. Within $\rho_{vg}(\boldsymbol{r}, t)$, these properties are 'encoded' in the interference pattern of the coherences $\rho_{vg}(t)$ built via ISRIXS. On the other hand, the $\phi_p(\boldsymbol{r})\phi_q(\boldsymbol{r})$ products 'filtered out' through γ^{vg}_{pq} present a symmetry proper of the considered valence-excited state, which is reflected in the spatial distribution of the corresponding transition densities, $\rho_{vg}(\boldsymbol{r})$. Accordingly, the symmetry of the valence-excited states, whose inclusion in the WP is controlled via the pulse polarisation, is directly reflected in $\rho_{vg}(\boldsymbol{r}, t)$'s spatial distribution.

4.4.1 x polarisation

A pulse polarised along the x-axis allows the excitation of coherences relative to $\Delta_{x^2-y^2}$-symmetric and Σ^+-symmetric valence-excited states. The time-evolution of

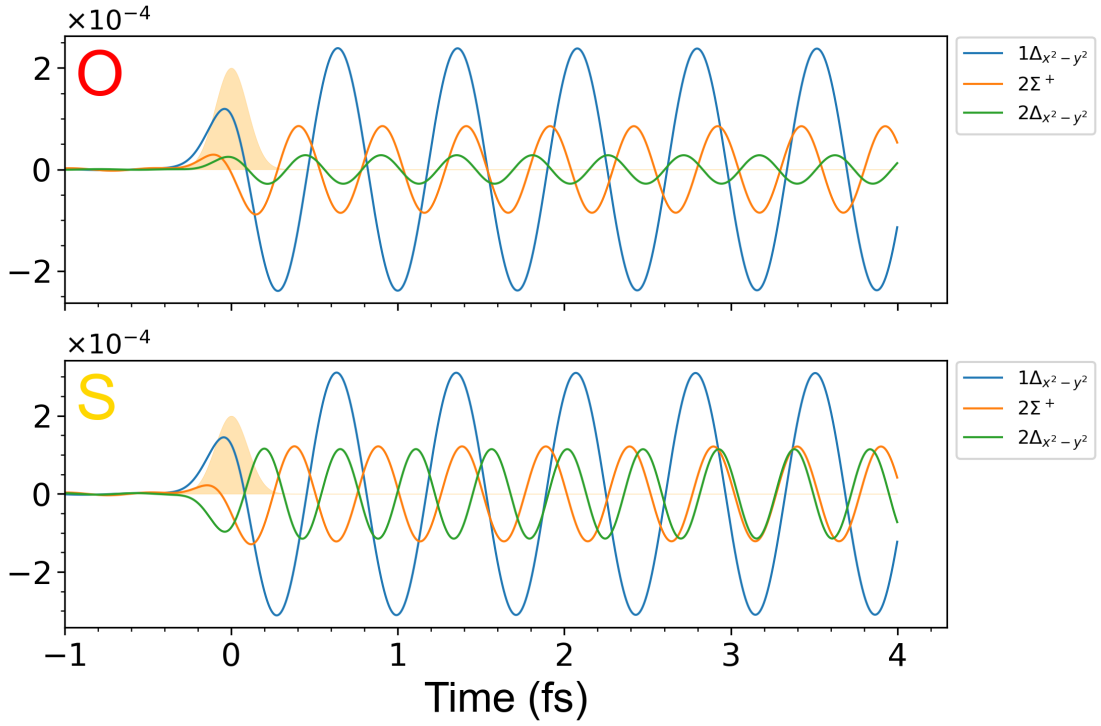

Figure 4.22: *Time-evolution of* $2\,\mathrm{Re}\{\rho_{vg}(t)\}$ *relative to an excitation with a pulse linearly polarised along the x-axis. Each curve corresponds to a different valence-excited state. The upper panel is relative to the excitation at the O K-Edge, the lower panel to the excitation at the S L1-Edge. The yellow Gaussian corresponds to the time-domain pulse envelope, whose intensity scale is not shown.*

the coherences is shown in fig. 4.22 where, both at the O K-Edge and S L1-Edge, the coherence relative to the $1\Delta_{x^2-y^2}$ state prevails. The comparison between the upper and lower panels shows a difference in the relative amplitude of the $2\Sigma^+$ and $2\Delta_{x^2-y^2}$ coherences: while $2\Sigma^+$ prevails over $2\Delta_{x^2-y^2}$ at the O K-Edge, at the S L1-Edge their amplitudes are very similar. The construction of $\rho_{vg}(\boldsymbol{r}, t)$ is based on the combination of the coherences shown in fig. 4.22 with the respective transition densities. As discussed in section 3.1, both the coherences and the transition densities are determined up to a ± 1 factor, which changes from one calculation to the other. This can be seen in fig. 4.23, where the upper and lower panels compare the same transition densities obtained in the calculations at the O K-Edge and S L1-Edge. Here, it is evident how the transition densities are the same up to a ± 1 factor. The correct construction of $\rho_{vg}(\boldsymbol{r}, t)$, which is immune from the ± 1 factor, entails combining the coherences and the transition densities relative to the same calculation. Thus, in the present example, $\rho_{vg}(\boldsymbol{r}, t)$ is constructed considering the coherences and transition densities from the upper panels of figs. 4.22 and 4.23 at the O K-Edge and the same quantities from the lower panels of figs. 4.22 and 4.23 at the S L1-Edge. As anticipated in this section's introduction, the symmetry of the transition densities reflects that of the corresponding valence-excited states. In

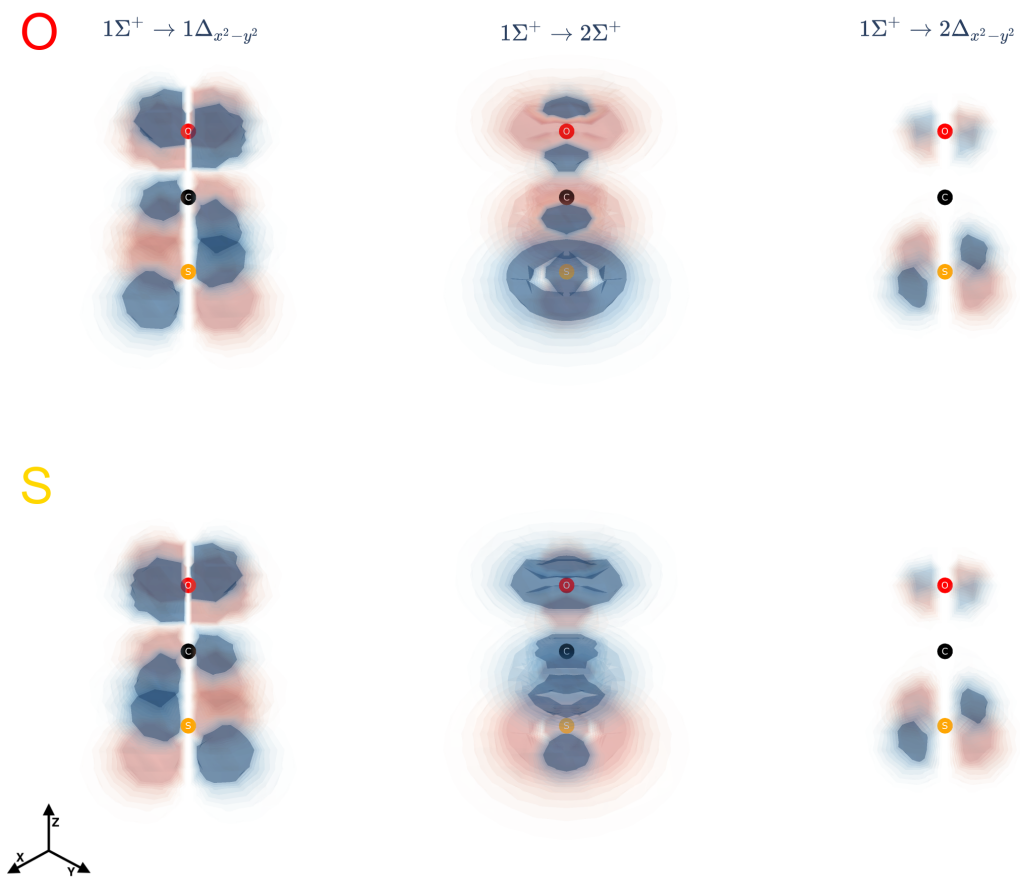

Figure 4.23: *Transition densities relative to the transition between the ground state* $1\Sigma^+$ *and the valence-excited states* $1\Delta_{x^y-y^2}$ *(left),* $2\Sigma^+$ *(centre) and* $2\Delta_{x^y-y^2}$ *(right). The upper panel is relative to the O K-Edge calculation, the lower panel to the S L1-Edge calculation. The axes orientation is illustrated in the lower left corner. Blue is positive, red is negative, with the colour scale being the same for all the plots.*

particular, the transition densities relative to the $\Delta_{x^y-y^2}$ states are symmetric with respect to both the σ_{xz} and σ_{yz} planes, resembling the shape of a $d_{x^2-y^2}$ orbital on each atom. On the other hand, the transition density relative to the $2\Sigma^+$ state reflects the cylindrical symmetry characteristic of the Σ^+ irreducible representation. Due to the prevalence of the $1\Delta_{x^y-y^2}$ coherence both at the O K-Edge and S L1-Edge, the time-evolution of $\rho_{vg}(\boldsymbol{r}, t)$ is dominated by the oscillation of the $1\Sigma^+ \rightarrow 1\Delta_{x^2-y^2}$ transition density. The changes in $\rho_{vg}(\boldsymbol{r}, t)$ due to the interference of its components can be seen at particular moments in time, at which the amplitude of the involved coherences is comparable. The time-evolution of $\rho_{vg}(\boldsymbol{r}, t)$ relative to the excitation at the O K-Edge is shown in the upper panel of fig. 4.24. At 425 *as*, the interference of the components is destructive along the x-axis and constructive along the y-axis, resulting in $\rho_{vg}(\boldsymbol{r}, t)$ lying in the σ_{yz} plane. Here, the positively-valued regions accumulate mostly on S, while the negatively-valued regions mostly on C and O. The spatial effects of interference are reversed at 1150 *as*. Here, $\rho_{vg}(\boldsymbol{r}, t)$ lies in the σ_{xz} plane, with the negatively-valued regions accumulating predominantly on S and the positively-valued regions around C and O. At 2650 *as* the distribution of the positively- and negatively-valued regions is similar to that found at 1150 *as*. However, the spatial pattern of constructive and destruc-

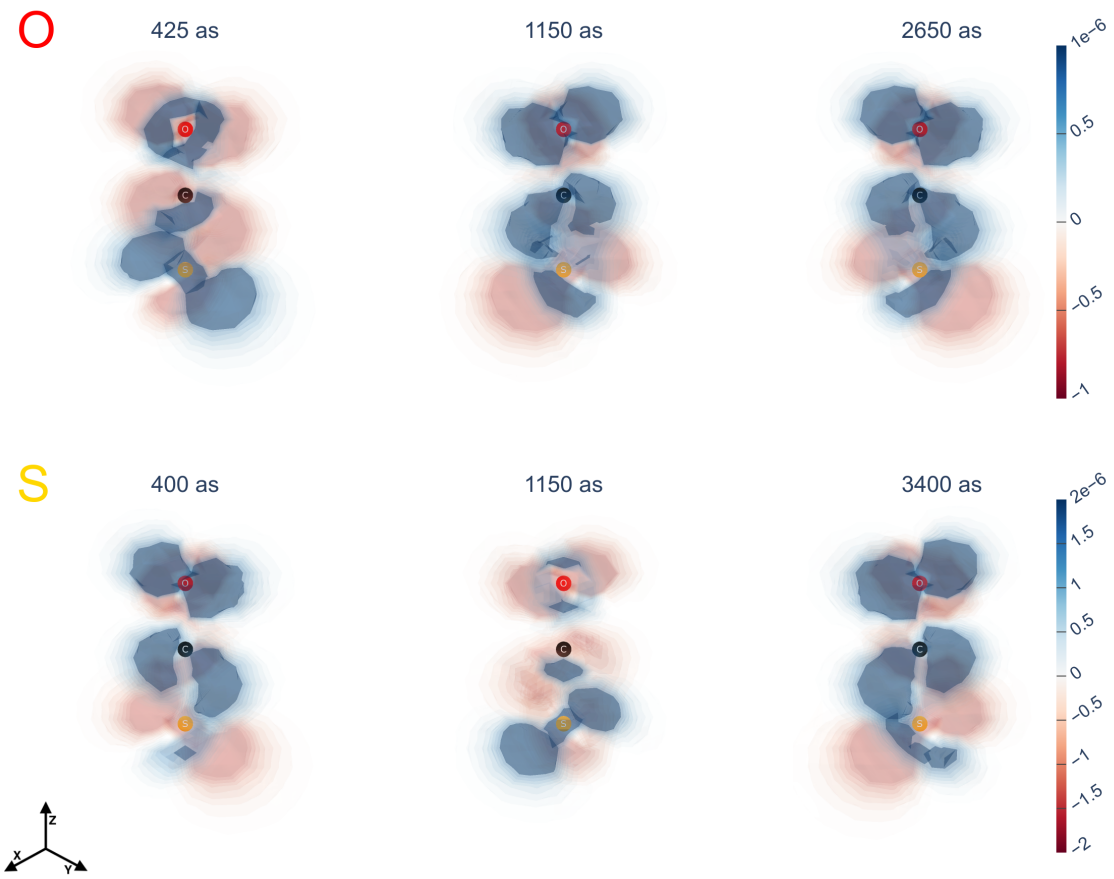

Figure 4.24: *Snapshots of $\rho_{vg}(\boldsymbol{r}, t)$ relative to a pulse linearly polarised along the x-axis. The upper panel is relative to the excitation at the O K-Edge, the lower panel to the excitation at the S L1-Edge. The axes orientation is illustrated in the lower left corner.*

tive interference is different, with $\rho_{vg}(\boldsymbol{r}, t)$ now lying in the σ_{yz} plane. The spatial effects of interference on $\rho_{vg}(\boldsymbol{r}, t)$ follow a similar pattern when OCS is excited at the S L1-Edge. Some examples are illustrated in the snapshots in the lower panel of fig. 4.24, which correspond to time-points at which the amplitudes of the coherences in the lower panel of fig. 4.22 are comparable. Similarly to the O-K Edge case, the interference of $\rho_{vg}(\boldsymbol{r}, t)$'s components manifests as a variation of spatial orientation – between the σ_{xz} and σ_{yz} planes – and the distribution of the positively-valued and negatively-valued regions between S and the CO moiety.

4.4.2 z polarisation

Due to the selection rules, when a pulse linearly polarised along the z-axis is considered, only transitions to Σ^+-symmetric valence-excited states are allowed. In the present case, owing to the limited pulse bandwidth, only the coherence relative to the $2\Sigma^+$ state is excited. Consequently, as shown in fig. 4.25, the time-evolution of $\rho_{vg}(\boldsymbol{r}, t)$ trivially corresponds to the oscillation of the $1\Sigma^+ \rightarrow 2\Sigma^+$ transition density illustrated in fig. 4.23.

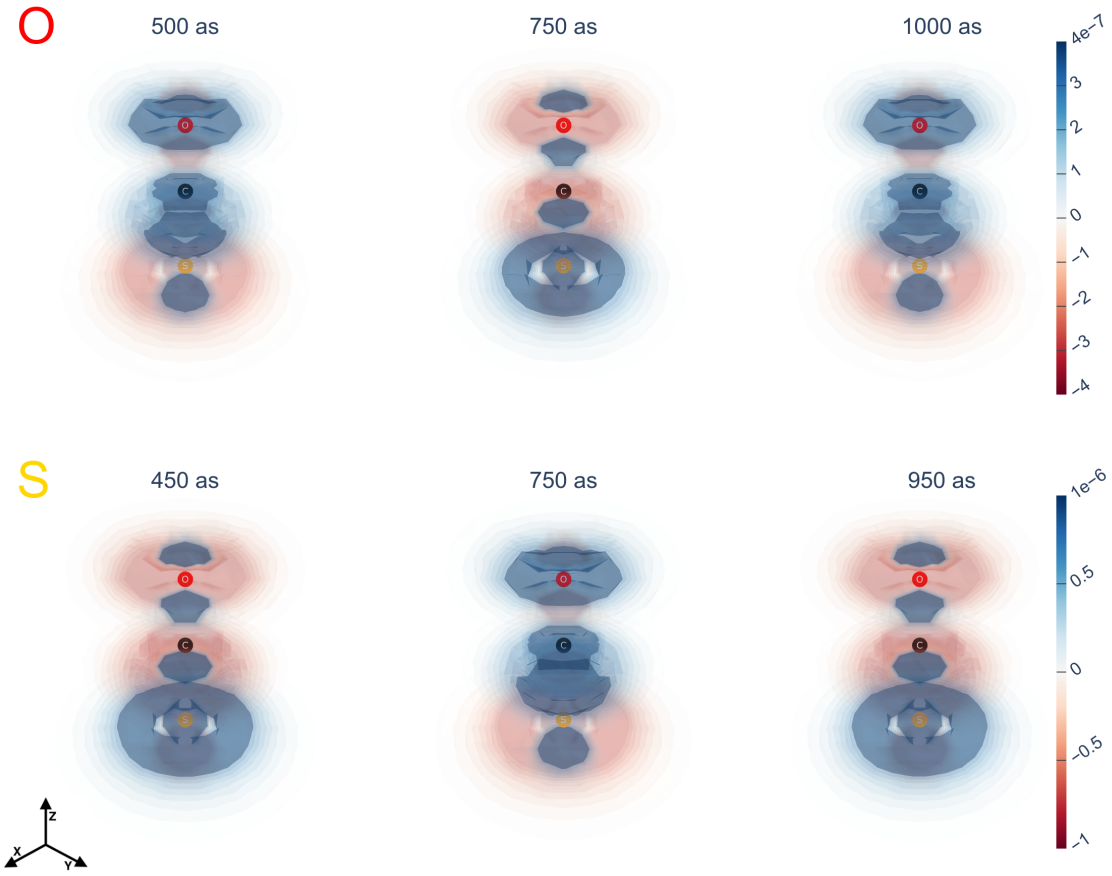

Figure 4.25: *Snapshots of $\rho_{vg}(\boldsymbol{r}, t)$ relative to a pulse linearly polarised along the z-axis. The upper panel is relative to the excitation at the O K-Edge, the lower panel to the excitation at the S L1-Edge. The axes orientation is illustrated in the lower left corner.*

4.4.3 xz polarisation

The coherences excited by a pulse linearly polarised at 45 degrees in the σ_{xz} plane are shown in fig. 4.26. The selection rules associated to this polarisation allow

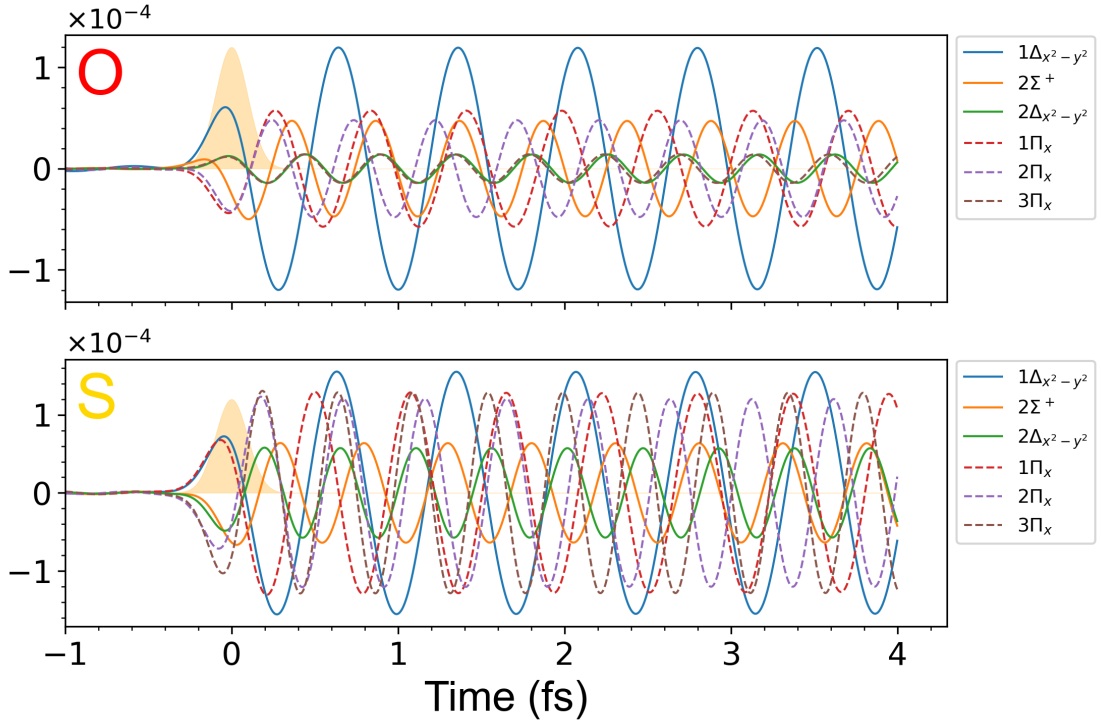

Figure 4.26: *Time-evolution of* $2\,\mathrm{Re}\{\rho_{vg}(t)\}$ *relative to an excitation with a pulse linearly polarised at 45 degrees in* σ_{xz}*. Each curve corresponds to a different valence-excited state. The upper panel is relative to the excitation at the O K-Edge, the lower panel to the excitation at the S L1-Edge. The yellow Gaussian corresponds to the time-domain pulse envelope, whose intensity scale is not shown.*

the coherent population not only of $\Delta_{x^2-y^2}$- and Σ^+-symmetric states, as in the x- and z-polarised cases, but also of Π_x-symmetric states. The initial stages of the time-evolution correspond to the 'preparation' of the WP, which coincides with the initial build-up of the coherences during the pulse. In fig. 4.26, the preparation phase corresponds to the first 200 as leading up to 0, during which $\rho_{vg}(\boldsymbol{r}, t)$ grows in size without moving – in accordance with the discussion by Brummer and Shapiro in [114] – leading to the initial electronic redistribution shown in the snapshots in fig. 4.27. Here, both at the O K-Edge (left) and S L1-Edge (right) positively-valued regions are localised on all atoms, with a slight polarisation towards O at the O K-Edge and a more pronounced polarisation towards S at the S L1-Edge. In both cases, $\rho_{vg}(\boldsymbol{r}, t)$ is symmetric with respect to the σ_{xz} plane but not with respect to the σ_{yz}. This is due to the contribution of the transition densities associated with the Π_x states, which, unlike those associated to the $\Delta_{x^2-y^2}$ and Σ^+ states, are symmetric only with respect to the σ_{xz} plane. As the pulse wanes, the motion of the WP is released, triggering complex electronic dynamics across the molecule. At the O K-Edge, the time-evolution of $\rho_{vg}(\boldsymbol{r}, t)$ is largely determined by the oscillation of the $1\Delta_{x^2-y^2}$ transition density, as already suggested by the dominant character of the respective coherence in fig. 4.26. Despite this, during particular periods of the

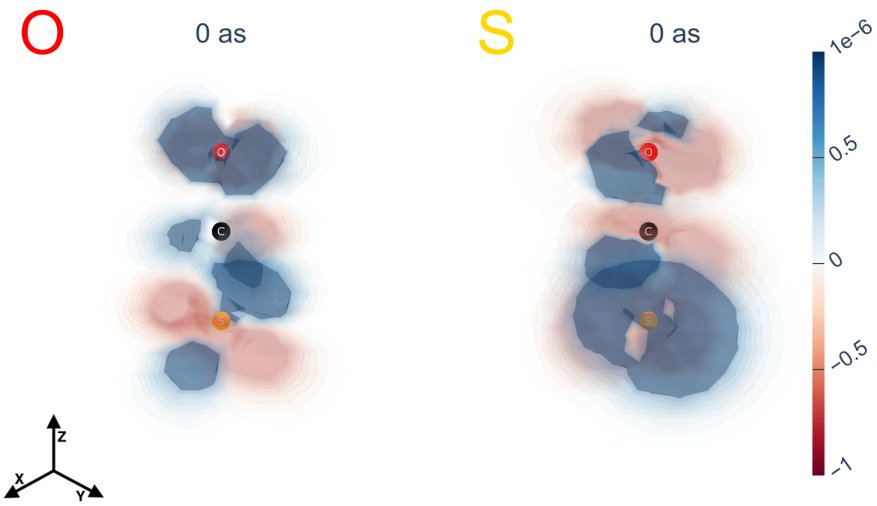

Figure 4.27: *Snapshots of the initial redistribution of $\rho_{vg}(\boldsymbol{r}, t)$ at 0 as resulting from the static build-up during the previous 100 as. The left panel is relative to the excitation at the O K-Edge, the right panel to the excitation at the S L1-Edge. The axes orientation is shown in the lower left corner.*

time-evolution (where the coherences have comparable amplitudes) the electronic migration takes place between C and S, manifesting as the positively-valued regions of $\rho_{vg}(\boldsymbol{r}, t)$ move between the atoms similarly to a classical 'current'. This process is shown in fig. 4.28 at two different moments of the time-evolution. The interatomic migration unfolds as the lobes oriented along the x-axis on one atom connect with those oriented along the y-axis on the next atom, while preserving the symmetry with respect to σ_{xz} but not with respect to σ_{yz}. The migration does not extend to

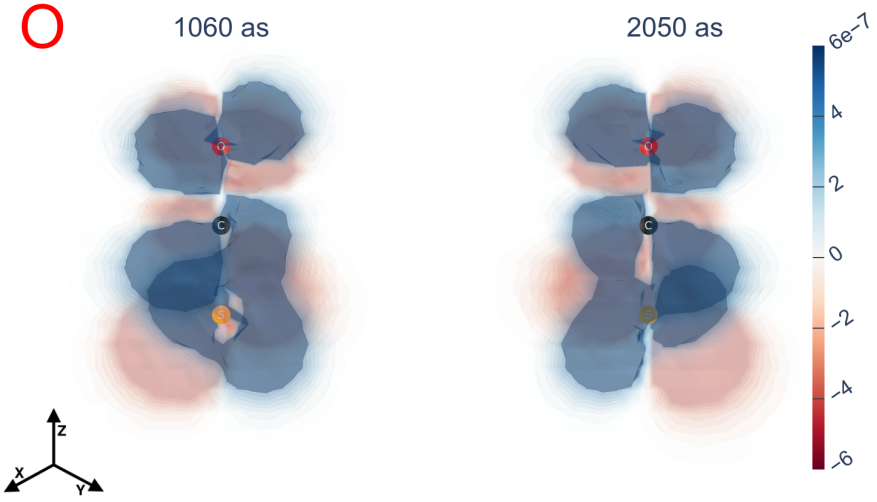

Figure 4.28: *Snapshots of $\rho_{vg}(\boldsymbol{r}, t)$ showing the electronic migration between C and S; the snapshots are relative to the excitation at the O K-Edge with a pulse linearly polarised at 45 degrees in σ_{xz}. The axes orientation is shown in the lower left corner.*

the O, around which $\rho_{vg}(\boldsymbol{r}, t)$ oscillates as the $1\Sigma^+ \rightarrow 1\Delta_{x^2-y^2}$ transition density in fig. 4.23. This is due to the characteristics of the transition densities involved, in

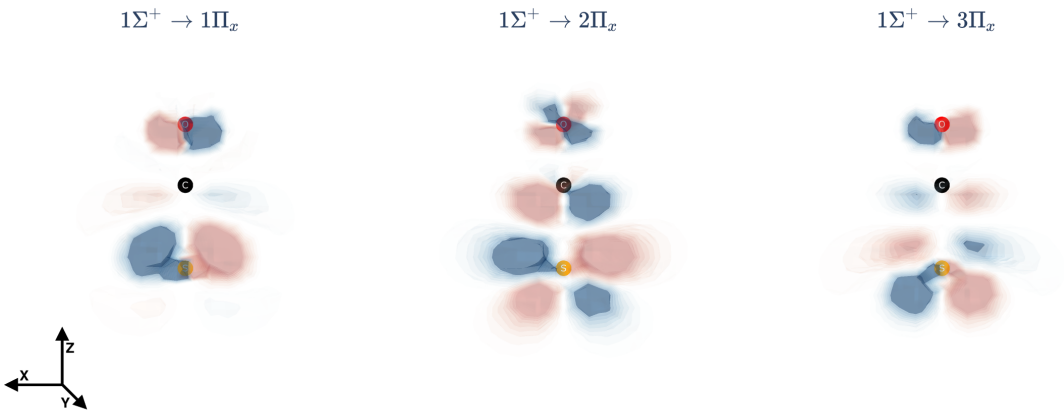

Figure 4.29: *Transition densities relative to the transitions between the ground state* $1\Sigma^+$ *and the* $1\Pi_x$, $2\Pi_x$ *and* $3\Pi_x$ *valence-excited states. The transition densities are relative to the calculation at the O K-Edge. The distribution in the* σ_{xz} *plane is shown (as indicated in lower left corner), owing to the transition densities being symmetric with respect to* σ_{xz}.

particular those related to the Π_x states. As shown in fig. 4.29, the Π_x-symmetric transition densities possess negatively- or positively-valued regions between C and S but not between C and O, with the latter being 'isolated' from the CS moiety. The excitation at the S L1-Edge prepares $1\Delta_{x^2-y^2}$ and Π_x coherences with comparable amplitudes. This leads to electronic dynamics – characterised by a mechanism similar to that shown in fig. 4.28 – unfolding over the whole duration of $\rho_{vg}(\boldsymbol{r}, t)$'s time-evolution. In particular, a cyclic motion across the σ_{yz} plane can take place, as shown in the snapshots in fig. 4.30. Here, at 2310 as the electrons migrate from C to S on the right side of σ_{yz}, subsequently migrating through σ_{yz} and then back to C at 2445 as. The cyclic motion proceeds in the opposite direction through σ_{yz} until the migration from C to S repeats, as shown in the 2780 as snapshot.

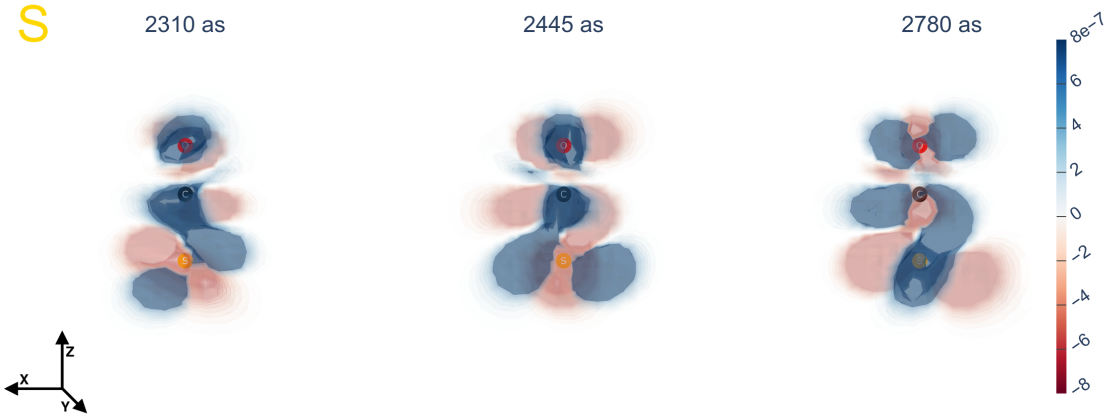

Figure 4.30: *Snapshots of* $\rho_{vg}(\boldsymbol{r}, t)$ *showing the cyclic migration between C and S triggered by an excitation at the S L1-Edge with a pulse linearly polarised at 45 degrees in* σ_{xz}. *As indicated in the lower left corner, the electronic motion in the* σ_{xz} *plane is shown.*

4.4.4 Rxy and Lxy polarisations

The coherences excited considering a Rxy-polarised pulse are shown in fig. 4.31. Since the consideration of a Lxy-polarised pulse leads to the same results, only the right-handed case is discussed. Besides the excitation of the coherence relative to

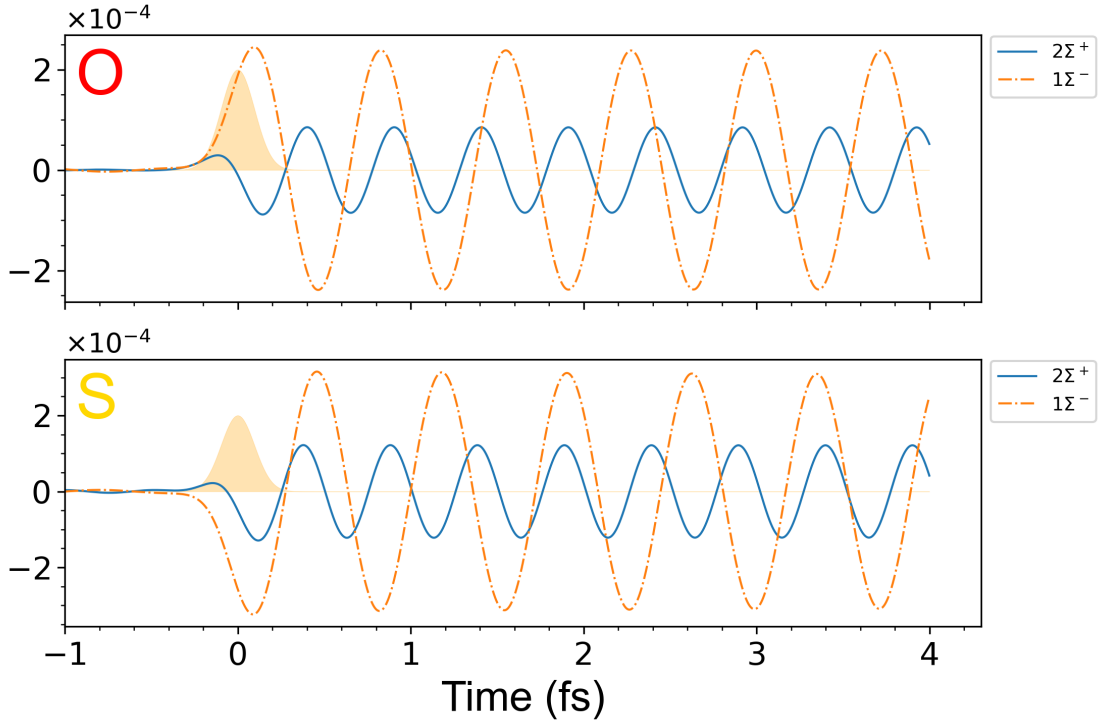

Figure 4.31: *Time-evolution of* $2\,\mathrm{Re}\{\rho_{vg}(t)\}$ *relative to an excitation with a right-handed, circularly polarised pulse. Each curve corresponds to a different valence-excited state. The upper panel is relative to the excitation at the O K-Edge, the lower panel to the excitation at the S L1-Edge. The yellow Gaussian corresponds to the time-domain pulse envelope, whose intensity scale is not shown.*

the $2\Sigma^+$ state, also the coherence associated to the $1\Sigma^-$ state is excited. This is due to the R_z rotation function forming the basis for the Σ^- irreducible representation of the $C_{\infty v}$ group. Despite this, a dipole transition to a Σ^--symmetric state is forbidden by the selection rules. This translates into the transition density associated to the $1\Sigma^-$ coherence corresponding to the zero density (i.e. zero-valued everywhere). As a consequence, only the $2\Sigma^+$ component contributes to $\rho_{vg}(\boldsymbol{r}, t)$, which behaves similarly to the z-polarised case.

4.5 $\rho_{cc'}(\boldsymbol{r}, t)$ component

The $\rho_{cc'}(\boldsymbol{r}, t)$ component to $\rho_{\Delta}(\boldsymbol{r}, t)$ is constructed by considering the coherences established between the core-excited states, $\rho_{cc'}(t)$, and the respective transition densities, $\rho_{cc'}(\boldsymbol{r})$. The spatial information carried by the transition densities is encoded in the transition 1PDM $\gamma_{pq}^{cc'} = \langle \psi_{c'} | \hat{c}_q^{\dagger} \hat{c}_p | \psi_c \rangle$, an example of which is shown in fig. 4.32. The only prominent non-zero coefficients are present in particle-particle

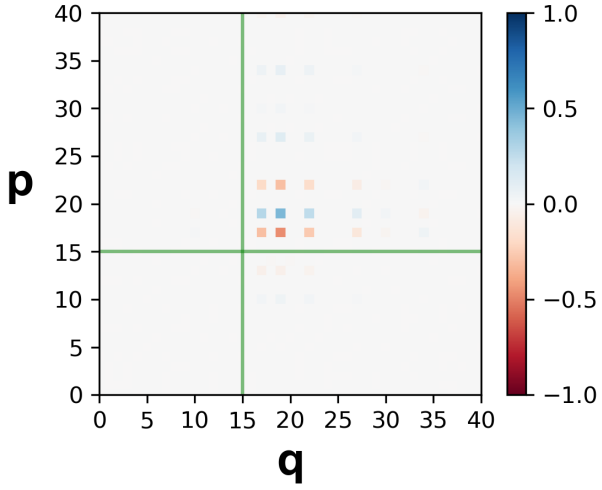

Figure 4.32: *Transition density matrix $\gamma_{pq}^{cc'}$ for $c \equiv 1^{c}\Pi_x$ and $c' \equiv 2^{c}\Pi_x$, expanded in the basis of canonical MOs. The green lines divide the molecular orbitals according to the particle-hole formalism as in fig. 4.6.*

part located in the upper-right quadrant of the matrix. This contrasts with e.g. γ_{pq}^{cg}, which presents non-zero coefficients only in the particle-hole part of the matrix. In γ_{pq}^{cg} the particle MOs can be considered as the 'destination' of the core-excitation, following the annihilation of an electron in a core hole MO. In this sense, $\gamma_{pq}^{cc'}$ describes the transition between these 'destination' particle MOs, providing information on the differences between the spatial regions the core-electron is excited to, characteristic of each of the involved core-excited states.

4.5.1 x polarisation

The main $\rho_{cc'}(t)$ coherences excited between the core-excited states, considering a pulse linearly polarised along the x-axis, are shown in fig. 4.33. In compliance

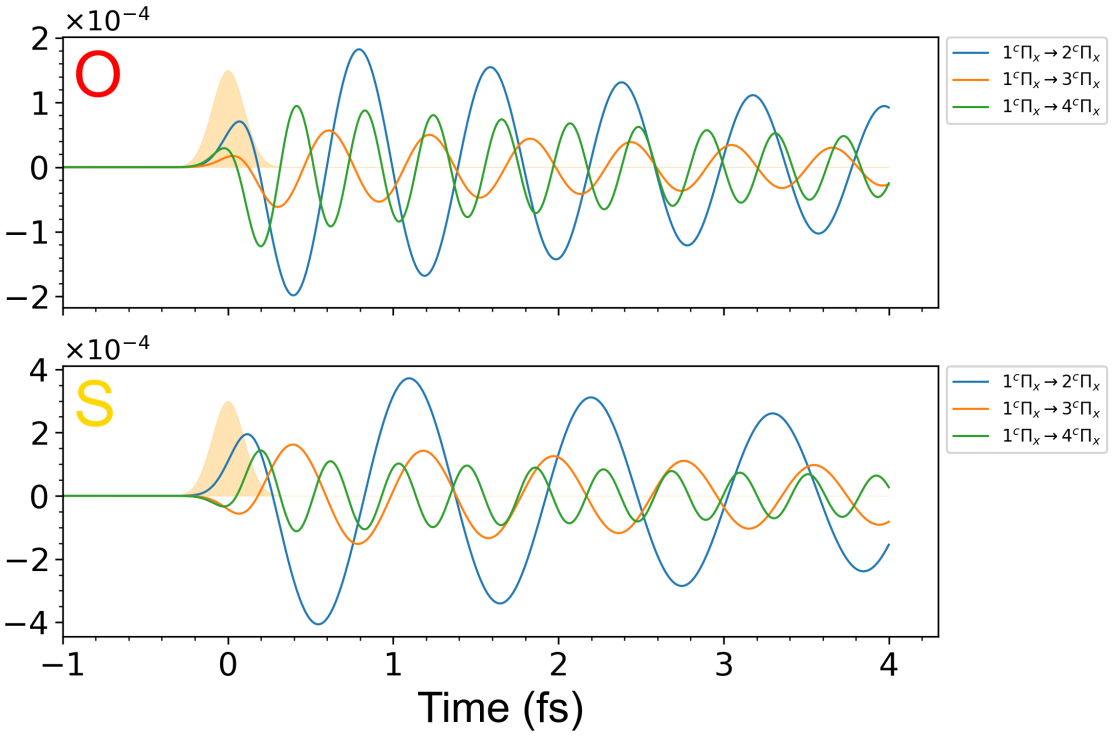

Figure 4.33: *Time-evolution of* $2\,\mathrm{Re}\{\rho_{cc'}(t)\}$ *relative to the excitation with a pulse linearly polarised along the x-axis. Each curve corresponds to a different couple of core-excited states. The upper panel is relative to the excitation at the O K-Edge, the lower panel to the excitation at the S L1-Edge. The yellow Gaussian corresponds to the time-domain pulse envelope, whose intensity scale is not shown.*

with the selection rules, only coherences between Π_x-symmetric states are excited, with those involving the $1^c\Pi_x$ state being dominant. This is consistent with the distribution of the populations among the Π_x-symmetric states shown in fig. 4.13, which is also reflected in the exponential decay of the coherences. The dominant coherence corresponds to $c \equiv 1^c\Pi_x$ and $c' \equiv 2^c\Pi_x$, with its preponderance being more marked at the S L1-Edge than at the O K-Edge. As shown in fig. 4.34, the symmetry of the Π_x-symmetric states is reflected in that of $\rho_{cc'}(\boldsymbol{r}, t)$, which is accordingly oriented along the x-axis. The snapshots relative to the excitation at the O K-Edge represent the oscillation of $\rho_{cc'}(\boldsymbol{r}, t)$ driven by the $1^c\Pi_x \rightarrow 2^c\Pi_x$ coherence. At 400 *as* and 1200 *as* the positively-valued region is concentrated on C, while the negatively-valued region is of smaller magnitude and located on S. At 800 *as* the positively-valued region localises mostly on O (with some traces on S), while the negatively-valued regions is mostly located on C. Also at the S L1-Edge the $1^c\Pi_x \rightarrow 2^c\Pi_x$ coherence drives the main oscillation of $\rho_{cc'}(\boldsymbol{r}, t)$. However, owing to the atom-specific characteristics of the core-excitation reflected in the transition density, the oscillation involves mainly C and S, with a very small, positively-valued contribution being present on O at 1100 *as*. As a reflection of the smaller energy difference between the $1^c\Pi_x$ and $2^c\Pi_x$ states at the S L1-Edge (c.f. table 4.2), the

oscillation period is longer than at the O K-Edge.

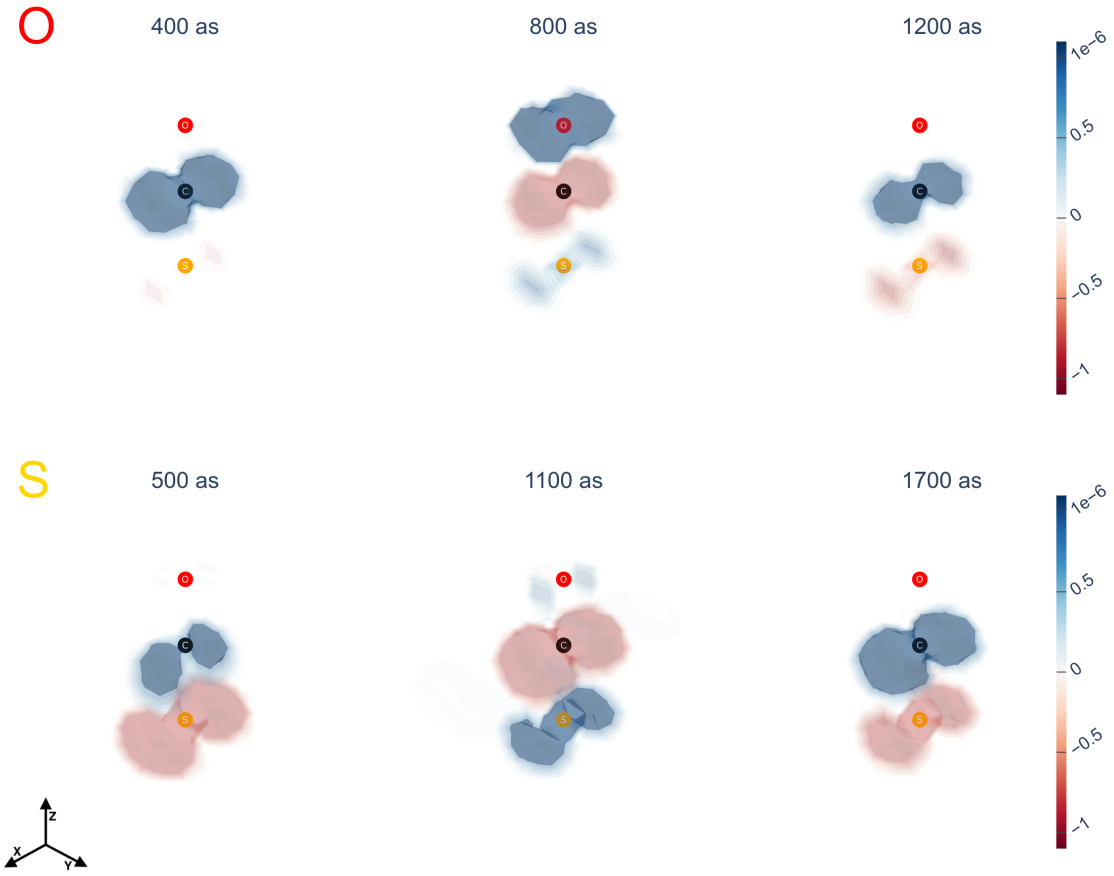

Figure 4.34: *Snapshots of $\rho_{cc'}(\boldsymbol{r}, t)$ relative to the excitation with a pulse linearly polarised along the x-axis. The upper panel is relative to the excitation at the O K-Edge, the lower panel to the excitation at the S L1-Edge. The axes orientation is illustrated in the lower left corner.*

4.5.2 z polarisation

The main coherences excited between the core-excited states, considering a pulse linearly polarised along the z-axis, are shown in fig. 4.35. At the O K-Edge, the most prominent coherence is relative to the $1^c\Sigma^+ \rightarrow 2^c\Sigma^+$ transition. The same is valid at the S L1-Edge, where also the coherence relative to the $1^c\Sigma^+ \rightarrow 3^c\Sigma^+$ transition plays a prominent role. The snapshots shown in fig. 4.36 represent the main features

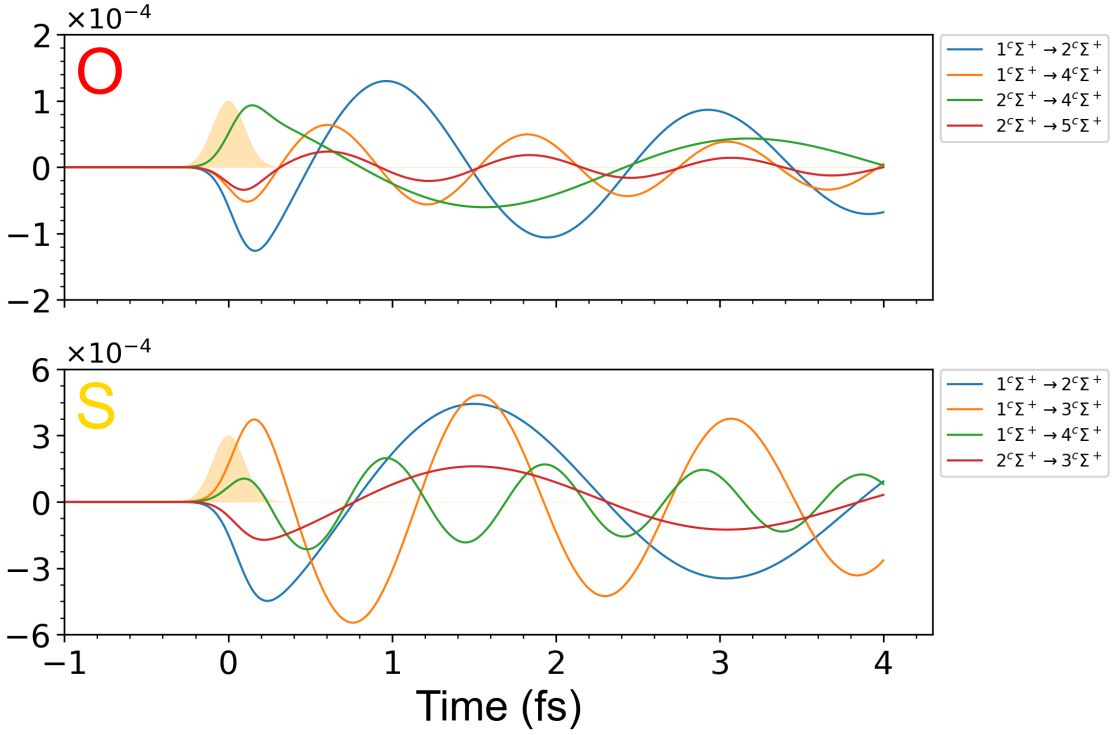

Figure 4.35: *Time-evolution of* $2\,\mathrm{Re}\{\rho_{cc'}(t)\}$ *relative to the excitation with a pulse linearly polarised along the z-axis. Each curve corresponds to a different couple of core-excited states. The upper panel is relative to the excitation at the O K-Edge, the lower panel to the excitation at the S L1-Edge. The yellow Gaussian corresponds to the time-domain pulse envelope, whose intensity scale is not shown.*

$\rho_{cc'}(\boldsymbol{r}, t)$'s time evolution. The Σ^+ symmetry of the involved states is reflected in the cylindrical symmetry of $\rho_{cc'}(\boldsymbol{r}, t)$ around the z-axis. The comparison of the 200 *as* snapshots in the upper and lower panels indicates that, in the initial stages of the time evolution, a slight polarisation of $\rho_{cc'}(\boldsymbol{r}, t)$ towards O (when exciting at the O K-Edge) or S (when exciting at the S L1-Edge) is present. At later moments of time, the spatial distribution and oscillation of $\rho_{cc'}(\boldsymbol{r}, t)$ around O resembles that of a p_z atomic orbital. This can be seen by comparing the region around O in the 1000 *as* and 1950 *as* snapshots at the O K-Edge, and in the 1750 *as* and 2500 *as* snapshots at the S L1-Edge. On the other hand, the characteristics of $\rho_{cc'}(\boldsymbol{r}, t)$ around C and S can be mapped to those of a d_{z^2} atomic orbital centred on C, superimposing with a p_z-shaped density centred on S.

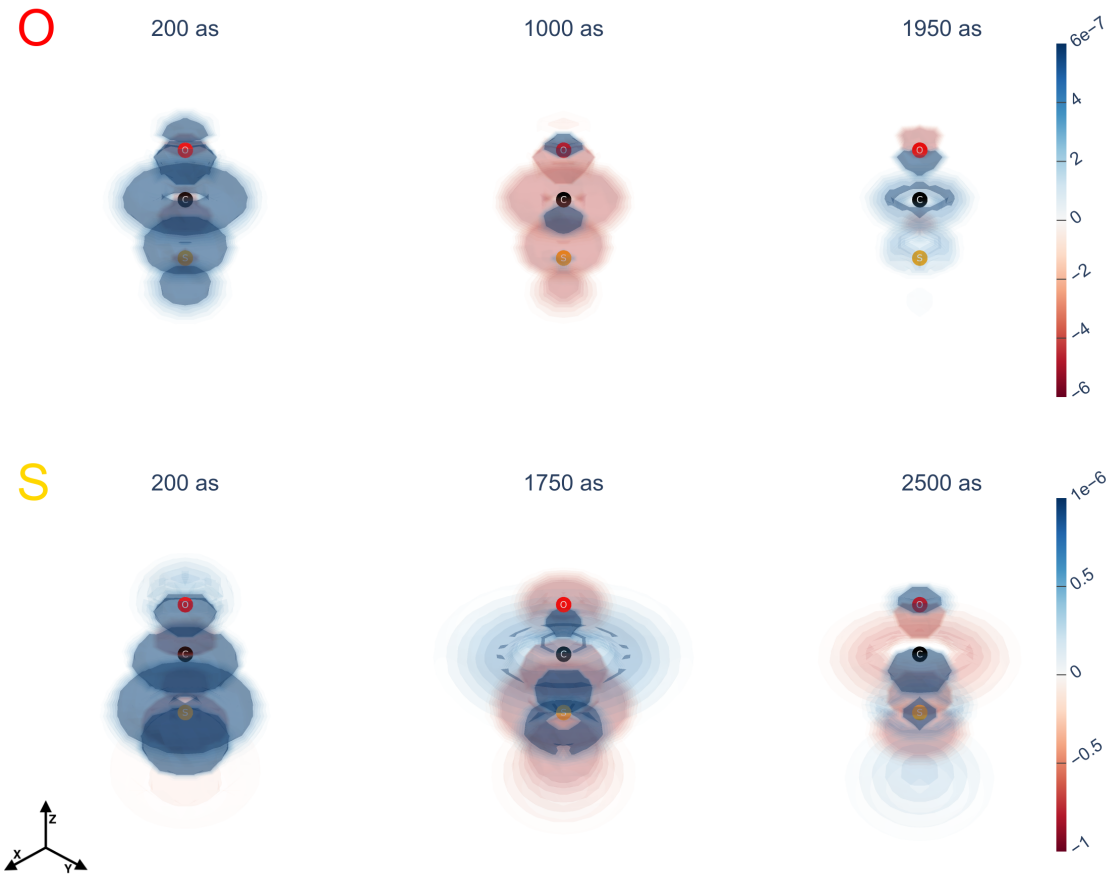

Figure 4.36: *Snapshots of $\rho_{cc'}(\boldsymbol{r}, t)$ relative to the excitation with a pulse linearly polarised along the z-axis. The upper panel is relative to the excitation at the O K-Edge, the lower panel to the excitation at the S L1-Edge. The axes orientation is illustrated in the lower left corner.*

4.5.3 xz polarisation

The main coherences, $\rho_{cc'}(t)$, excited by a pulse linearly polarised at 45 degrees in the σ_{xz} plane, are shown in fig. 4.35. Both at the O K-Edge and at the S L1-Edge

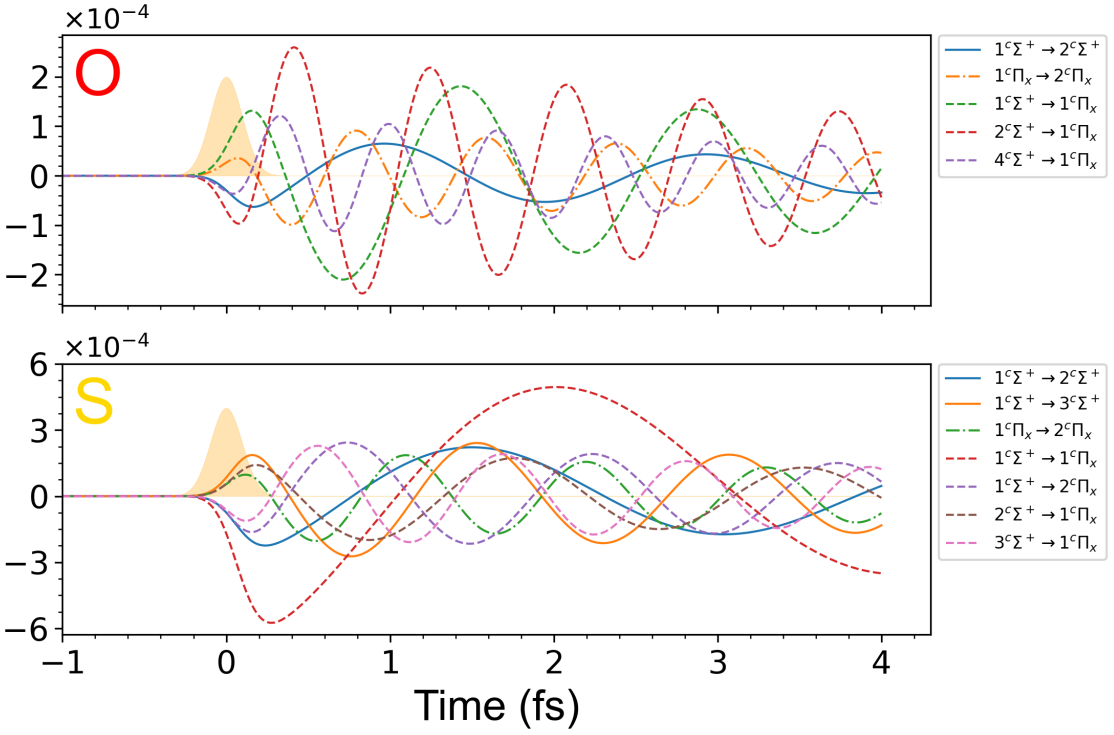

Figure 4.37: *Time-evolution of* $2\,\mathrm{Re}\{\rho_{cc'}(t)\}$ *relative to an excitation with a pulse linearly polarised at 45 degrees in the xz plane. Each curve corresponds to a different couple of core-excited states. The upper panel is relative to the excitation at the O K-Edge, the lower panel to the excitation at the S L1-Edge. The yellow Gaussian corresponds to the time-domain pulse envelope, whose intensity scale is not shown.*

the dominant coherences involve core-excited states of different symmetry, with the $1^c\Pi_x$ core-excited state playing a prominent role. The comparison between the two panels shows how the same coherences (e.g. $1^c\Sigma^+ \rightarrow 1^c\Pi_x$) present very different oscillation frequencies. This directly reflects the different energy gaps between the $1^c\Pi_x$ states and the Σ^+-symmetric states for excitations at the O K-Edge or S L1-Edge (vide table 4.2). At the O K-Edge, the $1^c\Sigma^+ \rightarrow 1^c\Pi_x$ and $2^c\Sigma^+ \rightarrow 1^c\Pi_x$ coherences are dominant and correspond to the transition densities shown in the left and central panels of fig. 4.38. Here, the transition densities are shown in the σ_{xz} plane, given their symmetry with respect to the σ_{yz} plane. As can be seen in the 400 *as* and 1450 *as* snapshots in the upper panel of fig. 4.39, at the O K-Edge the time-evolution of $\rho_{cc'}(\boldsymbol{r}, t)$ corresponds to the oscillation between the $1^c\Sigma^+ \rightarrow 1^c\Pi_x$ and $2^c\Sigma^+ \rightarrow 1^c\Pi_x$ transition densities. The interference between the dominant transition densities manifests e.g. at 700 *as*, where the respective coherences have about the same amplitude and sign. Considering the excitation at the S L1-Edge, the behaviour of the coherences in fig. 4.37 is dominated by the $1^c\Sigma^+ \rightarrow 1^c\Pi_x$ term, with the evolution of $\rho_{cc'}(\boldsymbol{r}, t)$ – shown in the lower panel of fig. 4.39 – being accordingly dominated by the corresponding transition density (shown in the rightmost panel of fig. 4.38). Complying with the behaviour of the dominant coherence, $\rho_{cc'}(\boldsymbol{r}, t)$

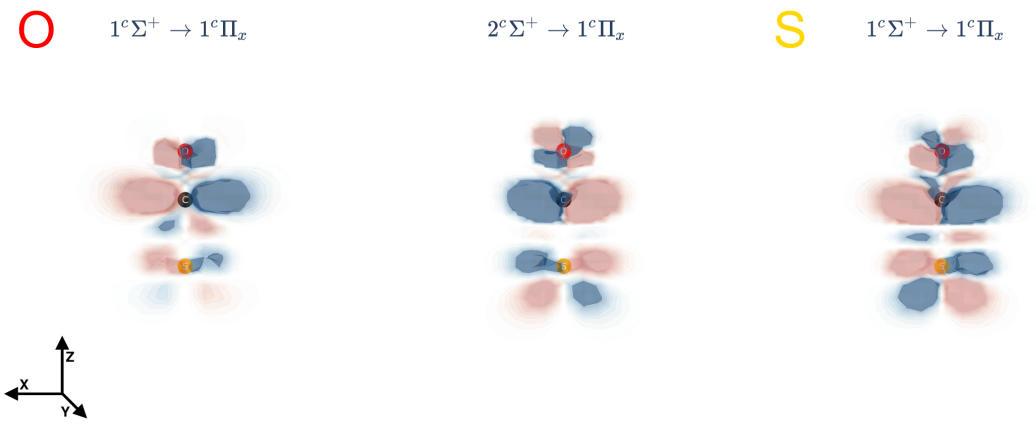

Figure 4.38: *Transition densities corresponding to the transition between the states* $1^c\Sigma^+$ *and* $1^c\Pi_x$ *(left and right) and between the states* $2^c\Sigma^+$ *and* $1^c\Pi_x$ *(centre). The left and central panels are relative to the O K-Edge calculation, the right panel to the S L1-Edge calculation. The axes orientation is illustrated in the lower left corner. Blue is positive, red is negative.*

oscillates with a long period between the negatively-signed (i.e. 250 *as* snapshot) and positively-signed (i.e. 2000 *as* snapshot) $1^c\Sigma^+ \rightarrow 1^c\Pi_x$ transition density. The 1000 *as* snapshot is relative to an instant at which the dominant $1^c\Sigma^+ \rightarrow 1^c\Pi_x$ coherence is roughly zero and the effects due to the interference between all the other coherences emerge. Here, the spatial distribution of $\rho_{cc'}(\boldsymbol{r}, t)$ is similar (especially on O and C) to that found in the 700 *as* snapshot at the O K-Edge.

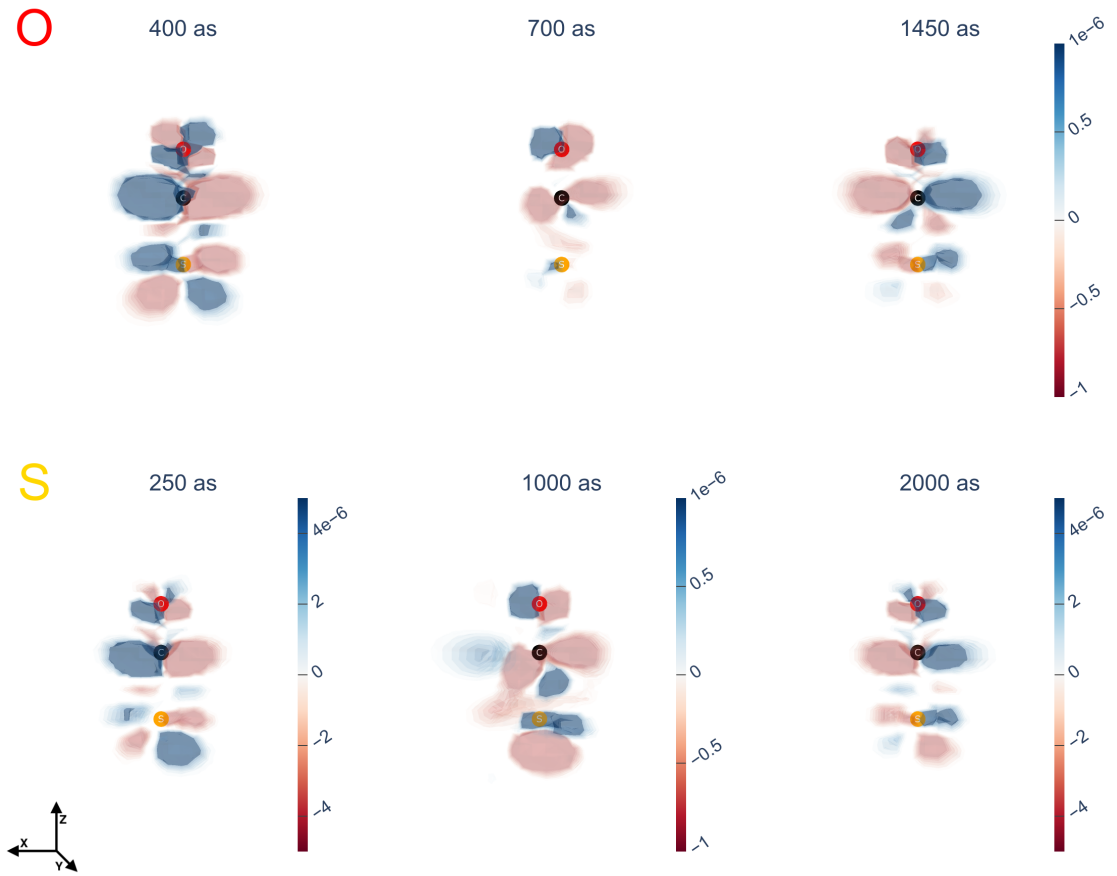

Figure 4.39: *Snapshots of $\rho_{cc'}(\boldsymbol{r}, t)$ relative to the excitation with a pulse linearly polarised at 45 degrees in the xz plane. The upper panel is relative to the excitation at the O K-Edge, the lower panel to the excitation at the S L1-Edge. The axes orientation is illustrated in the lower left corner.*

4.5.4 Rxy and Lxy polarisations

Considering a Rxy or a Lxy polarised pulse leads to the excitation of coherences between ${}^c\Pi_x$-symmetric states and between ${}^c\Pi_y$-symmetric states. The time evo-

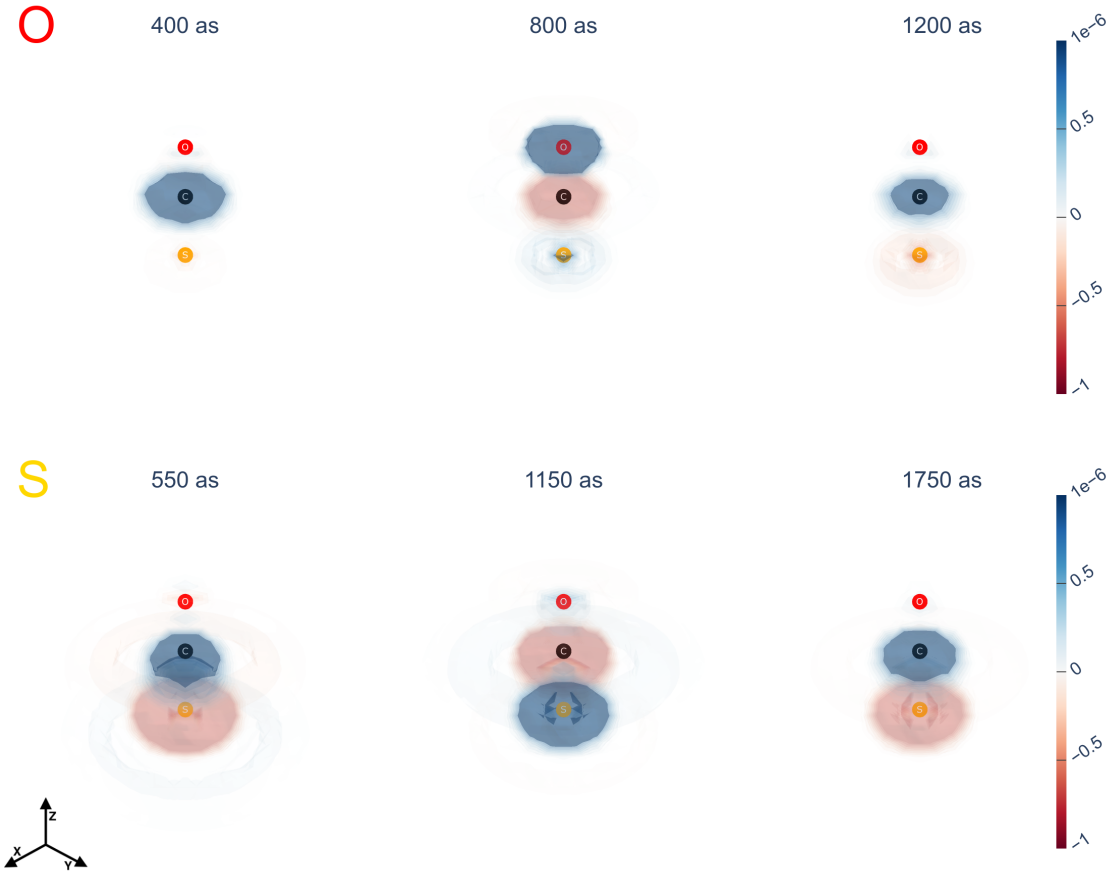

Figure 4.40: *Snapshots of $\rho_{cc'}(\boldsymbol{r},t)$ relative to the excitation relative to an excitation with a right-handed, circularly polarised pulse. The upper panel is relative to the excitation at the O K-Edge, the lower panel to the excitation at the S L1-Edge. The axes orientation is illustrated in the lower left corner.*

lution of the two groups of coherences is perfectly coincident and is similar to the x-polarised case in fig. 4.33. The handedness of the polarisation does not lead to qualitative differences in the excited coherences, which allows to limit the analysis to the Rxy case. The similarities to the x-polarised case are limited to the oscillation of $\rho_{cc'}(\boldsymbol{r},t)$, which mimics that shown in fig. 4.34. Unlike in the x-polarised case, $\rho_{cc'}(\boldsymbol{r},t)$ presents a cylindrical symmetry with respect to the z-axis, which is connected to the involvement of both ${}^c\Pi_x$- and ${}^c\Pi_y$-symmetric states in its construction. The difference between the ${}^c\Pi_x$ and ${}^c\Pi_y$ states lies in the orientation of the respective transition densities: while the ${}^c\Pi_x$ transition densities are oriented along the x-axis, those relative to the ${}^c\Pi_y$ states are oriented along the y-axis. $\rho_{cc'}(\boldsymbol{r},t)$ is constructed through the equal contribution of ${}^c\Pi_x$ and ${}^c\Pi_y$ transition densities, whose in-phase combination mediated by the coherences leads to the cylindrical symmetry of $\rho_{cc'}(\boldsymbol{r},t)$.

4.6 Summary and discussion

The characteristics of $\rho_{\Delta}(\boldsymbol{r},t)$'s dynamics reflect the perturbative hierarchy of the density matrix components, with the first order component $\rho_{cg}(\boldsymbol{r},t)$ and the second order component $\Delta_{cg}(\boldsymbol{r},t)$ playing the dominant role. The regions of $\rho_{\Delta}(\boldsymbol{r},t)$ centred on the pumped atoms are dominated by $\rho_{cg}(\boldsymbol{r},t)$. This component extends over a region tightly localised around the pumped atom and is characterised by a very fast oscillation with a period of few *as*. The distribution of $\rho_{\Delta}(\boldsymbol{r},t)$ over the rest of the molecule is dominated by $\Delta_{cg}(\boldsymbol{r},t)$. This corresponds to the 'incoherent' contribution, which would be present also in the case an excitation with incoherent radiation was considered. Its time-evolution reflects the spontaneous decay of the core-excited states, which manifests as the progressive prevalence of the negatively-valued regions over the positively-valued ones. In particular, the initial distribution of the positively-valued regions (shown in the 400 *as* snapshots) is always found to be polarised towards (and in many cases localised on) the pumped atom. The structures of $\rho_{cg}(\boldsymbol{r},t)$ and $\Delta_{cg}(\boldsymbol{r},t)$ provide a spatial visualisation of the dominant core-excitation mechanism: the X-Ray pulse deposits its energy locally to the pumped atom, exciting the electrons from the core to the valence shells of the electronic structure in a (spatially) 'vertical' way. This results in the creation of a superposition of core particle-hole density pairs localised around the pumped atom. The $\rho_{cg}(\boldsymbol{r},t)$ and $\Delta_{cg}(\boldsymbol{r},t)$ components create only a substantially local modification of the electronic distribution over time, which changes its localisation and spatial symmetry/orientation in correspondence to the selected excitation edge and the pulse polarisation, respectively. The changes in the electronic distribution associated to the core-excitation are supported by the $\rho_{cc'}(\boldsymbol{r},t)$ component, whose contribution to $\rho_{\Delta}(\boldsymbol{r},t)$ is 'buried' under those of the dominant components. The electronic dynamics supported by $\rho_{cc'}(\boldsymbol{r},t)$ are relative to the 'particle' part of the superposition of core particle-hole density pairs created by the core excitation. In the examined cases, the electronic dynamics correspond to the oscillation of few (often a single) transition densities, owing to the dominant nature of the corresponding coherences. The dynamics within $\rho_{cc'}(\boldsymbol{r},t)$ reflect directly the atom-specificity and symmetry properties of the core-excited states, which can be tuned by acting on the pulse's central frequency and polarisation.

The electronic dynamics within the $\rho_{vg}(\boldsymbol{r},t)$ component correspond to those of the particle-hole pairs 'located' in the valence-shells of the electronic structure. Similarly to $\rho_{cc'}(\boldsymbol{r},t)$, also the contribution of $\rho_{vg}(\boldsymbol{r},t)$ to $\rho_{\Delta}(\boldsymbol{r},t)$ is 'buried' under the dominant contributions from $\rho_{cg}(\boldsymbol{r},t)$ and $\Delta_{cg}(\boldsymbol{r},t)$. This indicates that a smaller portion of the pulse energy is used for the valence-excitation compared to the core-excitation. However, owing to the absence of short-lived core-holes in the structure of $\rho_{vg}(\boldsymbol{r},t)$, its lifetime is much longer than that of the core-excited states' components. This makes $\rho_{vg}(\boldsymbol{r},t)$'s contribution to $\rho_{\Delta}(\boldsymbol{r},t)$ the dominant one on a timescale longer than the core-holes' lifetimes. In most polarisation cases, the WP includes only few valence-excited states, whose symmetry depends on the pulse polarisation. In these cases, the dynamic evolution of $\rho_{vg}(\boldsymbol{r},t)$ is dominated by the oscillation of a single coherence/transition density and the effects of the interference process can be observed only in certain precise moments of the time-evolution. Here, the constructive and destructive interference of the transition densities determines the formation of regions of electronic accumulation/decumulation. The

localisation of these regions over time depends on the spatial characteristics of the transition densities and the relative amplitudes and phases of the coherences. In particular, the properties of the coherences 'encode' the atom-specific character of the ISRIXS excitation. This can be seen especially in the xz-polarised case, where several coherences with comparable amplitudes are excited, involving multiple transition densities in the interference process. The atom-specific properties manifest already during the 'preparation' stage, where exciting at the O K-Edge or S L1-Edge produces different initial electronic distributions. In particular, the accumulation of the positively-valued regions is slightly polarised towards the pumped atom, with the effect being more pronounced at the S L1-Edge. The participation of many coherences/transition densities in the interference process allows visualising the electronic migration in a 'classical' way, likening it to a 'fluid' flowing between the atoms. This is particularly evident at the S L1-Edge, where many coherences with a comparable amplitude are excited. The symmetry of the electronic migration and the limitation of its interatomic character to the CS moiety result from the properties of the transition densities involved in the interference. This suggests that the spatial characteristics of the interfering transition densities play a crucial role in determining the spatial pathway followed by the electronic migration. These results suggest that the inclusion of many (comparably populated) valence-excited states in the WP is necessary to support the intramolecular electronic migration and to test the WP's atom-specific properties, such as the initial localisation. Based on this hypothesis, in the next chapter the analysis applied to OCS will be extended to the ring-shaped molecule Oxazole, which presents a larger number of low-lying valence-excited states compared to OCS.

CHAPTER 5

Wave packet in Oxazole

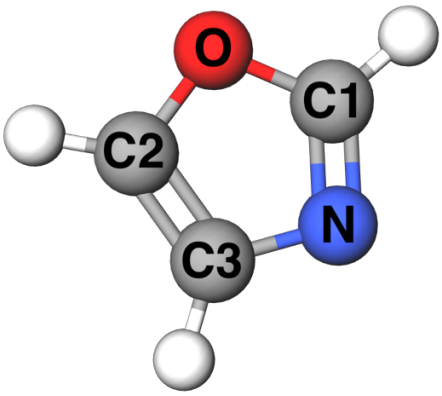

Oxazole is a heterocyclic aromatic molecule containing H, N, C and O atoms. The molecule presents a planar structure with a symmetry described by the C_s point group. The plane of the molecule corresponds to the plane σ_h[I], according to which the symmetry of the molecule is defined. As shown in the character table on the right side of table 5.1, the states are classified according to two irreducible representations: the A' irreducible representation, whose states are symmetric with respect to σ_h, and the A'' irreducible representation, whose states are antisymmetric with respect to σ_h. The choice of Oxazole was motivated by the interest in the electronic dynamics in heterocyclic aromatic molecules [126] and by its peculiar electronic structure, which allows including a larger number of valence-excited states in the WP compared to OCS. In fact, as shown on the left side of table 5.1, Oxazole presents 20 valence-excited states within an energy interval of about 9 eV. This allows to include more valence-excited states (i.e. 20 vs 7) within the 8 eV of the pulse bandwidth compared to OCS. The selection rules associated with the ISRIXS process allow, by varying the orientation of the pulse polarisation with respect to σ_h, to control the symmetry of the states included in the WP. This is shown in more detail on the right side of table 5.1, where each irreducible representation is associated with a pulse polarisation. In particular, it is interesting to notice how the Raman selection rules allow to populate A' valence-excited states in all polarisation cases, while A'' valence-excited states only in the xz-polarised case.

[I] In this work, the molecule is aligned such that σ_h coincides with σ_{xy}.

$\|\psi_v\rangle$	ω_{vg} (eV)	$\|\psi_v\rangle$	ω_{vg} (eV)
$2A'$	6.76	$1A''$	6.78
$3A'$	7.42	$2A''$	6.97
$4A'$	8.18	$3A''$	7.57
$5A'$	8.31	$4A''$	7.90
$6A'$	8.80	$5A''$	8.06
$7A'$	8.99	$6A''$	8.41
$8A'$	9.23	$7A''$	8.57
$9A'$	9.33	$8A''$	8.76
$10A'$	9.48	$9A''$	8.82
$11A'$	9.68	$10A''$	9.45

C_s	E	σ_h	ϵ
A'	1	1	$x^{*\dagger}$, $Cxy^{*\dagger}$, $xz^{*\dagger}$, $z^{\dagger}$
A''	1	-1	z^{*}, $xz^{*\dagger}$

Table 5.1: *Transition energies of the considered valence-excited states (left) and character table of the C_s point group (right). The transition energies in the left table are referred to the ground state $1A'$. Each irreducible representation in the character table is associated with a pulse polarisation, in accordance with the selection rules defined in the C_s point group. The superscripts * and † indicate dipole-allowed and Raman-allowed transitions, respectively. Both the right-handed and left-handed circular polarisations are indicated as Cxy.*

Just like the valence-excited states, also a larger number of core-excited states than OCS is included within the 8 eV-broad bandwidth. The considered core-excited states are listed in table 5.2. In this work, only the excitations at the O K-Edge and N K-Edge are studied, given that the broad pulse bandwidth does not allow to specifically target excitations at the K-Edge of the different C atoms [127]. The pulse's central frequency, ω_0, is set resonant to the $1A' \rightarrow 1^cA''$ transition (i.e. the $1s \rightarrow \pi^*$ line), with $\omega_0 = 400.87$ eV at the N K-Edge and $\omega_0 = 536.99$ eV at the O K-Edge, at the considered level of theory. The $\delta\omega_N$ and $\delta\omega_O$ columns show the energy differences between $1^cA''$ and the other core-excited states. These energy differences correspond to the detuning of the core-excitation energies from the $1s \rightarrow \pi^*$ line at the N K-Edge and O K-Edge, respectively. The A' states are all comprised within a ≈ 9 eV energy interval, while the A''-symmetric states are distributed over a much bigger energy interval. This allows, by varying the pulse polarisation, to greatly affect the number of core-excited states included in the WP. In fact, as shown in the left side of table 5.1, changing the polarisation orientation between parallel (i.e. along x) or perpendicular (i.e. along z) to σ_h allows to selectively excite A' or A'' core-excited states.

$\|\psi_c\rangle$	$\delta\omega_N$ (eV)	$\delta\omega_O$ (eV)	$\|\psi_c\rangle$	$\delta\omega_N$ (eV)	$\delta\omega_O$ (eV)
$1^cA'$	3.12	2.17	$1^cA''$	0	0
$2^cA'$	3.86	3.11	$2^cA''$	2.96	3.33
$3^cA'$	4.10	3.30	$3^cA''$	4.26	3.80
$4^cA'$	4.14	3.68	$4^cA''$	5.47	4.99
$5^cA'$	4.62	4.00	$5^cA''$	6.10	5.67
$6^cA'$	5.01	4.35	$6^cA''$	8.03	8.08
$7^cA'$	6.21	5.18	$7^cA''$	10.08	8.75
$8^cA'$	6.42	5.74	$8^cA''$	16.45	17.13
$9^cA'$	6.84	5.83	$9^cA''$	17.15	17.37
$10^cA'$	7.46	6.47	$10^cA''$	18.06	19.29
$11^cA'$	7.64	6.97	$11^cA''$	18.71	19.55
$12^cA'$	7.78	7.59	$12^cA''$	19.62	22.64
$13^cA'$	8.13	7.77	$13^cA''$	21.13	23.79
$14^cA'$	8.70	8.05	$14^cA''$	21.52	24.00
$15^cA'$	9.12	8.89	$15^cA''$	22.65	24.16

Table 5.2: *Energy difference between the core-excited states and the $1^cA''$ core-excited state at the N K-Edge ('$\delta\omega_N$' column) and at the O K-Edge ('$\delta\omega_O$' column). The core-excited states are labelled according to the irreducible representations of the C_s point group, with the superscript ^{c} standing for core-excited.*

In this study, the analysis scheme of $\rho_\Delta(\boldsymbol{r}, t)$ developed for OCS is applied to Oxazole, considering the same 8 eV pulse bandwidth. In particular, a more detailed analysis of the preparation of the $\rho_{vg}(\boldsymbol{r}, t)$ component is presented, with the aim of improving the investigation of its initial, atom-specific localisation due to ISRIXS.

5.1 Difference density $\rho_\Delta(\boldsymbol{r}, t)$

5.1.1 x polarisation

Snapshots of the time-evolution of $\rho_\Delta(\boldsymbol{r}, t)$, relative to the excitation with a pulse linearly polarised along the x-axis, are shown in fig. 5.1. Here, a similar behaviour of $\rho_\Delta(\boldsymbol{r}, t)$ as that encountered in OCS is present: right after the pulse has faded, a region of positive density localised on the pumped atom is present. In the rest of the molecule, negatively-valued regions of $\rho_\Delta(\boldsymbol{r}, t)$ prevail, with this prevalence becoming progressively more extensive with time, as shown in the 1000 *as* and 2000 *as* snapshots.

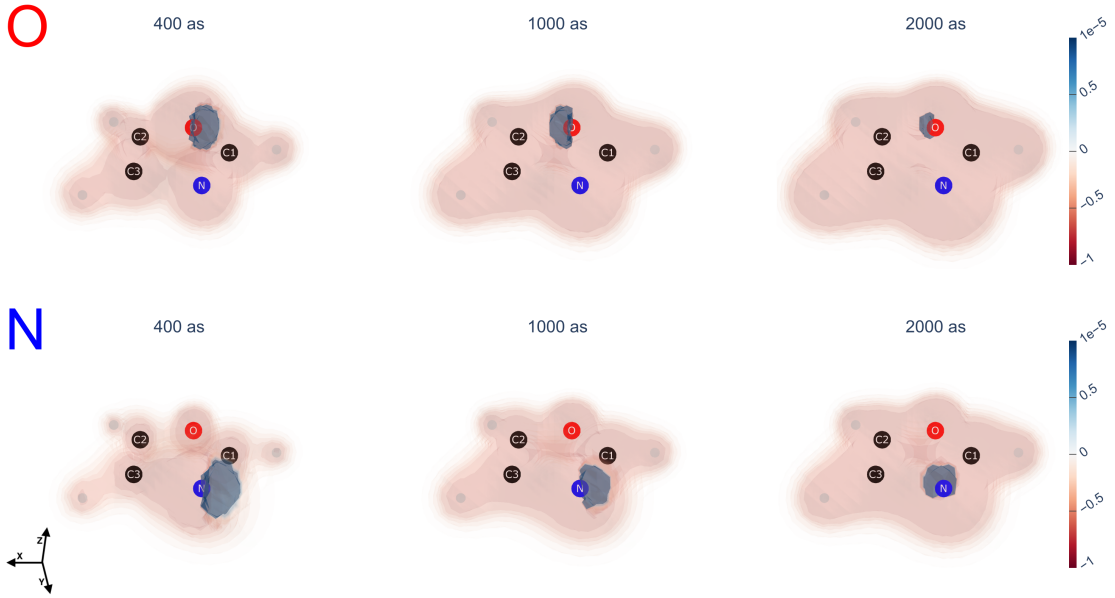

Figure 5.1: *Snapshots of $\rho_\Delta(\boldsymbol{r}, t)$ relative to the excitation with a pulse linearly polarised along the x-axis. The upper panel is relative to the excitation at the O K-Edge, the lower panel to the excitation at the N K-Edge. The orientation of the axes is illustrated in the lower left corner.*

5.1.2 z polarisation

Snapshots of the time-evolution of $\rho_\Delta(\boldsymbol{r}, t)$, relative to the excitation with a pulse linearly polarised along the z-axis, are shown in fig. 5.2. At 400 *as*, positively-valued

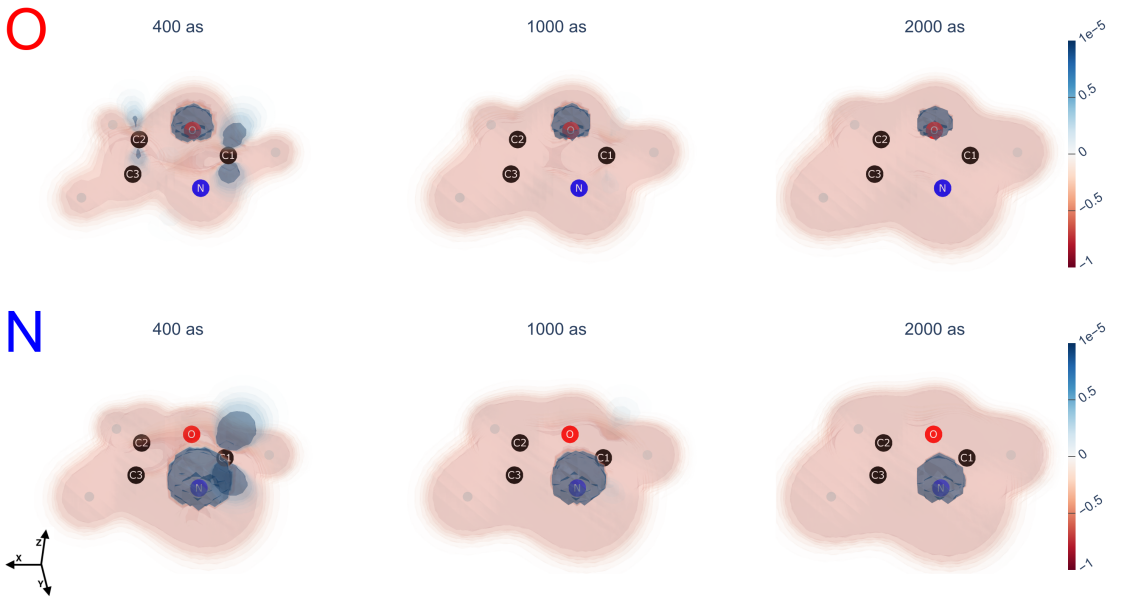

Figure 5.2: *Snapshots of $\rho_\Delta(\boldsymbol{r}, t)$ relative to the excitation considering a pulse linearly polarised along the z-axis. The upper panel is relative to the excitation at the O K-Edge, the lower panel to the excitation at the N K-Edge. The orientation of the axes is illustrated in the lower left corner.*

regions are localised on O and N depending on the molecule being excited at the O K-Edge or N K-Edge, respectively; the symmetry of these regions appears to be antisymmetric with respect to σ_h, contrary to the same regions in the x-polarised case in fig. 5.1. Differently from the same snapshots in fig. 5.1, the positively-valued regions extend to the C atoms neighbouring the pumped atoms. In particular, at the O K-Edge additional positively-valued regions are present on C1 and C2, while at the N K-Edge an additional positively-valued lobe is present on C1. As time progresses through the 1000 *as* and 2000 *as* snapshots, the positively-valued regions on the C atoms disappear in favour of negatively-valued regions, with only the positively-valued regions on the pumped atom being still present at 2000 *as*.

5.1.3 xz polarisation

The time-evolution of $\rho_\Delta(\boldsymbol{r}, t)$, relative to the excitation with a pulse linearly polarised at 45 degrees in the σ_{xz} plane, is illustrated in fig. 5.3. This polarisation mixes the contributions from the x-polarised and z-polarised cases shown in figs. 5.1 and 5.2. In particular, at 400 *as* the contribution of the z-polarised case is made evident by the presence of a faint positively-valued region on C1 at the O K-edge and a much more-pronounced positively-valued region on the same atom at the N K-Edge. The participation of the x-polarised contribution is evident in the 400 *as* and 1000 *as* snapshots at the O K-Edge, where the positively-valued region on O is 'tilted' in the σ_{xz} plane. The same is not true in the N K-Edge case, where the positively-valued regions centred on N are very similar to those found in the lower panel of fig. 5.2. As in the other polarisation cases analysed so far, as time progresses, $\rho_\Delta(\boldsymbol{r}, t)$ becomes progressively dominated by negatively-valued regions.

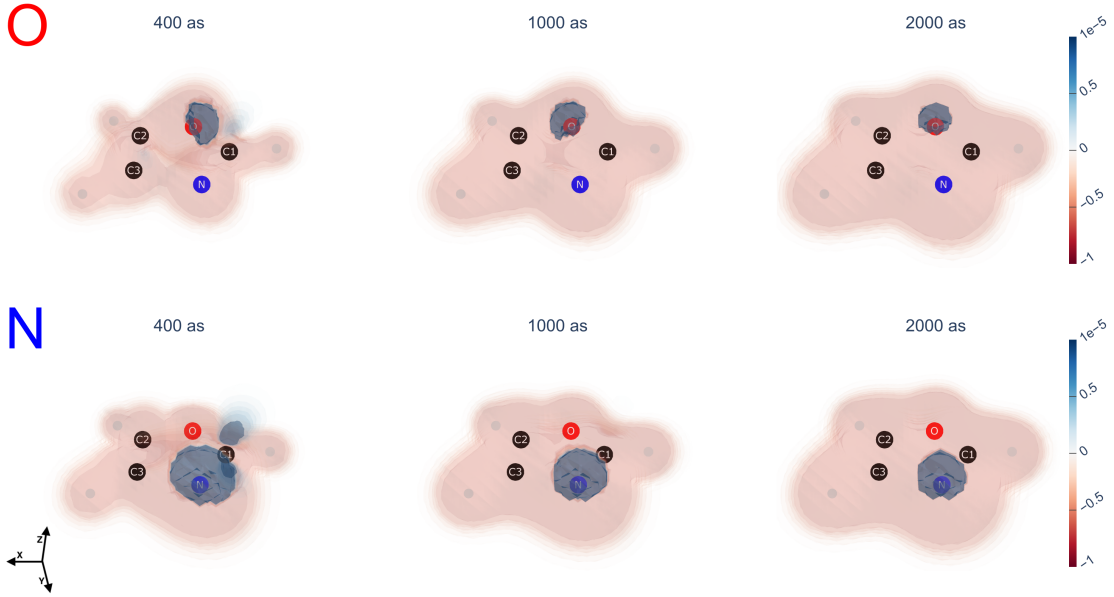

Figure 5.3: *Snapshots of $\rho_\Delta(\boldsymbol{r}, t)$ relative to the excitation considering a pulse linearly polarised at 45 degrees in the σ_{xz} plane. The upper panel is relative to the excitation at the O K-Edge, the lower panel to the excitation at the N K-Edge. The orientation of the axes is illustrated in the lower left corner.*

5.1.4 Rxy and Lxy polarisations

Snapshots illustrating the time-evolution of $\rho_\Delta(\boldsymbol{r}, t)$, relative to the excitation considering a right-handed, circularly polarised pulse in the σ_{xy} plane, are shown in fig. 5.4. Here, only the right-handed case is shown since the left-handed case leads

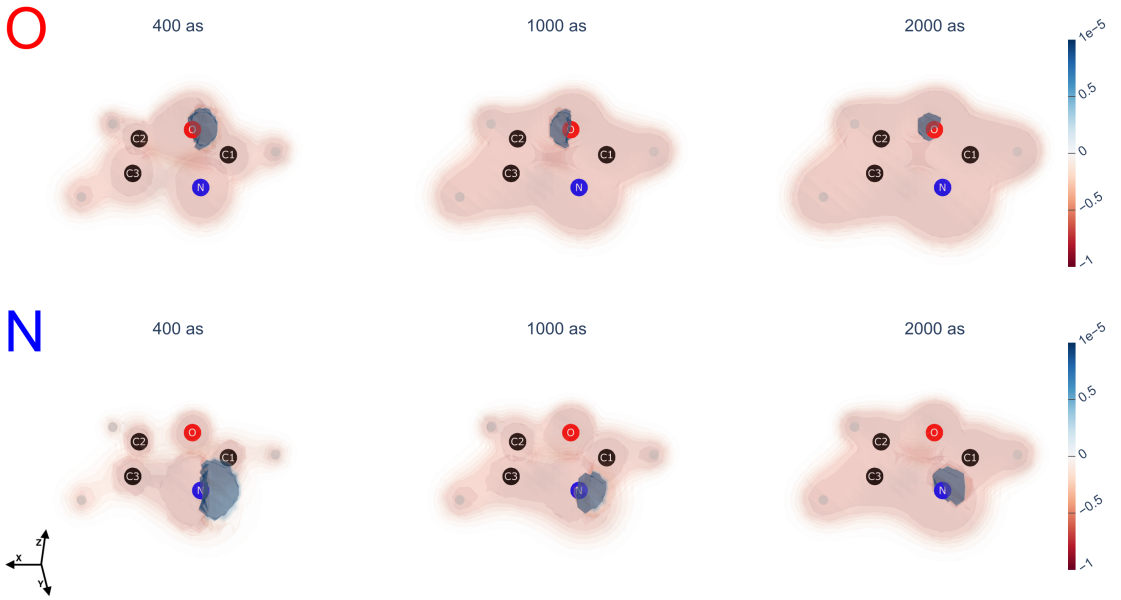

Figure 5.4: *Snapshots of $\rho_\Delta(\boldsymbol{r}, t)$ relative to the excitation with a right-handed, circularly polarised pulse in the σ_{xy} plane. The upper panel is relative to the excitation at the O K-Edge, the lower panel to the excitation at the N K-Edge. The orientation of the axes is illustrated in the lower left corner.*

to very similar results. At 400 *as* the positively-valued regions of $\rho_\Delta(\boldsymbol{r}, t)$ are found only on O or N depending on the excitation being at the O K-Edge or N K-Edge, respectively. The characteristics of $\rho_\Delta(\boldsymbol{r}, t)$ are very similar to those of the x-polarised case in fig. 5.1, with no positively-valued regions found on the neighbouring C atoms (as in the z-polarised and xz-polarised cases in figs. 5.2 and 5.3). Just like in the other polarisation cases, as time progresses through the 1000 *as* and 2000 *as* snapshots, $\rho_\Delta(\boldsymbol{r}, t)$ becomes progressively dominated by negatively-valued regions.

5.2 $\rho_{cg}(\boldsymbol{r}, t)$ component

Owing to the characteristics of the transition densities $\rho_{cg}(\boldsymbol{r})$ associated to the coherences $\rho_{cg}(t)$, $\rho_{cg}(\boldsymbol{r}, t)$ shows an edge-dependent localisation either on O or N. Given the straightforward explanation of the element-specific localisation, this section will be dedicated to the analysis of the symmetry characteristics of $\rho_{cg}(\boldsymbol{r}, t)$ and their dependence on the pulse polarisation.

5.2.1 x polarisation

The snapshots in fig. 5.5 illustrate the oscillation of $\rho_{cg}(\boldsymbol{r}, t)$ relative to the excitation with a pulse linearly polarised along the x-axis. $\rho_{cg}(\boldsymbol{r}, t)$ is symmetric with respect to the σ_{xy} plane (i.e. coinciding with the σ_h plane) consistently with the A' symmetry of the core-excited states involved. Consequently, the oscillation of $\rho_{cg}(\boldsymbol{r}, t)$ takes place along the x-axis, with a period of ≈ 8 *as* at the O K-Edge and ≈ 10 *as* at the N K-Edge.

Figure 5.5: *Snapshots of $\rho_{cg}(\boldsymbol{r}, t)$ relative to the excitation considering a pulse linearly polarised along the x-axis. The upper panel is relative to the excitation at the O K-Edge, the lower panel to the excitation at the N K-Edge. The orientation of the axes is illustrated in the lower left corner.*

5.2.2 z polarisation

The snapshots in fig. 5.6 illustrate the oscillation of $\rho_{cg}(\boldsymbol{r}, t)$, relative to the excitation with a pulse linearly polarised along the z-axis. Here, $\rho_{cg}(\boldsymbol{r}, t)$ shows the same oscillations periods at the respective edges as those characterising the x-polarised case in fig. 5.5. The crucial difference resides in the antisymmetry of $\rho_{cg}(\boldsymbol{r}, t)$ with respect to the σ_{xy} plane, in accordance with the A'' symmetry of the core-excited states involved. As a consequence, the corresponding oscillation of $\rho_{cg}(\boldsymbol{r}, t)$ takes place along the z-axis.

Figure 5.6: *Snapshots of $\rho_{cg}(\boldsymbol{r}, t)$ relative to the excitation considering a pulse linearly polarised along the z-axis. The upper panel is relative to the excitation at the O K-Edge, the lower panel to the excitation at the N K-Edge. The orientation of the axes is illustrated in the lower left corner.*

5.2.3 xz polarisation

The time-evolution of $\rho_{cg}(\boldsymbol{r}, t)$, considering a pulse linearly polarised at 45 degrees in the σ_{xz} plane, is represented in fig. 5.7. Here, both at the O K-Edge and at the N K-Edge, $\rho_{cg}(\boldsymbol{r}, t)$ undergoes a rotational motion around the y-axis, with the handedness of the rotation being the same at both edges. The rotational motion can be seen as deriving from the combination of the A'-symmetric and the A''-symmetric components with the appropriate relative phase, which results in the rotation of $\rho_{cg}(\boldsymbol{r}, t)$ about the y-axis in the σ_{xz} plane.

Figure 5.7: *Snapshots of $\rho_{\Delta}(\boldsymbol{r}, t)$ relative to the excitation with a pulse linearly polarised at 45 degrees in the σ_{xz} plane. The upper panel is relative to the excitation at the O K-Edge, the lower panel to the excitation at the N K-Edge. The orientation of the axes is illustrated in the lower left corner.*

5.2.4 Rxy and Lxy polarisations

The time-evolution of $\rho_{cg}(\boldsymbol{r}, t)$, considering a right-handed, circularly polarised pulse in the σ_{xy} plane, is represented by the snapshots in fig. 5.8. Here, $\rho_{cg}(\boldsymbol{r}, t)$ is shown in the σ_{xy} plane since, consistently with the handedness of the circular polarisation, its time-evolution corresponds to a rotational motion about the z-axis. The spatial distribution of $\rho_{cg}(\boldsymbol{r}, t)$ is symmetric with respect to the σ_{xy} plane, in accordance with the A' symmetry of the core-excited states involved. The characteristics of $\rho_{cg}(\boldsymbol{r}, t)$, obtained by considering a left-handed, circular polarisation, coincide with those shown in fig. 5.8 for the right-handed case, the sole difference being the left-handed rotation of $\rho_{cg}(\boldsymbol{r}, t)$ in the σ_{xy} plane.

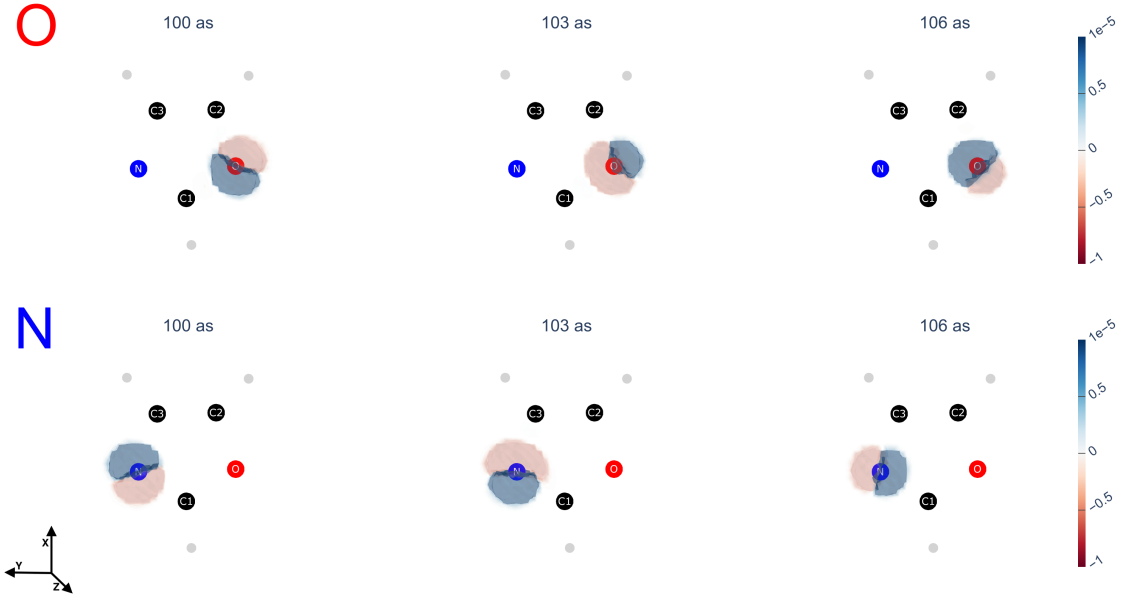

Figure 5.8: *Snapshots of $\rho_{\Delta}(\boldsymbol{r}, t)$ relative to the excitation with a right-handed, circularly polarised pulse in the σ_{xy} plane. The upper panel is relative to the excitation at the O K-Edge, the lower panel to the excitation at the N K-Edge. The orientation of the axes is illustrated in the lower left corner.*

5.3 $\Delta_{cg}(\boldsymbol{r}, t)$ component

5.3.1 x polarisation

The most prominent populations of the core-excited states, excited by means of a pulse linearly polarised along the x-axis, are shown as dashed curves in fig. 5.9. In

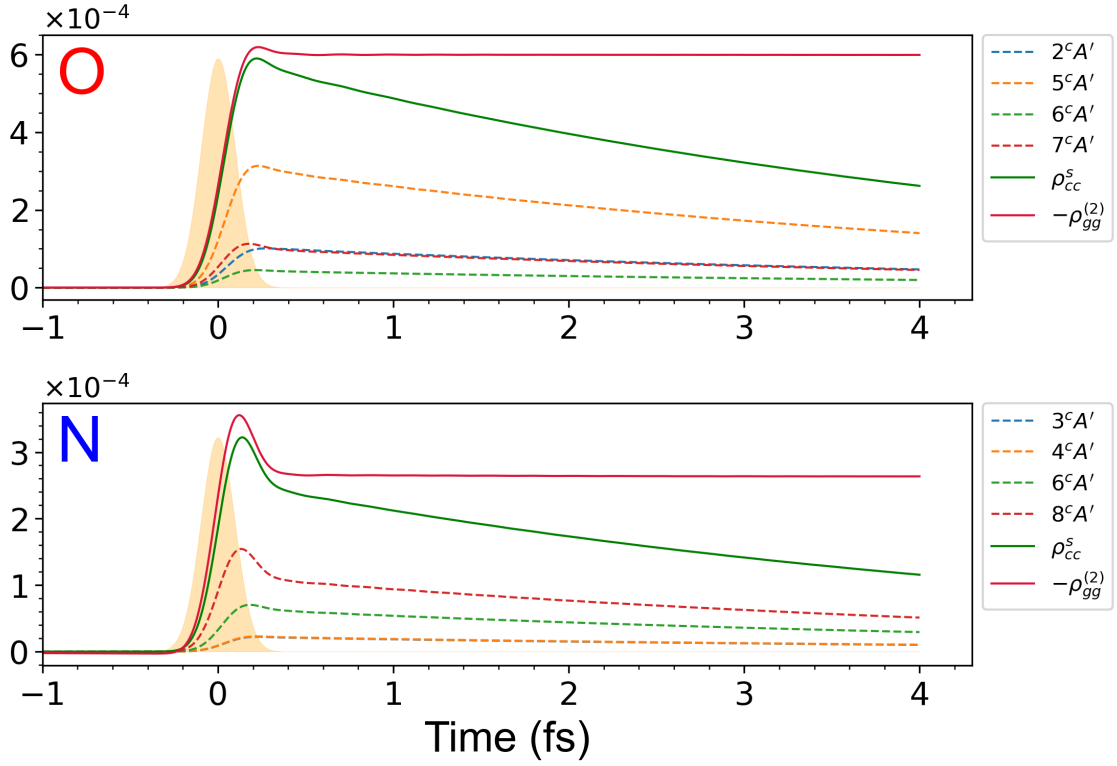

Figure 5.9: *Most prominent populations relative to an excitation with a pulse linearly polarised along the x-axis. The dashed lines indicate the populations of the single core-excited states, the green solid line the total population of the core-excited states, while the red solid line the (opposite of) ground state depopulation. The upper panel is relative to the excitation at the O K-Edge, the lower panel to the excitation at the N K-Edge.*

accordance to the selection rules, only A'-symmetric core-excited states are populated. Apart from the $6^cA'$ state, different states are populated at the two edges, with the $5^cA'$ state showing the largest population at the O K-Edge and the $8^cA'$ state showing the largest population at the N K-Edge. The green and red solid curves in fig. 5.9 represent the sum of the populations of the core-excited states, ρ^s_{cc}, and the (opposite of the) depopulation of the ground state, $-\rho^{(2)}_{gg}$, respectively. The shape of both curves is indicative of the detuning of the excitation energies associated with the A'-symmetric states with respect to the $1s \rightarrow \pi^*$ transition. As shown in table 5.2, such detuning are bigger at the N K-Edge than at the O K-Edge, which is reflected in the shapes of the ρ^s_{cc} and $-\rho^{(2)}_{gg}$ curves. The time-evolution of $\Delta_{cg}(\boldsymbol{r}, t)$, corresponding to the populations shown in fig. 5.9, is shown in fig. 5.10. At 400 *as* a positively-valued region of $\Delta_{cg}(\boldsymbol{r}, t)$ is localised on O or N, depending on the excitation being at the O K-Edge or N K-Edge. The regions disappear as time progresses through the 1000 *as* and 2000 *as* snapshots, which show the gradual prevalence of the negatively-valued regions. As shown in fig. 5.9, this is due to

the decay of ρ^s_{cc} and the consequent prevalence of $-\rho^{(2)}_{gg}$, which leads eventually to $\Delta_{cg}(\boldsymbol{r}, t) \equiv -\rho_{gg}(\boldsymbol{r})$.

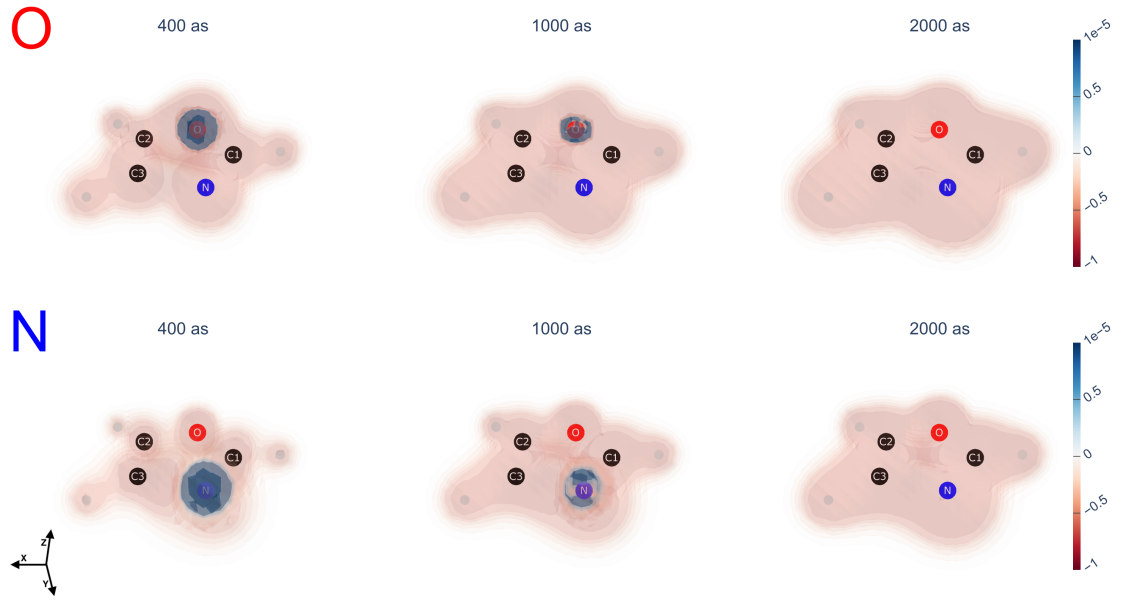

Figure 5.10: *Snapshots of $\Delta_{cg}(\boldsymbol{r}, t)$ relative to the excitation considering a pulse linearly polarised along the x-axis. The upper panel is relative to the excitation at the O K-Edge, the lower panel to the excitation at the N K-Edge. The orientation of the axes is illustrated in the lower left corner.*

Advantage of the non-truncated implementation

The comparison between $\rho^{(2)}_{gg}$ and ρ^s_{cc} allows to showcase the advantages of the non-truncated implementation. In the perturbative model applied in this work, the depopulation of the ground state corresponds to the total population of the core-excited states, i.e. $|\rho^{(2)}_{gg}| = |\rho^s_{cc}|$. The expression for $\rho^{(2)}_{gg}$ depends on a second order probability amplitude, $a^{(2)}_g(t)$, whose calculation involves the evaluation of a SOS. On the other hand, each term composing ρ^s_{cc} is obtained as a product of first order probability amplitudes, $a^{(1)}_c(t)$, whose calculation 'simply' involves a transition dipole moment. Within a 'truncated' approach, the SOS would be truncated in terms of the manifold of considered core-excited states and built in terms of the same transition dipole moments involved in the calculation of ρ^s_{cc}. In this context, $|\rho^{(2)}_{gg}| = |\rho^s_{cc}|$ by construction at every level of truncation. However, how can it be established *a priori*, within the given set of pulse parameters, how many core-excited states need to be considered to obtain 'converged', quantitatively correct values for $|\rho^{(2)}_{gg}|$ and $|\rho^s_{cc}|$? The 'non-truncated' approach to the calculation of the SOS solves this problem by formally including all the intermediate states; this allows to obtain the 'converged' result for every set of pulse parameters. Two examples are shown in fig. 5.11, where $-\rho^{(2)}_{gg}$ and ρ^s_{cc} (in the interaction picture) are compared in the context of two excitations considering pulses with a bandwidth of 8 eV and 5 eV. The relative contribution to ρ^s_{cc} from each core-excited state is shown by the respective coloured bar in the stack present in each plot. In both cases, $-\rho^{(2)}_{gg}$ provides the 'converged' limit, giving a quantitative reference as to how many core-excited states to include

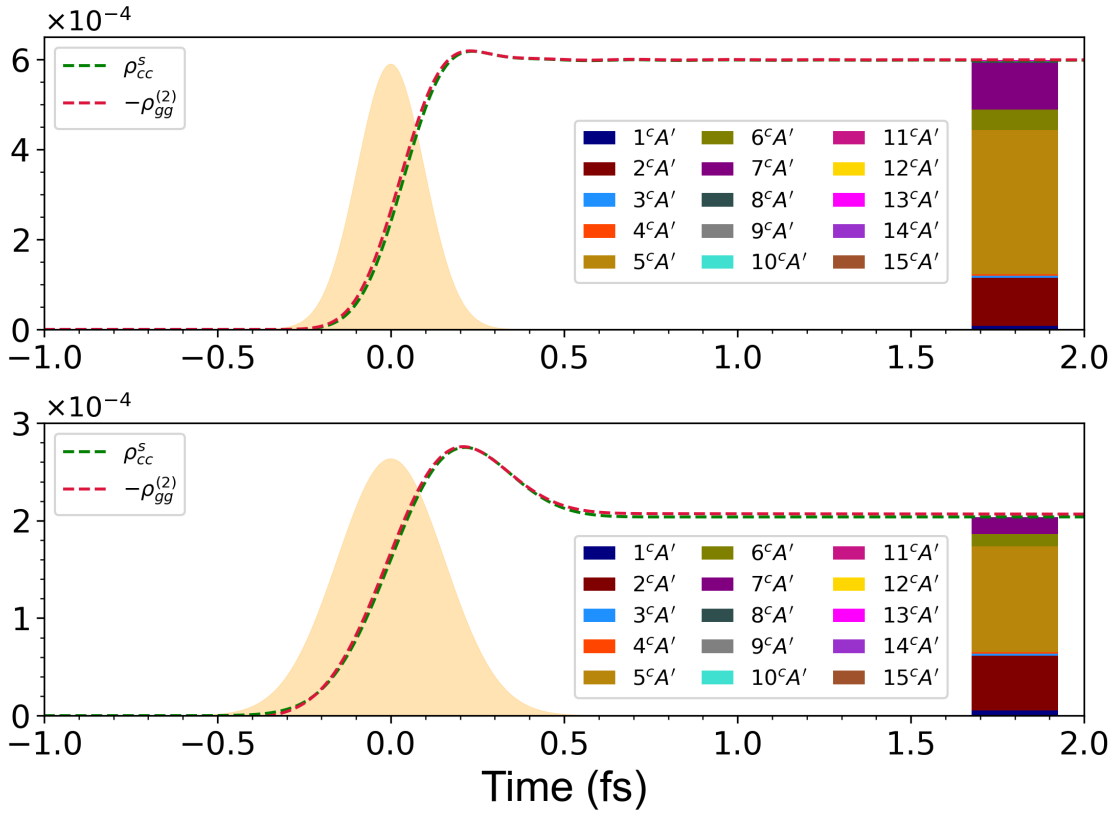

Figure 5.11: *Comparison between $-\rho^{(2)}_{gg}$ and ρ^s_{cc} in the interaction picture relative to the excitation at the O K-Edge with a pulse linearly polarised along the x-axis. The upper panel is relative to a pulse bandwidth of 8 eV, the lower panel to a pulse bandwidth of 5 eV. The full bars correspond to ρ^s_{cc}, with the coloured blocks representing the relative contributions from each core-excited state.*

in the description to satisfy $|\rho^{(2)}_{gg}| = |\rho^s_{cc}|$ for every set of pulse parameters. On one hand, this allows to understand how many core-excited states are necessary to completely describe the core-excitation within the given set of pulse parameters. On the other hand, this result implies that the values obtained for $\rho^{(2)}_{gg}$ and $\rho^{(2)}_{vg}$, which depend on the non-truncated calculation of the SOS, are 'converged' within the given set of pulse parameters. This allows to avoid lengthy convergence studies while consistently obtaining an accurate description of the ISRIXS process across different systems.

5.3.2 z polarisation

The most prominent populations of the core-excited states, excited by means of a pulse linearly polarised along the z-axis, are shown as dashed curves in fig. 5.12. Here, in compliance with the selection rules, only A''-symmetric states are populated.

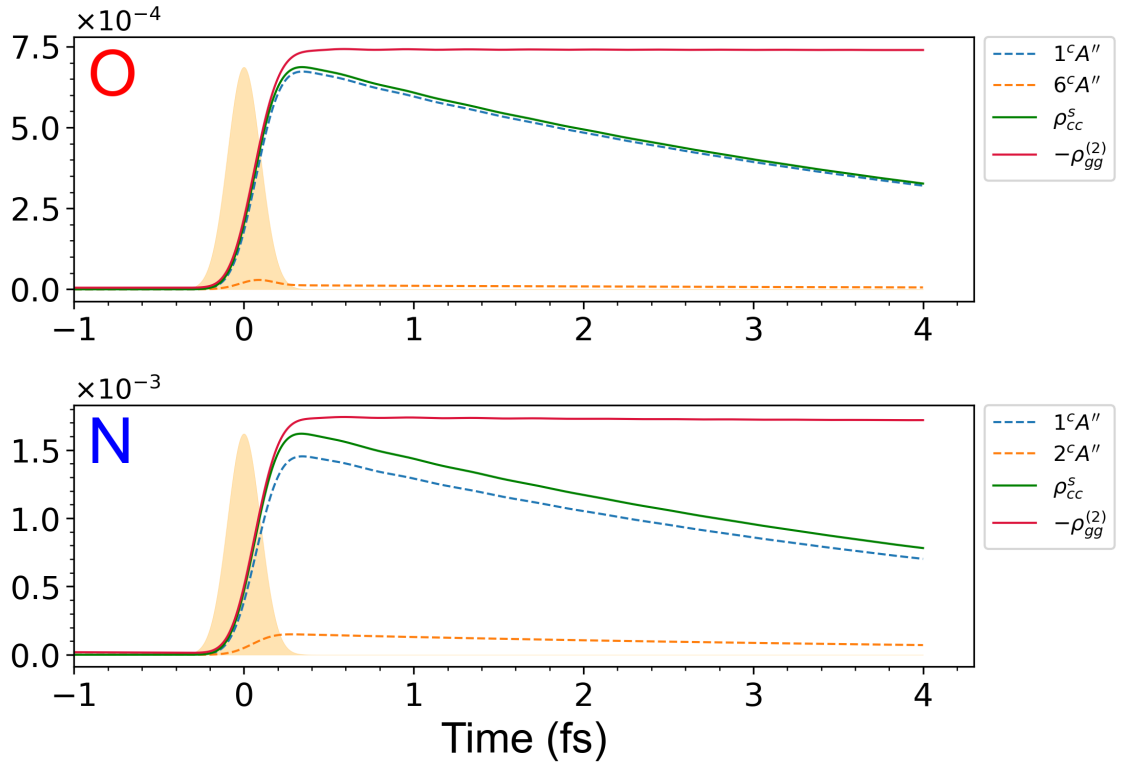

Figure 5.12: *Most prominent populations relative to an excitation with a pulse linearly polarised along the z-axis. The dashed lines indicate the populations of the single core-excited state, the green solid line the total population of the core-excited states while the red solid line the (opposite of) ground state depopulation. The upper panel is relative to the excitation at the O K-Edge, the lower panel to the excitation at the N K-Edge.*

Since the central frequency of the pulse is set resonant to the $1s \rightarrow \pi^*$ line, the total population of the core-excited states is dominated, both at the O K-Edge and N K-Edge, by the $1^cA''$ state. The small population of the other levels is due both to the large detuning of their excitation energies from the $1s \rightarrow \pi^*$ line and to the smaller transition dipole moments associated to them. The time-evolution of $\Delta_{cg}(\boldsymbol{r}, t)$, corresponding to the populations in fig. 5.12, is represented by the snapshots shown in fig. 5.13. At 400 *as* positively-valued regions form in correspondence to O at the O K-Edge and N at the N K-Edge. In addition to that, positively-valued regions are also present on C2 and C1 at the O K-Edge and on C1 at the N K-Edge. This explains the presence of the same regions in $\rho_\Delta(\boldsymbol{r}, t)$ in fig. 5.2 and indicates a smaller degree of localisation on the pumped atom than the x-polarised case in fig. 5.10. The time-evolution continues as in the x-polarised case, i.e. the negatively-valued regions progressively prevail on the positively-valued regions, with $\Delta_{cg}(\boldsymbol{r}, t)$ eventually coinciding with $-\rho_{gg}(\boldsymbol{r})$.

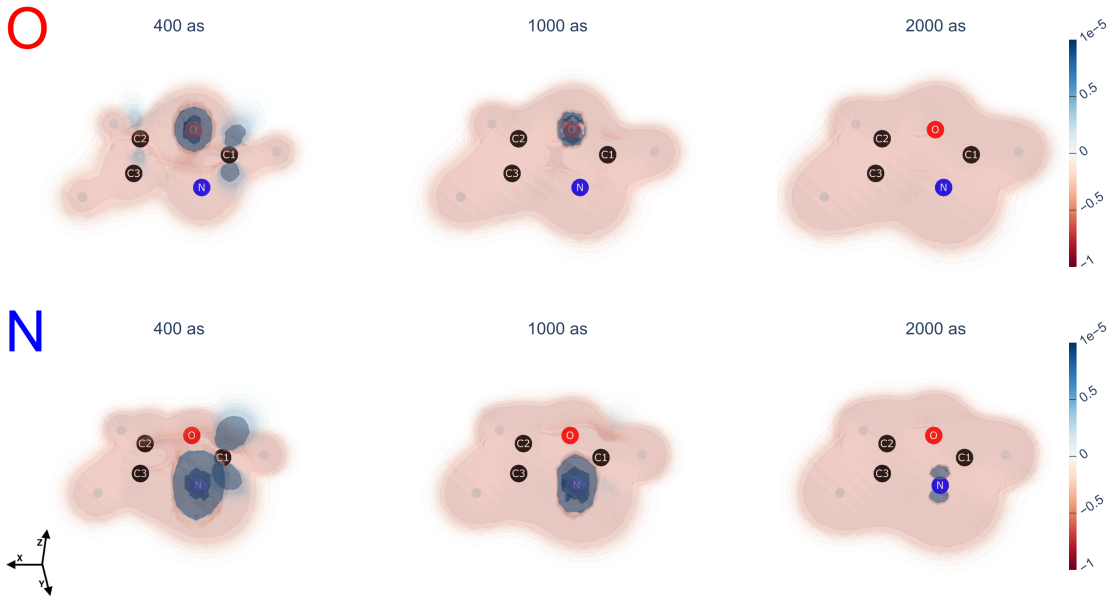

Figure 5.13: *Snapshots of $\Delta_{cg}(\boldsymbol{r}, t)$ relative to the excitation with a pulse linearly polarised along the z-axis. The upper panel is relative to the excitation at the O K-Edge, the lower panel to the excitation at the N K-Edge. The orientation of the axes is illustrated in the lower left corner.*

5.3.3 xz polarisation

The most prominent populations of the core-excited states, excited by means of a pulse linearly polarised at 45 degree in the σ_{xz} plane, are shown as dashed and dash-dotted curves in fig. 5.14. Both at the O K-Edge and at the N K-Edge, the

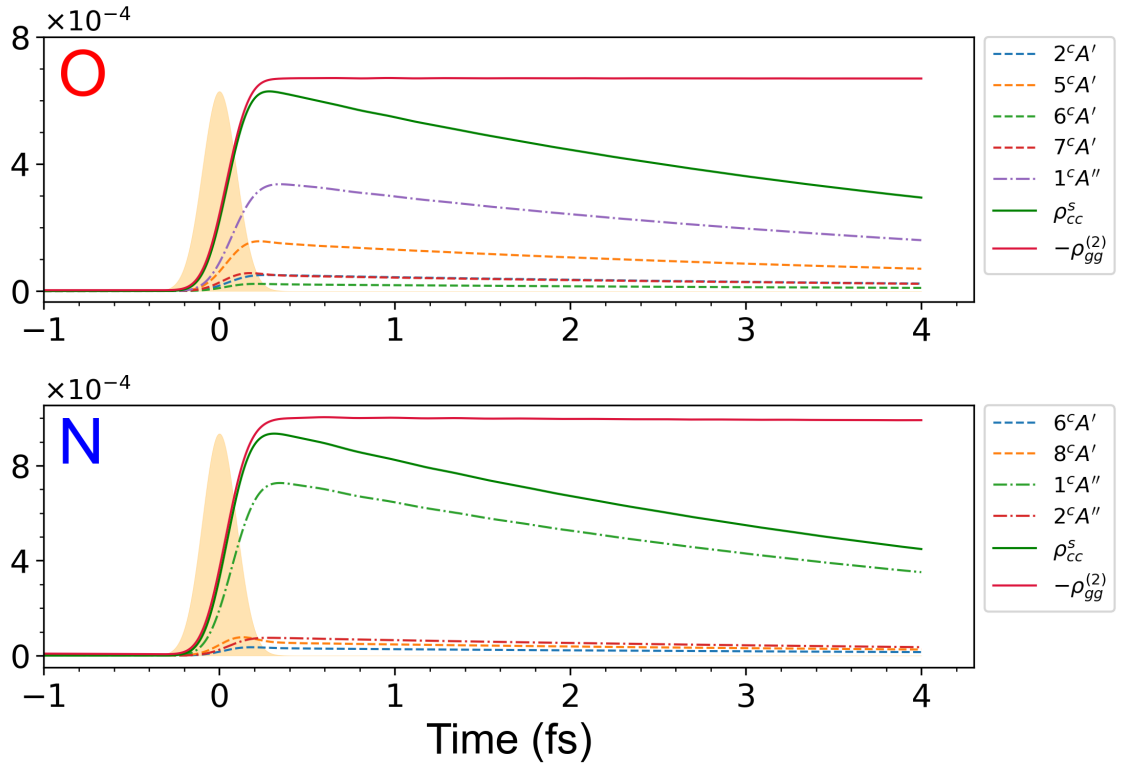

Figure 5.14: *Most prominent populations relative to an excitation with a pulse linearly polarised at 45 degrees in the σ_{xz} plane. The dashed lines indicate the populations of the A'-symmetric core-excited states, the dash-dotted lines indicate the populations of the A''-symmetric core-excited states, the green solid line the total population of the core-excited states while the red solid line the (opposite of) ground state depopulation. The upper panel is relative to the excitation at the O K-Edge, the lower panel to the excitation at the N K-Edge.*

largest population is associated to the $1^cA''$ state. While at the N K-Edge the population of the $1^cA''$ state dominates over the other populations, at the O K-Edge the distribution of the populations between the A'-symmetric and the A''-symmetric states is more balanced. The distribution of the populations is reflected in the characteristics of $\Delta_{cg}(\boldsymbol{r}, t)$, snapshots of which are shown in fig. 5.15. In the 400 *as* snapshot at the O K-Edge, the positively-valued region of $\Delta_{cg}(\boldsymbol{r}, t)$ is localised solely on O. This distribution resembles that of the analogous snapshot in the x-polarised case in fig. 5.10, indicating the prevalence of the A'-symmetric contributions to $\Delta_{cg}(\boldsymbol{r}, t)$. On the other hand, in the 400 *as* snapshot at the N K-Edge, $\Delta_{cg}(\boldsymbol{r}, t)$ shows positively-valued regions in correspondence of both the N and C1 atoms, consistently with the characteristics of the A''-symmetric contributions to $\Delta_{cg}(\boldsymbol{r}, t)$ (shown in the z-polarised case in fig. 5.12) and the dominant role of the $1^cA''$ state's population shown in fig. 5.14. The subsequent time-evolution, described by the 1000 *as* and 2000 *as* snapshots, takes place similarly to the x-polarised and z-polarised cases analysed in the previous sections.

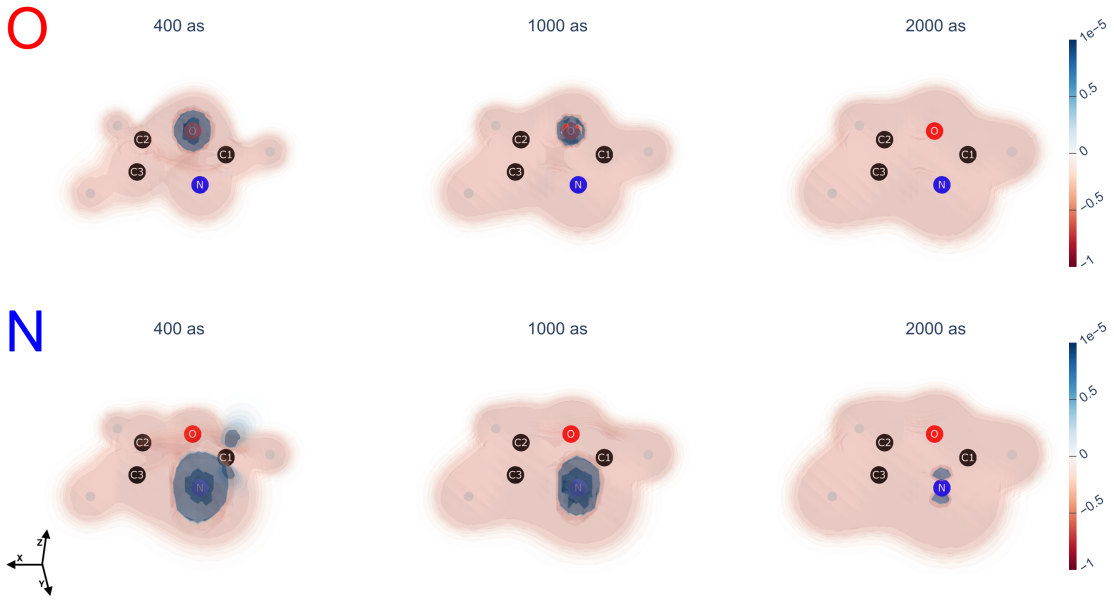

Figure 5.15: *Snapshots of $\Delta_{cg}(\boldsymbol{r}, t)$ relative to the excitation with a pulse linearly polarised at 45 degrees in the σ_{xz} plane The upper panel is relative to the excitation at the O K-Edge, the lower panel to the excitation at the N K-Edge. The orientation of the axes is illustrated in the lower left corner.*

5.3.4 Rxy and Lxy polarisations

The most prominent populations of the core-excited states, excited by means of a right-handed, circularly polarised pulse in the σ_{xy} plane, are shown as dashed curves in fig. 5.16. Only the right-handed case will be discussed here since the results obtained in the left-handed case are exactly the same. Since the pulse polarisation is parallel to σ_{xy} only A'-symmetric states are excited. As can be seen in fig. 5.17,

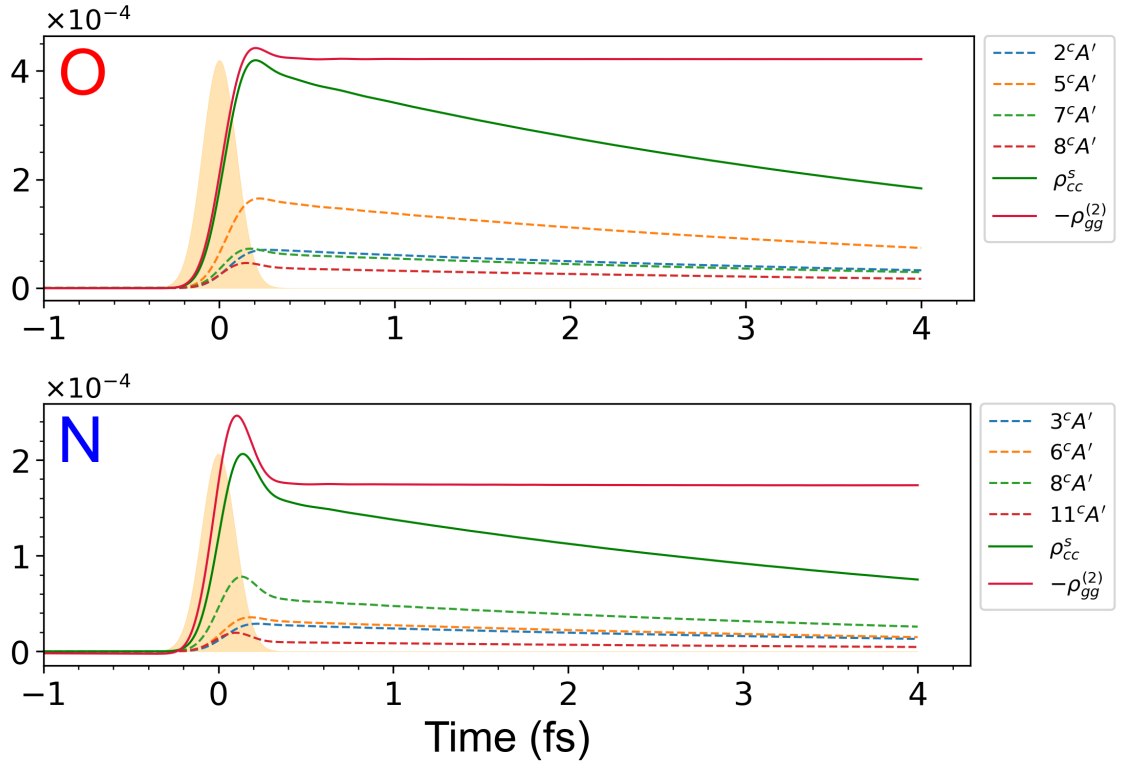

Figure 5.16: *Most prominent populations as a function of time relative to an excitation with a right-handed, circularly polarised pulse in the σ_{xy} plane. The dashed lines indicate the populations of the single core-excited states, the green solid line corresponds to the total population of the core-excited states while the red solid line to the (opposite of) ground state depopulation. The upper panel is relative to the excitation at the O K-Edge, the lower panel to the excitation at the N K-Edge.*

this leads $\Delta_{cg}(\boldsymbol{r}, t)$ to possess similar properties to those relative to the x-polarised case in fig. 5.10. In fact, at 400 *as* the positively-valued region of $\Delta_{cg}(\boldsymbol{r}, t)$ is very localised on the pumped atom, with $\Delta_{cg}(\boldsymbol{r}, t)$ being negatively-valued in the rest of the molecule. Finally, as time progresses through the 1000 *as* and 2000 *as* snapshots, $\Delta_{cg}(\boldsymbol{r}, t)$ behaves very similarly to the other polarisation cases considered so far.

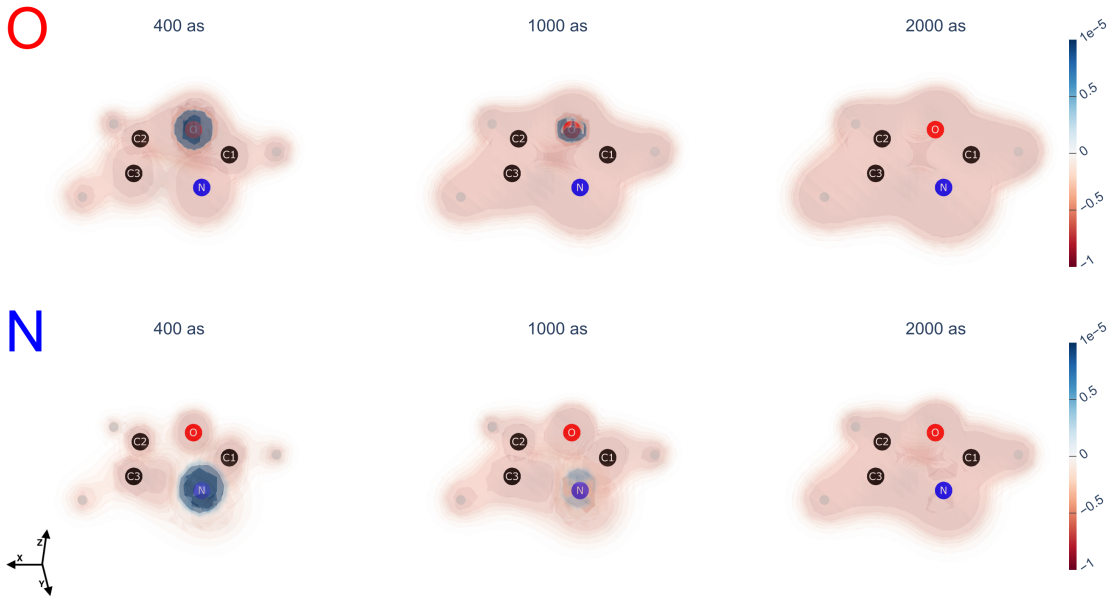

Figure 5.17: *Snapshots of $\Delta_{cg}(\boldsymbol{r}, t)$ relative to the excitation considering a right-handed, circularly polarised pulse in the σ_{xy} plane. The upper panel is relative to the excitation at the O K-Edge, the lower panel to the excitation at the N K-Edge. The orientation of the axes is illustrated in the lower left corner.*

5.4 $\rho_{vg}(\boldsymbol{r}, t)$ component

The first part of each analysis conducted in this section focuses on the WP preparation. As discussed in the xz-polarized case of OCS, the preparation corresponds to the creation of an initial intramolecular electronic redistribution, which grows statically in size while the pulse intensity builds up. As the pulse reaches its peak intensity and begins to fade, the WP motion is released, triggering the electronic migration across the molecule. The first part focuses on the analysis of the time-point marking the end of the WP preparation and the beginning of its motion. This time-point corresponds to the photochemically 'activated' state of the molecule – which is analogous to the 'reagent' time-point proposed by Tremblay *et al.* [128, 129] – whose properties depend on those of the pulse and determine the characteristics of the subsequent electronic dynamics. The analysis of the 'activated' state point is also important for the investigation of the ISRIXS process. In fact, it is at this time-point that, if present, the initial atom-specific electronic localisation induced by ISRIXS should be observed. The second part of the analyses focuses on the electronic migration following the WP preparation, on its dependence on the characteristics of the 'activated' state and on the pulse parameters.

5.4.1 x polarisation

The excitation at the O K-Edge with a pulse polarised along the x-axis prepares the coherences $\rho_{vg}(t)$ shown in the left panel of fig. 5.18. According to the selection rules,

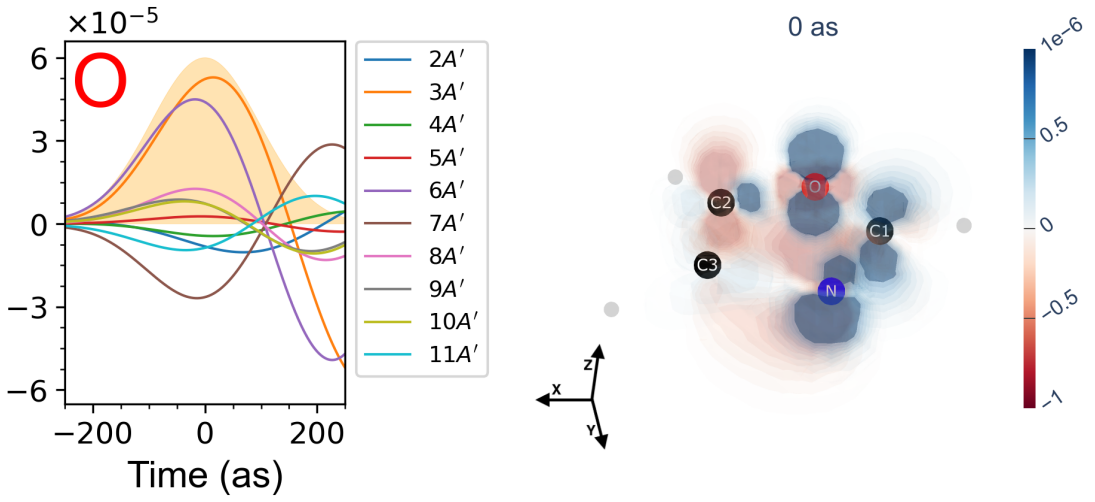

Figure 5.18: *Preparation of* $2\,\mathrm{Re}\{\rho_{vg}(t)\}$ *during the pulse (left) relative to the excitation at the O K-Edge with a pulse linearly polarised along the x-axis. The right panel shows the initial electronic distribution prepared during the excitation.*

only coherences relative to A'-symmetric valence-excited states are excited. In particular, the coherences $3A'$, $6A'$ and $7A'$ provide the most prominent contributions. The preparation of the coherences takes place as the pulse intensity progressively builds up, determining the static growth of $\rho_{vg}(\boldsymbol{r}, t)$ until about 0 *as*. At this point, $\rho_{vg}(\boldsymbol{r}, t)$ presents the spatial distribution displayed in the right panel of fig. 5.18. Here, the positively-valued regions are mainly localised on O, N and C1, with traces also on C2. As the pulse fades, the electronic migration is released following a mech-

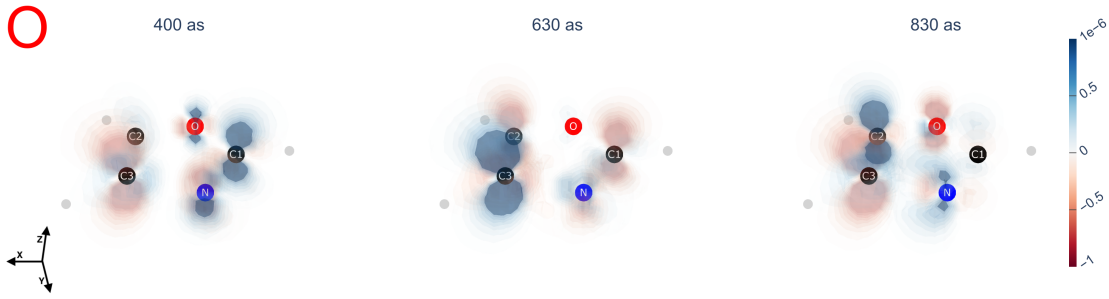

Figure 5.19: *Snapshots of* $\rho_{vg}(\boldsymbol{r}, t)$ *relative to the excitation at the O K-Edge with a pulse linearly polarised along the x-axis. The snapshots illustrate the clockwise electronic migration in the time period comprised between 400 as and 830 as.*

anism seemingly including three 'modes': the oscillation of the regions centred on O and N, a clockwise rotation and an anticlockwise rotation. The rotational motion is observed as positively-valued regions of $\rho_{vg}(\boldsymbol{r}, t)$ accumulate alternatively on C1, C2 or C3. An example of clockwise migration is shown in fig. 5.19, where the positively-valued region on C1 at 400 *as* moves on C3 at 630 *as* and subsequently on C2 at 830

as. The clockwise rotation prevails during the first 1400 as of the time-evolution, during which it is accompanied by the in-phase oscillation of the regions localised on N and O. As the oscillation of these regions becomes progressively out-of-phase, $\rho_{vg}(\boldsymbol{r}, t)$ accumulates on C3 from which it moves alternatively towards C1 and C2 until about 1960 *as*. This suggests a 'competition' between the clockwise and anticlockwise modes, with the latter prevailing until about 2500 *as*. An example of

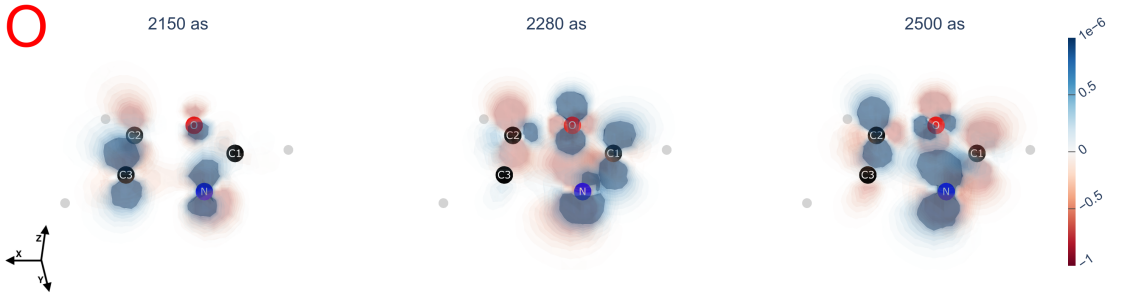

Figure 5.20: *Snapshots of $\rho_{vg}(\boldsymbol{r}, t)$ relative to the excitation at the O K-Edge with a pulse linearly polarised along the x-axis. The snapshots illustrate the anticlockwise rotational motion between 2150 as and 2500 as*

anticlockwise migration is shown in fig. 5.20 where, after having departed from C2 at 1960 *as*, $\rho_{vg}(\boldsymbol{r}, t)$ migrates to C3 at 2150 *as*, to C1 at 2280 *as* and back to C2 at 2500 *as*. After 2500 *as*, the electronic dynamics are characterised by the competition between the clockwise and anticlockwise modes, with positively-valued regions oscillating between C1 and C2. Meanwhile, the regions centred on O and N resume their in-phase oscillation, which is accompanied by a renewed prevalence of the clockwise rotational mode between about 3300 *as* and 3630 *as*. The excitation at the N K-

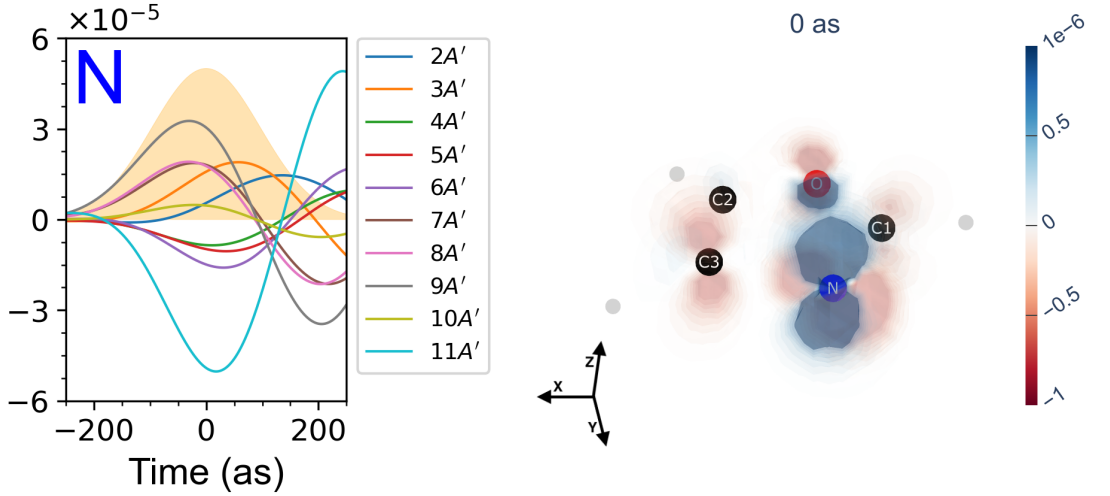

Figure 5.21: *Preparation of $2\,\mathrm{Re}\{\rho_{vg}(t)\}$ during the pulse (left) relative to the excitation at the N K-Edge with a pulse linearly polarised along the x-axis. The right panel shows the initial electronic distribution prepared during the excitation.*

Edge leads to a different coherent population of the valence-excited states compared to the O K-Edge case. In fact, as shown in the left panel of fig. 5.21, the main contributions come from the $11A'$ and $9A'$ valence-excited states. The preparation

of the coherences during the pulse build-up, leads, as shown in the right panel of fig. 5.21, to the initial accumulation of $\rho_{vg}(\boldsymbol{r}, t)$ on N, with some trace being present also on O. This is the starting point of the electronic motion, which is released as

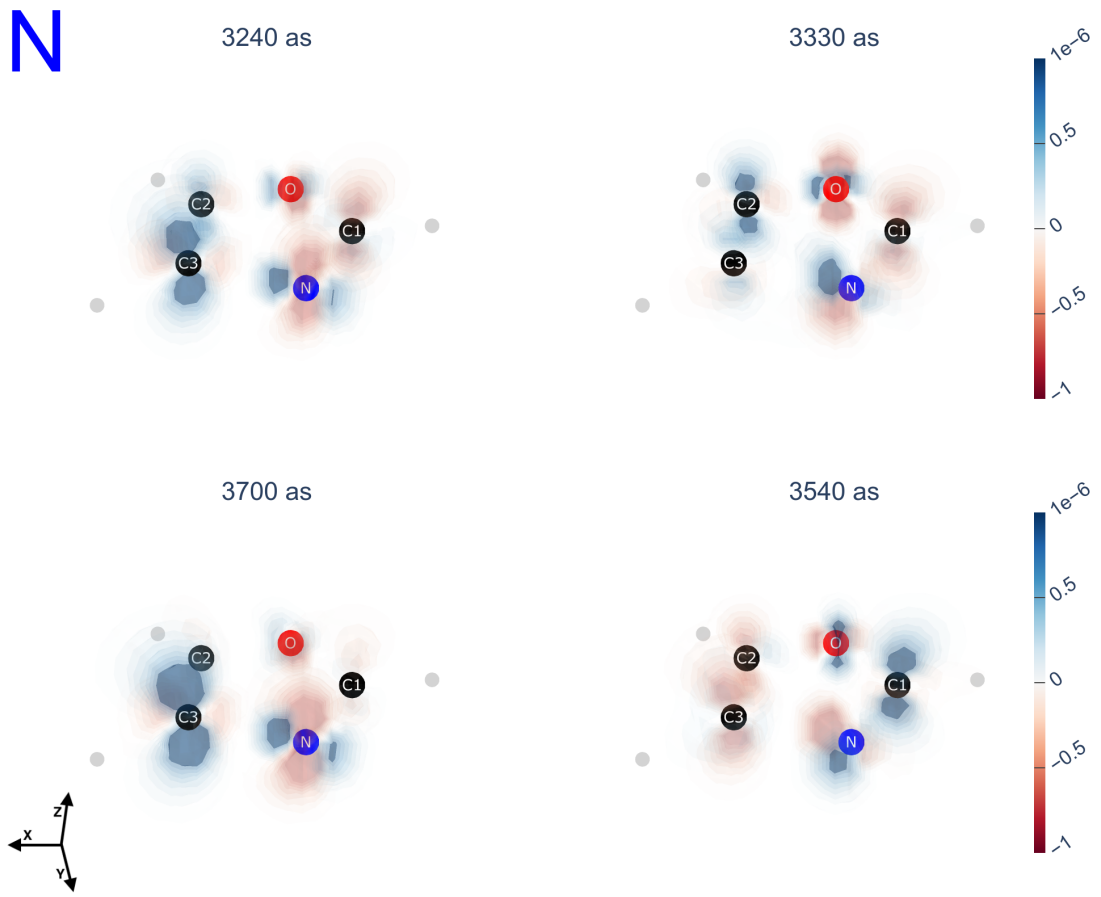

Figure 5.22: *Snapshots of $\rho_{vg}(\boldsymbol{r}, t)$ relative to the excitation at the N K-Edge with a pulse linearly polarised along the x-axis. The snapshots illustrate the clockwise circular electronic migration taking place between about 3240 as and 3700 as.*

the pulse fades. The electronic motion unfolds mostly in terms of the oscillation of the regions on N and O, whose oscillation is out-of-phase during the first 2500 *as* of $\rho_{vg}(\boldsymbol{r}, t)$'s time-evolution. During the same period – besides some faint hints during the first 680 *as* – no circular electronic migration is established across the molecule. On the other hand, the migration manifests as an oscillation between couples of C atoms centred on C3. After 2500 *as*, the oscillation of the regions on N and O gradually becomes in-phase. This coincides with the establishment of a clockwise circular migration starting from about 3000 *as*. This clockwise motion is represented in fig. 5.22, where a positively-valued region departs from C3 at 3240 *as*, quickly reaching C2 at about 3330 *as*, C1 at 3540 *as* and eventually returning to C3 at 3700 *as*.

5.4.2 z polarisation

The coherences $\rho_{vg}(t)$ excited at the O K-Edge by a pulse polarised along the z-axis are shown in the left panel of fig. 5.23. In accordance with the selection rules, only A'-symmetric valence-excited states are coherently populated, with the most prominent contributions being associated with the $3A'$, $6A'$ and $2A'$ valence-excited states. As the pulse grows in intensity, the coherences go through an oscillation

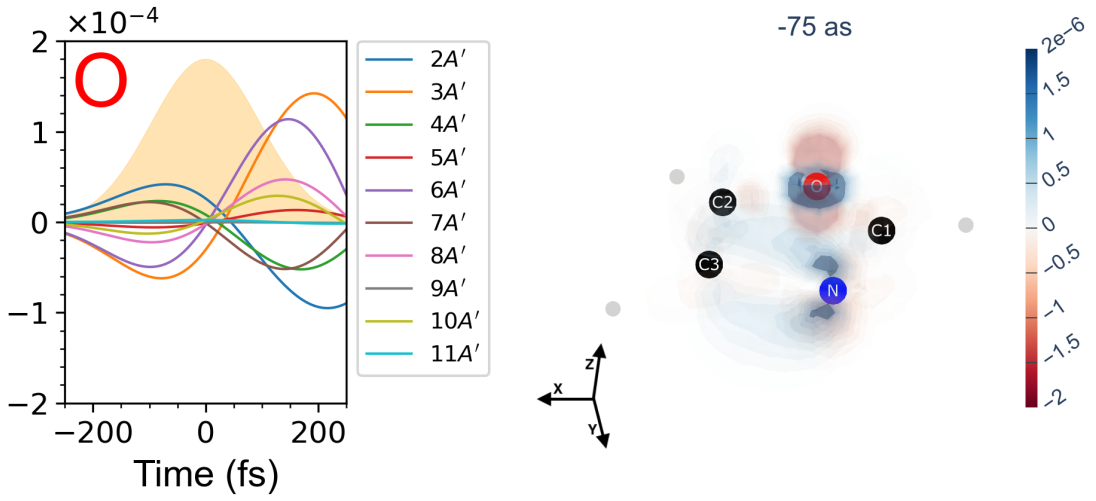

Figure 5.23: *Preparation of* $2\,\mathrm{Re}\{\rho_{vg}(t)\}$ *during the pulse (left) relative to the excitation at the O K-Edge with a pulse linearly polarised along the z-axis. The right panel shows a snapshot of* $\rho_{vg}(\boldsymbol{r}, t)$ *corresponding to the 'early' phase of the coherences preparation, preceding the pulse intensity peak at 0 as.*

centred at about 0 *as*. This leads to an 'early' build-up of the electronic density – until about 25 *as* before the pulse's peak intensity – to the configuration shown in the right panel of fig. 5.23. Here, the excitation appears to be centred mostly on O, with positively-valued regions accumulating both on O and N. The oscillation of the coherences around 0 *as* leads to a change in the electronic distribution within $\rho_{vg}(\boldsymbol{r}, t)$, which at about 120 *as* assumes a configuration similar to that shown in fig. 5.18 for the x-polarised case. From this point, the electronic dynamics are characterised by the relative oscillation of the regions centred on N and O and by the alternation of clockwise and anticlockwise motions. The clockwise rotational motion prevails until about 1560 *as*, manifesting as a circulation of positively-valued regions of $\rho_{vg}(\boldsymbol{r}, t)$ across the C atoms. An example of this is shown in fig. 5.24, where the positively-valued region on C3 at 800 *as* moves in a clockwise direction on C2 at 980 *as*, on C1 at 1140 *as* and returns on C3 at 1300 *as*. As the clockwise migration proceeds, the electronic density shows a tendency to accumulate on C3, which is accompanied by the inversion of the migration to an anticlockwise direction until about 2700 *as*. An example of anticlockwise migration is shown in fig. 5.25, which starts from C1 at 1930 *as*, moving to C2 at 2150 *as*, to C3 at 2285 *as* and back to C1 at 2460 *as*. The snapshot at 2460 *as* shows also a smaller accumulation of electronic density on C2, which preludes the renewed prevalence of the clockwise migration in the rest of the examined dynamics.

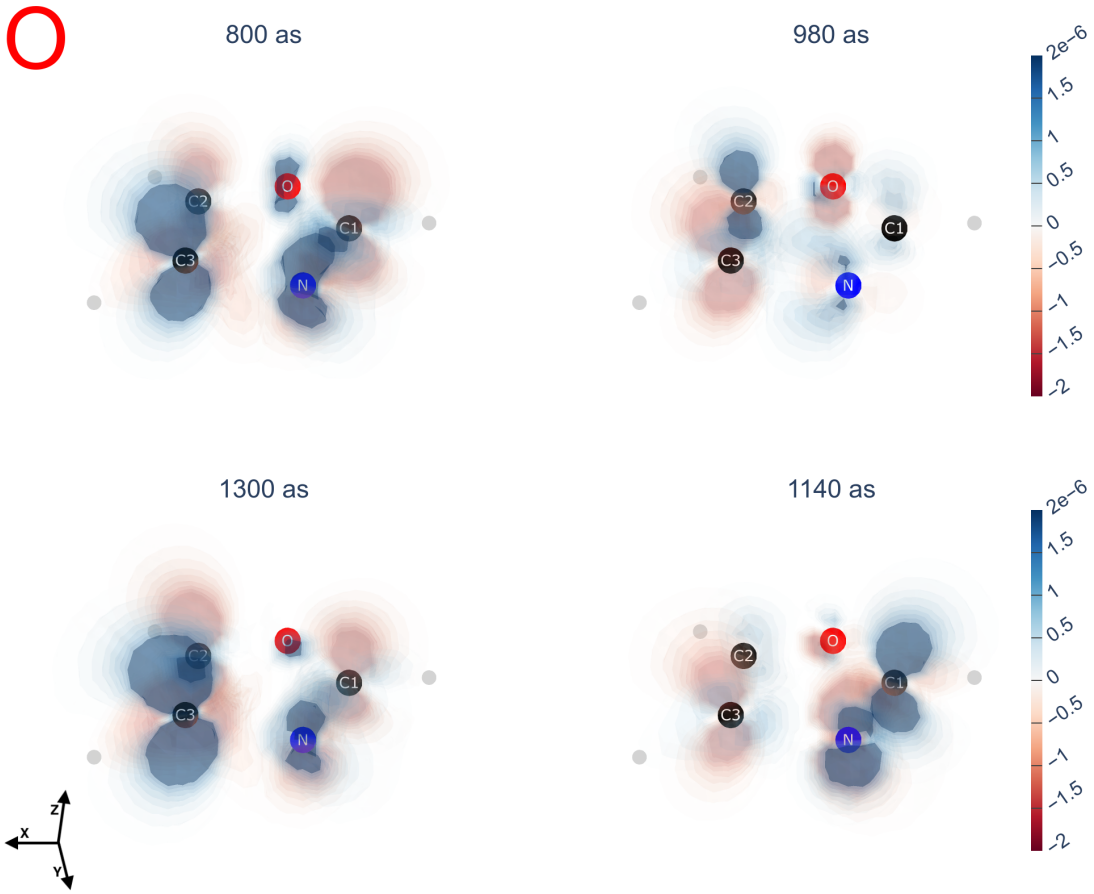

Figure 5.24: *Snapshots of $\rho_{vg}(\boldsymbol{r}, t)$ relative to the excitation at the O K-Edge with a pulse linearly polarised along the z-axis. The snapshots illustrate the clockwise migration of $\rho_{vg}(\boldsymbol{r}, t)$ in the time-interval comprised between 800 as and 1300 as.*

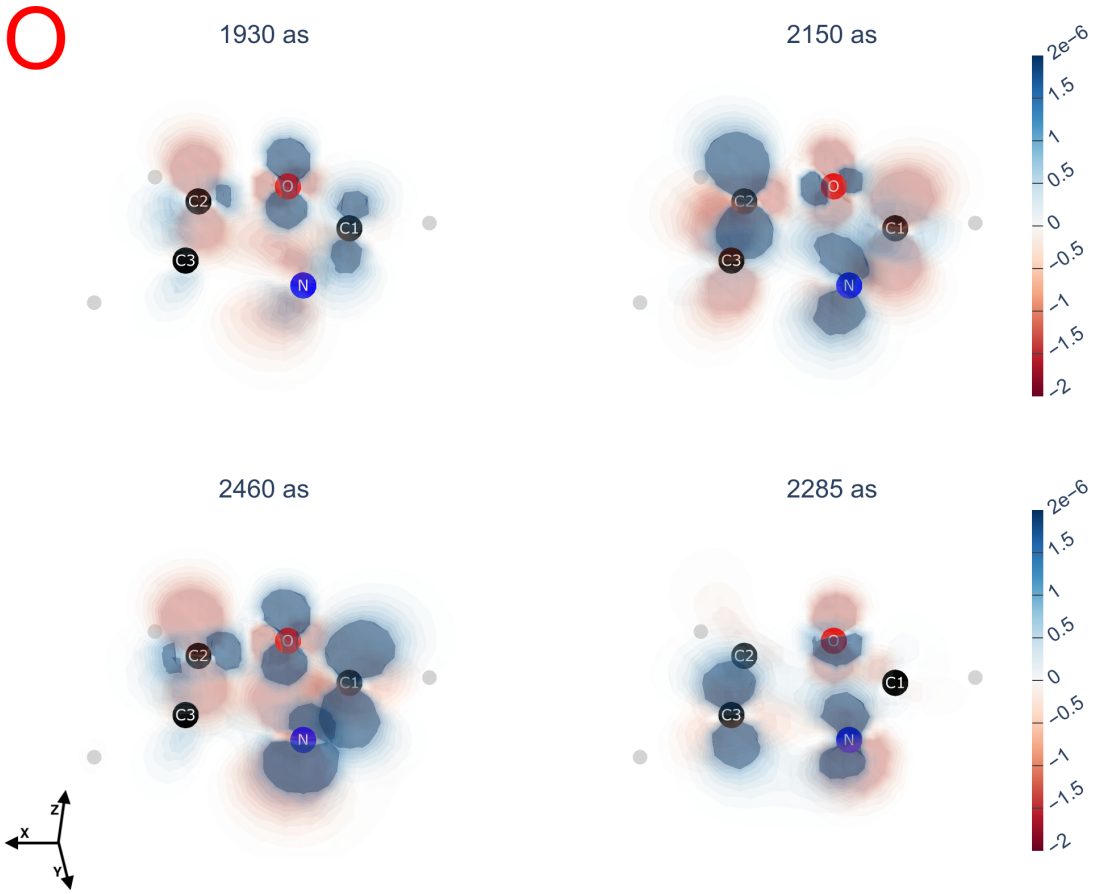

Figure 5.25: *Snapshots of $\rho_{vg}(\boldsymbol{r}, t)$ relative to the excitation at the O K-Edge with a pulse linearly polarised along the z-axis. The snapshots illustrate the anticlockwise migration of $\rho_{vg}(\boldsymbol{r}, t)$ in the time-interval comprised between 1930 as and 2460 as.*

The coherences $\rho_{vg}(t)$ relative to the excitation at the N K-Edge are shown in the left panel of fig. 5.26, where the main contributions come from the $3A'$, $6A'$ and $11A'$ valence-excited states. As for the excitation at the O K-Edge, the coherences

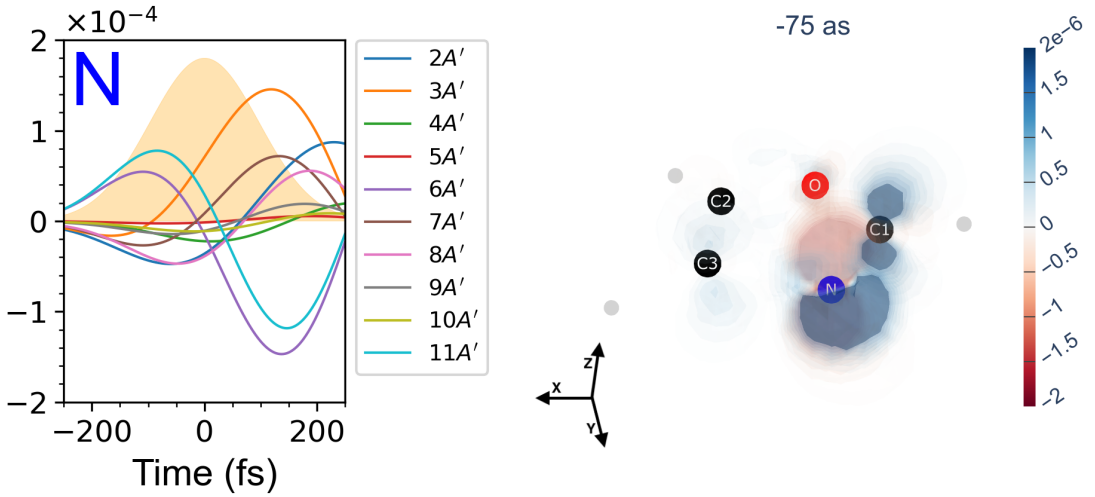

Figure 5.26: *Preparation of* $2\,\mathrm{Re}\{\rho_{vg}(t)\}$ *during the pulse (left) relative to the excitation at the N K-Edge with a pulse linearly polarised along the z-axis. The right panel shows a snapshot of* $\rho_{vg}(\boldsymbol{r}, t)$ *corresponding to the 'early' phase of the coherences preparation, preceding the pulse intensity peak at 0 as.*

go through an oscillation around 0 *as*; the 'early' build-up of the coherences – until about 25 *as* before the pulse peak intensity at 0 *as* – corresponds to an initial accumulation of electronic density mostly on N and C1, as shown in the right panel of fig. 5.26. Following the oscillation around 0 *as*, $\rho_{vg}(\boldsymbol{r}, t)$ builds up until about 150 *as* to the configuration shown in the corresponding snapshot in fig. 5.27. Here, large positively-valued regions localise especially on N and C2, with smaller regions being present also on O and C1. Starting from 150 *as*, the electronic migration unfolds in a clockwise direction, which is accompanied by the oscillation of the regions centred on N and O. The clockwise migration, illustrated in the snapshots in fig. 5.27, continues until about 750 *as*.

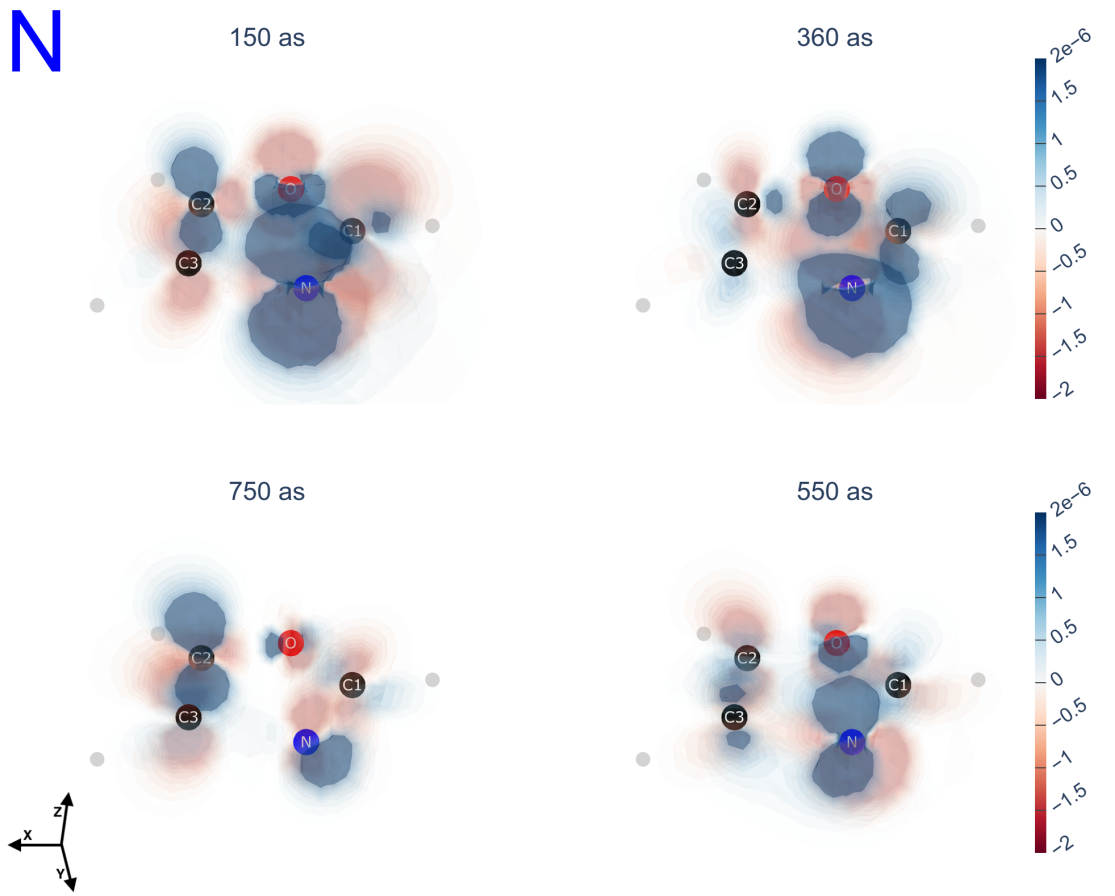

Figure 5.27: *Snapshots of $\rho_{vg}(\boldsymbol{r}, t)$ relative to the excitation at the N K-Edge with a pulse linearly polarised along the z-axis. The snapshots illustrate the clockwise migration in the time-interval comprised between 150 as and 750 as.*

After this moment, until about 2070 *as*, the electronic density starts an oscillation which, as illustrated in the snapshots shown in fig. 5.28, takes place between C3 and the other C atoms. This suggests that a 'competition' is established between the clockwise and anticlockwise 'modes', with neither mode prevailing on the other. Accordingly, the electronic migration does not unfold as a circular motion in the subsequent moments, but rather according to oscillations between pairs of C atoms.

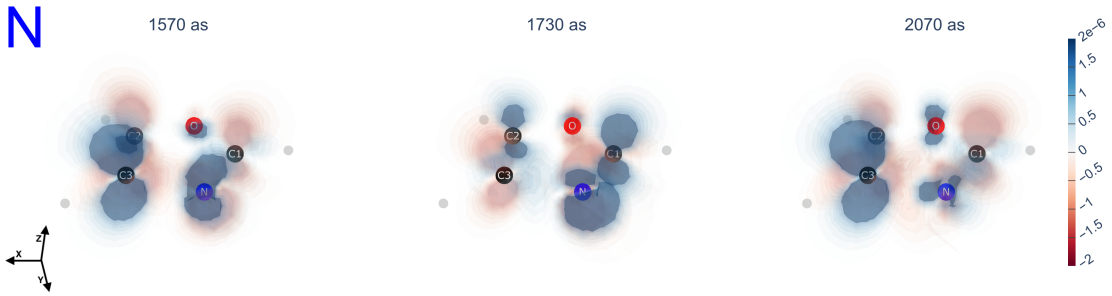

Figure 5.28: *Snapshots of $\rho_{vg}(\boldsymbol{r}, t)$ relative to the excitation at the N K-Edge with a pulse linearly polarised along the z-axis. The snapshots illustrate the oscillation between C3 and the other C atoms in the time interval comprised between 1570 as and 2070 as.*

5.4.3 xz polarisation

The coherences prepared by a pulse polarised at 45 degrees in the σ_{xz} plane and relative to the excitation at the O K-Edge are shown in the left panel of fig. 5.29. In compliance with the selection rules, coherences relative to both A'-symmetric and A''-symmetric valence-excited states are excited. The main contributions come from the $3A'$, $6A'$ and $2A'$ valence-excited states, with the contributions from the A'' valence-excited states being negligible. As in the z-polarised case, the coherences

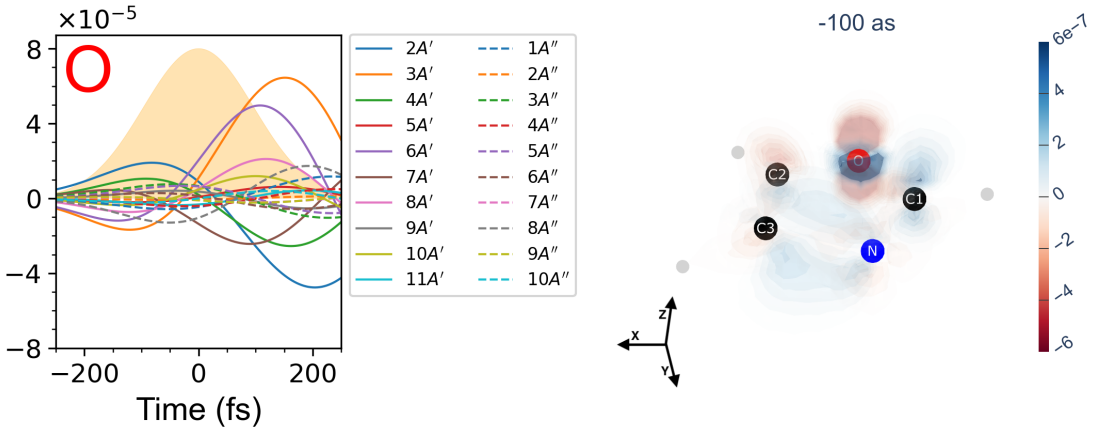

Figure 5.29: *Preparation of* $2\,\mathrm{Re}\{\rho_{vg}(t)\}$ *during the pulse (left) relative to the excitation at the O K-Edge with a pulse linearly polarised at 45 degrees in the* σ_{xz} *plane. The right panel shows a snapshot of* $\rho_{vg}(\boldsymbol{r}, t)$ *corresponding to the initial build-up of the coherences during their preparation, which precedes the pulse peak intensity at 0 as.*

undergo an oscillation centred at about 0 *as*, which determines an initial build-up of $\rho_{vg}(\boldsymbol{r}, t)$ until about 100 *as* before the pulse peak intensity at 0 *as*. As shown in the right panel of fig. 5.29, this initial build-up takes place mainly around O, with a small, positively-valued trace being present also on C1. After undergoing an oscillation across 0 *as*, the configuration of $\rho_{vg}(\boldsymbol{r}, t)$ becomes similar to that shown in fig. 5.18 for the x-polarised case. Owing to the dominant contributions of the A'-symmetric valence-excited states, after the initial oscillation around 0 *as*, the electronic dynamics unfold similarly to the x- and z-polarised cases: the phased and dephased relative oscillation of the regions centred on N and O is accompanied by electronic motion in an alternatively clockwise and anticlockwise direction. Contrary to the O K-Edge case, the excitation at the N K-Edge leads to more prominent contributions from the A''-symmetric states, as can be seen in the left panel of fig. 5.30. Here, in addition to the contributions from the $3A'$, $6A'$, $11A'$ and $2A'$ states, prominent contributions come also from the $1A''$ and $6A''$ states. Similarly to the O K-Edge, the coherences go through an oscillation centred at about 0 *as*. This determines an early build-up of $\rho_{vg}(\boldsymbol{r}, t)$ to the configuration shown in the right panel of fig. 5.30. Here, the excitation is localised especially on regions centred on N and C1. The contribution of the A''-symmetric states is particularly noticeable on N, where $\rho_{vg}(\boldsymbol{r}, t)$ is antisymmetric with respect to σ_{xy}. As the coherences oscillate through 0 *as*, a new configuration of $\rho_{vg}(\boldsymbol{r}, t)$ is reached – with positively-valued regions localised especially on N and C2, with traces also on O – which is the starting point of the electronic dynamics. These develop according to mechanisms similar to those encountered in the previous polarisation cases: the oscillation of the regions

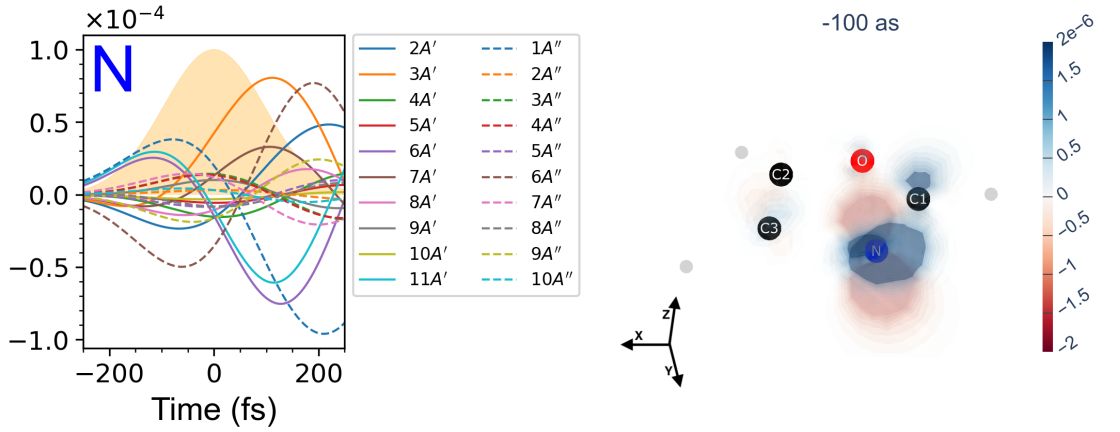

Figure 5.30: *Preparation of* $2\,\mathrm{Re}\{\rho_{vg}(t)\}$ *during the pulse (left) relative to the excitation at the N K-Edge with a pulse linearly polarised at 45 degrees in the* σ_{xz} *plane. The right panel shows a snapshot of* $\rho_{vg}(\boldsymbol{r}, t)$ *relative to the initial build-up of the coherences, preceding the pulse peak intensity at 0 as.*

centred on N and O is accompanied by the alternation of clockwise or anticlockwise electronic circulations, which often 'compete' with each other determining momentary oscillations between couples of C atoms before one of the two 'modes' prevails. An instance of anticlockwise migration is pictorially represented in fig. 5.31. Here,

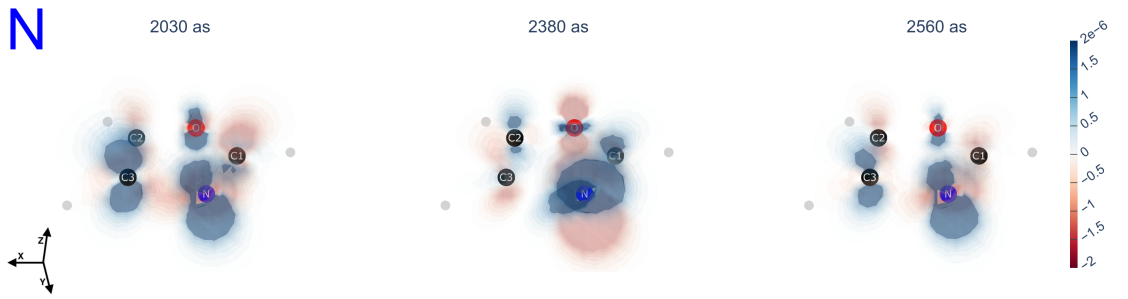

Figure 5.31: *Snapshots of* $\rho_{vg}(\boldsymbol{r}, t)$ *relative to the excitation at the N K-Edge with a pulse linearly polarised at 45 degrees in the* σ_{xz} *plane. The snapshots illustrate the anticlockwise migration in the time-interval comprised between 2030 as and 2560 as.*

the positively-valued region on C3 at 2030 *as* transfers to C1 and then quickly to C2, as shown in the 2380 *as* snapshot. Another quick transfer between C2 and C3 concludes the circular migration, with the electronic density accumulating on C3 at 2560 *as*. An interesting feature of the dynamics is the motion of the electronic density between the two sides of the σ_{xy} plane. This motion manifests as a 'rotation' of the lobes centred on each atom about the x-axis, an example of which can be observed in the evolution of $\rho_{vg}(\boldsymbol{r}, t)$ around N across the snapshots in fig. 5.31.

5.4.4 Rxy polarisation

The coherences $\rho_{vg}(t)$, prepared by a right-handed, circularly polarised pulse in the σ_{xy} plane and relative to the excitation at the O K-Edge, are shown in the left panel of fig. 5.32. Consistently with the selection rules, only coherences relative to

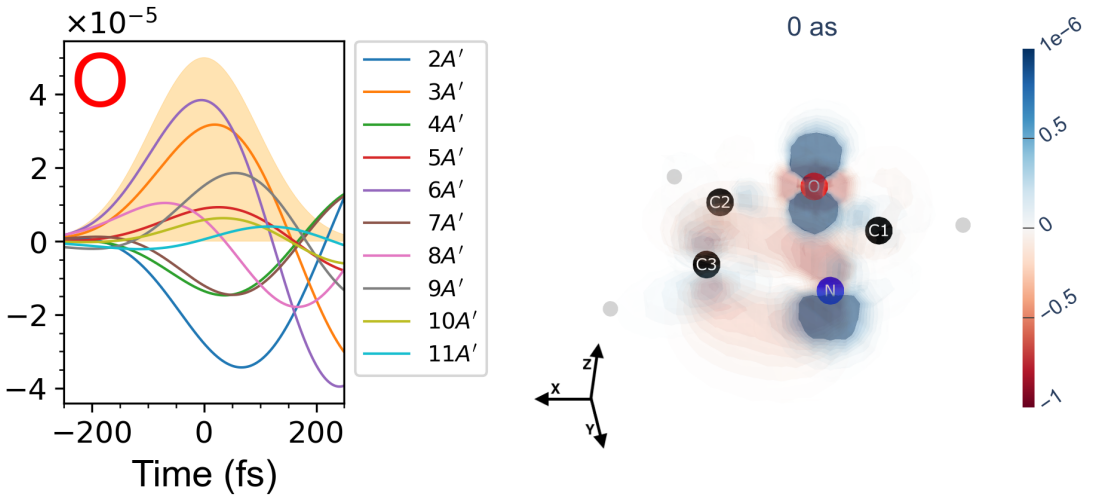

Figure 5.32: *Preparation of* $2\,\mathrm{Re}\{\rho_{vg}(t)\}$ *during the pulse (left) relative to the excitation at the O K-Edge with a right-handed, circularly polarised pulse in the* σ_{xy} *plane. The right panel shows the initial electronic distribution prepared during the excitation.*

A'-symmetric states are excited, with the $3A'$, $6A'$ and $2A'$ valence-excited states providing the main contributions. The WP preparation proceeds until about 0 *as*, determining the initial electronic distribution shown in the right panel of fig. 5.32. Here, the electronic density accumulates particularly on O, with a smaller positively-valued region being present also on N. From the configuration at 0 *as*, the electronic dynamics unfold initially in an anticlockwise direction, as shown in the snapshots in fig. 5.33. Here, a small accumulation on C2 at 140 *as* precedes, as shown in the 250 *as* snapshot, a quick passage through C3 towards N. The anticlockwise migration continues towards C1, where the density accumulates briefly at around 400 *as*, before returning at 550 *as* to a configuration similar to the initial one at 0 *as*. In the following, the electronic dynamics are characterised by the 'competition' between the clockwise and anticlockwise rotational modes; this leads to the periodic alternation of the electronic migration's direction, which is accompanied by the progressive de- and rephasing of the oscillation of the regions centred on N and O.

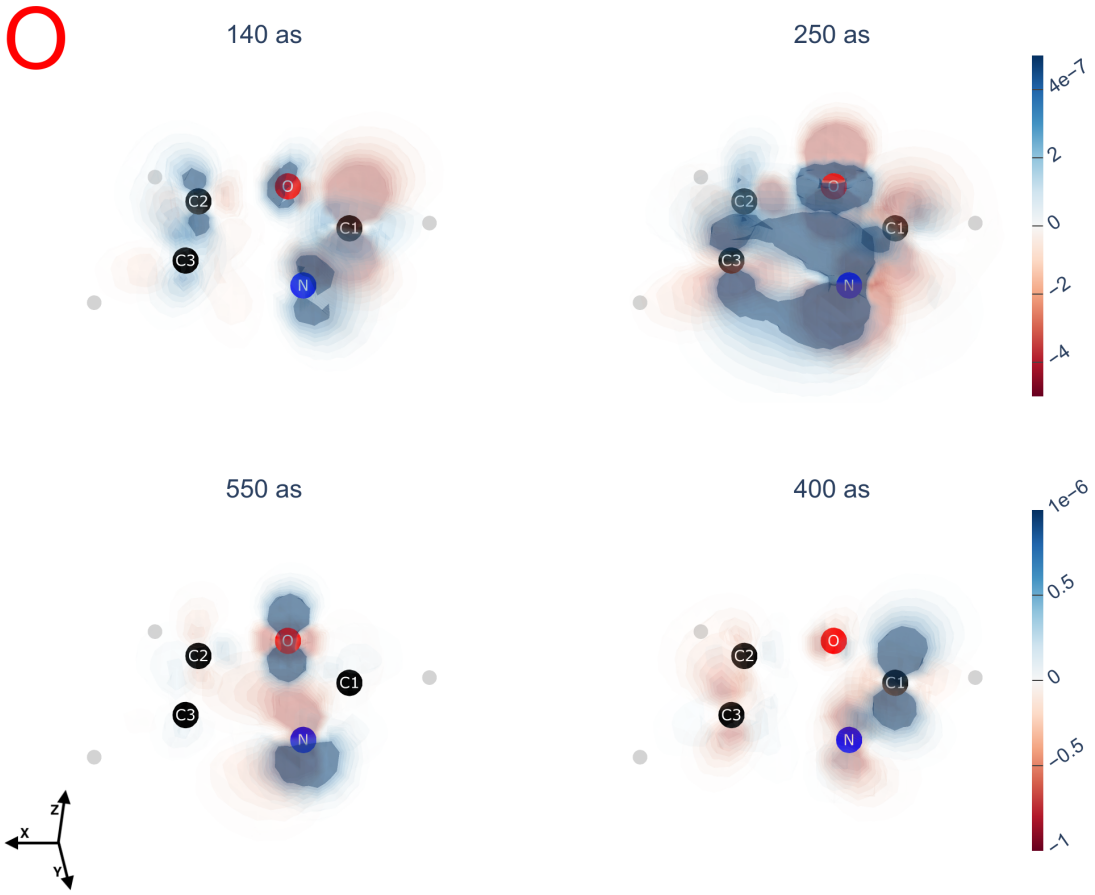

Figure 5.33: *Snapshots of $\rho_{vg}(\boldsymbol{r}, t)$ relative to the excitation at the O K-Edge with a right-handed, circularly polarised pulse in the σ_{xy} plane. The snapshots illustrate the initial, anticlockwise intramolecular electronic migration – started at 0 as – unfolding in the time-interval between 140 as and 550 as.*

The excitation at the N K-Edge is characterised, as shown in the left panel of fig. 5.34, by prominent contributions from the $8A'$, $9A'$, $11A'$, $6A'$ and $7A'$ valence-excited states.

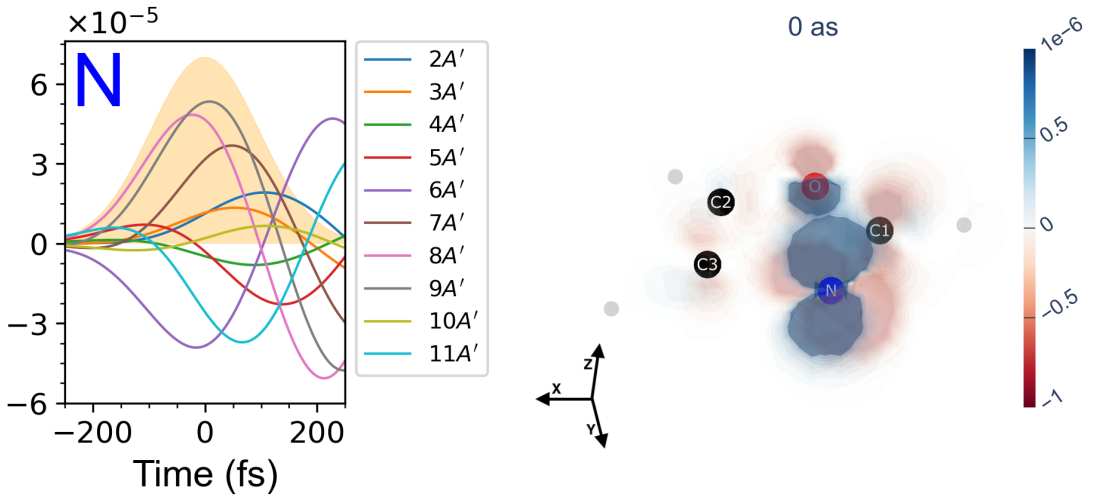

Figure 5.34: *Preparation of* $2\,\mathrm{Re}\{\rho_{vg}(t)\}$ *during the pulse (left) relative to the excitation at the N K-Edge with a right-handed, circularly polarised pulse in the* σ_{xy} *plane. The right panel shows the initial electronic distribution prepared during the excitation.*

The preparation stage corresponds to the static growth of $\rho_{vg}(\boldsymbol{r}, t)$ until about 0 *as* to the configuration shown in the right panel of fig. 5.34. Oppositely to the excitation at the O K-Edge in fig. 5.32, the electronic density accumulates mostly on N, with some traces of positively-valued density being present also on O. The subsequent electronic dynamics proceed initially through an oscillation involving N, C1, O and C2; this leads to the progressive accumulation of electronic density on C2, which has its peak at about 700 *as*. From this point, the electronic dynamics follow the anticlockwise pathway described in the snapshots in fig. 5.35. Here, at 1000 *as*

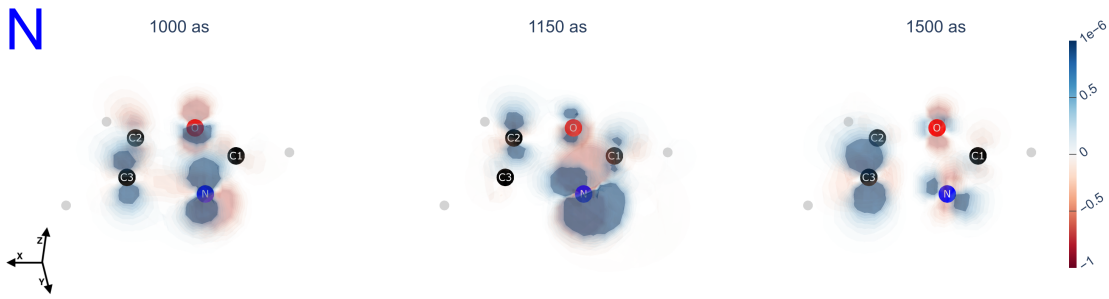

Figure 5.35: *Snapshots of* $\rho_{vg}(\boldsymbol{r}, t)$ *relative to the excitation at the N K-Edge with a right-handed, circularly polarised pulse in the* σ_{xy} *plane. The snapshots illustrate the anti-clockwise intramolecular migration of* $\rho_{vg}(\boldsymbol{r}, t)$ *in the time-interval comprised between 1000 as and 1500 as.*

the electronic density accumulates on C3, before moving across N towards C1 and then rapidly to C2, as shown in the 1150 *as* snapshot. At about 1500 *as* the circular migration reaches C3, where $\rho_{vg}(\boldsymbol{r}, t)$ presents a bigger dimension compared to the 1000 *as* snapshot. The tendency of the electronic density to accumulate on C3 is

the main feature of the subsequent dynamics, which continue in an anticlockwise direction until about 2000 as. At this point, an oscillation centred on C3 starts, with an alternative accumulation of the electronic density on C2 and (mostly) on C1. As in the other cases, the circular migration of the electronic density is accompanied by the relative oscillation of the regions centred on O and N.

5.4.5 Lxy polarisation

The coherences $\rho_{vg}(t)$, prepared by a left-handed, circularly polarised pulse in the σ_{xy} plane and relative to the excitation at the O K-Edge, are shown in the left panel of fig. 5.36. The components associated to the $3A'$, $6A'$, $8A'$ and $2A'$ valence-excited

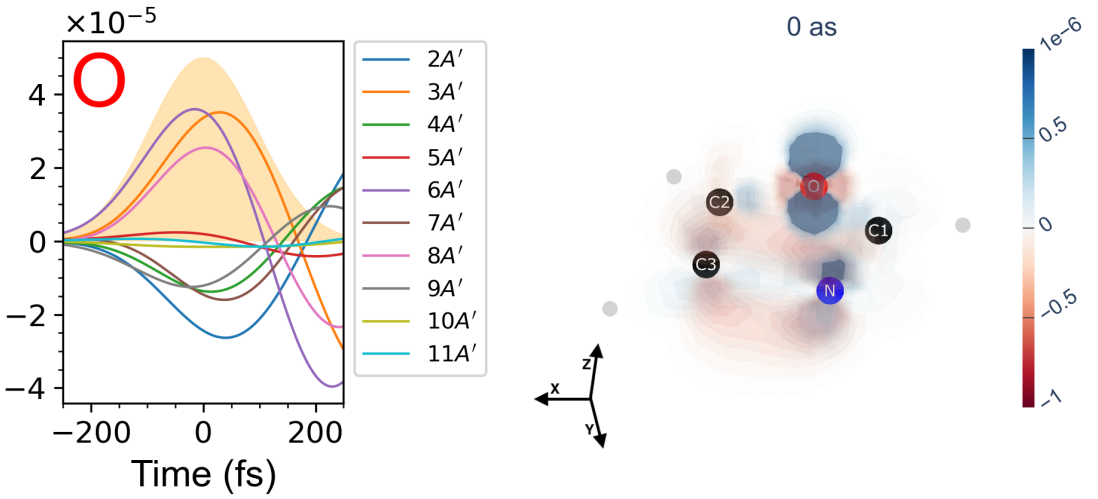

Figure 5.36: *Preparation of* $2\,\mathrm{Re}\{\rho_{vg}(t)\}$ *during the pulse (left) relative to the excitation at the O K-Edge with a left-handed, circularly polarised pulse in the* σ_{xy} *plane. The right panel shows the initial electronic distribution prepared during the excitation.*

states provide the most prominent contributions to $\rho_{vg}(\boldsymbol{r}, t)$. The preparation of the coherences proceeds until about 0 *as* and is associated with the progressive initial accumulation of the electronic density on O. This is shown in the right panel of fig. 5.36, where the biggest positively-valued region is centred on O, with a little trace being present also on N. From this point, the electronic dynamics proceed first as an oscillation along an arc comprised between O and C3. This is illustrated in fig. 5.37 where, following a fast transfer between O and N via C1, the migration proceeds towards C3 via N – which exchange the electronic density as shown in the 250 *as* snapshot – subsequently inverting its direction and migrating back towards O through C1, where the electronic density transiently accumulates at 400 *as*. After reaching O, the electronic migration inverts again its direction, with the electronic density migrating back to C3, where the density accumulates at around 650 *as*. From this point, the electronic migration unfolds according to oscillations between couples of C atoms and the relative oscillation of the regions centred on N and O, without the prevalence of a clockwise or anticlockwise rotation. In particular, the competition between the rotational 'modes' leads to the transient accumulation of density mostly on one single C atom – changing with time as the migration proceeds – which acts as the centre of the oscillation with respect to the other C atoms.

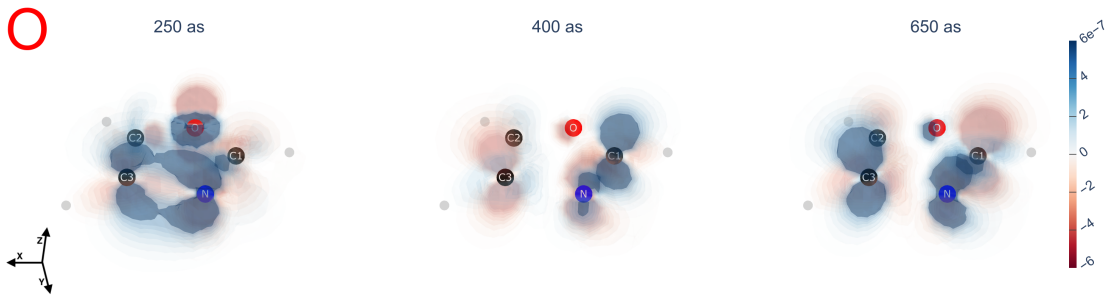

Figure 5.37: *Snapshots of $\rho_{vg}(\boldsymbol{r}, t)$ relative to the excitation at the O K-Edge with a left-handed, circularly polarised pulse in the σ_{xy} plane. The snapshots illustrate the oscillation along the 'arc' including between O, C1, N and C3, unfolding in the time-interval between 250 as and 650 as.*

The preparation of the WP considering the excitation at the N K-Edge is described in fig. 5.38. The left panel shows how the main contributions are associated with the $8A'$, $6A'$ and $9A'$ valence-excited states. As shown in the right panel of

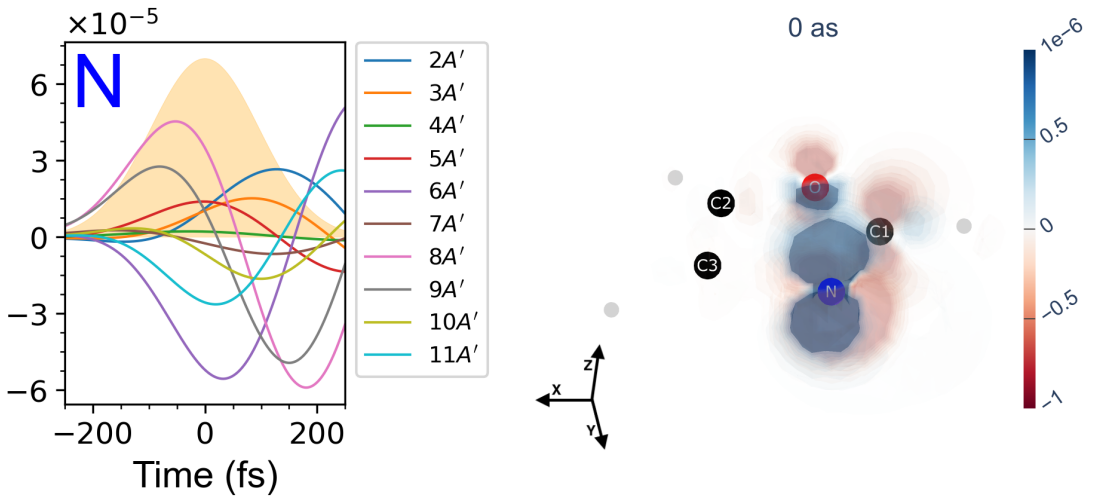

Figure 5.38: *Preparation of $2\,\mathrm{Re}\{\rho_{vg}(t)\}$ during the pulse (left) relative to the excitation at the N K-Edge with a left-handed, circularly polarised pulse in the σ_{xy} plane. The right panel shows the initial electronic distribution prepared during the excitation.*

fig. 5.38, the preparation of the coherences corresponds to the initial accumulation of the electronic density on N (with some traces also on O) until about 0 *as*. As the pulse fades, the electronic density departs from N, proceeding until about 700 *as* in a clockwise direction. The first step of this migration – represented in the 130 *as* in fig. 5.39 – corresponds to the motion towards C2, where the density arrives after a fast passage through C3. The motion proceeds towards C1 at about 340 *as*, C3 at about 570 *as* eventually reaching C2 at about 690 *as*. From this moment, the density shows a tendency to accumulate especially on C3 and oscillate alternatively with respect to C2 and (especially) to C1. As in all the other cases, the migration across the C atoms is accompanied by the relative oscillation of the regions centred on N and O.

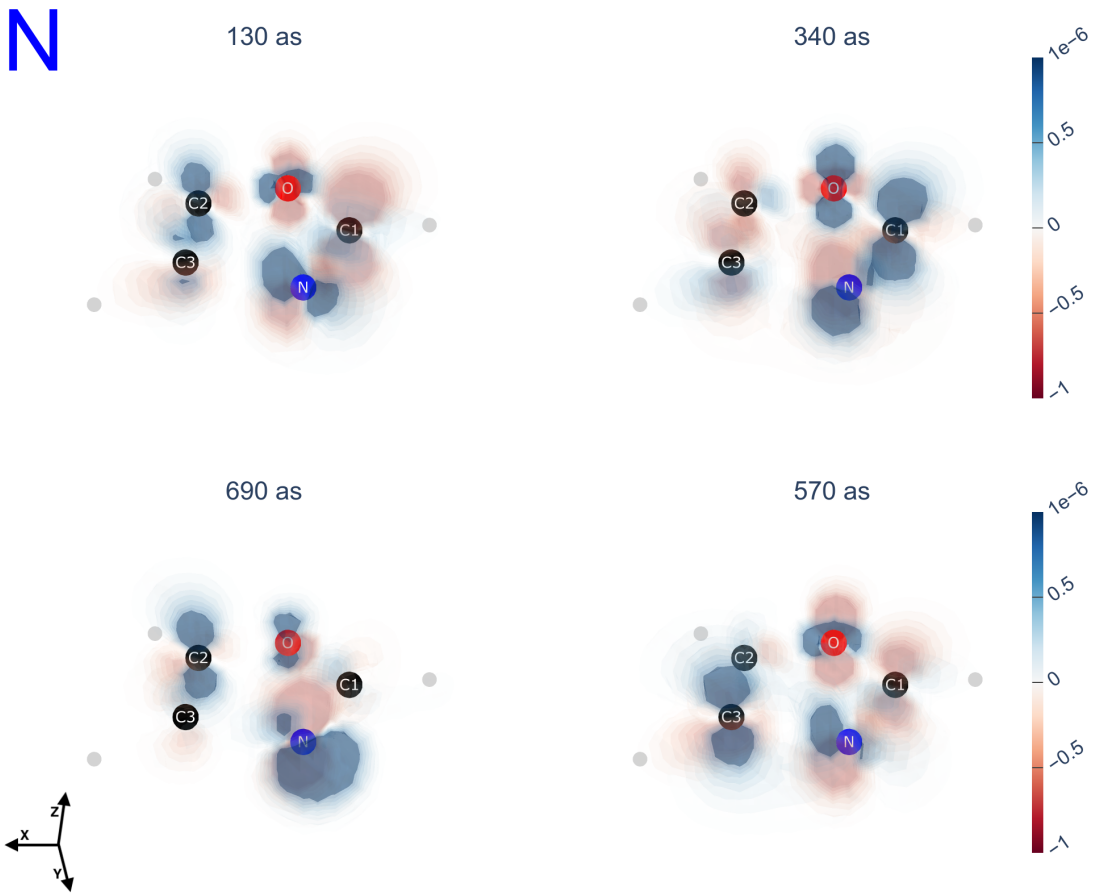

Figure 5.39: *Snapshots of $\rho_{vg}(\boldsymbol{r}, t)$ relative to the excitation at the N K-Edge with a left-handed, circularly polarised pulse in the σ_{xy} plane. The snapshots illustrate the clockwise electronic migration unfolding in the first 690 as, which started from N at 0 as.*

5.5 $\rho_{cc'}(\boldsymbol{r}, t)$ component

5.5.1 x polarisation

The most prominent coherences, excited with a pulse linearly polarised along the x-axis, are shown in fig. 5.40. At the O K-Edge, the dominant coherences are those

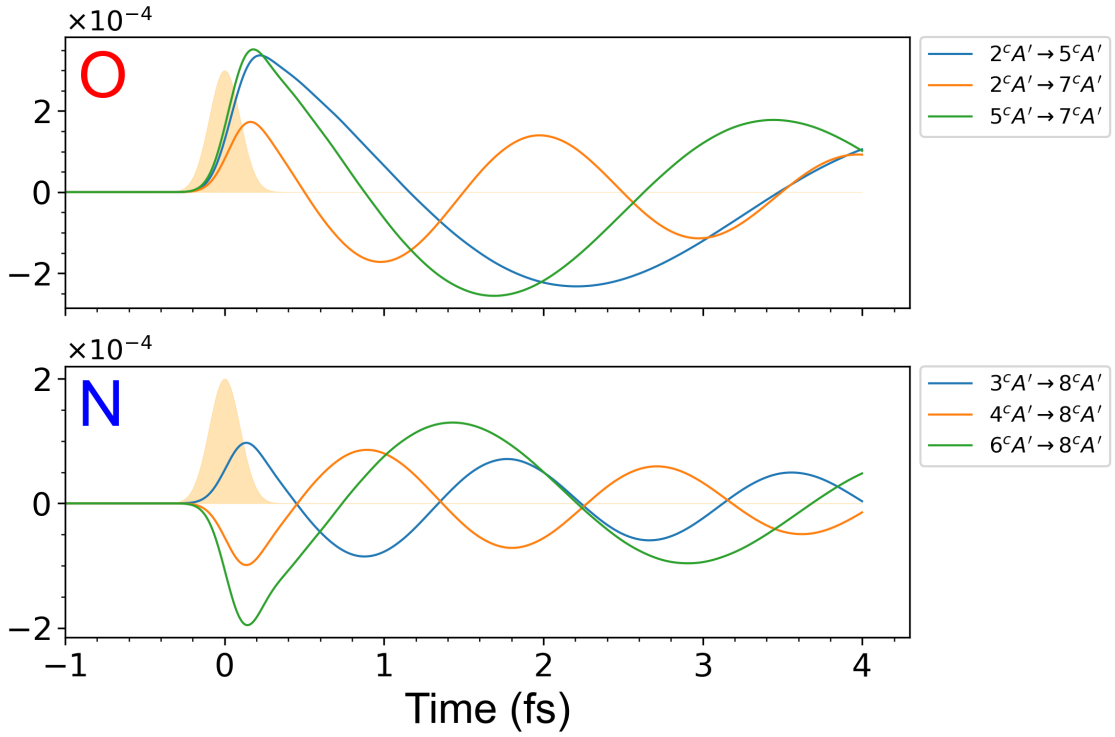

Figure 5.40: *Time-evolution of* $2\,\mathrm{Re}\{\rho_{cc'}(t)\}$ *relative to the excitation with a pulse linearly polarised along the x-axis. The upper panel is relative to the excitation at the O K-Edge, the lower panel to the excitation at the N K-Edge. The yellow Gaussian corresponds to the time-domain pulse envelope, whose intensity scale is not shown.*

relative to the $2^cA' \rightarrow 5^cA'$ and $5^cA' \rightarrow 7^cA'$ transitions, with the $2^cA' \rightarrow 7^cA'$ coherence playing a smaller role. The corresponding time-evolution of $\rho_{cc'}(\boldsymbol{r}, t)$ is described in the snapshots shown in the upper panel of fig. 5.41; here, only the density distribution in the σ_{xy} plane is shown, owing to the symmetric distribution with respect to the same plane. The 200 *as* snapshot in fig. 5.41 is relative to the end of the $\rho_{cc'}(t)$ preparation, which roughly corresponds to the peak of the coherences' linear growth in fig. 5.40. A complex distribution of positively-valued and negatively-valued regions spreads over all the atoms, with a concentration of negatively-valued density localising in particular in the region between C3 and N. Given the domination of the $2^cA' \rightarrow 5^cA'$ and $5^cA' \rightarrow 7^cA'$ coherences, the time-evolution of $\rho_{cc'}(\boldsymbol{r}, t)$ corresponds to the oscillation of the configuration found at 200 *as*. As time progresses, the $\rho_{cc'}(\boldsymbol{r}, t)$ progressively 'fades' reflecting the exponential decay of the coherences. In addition to this general trend, the 1000 *as* and 3000 *as* snapshots show examples relative to particular moments in the interference pattern of the coherences in the upper panel of fig. 5.40. For example, the 1000 *as* snapshot corresponds to an instant where the amplitude of the $2^cA' \rightarrow 7^cA'$ coherence is bigger than the other coherences. This allows to see the structure of the $2^cA' \rightarrow 7^cA'$

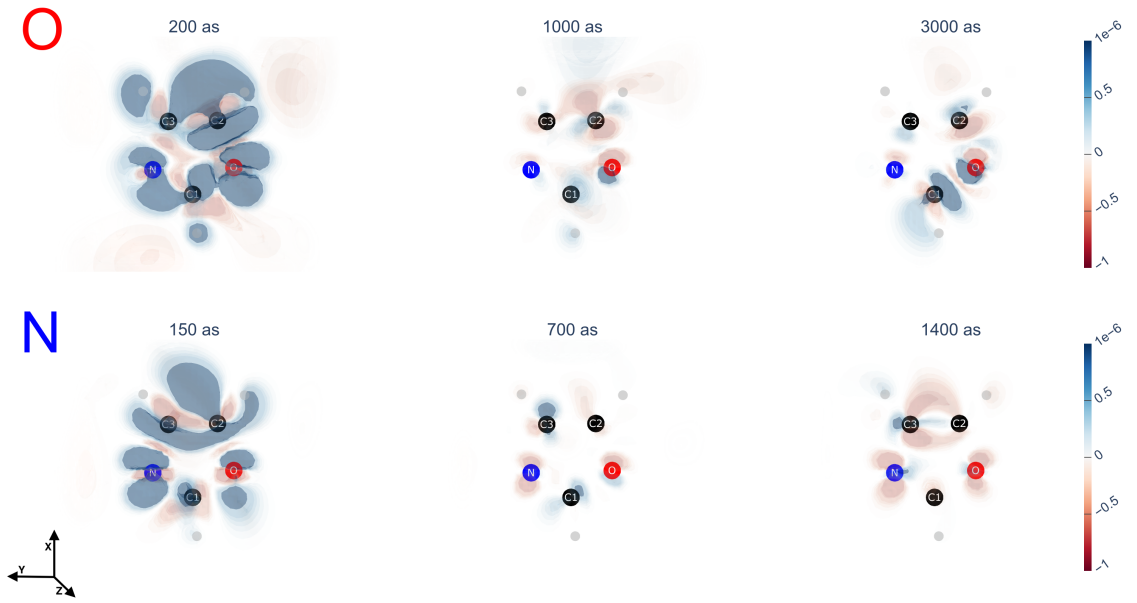

Figure 5.41: *Snapshots of $\rho_{cc'}(\boldsymbol{r},t)$ relative to the excitation with a linearly polarised pulse along the x-axis. The upper panel is relative to the excitation at the O K-Edge, the lower panel to the excitation at the N K-Edge. The orientation of the axes is illustrated in the lower left corner.*

contribution to $\rho_{cc'}(\boldsymbol{r},t)$ which, as seen in the upper panel of fig. 5.41, concerns mainly the region including C2, O and C1. Similar characteristics are found in the 3000 *as* snapshot, which corresponds to an instant where all the involved coherences interfere with the same amplitude. Compared to the 1000 *as* snapshot, positively-valued regions form in particular between C1 and O and in the region above C2, where a negatively-valued region at 1000 *as* is replaced by a small positively-valued region. Considering the excitation at the N K-Edge, the most prominent coherences are shown in the lower panel of fig. 5.40. All the coherences are relative to transitions involving the $8^cA'$ core-excited state, with the amplitude of the $6^cA' \rightarrow 8^cA'$ coherence being the biggest. Accordingly, the preparation stage is dominated by the $6^cA' \rightarrow 8^cA'$ coherence, culminating into the distribution of $\rho_{cc'}(\boldsymbol{r},t)$ shown in the 150 *as* snapshot in the lower panel of fig. 5.41. At this point, the density is distributed across the whole molecule, with a slight polarisation towards the region around N, C3 and C2. Similarly to the 200 *as* snapshot at the O K-Edge, a complex distribution of negatively- and positively-valued regions is present. The time-evolution of $\rho_{cc'}(\boldsymbol{r},t)$ is strongly influenced by the $6^cA' \rightarrow 8^cA'$ component, with the contributions corresponding to the other coherences emerging only at some particular moments. One of these moments is captured in the 700 *as* snapshot, which corresponds to a point in the time-evolution at which the $6^cA' \rightarrow 8^cA'$ coherence equals zero. Here, the distribution of $\rho_{cc'}(\boldsymbol{r},t)$ shows positively-valued regions localised predominantly around C1 and C3, with a relatively pronounced negatively-valued region located on N. On the other hand, the 1400 *as* snapshot corresponds to an instant at which only the $6^cA' \rightarrow 8^cA'$ coherence is non-zero. This allows to appreciate the characteristics of the associated transition density, whose distribution includes negatively-valued regions localised on O, N and extending over C2 and C3.

5.5.2 z polarisation

The time-evolution of the main coherences $\rho_{cc'}(t)$, excited by a pulse linearly polarised along the z-axis, is shown in fig. 5.42. Consistently with the related pop-

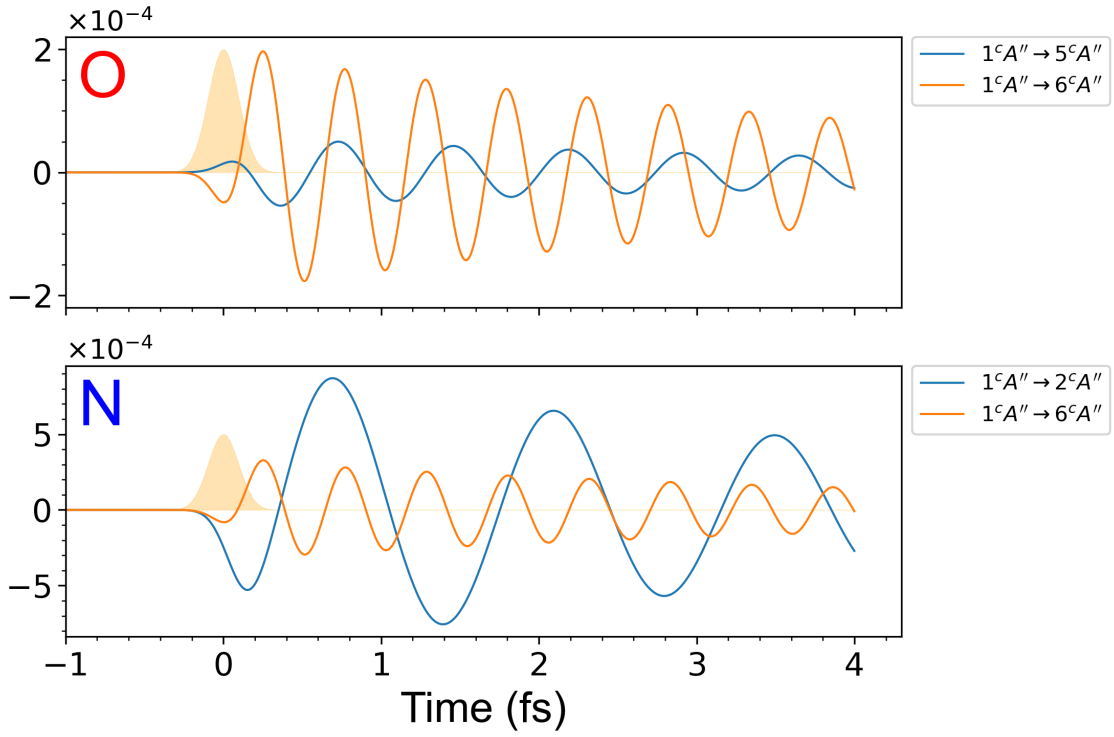

Figure 5.42: *Time-evolution of* $2\,\mathrm{Re}\{\rho_{cc'}(t)\}$ *corresponding to the excitation with a pulse linearly polarised along the z-axis. The upper panel is relative to the excitation at the O K-Edge, the lower panel to the excitation at the N K-Edge. The yellow Gaussian corresponds to the time-domain pulse envelope, whose intensity scale is not shown.*

ulations shown in fig. 5.13, both at the O K-Edge and N K-Edge, the dominant contributions involve the $1^cA''$ core-excited state. At the O K-Edge, the dominant coherence corresponds to the $1^cA'' \rightarrow 6^cA''$ transition, which interferes with the coherence relative to the $1^cA'' \rightarrow 5^cA''$ transition. The corresponding transition densities (shown in fig. 5.43) are symmetric with respect to the σ_{xy} plane, consistently with the fact that the two states involved in the transition belong to the same irreducible representation. The $1^cA'' \rightarrow 5^cA''$ transition density spreads mostly over C2 and C3, with a (positively-valued) region being present also on O. On the other hand, the $1^cA'' \rightarrow 6^cA''$ transition density involves mostly O and C1, with positively-valued traces on N and C2 and negatively-valued traces on C3. Some exemplary snapshots of the time-evolution of $\rho_{cc'}(\boldsymbol{r}, t)$, relative to the excitation at the O K-Edge, are shown in the upper panel of fig. 5.44. At 300 *as* the $1^cA'' \rightarrow 5^cA''$ and $1^cA'' \rightarrow 6^cA''$ coherences have opposite signs (vide fig. 5.42) with the amplitude of the former smaller than that of the latter. This corresponds to the density distribution shown in fig. 5.44, with positively-valued regions on C1 and C2 and a negatively-valued region on O. At 380 *as* the amplitudes of the $1^cA'' \rightarrow 6^cA''$ and $1^cA'' \rightarrow 5^cA''$ coherences are comparable, which allows the emergence of the contribution from the $1^cA'' \rightarrow 5^cA''$ component. Correspondingly, especially on C2 and C3, $\rho_{cc'}(\boldsymbol{r}, t)$ assumes a distribution similar to the (opposite of) the $1^cA'' \rightarrow 5^cA''$

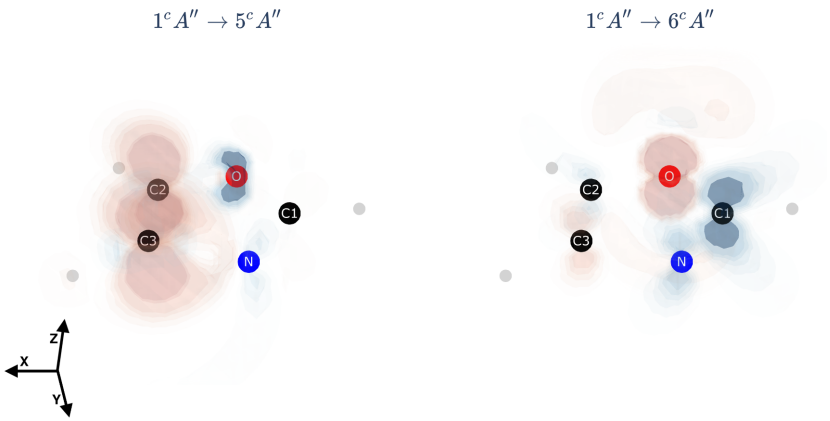

Figure 5.43: *Transition densities $\rho_{cc'}(\boldsymbol{r})$ associated to the $1^cA'' \rightarrow 5^cA''$ transition (left) and to the $1^cA'' \rightarrow 6^cA''$ transition (right), relative to the calculation at the O K-Edge. Blue is positive, red is negative. The orientation of the axes is illustrated in the lower left corner.*

transition density in fig. 5.43. At 700 *as* the $1^cA'' \rightarrow 6^cA''$ and the $1^cA'' \rightarrow 5^cA''$ coherences combine with the same signs, determining (in the corresponding snapshot in fig. 5.44) the formation of negatively-valued regions on C2, C3 and O and of positively-valued regions on C1 and N. Considering the excitation at the N K-

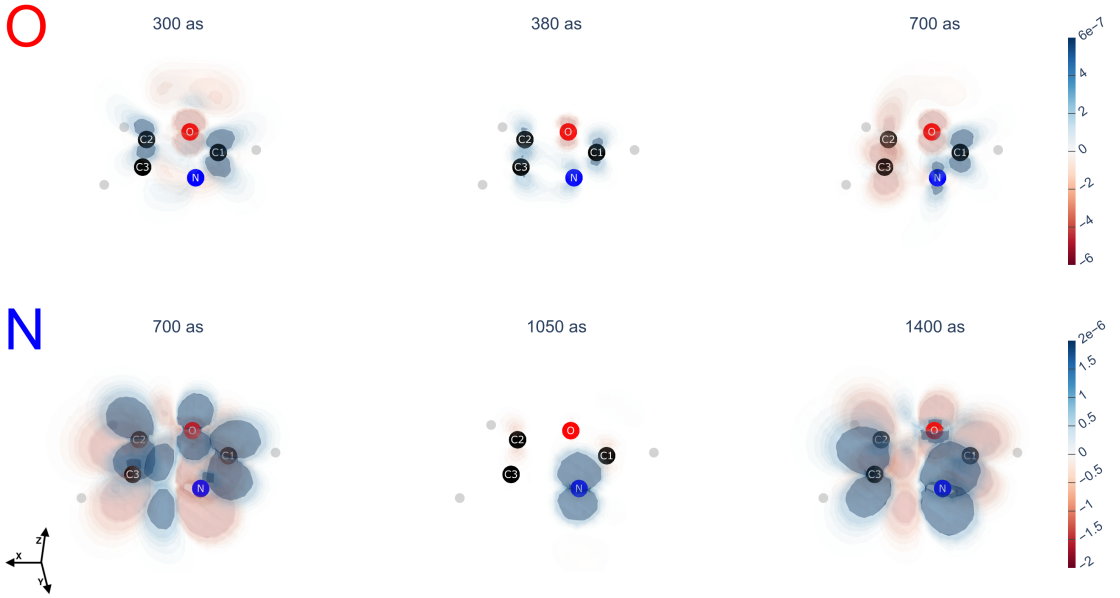

Figure 5.44: *Snapshots of $\rho_{cc'}(\boldsymbol{r},t)$ relative to the excitation with a linearly polarised pulse along the z-axis. The upper panel is relative to the excitation at the O K-Edge, the lower panel to the excitation at the N K-Edge. The orientation of the axes is illustrated in the lower left corner.*

Edge, the domination of the $1^cA'' \rightarrow 2^cA''$ coherence (shown in the lower panel of fig. 5.42), translates in the oscillation of $\rho_{cc'}(\boldsymbol{r},t)$ between the distributions at 700 *as* and 1400 *as* snapshots in the lower panel of fig. 5.44. Here, together with the lobes centred on the atoms, the oscillation involves especially the interatomic region between C3 and N, with smaller contributions from the interatomic regions between O and C3 and between O and C2. The 1050 *as* snapshot corresponds to a moment

where the $1^cA'' \rightarrow 2^cA''$ coherence goes through zero. This allows the contribution from the $1^cA'' \rightarrow 6^cA''$ component to transiently emerge, which determines a brief localisation of $\rho_{cc'}(\boldsymbol{r}, t)$ on N.

5.5.3 xz polarisation

The time-evolution of the $\rho_{cc'}(t)$ coherences, excited by a pulse linearly polarised at 45 degrees in the σ_{xz} plane, is shown in fig. 5.45. At the O K-Edge, the dominant co-

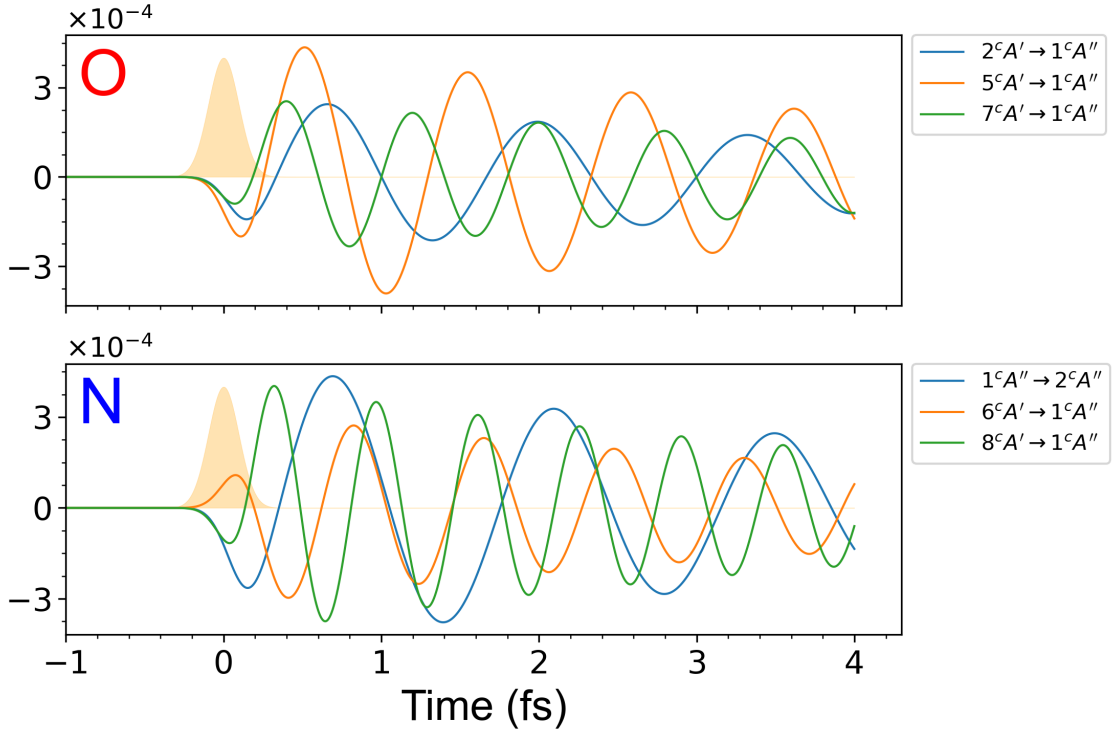

Figure 5.45: *Time-evolution of* $2\,\mathrm{Re}\{\rho_{cc'}(t)\}$ *relative to the excitation with a pulse linearly polarised at 45 degrees in the* σ_{xz} *plane. The upper panel is relative to the excitation at the O K-Edge, the lower panel to the excitation at the N K-Edge. The yellow Gaussian represents the time-domain pulse envelope, whose intensity scale is not shown.*

herences correspond to transitions between A'-symmetric and A''-symmetric states, with the $5^cA' \rightarrow 1^cA''$ coherence showing the biggest amplitude. Owing to the different symmetry of the core-excited states involved, the corresponding transition densities are asymmetric with respect to the σ_{xy} plane. As shown in the snapshots in fig. 5.46, this characteristic allows for a migrative motion of $\rho_{cc'}(\boldsymbol{r}, t)$ between the two sides of σ_{xy}. At 500 *as* the asymmetric distribution of the positively-valued regions between the two sides of σ_{xy} is evident on all the atoms. In particular, at C1 the positively-valued region is larger above σ_{xy}, with the opposite happening on C2 and N. The time-evolution of $\rho_{cc'}(\boldsymbol{r}, t)$ shown in the 900 *as* and 1480 *as* snapshots corresponds to the oscillation of positively- and negatively-valued regions between the two sides of σ_{xy}. Since the density is asymmetric with respect to σ_{xy}, this oscillatory motion produces a time-dependent asymmetric distribution of $\rho_{cc'}(\boldsymbol{r}, t)$ between the two sides of σ_{xy}, i.e. an electronic migration of $\rho_{cc'}(\boldsymbol{r}, t)$ across the σ_{xy} plane. The clearest evidence of this migration can be observed on C1, where at 900 *as* a portion of positively-valued density accumulates below σ_{xy}, subsequently

migrating above the plane as shown in the 1480 *as* snapshot. At the N K-Edge,

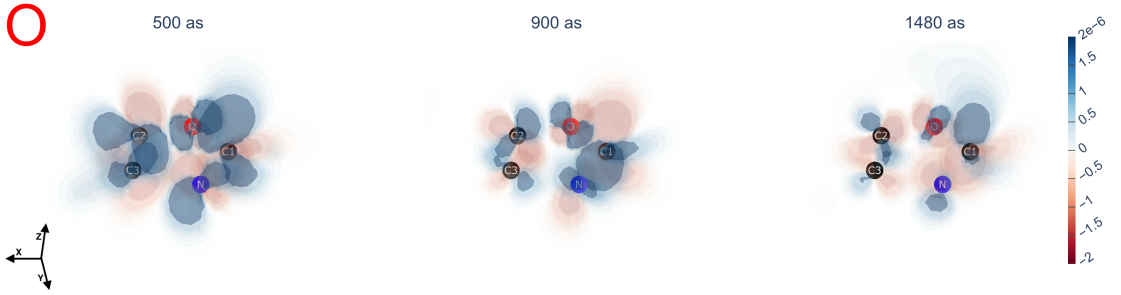

Figure 5.46: *Snapshots of $\rho_{cc'}(\boldsymbol{r},t)$ relative to the excitation at the O K-Edge with a pulse linearly polarised at 45 degrees in the σ_{xz} plane. The orientation of the axes is illustrated in the lower left corner.*

coherences relative to transitions between states of both the same symmetry (i.e. A'') and different symmetry play a prominent role, as it is shown in the lower panel of fig. 5.45. This entails that $\rho_{cc'}(\boldsymbol{r},t)$ is built from transition densities which are both symmetric (i.e. when the excitation involves states of the same symmetry) and asymmetric with respect to the σ_{xy} plane. The similar amplitude of the coherences in fig. 5.45, together with the higher number of 'asymmetric' coherences, leads the time-evolution of $\rho_{cc'}(\boldsymbol{r},t)$ to be similar to the O K-Edge case: the oscillation of the density entails its migration between the two sides of the σ_{xy} plane. This can be

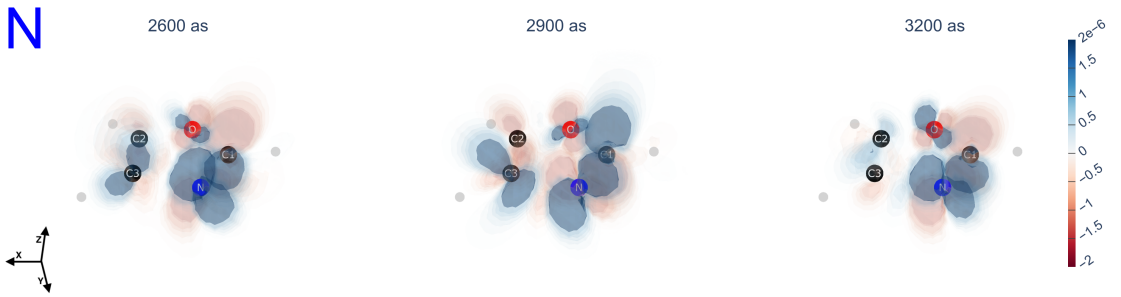

Figure 5.47: *Snapshots of $\rho_{cc'}(\boldsymbol{r},t)$ relative to the excitation at the N K-Edge with a pulse linearly polarised at 45 degrees in the σ_{xz} plane. The orientation of the axes is illustrated in the lower left corner.*

seen in the exemplary snapshots collected in fig. 5.47. The oscillation of the lobes on C3 and N leads to a small difference of the distribution of $\rho_{cc'}(\boldsymbol{r},t)$ between the two sides of σ_{xy}. As at the O K-Edge, the migration of $\rho_{cc'}(\boldsymbol{r},t)$ across σ_{xy} is particularly evident at C1. Here, at 2600 *as* a positively-valued region is localised below σ_{xy}, which migrates above σ_{xy} at 2900 *as* and eventually returns below σ_{xy} at 3200 *as*.

5.5.4 Rxy and Lxy polarisations

The time-evolution of the coherences $\rho_{cc'}(t)$, relative to the excitation at the O K-Edge with a right- and left-handed circularly polarised pulse, is shown in fig. 5.48. While the most prominent coherences are the same for both polarisations, differences

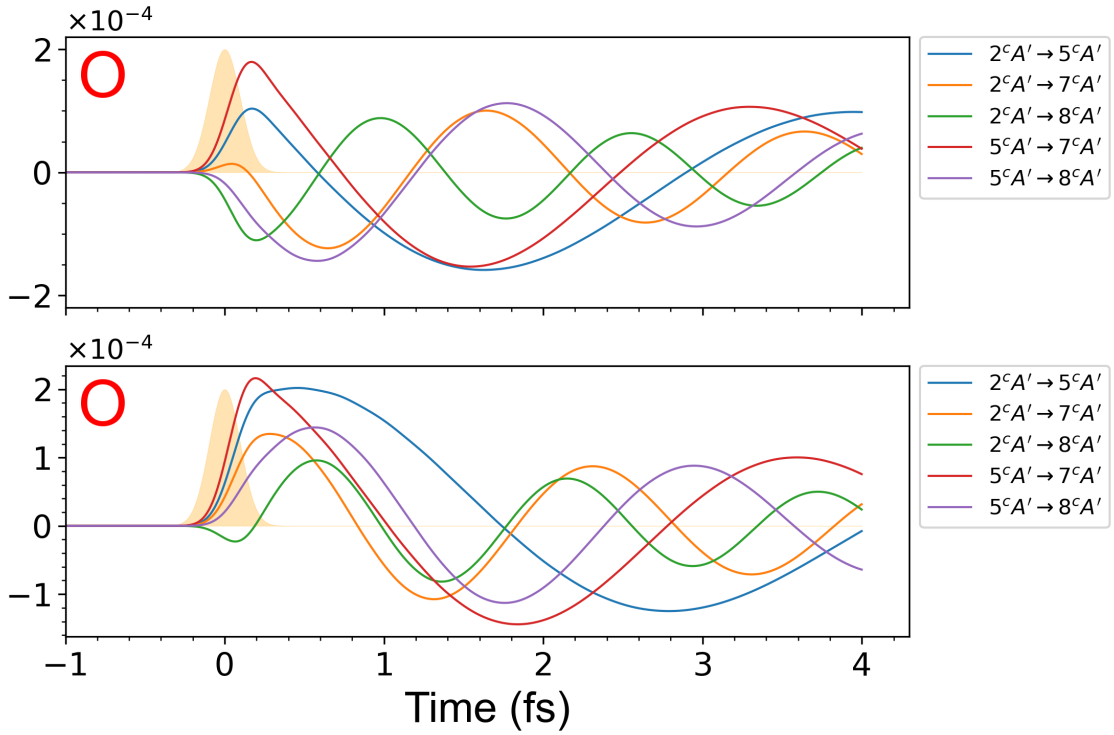

Figure 5.48: *Time-evolution of* $2\,\mathrm{Re}\{\rho_{cc'}(t)\}$ *relative to the excitation at the O K-Edge with a Rxy-polarised (upper panel) and Lxy-polarised (lower panel) pulse in the* σ_{xy} *plane. The yellow Gaussian represents the time-domain pulse envelope, whose intensity scale is not shown.*

between the two cases emerge already in the preparation stage. In fact, the comparison between the two panels in the time interval between 0 *as* and 200 *as*, shows how the initial phases of the $\rho_{cc'}(t)$ coherences differ. This leads to different interference patterns over time, which are directly reflected in the properties of $\rho_{cc'}(\boldsymbol{r}, t)$. Snapshots of $\rho_{cc'}(\boldsymbol{r}, t)$'s time-evolution are shown in fig. 5.49, where the lower and upper panels correspond to the excitation with a right-handed and left-handed circularly polarised pulse, respectively. Consistently with the A'-symmetry of the states involved, $\rho_{cc'}(\boldsymbol{r}, t)$ is symmetric with respect to the σ_{xy} plane. The preparation of $\rho_{cc'}(\boldsymbol{r}, t)$ culminates at about 180 *as*, at which its distribution over the σ_{xy} plane results similar between the Rxy- and Lxy-polarised cases. In particular, it can be seen that $\rho_{cc'}(\boldsymbol{r}, t)$ distributes over the whole molecule, showing a 'gap' between C3 and N. The differences imposed during the preparation of the coherences become more evident in the subsequent time-evolution. In fact, $\rho_{cc'}(\boldsymbol{r}, t)$ shows different properties in the exemplary snapshots at 700 *as* and 1800 *as*, corresponding to the differences in the interference of the coherences shown in fig. 5.48. At 700 *as*, the distribution of $\rho_{cc'}(\boldsymbol{r}, t)$ is more localised on C2 and O in the Rxy-polarised case (upper panel), while it spreads also on C3 and C1 in the Lxy-polarised case. Similarly, at 1800 *as* differences emerge in the distributions of $\rho_{cc'}(\boldsymbol{r}, t)$ especially in the

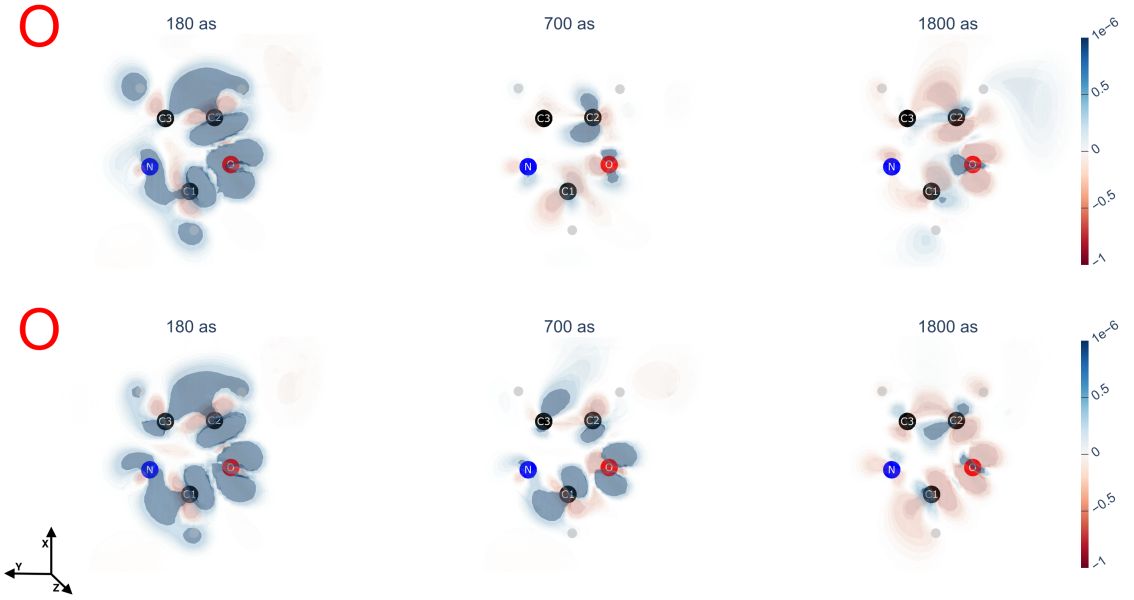

Figure 5.49: *Snapshots of $\rho_{cc'}(\boldsymbol{r},t)$ relative to the excitation at the O K-Edge with a right-handed (upper panel) and left-handed (lower panel), circularly polarised pulse in the σ_{xy} plane. Since $\rho_{cc'}(\boldsymbol{r},t)$ is symmetric with respect to σ_{xy}, its distribution in the σ_{xy} plane (as indicated by the axes orientation in the lower left corner).*

region including C1, O and C2. The time-evolution of the coherences $\rho_{cc'}(t)$, relative to the excitation at the N K-Edge with a right- and left-handed circularly polarised pulse, is shown in fig. 5.50. Compared to the excitation at the O K-Edge, a smaller number of coherences is excited, with the main differences between the Rxy- and Lxy-polarised cases residing in the initial phase of the coherences associated with the $3^cA' \rightarrow 8^cA'$ and $6^cA' \rightarrow 8^cA'$ transitions. The preparation of $\rho_{cc'}(\boldsymbol{r},t)$ terminates at about 150 *as*, with a distribution of the density which is similar in the Rxy- and Lxy-polarised cases, as shown in the 150 *as* snapshot in fig. 5.51. Compared to the 180 *as* snapshots in fig. 5.49, a slight polarisation towards N can be noticed in fig. 5.51 which counteracts the slight polarisation towards O found in fig. 5.49. The subsequent time-evolution of $\rho_{cc'}(\boldsymbol{r},t)$ prosecutes in slightly different ways in the Rxy- and Lxy-polarised cases, consistently with the differences in the interference patterns of the respective coherences. For example, in the snapshots of $\rho_{cc'}(\boldsymbol{r},t)$ at 1000 *as*, differences emerge in the distributions of the positively-valued regions at C3 and C1. Similarly, slight differences emerge also at 1600 *as*, where the positively- and negatively-valued regions of $\rho_{cc'}(\boldsymbol{r},t)$ show slightly different distributions around N, C3 and C1.

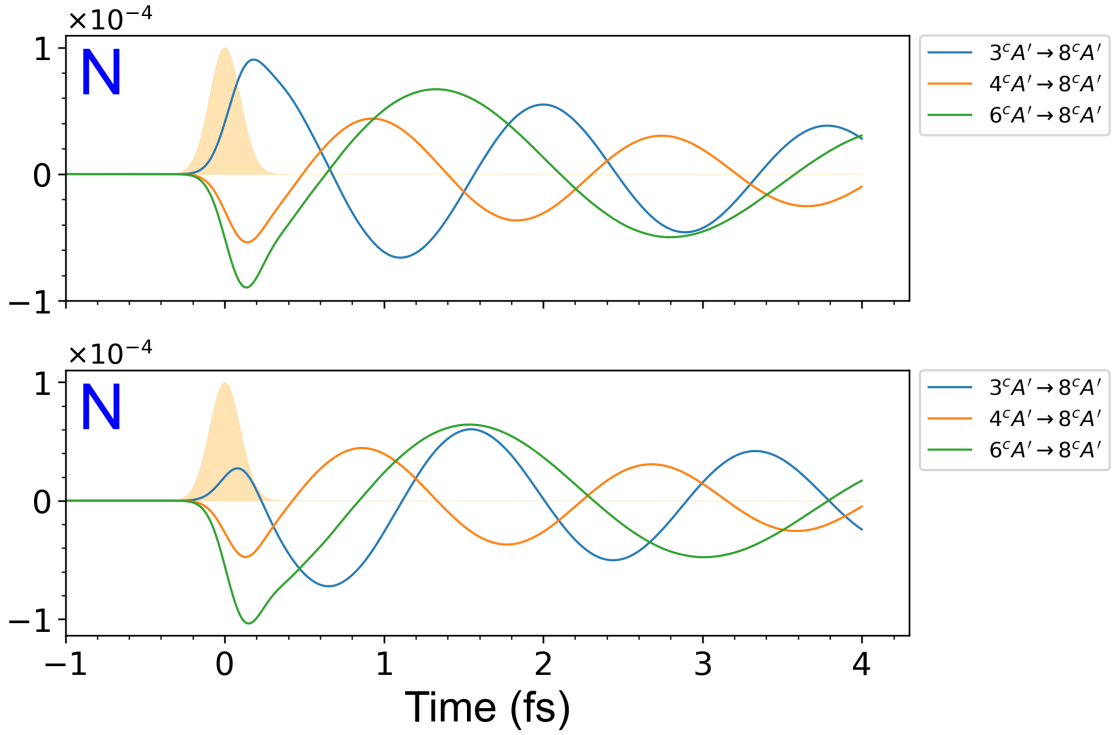

Figure 5.50: *Time-evolution of* $2\,\mathrm{Re}\{\rho_{cc'}(t)\}$ *relative to the excitation at the N K-Edge with a Rxy-polarised (upper panel) and Lxy-polarised (lower panel) pulse in the* σ_{xy} *plane. The yellow Gaussian corresponds to the time-domain pulse envelope, whose intensity scale is not shown.*

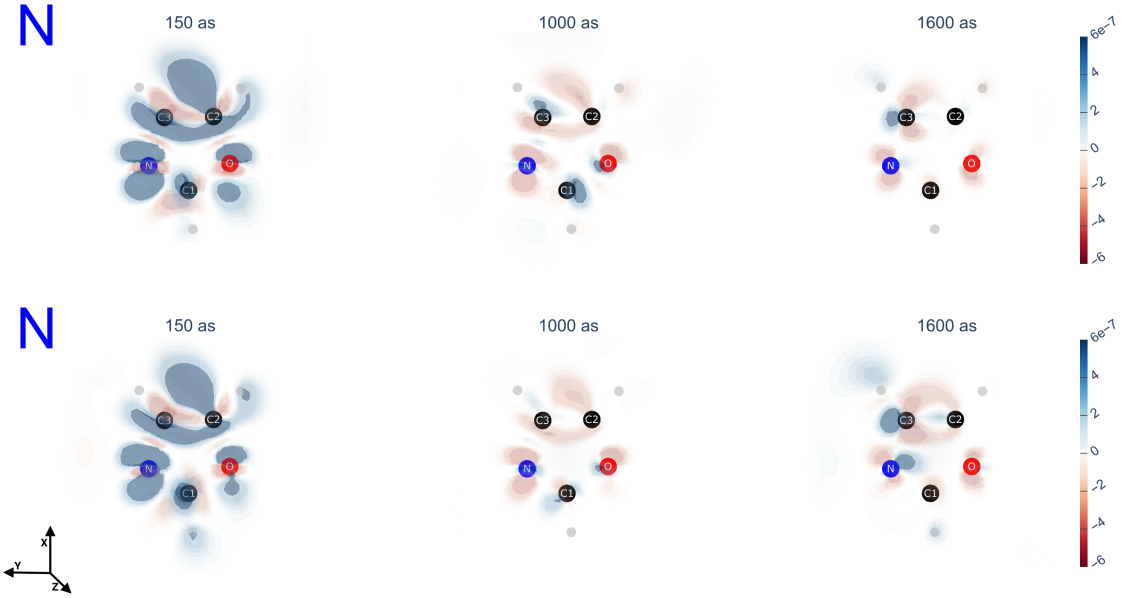

Figure 5.51: *Snapshots of* $\rho_{cc'}(\boldsymbol{r},t)$ *relative to the excitation at the N K-Edge with a right-handed (upper panel) and left-handed (lower panel), circularly polarised pulse in the* σ_{xy} *plane. The orientation of the axes is illustrated in the lower left corner.*

5.6 Summary and discussion

The structure and time-evolution of $\rho_{\Delta}(\boldsymbol{r},t)$ is dominated by the $\rho_{cg}(\boldsymbol{r},t)$ and $\Delta_{cg}(\boldsymbol{r},t)$ components, reflecting the same hierarchy found in OCS. The region of $\rho_{\Delta}(\boldsymbol{r},t)$ centred on the pumped atom is dominated by $\rho_{cg}(\boldsymbol{r},t)$; its localisation reflects the atom-specificity of the X-Ray excitation, while its spatial orientation and symmetry depend on the pulse polarisation. In particular, in the x-polarised case A' core-excited states are selected, with $\rho_{cg}(\boldsymbol{r},t)$ being symmetric with respect to the σ_{xy} plane; conversely, in the z-polarised case A'' core-excited states are selected, making $\rho_{cg}(\boldsymbol{r},t)$ antisymmetric with respect to σ_{xy}. In the xz-polarised case, the A'- and A''-symmetric contributions mix with similar weights and a $\pi/2$ relative phase, leading to the rotation of $\rho_{cg}(\boldsymbol{r},t)$ about the y-axis in the σ_{xz} plane. On the other hand, the rotational motion in the σ_{xy} plane observed in the circularly polarised cases follows from the corresponding rotation of the polarisation vector. As for OCS, the distribution of $\rho_{\Delta}(\boldsymbol{r},t)$ over the rest of the molecule is dominated by $\Delta_{cg}(\boldsymbol{r},t)$; its time-evolution reflects the decay of the core-excited states' population, which manifests as the gradual prevalence of the negatively-valued regions on the positively-valued ones. For every choice of pulse polarisation, the positively-valued region is mostly localised on the pumped atom, extending to the neighbouring C atoms when A''-symmetric core-excited states are selectively populated. This could be due to differences in the spatial properties of the core-excitation, which could be more localised in the case of A'-symmetric core-excited states than in the case of A''-symmetric ones. The characteristics of $\rho_{cg}(\boldsymbol{r},t)$ and $\Delta_{cg}(\boldsymbol{r},t)$ and their dominant role within $\rho_{\Delta}(\boldsymbol{r},t)$ corroborate the conclusions on the nature of the excitation reached in the OCS study. That is, the energy from the X-Ray pulse is deposited locally on the pumped atom by specifically exciting the corresponding core-electrons. The excitation proceeds 'vertically', creating a superposition of core particle-hole density pairs specifically localised on a region centred on the pumped atom. This does not lead to an extensive modification of the intramolecular electronic distribution, which remains substantially limited to the region centred on the pumped atom.

The dominant components of the excitation represented by $\rho_{cg}(\boldsymbol{r},t)$ and $\Delta_{cg}(\boldsymbol{r},t)$ 'hide' the contributions of the $\rho_{cc'}(\boldsymbol{r},t)$ and $\rho_{vg}(\boldsymbol{r},t)$ components, which conversely support the electronic motion across the molecule. The characteristics of $\rho_{cc'}(\boldsymbol{r},t)$ are closely related to the selected excitation edge and the pulse polarisation. The atomic-specificity of the core-excitation manifests as differences in the excited coherences and in the spatial characteristics of the corresponding transition densities. The pulse polarisation is crucially involved in controlling the spatial characteristics of the electronic migration supported by $\rho_{cc'}(\boldsymbol{r},t)$. If the polarisation only allows excitations between the A'- or the A''-symmetric states, the electronic motion unfolds symmetrically with respect to the σ_{xy} plane. On the other hand, when excitations between core-excited states of different symmetry are allowed, the electronic motion can also take place between the two sides of σ_{xy}. The results relative to the circularly polarised pulses also show how the information about the handedness of the polarisation is 'encoded' in the excited coherences. In fact, as the handedness of the polarisation changes, coherences relative to the same core-excited states are prepared with different initial amplitudes and relative phases. These differences are directly translated in the interference pattern of the coherences/transition densities,

leading to polarisation-handedness-dependent differences in the electronic distribution within $\rho_{cc'}(\boldsymbol{r}, t)$ over time. Despite its potential to support the electronic motion across the molecule, the few-*fs* lifetime of the core-excited states limits the time-window during which $\rho_{cc'}(\boldsymbol{r}, t)$ can affect the intramolecular electronic distribution.

This limitation does not affect the $\rho_{vg}(\boldsymbol{r}, t)$ component, which is characterised by a much longer lifetime. The first step of the analysis of $\rho_{vg}(\boldsymbol{r}, t)$ focused on its preparation, during which the initial electronic localisation on the pumped atom (due to the ISRIXS process) should take place. This is verified in the circularly polarised cases, wherein $\rho_{vg}(\boldsymbol{r}, t)$ accumulates particularly on O or N, in correspondence to excitations at the O K-Edge or at the N K-Edge, respectively. This observation demonstrates this feature of the ISRIXS process in a relatively small molecule like Oxazole, contrasting the results obtained in previous studies by Mukamel *et al.* [54, 55] in similarly small molecules. In particular, this observation contrasts the results from Yong *et al.* [55], who didn't observe an initial, atom-specific localisation of $\rho_{vg}(\boldsymbol{r}, t)$ in Oxazole. This result could be ascribed to the broader bandwidth used here (i.e. compared to the 6.8 eV bandwidth used in [55]) but also to the higher accuracy of the 'non-truncated' EOM-CC implementation, which allows a precise description of the preparation process and the molecular electronic structure. Compared to the 'truncated' EOM-CC description from Balbi *et al.* [56], the results presented in this analysis clarify the origin of the initial, atom-specific localisation of the excitation and its effects on $\rho_{\Delta}(\boldsymbol{r}, t)$'s distribution, separating the contributions involving the core-excited and the valence-excited states. The degree of localisation within $\rho_{vg}(\boldsymbol{r}, t)$ present in the Rxy and Lxy cases is not systematically observed across all the examined cases. This indicates that disposing of many valence-excited states potentially includable in the WP is only a necessary condition for the initial localisation. The other conditions could be related to the properties of the coherences – which regulate the interference process and 'encode' the atom- and polarisation-specific information – but also to the characteristic (system-specific) spatial distribution of the transition densities involved in the interference. The electronic dynamics in $\rho_{vg}(\boldsymbol{r}, t)$ behave akin to clockwise and anticlockwise ring currents, which often 'compete' with each other limiting the electronic dynamics to oscillations between couples of atoms. This behaviour is consistent with that observed in specialised works on ring-shaped molecules [128, 129, 130], wherein the ring currents corresponding to the valence electronic dynamics are fully characterised in terms of the electronic and electronic flux densities. According to these works, the circulation of the clockwise and anticlockwise ring currents is regulated by the presence of 'source' and 'sink' sites, whose position across the molecule is not necessarily fixed in time. A similar mechanism might be regulating the valence electronic motion in $\rho_{vg}(\boldsymbol{r}, t)$, with these sites being hypothetically located particularly on the electron-rich N and O. Accordingly, the relative oscillation of the respective regions of $\rho_{vg}(\boldsymbol{r}, t)$ might be linked with the 'regulation' of the circular electronic migration, with the ISRIXS process configuring itself as a valuable tool to selectively localise the initial 'source' of the migration.

CHAPTER 6

Conclusions and outlook

The study of the excitation in OCS and Oxazole has shown how, in the perturbative regime, the energy deposited by the X-Ray pulse in the molecules is predominantly used for the coherent population of the core-excited states. The structure of the $\rho_{cg}(\boldsymbol{r}, t)$ and $\Delta_{cg}(\boldsymbol{r}, t)$ components is indicative of how the energy from the X-Ray pulse is deposited locally to the pumped atom, 'vertically' exciting the electrons from the core-shells to the valence-shells of the electronic structure. This corresponds to the creation of a superposition of core particle-hole density pairs localised around the pumped atom. The electronic dynamics connected to $\rho_{cg}(\boldsymbol{r}, t)$ and $\Delta_{cg}(\boldsymbol{r}, t)$ are limited to the region in the immediate neighbourhood of the pumped atom, thus not determining extensive modifications of the intramolecular electronic distribution. The electronic motion connected with the coherent population of the core-excited states is supported by the $\rho_{cc'}(\boldsymbol{r}, t)$ component, which corresponds to the migration of the 'particle' part of the core-excitation in the valence-shells of the electronic structure. This indicates that the valence shells represent a molecule-wide 'platform' enabling the electronic migration across the molecules, with the core-excitation representing an atom-specific 'access' to this 'platform'. The dependence of $\rho_{cc'}(\boldsymbol{r}, t)$ on the pulse properties (i.e. polarisation and selected excitation edge) indicates that it is possible (in principle) to use the coherent population of the core-excited states to manipulate the electronic distribution and its dynamics in a neutral molecule. However, this possibility is crucially limited to only few *fs*, owing to the ultrashort lifetime of the core-excited states. In the considered organic molecules, the short lifetime of the core-excited states is mainly due to the (resonant) AM process, which transfers the properties of the WP of core-excited states to the manifold of valence-ionised states [131]. This was shown experimentally e.g. by Li *et al.* [132], who measured a time-dependent modulation in the emission of the AM electrons in nitric oxide; this modulation corresponds to the interference of the AM decay pathways connecting the core-excited to the valence-ionised states. The study of the WP launched in the manifold of valence-ionised states via the AM process might be an interesting new direction for the project, which could make use of Qchem's capabilities in the calculation of AM spectra at the EOM-CC level of theory [133, 134]. Of particular

interest could be the study of the charge migration, the localisation of its starting point and its dependence on the characteristics of the core-excitation.

While the majority of the pulse energy deposited in the neutral molecule is used for the core-excitation, a smaller portion is used for the coherent population of the valence-excited states via ISRIXS. The valence-excitation leads to the creation of particle-hole pairs within the valence shells of the electronic structure; this is the key feature supporting the molecule-wide electronic motion observed in $\rho_{vg}(\boldsymbol{r}, t)$. Compared to the core-excitation, the time-window available for the electronic motion supported by the valence-excitation is much longer. The longer lifetime of the valence-excited states leads, within few *fs*, to the variation of the hierarchy of the contributions to $\rho_{\Delta}(\boldsymbol{r}, t)$. In fact, $\rho_{vg}(\boldsymbol{r}, t)$ progressively becomes the dominant contribution to $\rho_{\Delta}(\boldsymbol{r}, t)$ as it outlives the (initially dominant) components relative to the core-excitation. Since on a longer timescale the nuclear dynamics start to play a significant role [135, 136], the possibility of manipulating $\rho_{vg}(\boldsymbol{r}, t)$ via the pulse properties is of fundamental importance to enable the control of the molecular dynamics. This possibility is demonstrated in the OCS and Oxazole examples, where the dynamics within $\rho_{vg}(\boldsymbol{r}, t)$ change as the pulse polarisation and the excitation edge are varied. In particular, the edge-dependence confirms the capability to transfer the atomic specificity of the core-excitation to the manifold of valence-excited states via the ISRIXS technique. Particularly in the Oxazole example, this can also translate into the initial localisation of $\rho_{vg}(\boldsymbol{r}, t)$ on the pumped atom, which indicates the possibility of transferring the localised character of the core-excitation – shown in $\rho_{cg}(\boldsymbol{r}, t)$ and $\Delta_{cg}(\boldsymbol{r}, t)$ – to the manifold of valence-excited states. In principle, this allows to control the localisation of the initial 'source' of the electronic migration, opening to the possibility of controlling where the electronic density preferentially accumulates at later times. Similarly to the concept of 'charge directed reactivity' in an ionised molecule [13, 14], this could enable a fine control over the bonding structure of the neutral molecule and its dynamics. This perspective motivates the extension of this investigation to a wider variety of linear conjugated or ring-shaped systems, with the aim of further researching the conditions – regulating the interference of the coherences/transition densities – supporting the initial electronic localisation within $\rho_{vg}(\boldsymbol{r}, t)$ and its systematic presence across different systems. The nature of the electronic migration, its dependence on the initial 'source' site and on the variation of the pulse parameters should also be explored more in depth. In particular, following the example of specialised works like [128, 129, 130], the description of the electronic migration should include, together with the electronic density, also the current density. The information provided by the current density might be similar to that shown during certain periods of $\rho_{vg}(\boldsymbol{r}, t)$'s time-evolution, where a 'classical' visualisation of the intramolecular electronic migration emerged. During these periods, the electronic migration showed characteristics similar to those of a current flowing through a conductor, which can be likened to a molecular 'wire' in the case of the linear OCS or a 'coil' in the case of the ring-shaped Oxazole. This induces to consider a more detailed study of the electronic migration important not only for attochemistry but also for the fields of molecular electronics and optoelectronics [137, 138, 139, 140]. The study of the dependence of the electronic migration on the pulse properties can be extended to a wider variety of pulse types, exploiting the flexibility of the code [122]. Possible candidate pulse-types include chirped [141], two-colour or realistic XFEL pulses. The latter option suggests a

further extension of the computational implementation to the calculation of experimental observables; this would enable the simulation of pump-probe experiments to reconstruct the coherent electronic motion. In particular, owing to the recent progresses in full X-Ray *as* pump-probe experiments at XFELs [142], X-Ray observables are desirable in order to obtain a spatial- and time-resolved reconstruction of the electronic dynamics. Possible observables include X-Ray diffraction [55], IS-RIXS [53], ultrafast X-Ray scattering [143, 144], X-Ray transient absorption [145] or quantum-beat AM spectroscopy [146]. The analysis of the $\rho_{vg}(\boldsymbol{r}, t)$ component showed how the valence-excitation represents the best platform for the manipulation of the electronic density in a neutral molecule on a relatively long timescale. It is therefore necessary to develop strategies to maximise the portion of pulse energy used for the valence-excitation, minimising that used for the core-excitation. Within the present perturbative model, a possible strategy relies on the optimisation of the pulse parameters (e.g. using a chirped or a two-colour pulse) to maximise the coherent population of the valence-excited states. On the other hand, this issue can be tackled by considering the Stimulated Raman Adiabatic Passage (STIRAP) process [147, 148]. In principle, the STIRAP process allows depositing the energy from the pulse specifically in the manifold of valence-excited states, avoiding the population of the core-excited states. The high pulse irradiance required for the implementation of STIRAP is not suitable for the perturbative model presented here, requiring the adoption of a non-perturbative theory for its simulation. For this purpose, a solution closely related to this work could be based on the TD-EOM-CC approach, which would make use of the same set of EOM-CC electronic eigenstates used in the present perturbative model while allowing the treatment of a non-perturbative excitation.

This work is specifically focused on the study of the purely electronic excitation and dynamics, with the nuclei kept frozen in the equilibrium configuration of the electronic ground state. The presented model is limited to a single ground-state configuration of the nuclei. Furthermore, the model neglects the nuclear dynamics upon electronic excitation. Both of these effects would result in a loss of electronic coherence [136, 105, 106] and are thus are not treated within the presented model. These effects are particularly important to take into account for molecules containing Hydrogen. The considered case of Oxazole containing Hydrogen therefore overestimates the electronic coherence in the wave packet. A complete description of the excitation and the subsequent molecular dynamics requires the explicit inclusion of the nuclear DOF in the model; this implies the computational challenge of coherently propagating nuclear WPs on multiple electronic states [149]. The study of the preparation of the vibronic WP, its decoherence due to the electron-nuclei coupling [136, 105] and the role of the conical intersections in the control of the chemical dynamics [150, 151] can provide a more realistic simulation of the photochemical reaction. This challenging development could lead to the creation of a valid platform for the accurate modelling of the chemical dynamics triggered by a perturbative X-Ray excitation in a neutral molecule, supporting the theoretical and experimental development of the attochemistry field in this exciting new direction.

Acknowledgments

In this final, decisively more personal, section I would like to express my gratitude to many colleagues, collaborators and friends without whom completing this dissertation wouldn't have been possible. First of all, I would like to thank my supervisor Prof. Nina Rohringer for giving me the opportunity to conduct research in her group and for all her help and support during these challenging years. I would like to express my gratitude to my co-supervisor Prof. Robin Santra for his input and support, which was of fundamental importance, especially during the most difficult moments of my doctoral journey. During this journey, I've been accompanied by a numerous group of colleagues and friends, whose extraordinary support helped me propel through the various ups and downs of these years. Firstly, I would like to express my deep gratitude to my friend and colleague Stasis Chuchurka for his competent and generous support, which played a fundamental part in completing this dissertation. I would like to thank Dr. Christina Bömer and Dr. Dietrich Krebs for their unwavering support and their precious friendship. I thank Vladislav Sukharnikov, Daniele Ronchetti, Xenia Brockmuller, Nicola Baark and Edoardo Zavatti for their friendship and for all the jokes and discussions we shared about the most disparate topics, which made coming to the office great fun. I'm grateful to Agata Azzolin for her help, especially in the most difficult moments, and for sharing with me long, sunny runs along the Elbe, which supported my never-ending marathon preparation. I thank Dr. Kirsten Schnorr, Dr. Sven Augustin and all the team at the Maloja beamline at SwissFel for teaching me so much about the experimental world and for the great moments we shared during our experimental collaboration. A fundamental support during these years has come from many fantastic people which, albeit being far away, never failed to make me feel their closeness and support. A special mention goes to my friend Kassandra and all my lifelong friends in Italy who, despite the distance and the rare occasions we see each other, never fail to make me feel loved and at home as if I never left. Last, but not least, I would like to express my deep gratitude to all my family and in particular to my parents for all their unconditional love and extraordinary support, which gave me the serenity and the strength to face the difficulties of these challenging years.

Bibliography

[1] Ksenija Glusac. "What has light ever done for chemistry?" *Nature Chemistry* 8.8 (Aug. 2016), pp. 734–735.

[2] G. Alber, H. Ritsch, and P. Zoller. "Generation and detection of Rydberg wave packets by short laser pulses". *Physical Review A* 34.2 (1986), pp. 1058–1064.

[3] John A. Yeazell, Mark Mallalieu, and C. R. Stroud. "Observation of the collapse and revival of a Rydberg electronic wave packet". *Physical Review Letters* 64.17 (1990), pp. 2007–2010.

[4] W. Sibbett, A. A. Lagatsky, and C. T. A. Brown. "The development and application of femtosecond laser systems". *Optics Express* 20.7 (Mar. 2012), p. 6989.

[5] Marcos Dantus, Mark J. Rosker, and Ahmed H. Zewail. "Femtosecond real-time probing of reactions. II. The dissociation reaction of ICN". *The Journal of Chemical Physics* 89.10 (1988), pp. 6128–6140.

[6] Mark J. Rosker, Marcos Dantus, and Ahmed H. Zewail. "Femtosecond real-time probing of reactions. I. The technique". *The Journal of Chemical Physics* 89.10 (1988), pp. 6113–6127.

[7] Paul Brumer and Moshe Shapiro. "Control of unimolecular reactions using coherent light". *Chemical Physics Letters* 126.6 (1986), pp. 541–546.

[8] Paul Brumer and Moshe Shapiro. "One photon mode selective control of reactions by rapid or shaped laser pulses: An emperor without clothes?" *Chemical Physics* 139.1 (1989), pp. 221–228.

[9] A Assion et al. "Control of Chemical Reactions by Feedback-Optimized Phase-Shaped Femtosecond Laser Pulses". *Science* 282 (1998).

[10] Ahmed H Zewail. "Laser Femtochemistry". *Science* 242 (1988).

[11] R. Weinkauf et al. "Elementary Processes in Peptides: Electron Mobility and Dissociation in Peptide Cations in the Gas Phase". *The Journal of Physical Chemistry* 99.28 (July 1995), pp. 11255–11265.

[12] L.S. Cederbaum and J. Zobeley. "Ultrafast charge migration by electron correlation". *Chemical Physics Letters* 307.3–4 (July 1999), pp. 205–210.

[13] F. Remacle, R.D. Levine, and M.A. Ratner. "Charge directed reactivity:: a simple electronic model, exhibiting site selectivity, for the dissociation of ions". *Chemical Physics Letters* 285.1 (1998), pp. 25–33.

[14] F. Remacle et al. "Electronic Control of Site Selective Reactivity: A Model Combining Charge Migration and Dissociation". *The Journal of Physical Chemistry A* 103.49 (Dec. 1999), pp. 10149–10158.

[15] F. Remacle and R. D. Levine. "An electronic time scale in chemistry". *Proceedings of the National Academy of Sciences* 103.18 (May 2006), pp. 6793–6798.

[16] P. M. Paul et al. "Observation of a Train of Attosecond Pulses from High Harmonic Generation". *Science* 292.5522 (2001), pp. 1689–1692.

[17] M. Hentschel et al. "Attosecond metrology". *Nature* 414.6863 (Nov. 2001), pp. 509–513.

[18] G. Sansone et al. "Electron localization following attosecond molecular photoionization". *Nature* 465.7299 (June 2010), pp. 763–766.

[19] M. F. Kling et al. "Control of Electron Localization in Molecular Dissociation". *Science* 312.5771 (Apr. 2006), pp. 246–248.

[20] F. Calegari et al. "Ultrafast electron dynamics in phenylalanine initiated by attosecond pulses". *Science* 346.6207 (Oct. 2014), pp. 336–339.

[21] Alexander I Kuleff and Lorenz S Cederbaum. "Ultrafast correlation-driven electron dynamics". *Journal of Physics B: Atomic, Molecular and Optical Physics* 47.12 (June 2014), p. 124002.

[22] Franck Lépine, Misha Y. Ivanov, and Marc J. J. Vrakking. "Attosecond molecular dynamics: fact or fiction?" *Nature Photonics* 8.3 (Mar. 2014), pp. 195–204.

[23] Nikolay V. Golubev and Alexander I. Kuleff. "Control of charge migration in molecules by ultrashort laser pulses". *Physical Review A* 91.5 (May 2015), p. 051401.

[24] Anthony Ferté and Morgane Vacher. "Recent advances in theoretical attosecond chemistry". *Chemical Modelling: Volume 17*. The Royal Society of Chemistry, Dec. 2022.

[25] Alicia Palacios and Fernando Martín. "The quantum chemistry of attosecond molecular science". *WIREs Computational Molecular Science* 10.1 (2020), e1430.

[26] P. M. Kraus et al. "Measurement and laser control of attosecond charge migration in ionized iodoacetylene". *Science* 350.6262 (Nov. 2015), pp. 790–795.

[27] Isabella C. D. Merritt, Denis Jacquemin, and Morgane Vacher. "Attochemistry: Is Controlling Electrons the Future of Photochemistry?" *The Journal of Physical Chemistry Letters* 12.34 (Sept. 2021), pp. 8404–8415.

[28] Sampad Bag et al. “The attochemistry of chemical bonding”. *International Reviews in Physical Chemistry* 40.3 (July 2021), pp. 405–455.

[29] Francesca Calegari and Fernando Martin. “Open questions in attochemistry”. *Communications Chemistry* 6.11 (Sept. 2023), pp. 1–5.

[30] Danylo T. Matselyukh et al. “Decoherence and revival in attosecond charge migration driven by non-adiabatic dynamics”. *Nature Physics* 18.10 (Oct. 2022), pp. 1206–1213.

[31] Allan S. Johnson et al. “Attosecond soft X-ray high harmonic generation”. *Philosophical Transactions of the Royal Society A: Mathematical, Physical and Engineering Sciences* 377.2145 (May 2019), p. 20170468.

[32] Joseph Duris et al. “Tunable isolated attosecond X-ray pulses with gigawatt peak power from a free-electron laser”. *Nature Photonics* 14.1 (Dec. 2019), pp. 30–36.

[33] Joachim Stohr. *NEXAFS Spectroscopy*. Springer series in surface sciences. Berlin, Germany": Springer, Dec. 2010.

[34] M. O. Krause. “Atomic radiative and radiationless yields for K and L shells”. *Journal of Physical and Chemical Reference Data* 8.2 (Apr. 1979), pp. 307–327.

[35] H. Aksela. “Resonant Auger spectroscopy of atoms and molecules”. *Journal of Electron Spectroscopy and Related Phenomena* 72 (Mar. 1995), pp. 235–242.

[36] Walter Bambynek et al. “X-Ray Fluorescence Yields, Auger, and Coster-Kronig Transition Probabilities”. *Rev. Mod. Phys.* 44 (4 Oct. 1972), pp. 716–813.

[37] A. Menzel et al. “Natural widths in open-shell atoms: The K absorption spectrum of atomic oxygen”. *Phys. Rev. A* 54 (2 Aug. 1996), R991–R994.

[38] Faris Gel’mukhanov et al. “Integral properties of channel interference in resonant X-ray scattering”. *Physics Letters A* 211.2 (Feb. 1996), pp. 101–108.

[39] Christophe Nicolas and Catalin Miron. “Lifetime broadening of core-excited and -ionized states”. *Journal of Electron Spectroscopy and Related Phenomena* 185.8 (2012), pp. 267–272.

[40] Noël Boens et al. “Fluorescence Lifetime Standards for Time and Frequency Domain Fluorescence Spectroscopy”. *Analytical Chemistry* 79.5 (2007), pp. 2137–2149.

[41] Faris Gel’mukhanov and Hans Ågren. “Resonant X-ray Raman scattering”. *Physics Reports* 312.3 (1999), pp. 87–330.

[42] A. Benkert et al. “Isotope Effects in the Resonant Inelastic Soft X-ray Scattering Maps of Gas-Phase Methanol”. *The Journal of Physical Chemistry A* 120.14 (Apr. 2016), pp. 2260–2267.

[43] L. Kjellsson et al. “Resonant Inelastic X-Ray Scattering Reveals Hidden Local Transitions of the Aqueous OH Radical”. *Physical Review Letters* 124.23 (June 2020), p. 236001.

[44] E. Paris et al. “Probing the interplay between lattice dynamics and short-range magnetic correlations in CuGeO3 with femtosecond RIXS”. *npj Quantum Materials* 6.1 (May 2021), p. 51.

[45] Satoshi Tanaka and Shaul Mukamel. “Coherent X-Ray Raman Spectroscopy: A Nonlinear Local Probe for Electronic Excitations”. *Physical Review Letters* 89.4 (July 2002), p. 043001.

[46] C. Pellegrini, A. Marinelli, and S. Reiche. “The physics of x-ray free-electron lasers”. *Reviews of Modern Physics* 88.1 (Mar. 2016), p. 015006.

[47] Nina Rohringer. “X-ray Raman scattering: a building block for nonlinear spectroscopy”. *Philosophical Transactions of the Royal Society A: Mathematical, Physical and Engineering Sciences* 377.2145 (May 2019), p. 20170471.

[48] Clemens Weninger et al. “Stimulated Electronic X-Ray Raman Scattering”. *Phys. Rev. Lett.* 111 (23 Dec. 2013), p. 233902.

[49] Victor Kimberg et al. “Stimulated X-ray Raman scattering – a critical assessment of the building block of nonlinear X-ray spectroscopy”. *Faraday Discuss.* 194 (0 2016), pp. 305–324.

[50] Jordan T. O’Neal et al. “Electronic Population Transfer via Impulsive Stimulated X-Ray Raman Scattering with Attosecond Soft-X-Ray Pulses”. *Phys. Rev. Lett.* 125 (7 Aug. 2020), p. 073203.

[51] Oliver Alexander et al. “Attosecond impulsive stimulated X-ray Raman scattering in liquid water”. *Science Advances* 10.39 (Sept. 2024), eadp0841.

[52] Adam E. A. Fouda and Phay J. Ho. “Site-specific generation of excited state wavepackets with high-intensity attosecond x rays”. *The Journal of Chemical Physics* 154.22 (June 2021), p. 224111.

[53] Igor V. Schweigert and Shaul Mukamel. “Probing valence electronic wavepacket dynamics by all x-ray stimulated Raman spectroscopy: A simulation study”. *Physical Review A* 76.1 (July 2007), p. 012504.

[54] Daniel Healion et al. “Entangled Valence Electron–Hole Dynamics Revealed by Stimulated Attosecond X-ray Raman Scattering”. *The Journal of Physical Chemistry Letters* 3.17 (Sept. 2012), pp. 2326–2331.

[55] Haiwang Yong, Stefano M. Cavaletto, and Shaul Mukamel. “Ultrafast Valence-Electron Dynamics in Oxazole Monitored by X-ray Diffraction Following a Stimulated X-ray Raman Excitation”. *The Journal of Physical Chemistry Letters* 12.40 (Oct. 2021), pp. 9800–9806.

[56] Alice Balbi, Andreas S. Skeidsvoll, and Henrik Koch. “Coupled Cluster Simulation of Impulsive Stimulated X-ray Raman Scattering”. *The Journal of Physical Chemistry A* 127.41 (Oct. 2023), pp. 8676–8684.

[57] Erich Runge and E. K. U. Gross. “Density-Functional Theory for Time-Dependent Systems”. *Phys. Rev. Lett.* 52 (12 Mar. 1984), pp. 997–1000.

[58] Valérie Véniard, Richard Taïeb, and Alfred Maquet. “Atomic clusters submitted to an intense short laser pulse: A density-functional approach”. *Physical Review A* 65.1 (Dec. 2001), p. 013202.

[59] Adam Bruner et al. “Attosecond Charge Migration with TDDFT: Accurate Dynamics from a Well-Defined Initial State”. *The Journal of Physical Chemistry Letters* 8.17 (Sept. 2017), pp. 3991–3996.

[60] Attila Szabo and Neil S. Ostlund. *Modern Quantum Chemistry: Introduction to Advanced Electronic Structure Theory*. Dover Publications, Inc., 1996.

[61] Loren Greenman et al. “Implementation of the time-dependent configuration-interaction singles method for atomic strong-field processes”. *Physical Review A* 82.2 (Aug. 2010), p. 023406.

[62] Stefanos Carlström, Michael Spanner, and Serguei Patchkovskii. “General time-dependent configuration-interaction singles. I. Molecular case”. *Physical Review A* 106.4 (Oct. 2022), p. 043104.

[63] Tillmann Klamroth. “Optimal control of ultrafast laser driven many-electron dynamics in a polyatomic molecule: N-methyl-6-quinolone”. *The Journal of Chemical Physics* 124.14 (Apr. 2006), p. 144310.

[64] Inga S. Ulusoy, Zachary Stewart, and Angela K. Wilson. “The role of the CI expansion length in time-dependent studies”. *The Journal of Chemical Physics* 148.1 (Jan. 2018), p. 014107.

[65] Pascal Krause, Tillmann Klamroth, and Peter Saalfrank. “Molecular response properties from explicitly time-dependent configuration interaction methods”. *The Journal of Chemical Physics* 127.3 (July 2007), p. 034107.

[66] Pascal Krause, Tillmann Klamroth, and Peter Saalfrank. “Time-dependent configuration-interaction calculations of laser-pulse-driven many-electron dynamics: Controlled dipole switching in lithium cyanide”. *The Journal of Chemical Physics* 123.7 (Aug. 2005), p. 074105.

[67] H.-D. Meyer, U. Manthe, and L.S. Cederbaum. “The multi-configurational time-dependent Hartree approach”. *Chemical Physics Letters* 165.1 (Jan. 1990), pp. 73–78.

[68] Axel U. J. Lode et al. “Colloquium: Multiconfigurational time-dependent Hartree approaches for indistinguishable particles”. *Reviews of Modern Physics* 92.1 (Feb. 2020), p. 011001.

[69] J. Caillat et al. “Correlated multielectron systems in strong laser fields: A multiconfiguration time-dependent Hartree-Fock approach”. *Physical Review A* 71.1 (Jan. 2005), p. 012712.

[70] D. Hochstuhl, C.M. Hinz, and M. Bonitz. “Time-dependent multiconfiguration methods for the numerical simulation of photoionization processes of many-electron atoms”. *The European Physical Journal Special Topics* 223.2 (Jan. 2014), pp. 177–336.

[71] Takeshi Sato and Kenichi L. Ishikawa. “Time-dependent complete-active-space self-consistent-field method for multielectron dynamics in intense laser fields”. *Physical Review A* 88.2 (Aug. 2013), p. 023402.

[72] Haruhide Miyagi and Lars Bojer Madsen. “Time-dependent restricted-active-space self-consistent-field theory with space partition”. *Physical Review A* 95.2 (Feb. 2017), p. 023415.

[73] Tsuyoshi Kato and Hirohiko Kono. "Time-dependent multiconfiguration theory for electronic dynamics of molecules in an intense laser field". *Chemical Physics Letters* 392.4–6 (July 2004), pp. 533–540.

[74] Kenneth C. Kulander. "Time-dependent Hartree-Fock theory of multiphoton ionization: Helium". *Physical Review A* 36.6 (Sept. 1987), pp. 2726–2738.

[75] Andreas Dreuw and Michael Wormit. "The algebraic diagrammatic construction scheme for the polarization propagator for the calculation of excited states". *WIREs Computational Molecular Science* 5.1 (Jan. 2015), pp. 82–95.

[76] Alexander I. Kuleff, Jörg Breidbach, and Lorenz S. Cederbaum. "Multielectron wave-packet propagation: General theory and application". *The Journal of Chemical Physics* 123.4 (July 2005), p. 044111.

[77] M. Ruberti, P. Decleva, and V. Averbukh. "Full Ab Initio Many-Electron Simulation of Attosecond Molecular Pump–Probe Spectroscopy". *Journal of Chemical Theory and Computation* 14.10 (Oct. 2018), pp. 4991–5000.

[78] Benedicte Sverdrup Ofstad et al. "Time-dependent coupled-cluster theory". *WIREs Computational Molecular Science* 13.5 (Sept. 2023), e1666.

[79] Rodney J. Bartlett and Monika Musiał. "Coupled-cluster theory in quantum chemistry". *Rev. Mod. Phys.* 79 (1 Feb. 2007), pp. 291–352.

[80] Henrik Koch and Poul Jo/rgensen. "Coupled cluster response functions". *The Journal of Chemical Physics* 93.5 (Sept. 1990), pp. 3333–3344.

[81] Andreas S. Skeidsvoll, Alice Balbi, and Henrik Koch. "Time-dependent coupled-cluster theory for ultrafast transient-absorption spectroscopy". *Physical Review A* 102.2 (Aug. 2020), p. 023115.

[82] Simen Kvaal. "Ab initio quantum dynamics using coupled-cluster". *The Journal of Chemical Physics* 136.19 (May 2012), p. 194109.

[83] Takeshi Sato et al. "Communication: Time-dependent optimized coupled-cluster method for multielectron dynamics". *The Journal of Chemical Physics* 148.5 (Feb. 2018), p. 051101.

[84] Himadri Pathak, Takeshi Sato, and Kenichi L. Ishikawa. "Time-dependent optimized coupled-cluster method for multielectron dynamics. IV. Approximate consideration of the triple excitation amplitudes". *The Journal of Chemical Physics* 154.23 (June 2021), p. 234104.

[85] John F. Stanton and Rodney J. Bartlett. "The equation of motion coupled-cluster method. A systematic biorthogonal approach to molecular excitation energies, transition probabilities, and excited state properties". *The Journal of Chemical Physics* 98.9 (May 1993), pp. 7029–7039.

[86] Anna I Krylov. "Equation-of-motion coupled-cluster methods for open-shell and electronically excited species: the Hitchhiker's guide to Fock space". *Annu. Rev. Phys. Chem.* 59.1 (2008), pp. 433–462.

[87] Jason A. Sonk, Marco Caricato, and H. Bernhard Schlegel. "TD-CI Simulation of the Electronic Optical Response of Molecules in Intense Fields: Comparison of RPA, CIS, CIS(D), and EOM-CCSD". *The Journal of Physical Chemistry A* 115.18 (May 2011), pp. 4678–4690.

[88] Eleonora Luppi and Martin Head-Gordon. "Computation of high-harmonic generation spectra of H 2 and N 2 in intense laser pulses using quantum chemistry methods and time-dependent density functional theory". *Molecular Physics* 110.9–10 (May 2012), pp. 909–923.

[89] Andreas S. Skeidsvoll et al. "Simulating weak-field attosecond processes with a Lanczos reduced basis approach to time-dependent equation-of-motion coupled-cluster theory". *Physical Review A* 105.2 (Feb. 2022), p. 023103.

[90] Kaushik D. Nanda and Anna I. Krylov. "Two-photon absorption cross sections within equation-of-motion coupled-cluster formalism using resolution-of-the-identity and Cholesky decomposition representations: Theory, implementation, and benchmarks". *The Journal of Chemical Physics* 142.6 (Feb. 2015), p. 064118.

[91] Kaushik D. Nanda et al. "How to stay out of trouble in RIXS calculations within equation-of-motion coupled-cluster damped response theory? Safe hitchhiking in the excitation manifold by means of core–valence separation". *Phys. Chem. Chem. Phys.* 22 (5 2020), pp. 2629–2641.

[92] Ahmed H. Zewail. "Femtochemistry: Atomic-Scale Dynamics of the Chemical Bond". *The Journal of Physical Chemistry A* 104.24 (2000), pp. 5660–5694.

[93] David Parker Craig and Thiru Thirunamachandran. *Molecular quantum electrodynamics: an introduction to radiation-molecule interactions*. Courier Corporation, 1998.

[94] Robin Santra. "Concepts in x-ray physics". *Journal of Physics B: Atomic, Molecular and Optical Physics* 42.2 (Dec. 2008), p. 023001.

[95] Jun John Sakurai. *Modern quantum mechanics; rev. ed.* Reading, MA: Addison-Wesley, 1994.

[96] Marlan O. Scully and M. Suhail Zubairy. "Atom–field interaction – semiclassical theory". *Quantum Optics*. Cambridge University Press, 1997, pp. 145–192.

[97] Paul Adrien Maurice Dirac. *The Principles of Quantum Mechanics*. Clarendon Press, 1930.

[98] Yi-Jen Chen. "Light-induced ultrafast tunneling dynamics of a many-electron system: from weak to strong fields". PhD thesis. Universität Hamburg, Hamburg, 2019.

[99] Markus Reiher and Alexander Wolf. *Relativistic quantum chemistry*. en. 2nd ed. Weinheim, Germany: Wiley-VCH Verlag, Nov. 2014.

[100] Bossmann Lea. *On the dipole approximation*. Master's thesis. 2016.

[101] Maria Göppert-Mayer. "Über Elementarakte mit zwei Quantensprüngen". *Annalen der Physik* 401.3 (1931), pp. 273–294.

[102] M. Born and V. Fock. "Beweis des Adiabatensatzes". *Zeitschrift für Physik* 51.3–4 (1928), pp. 165–180.

[103] M. Born and R. Oppenheimer. "Zur Quantentheorie der Molekeln". *Annalen der Physik* 389.20 (1927), pp. 457–484.

[104] B H Bransden and C J Joachain. *Physics of atoms and molecules.* en. 2nd ed. London, England: Prentice-Hall, Apr. 2003.

[105] Morgane Vacher et al. "Electron Dynamics upon Ionization of Polyatomic Molecules: Coupling to Quantum Nuclear Motion and Decoherence". *Physical Review Letters* 118.8 (Feb. 2017), p. 083001.

[106] Caroline Arnold, Oriol Vendrell, and Robin Santra. "Electronic decoherence following photoionization: Full quantum-dynamical treatment of the influence of nuclear motion". *Physical Review A* 95.3 (Mar. 2017), p. 033425.

[107] W. Pauli. "Über den Zusammenhang des Abschlusses der Elektronengruppen im Atom mit der Komplexstruktur der Spektren". *Zeitschrift für Physik* 31.1 (Feb. 1925), pp. 765–783.

[108] E.K.U. Gross, E. Runge, and O. Heinonen. *Many-Particle Theory,* Taylor & Francis, 1991.

[109] Isaiah Shavitt and Rodney J. Bartlett. *Many-Body Methods in Chemistry and Physics: MBPT and Coupled-Cluster Theory.* Cambridge Molecular Science. Cambridge University Press, 2009.

[110] Rodney J. Bartlett. "Coupled-cluster approach to molecular structure and spectra: a step toward predictive quantum chemistry". *The Journal of Physical Chemistry* 93.5 (1989), pp. 1697–1708.

[111] Trygve Helgaker, Poul Jørgensen, and Jeppe Olsen. "Coupled-Cluster Theory". *Molecular Electronic-Structure Theory.* John Wiley Sons, Ltd, 2000. Chap. 13, pp. 648–723.

[112] Mark R. Hoffmann and Jack Simons. "A unitary multiconfigurational coupled-cluster method: Theory and applications". *The Journal of Chemical Physics* 88.2 (Jan. 1988), pp. 993–1002.

[113] Rodney J. Bartlett, Stanislaw A. Kucharski, and Jozef Noga. "Alternative coupled-cluster ansätze II. The unitary coupled-cluster method". *Chemical Physics Letters* 155.1 (1989), pp. 133–140.

[114] Moshe Shapiro and Paul Brummer. "Preliminaries of the Interaction of Light with Matter". *Quantum Control of Molecular Processes.* John Wiley & Sons, Ltd, 2011. Chap. 1.

[115] Felix Plasser, Michael Wormit, and Andreas Dreuw. "New tools for the systematic analysis and visualization of electronic excitations. I. Formalism". *The Journal of Chemical Physics* 141.2 (July 2014), p. 024106.

[116] Dimitrios Maganas et al. "Combined Experimental and Ab Initio Multireference Configuration Interaction Study of the Resonant Inelastic X-ray Scattering Spectrum of CO2". *The Journal of Physical Chemistry C* 118.35 (2014), pp. 20163–20175.

[117] Emelie Ertan et al. "Ultrafast dissociation features in RIXS spectra of the water molecule". *Phys. Chem. Chem. Phys.* 20 (21 2018), pp. 14384–14397.

[118] Patrick Norman. "A perspective on nonresonant and resonant electronic response theory for time-dependent molecular properties". *Phys. Chem. Chem. Phys.* 13 (46 2011), pp. 20519–20535.

[119] Joanna Kauczor et al. “Communication: A reduced-space algorithm for the solution of the complex linear response equations used in coupled cluster damped response theory”. *The Journal of Chemical Physics* 139.21 (Dec. 2013), p. 211102.

[120] Evgeny Epifanovsky et al. “Software for the frontiers of quantum chemistry: An overview of developments in the Q-Chem 5 package”. *The Journal of Chemical Physics* 155.8 (Aug. 2021), p. 084801.

[121] Marta L. Vidal et al. “New and Efficient Equation-of-Motion Coupled-Cluster Framework for Core-Excited and Core-Ionized States”. *Journal of Chemical Theory and Computation* 15.5 (2019), pp. 3117–3133.

[122] Emanuele Rossi, Stasis Chuchurka, and Mads Jakobsen. *Wave-packet in neutral molecule launched by an attosecond X-Ray pulse: perturbative code.* URL: `https://github.com/emarossi/wave_packet_calc/`.

[123] Jie Li et al. “53-attosecond X-ray pulses reach the carbon K-edge”. *Nature Communications* 8.1 (Aug. 2017), p. 186.

[124] Edward Collett. *Field Guide to Polarization.* SPIE, Sept. 2005.

[125] Pekka Pyykkö and Michiko Atsumi. “Molecular Double-Bond Covalent Radii for Elements Li–E112”. *Chemistry – A European Journal* 15.46 (2009), pp. 12770–12779.

[126] Sucharita Giri, Gopal Dixit, and Jean Christophe Tremblay. “Attosecond charge migration in heterocyclic five-membered rings”. en. *Eur. Phys. J. Spec. Top.* 232.12 (Sept. 2023), pp. 1935–1943.

[127] Anna Kristina Schnack-Petersen et al. “Core spectroscopy of oxazole”. *The Journal of Chemical Physics* 157.21 (Dec. 2022), p. 214305.

[128] Gunter Hermann et al. “Multidirectional Angular Electronic Flux during Adiabatic Attosecond Charge Migration in Excited Benzene”. *The Journal of Physical Chemistry A* 120.27 (July 2016), pp. 5360–5369.

[129] Dongming Jia et al. “Quantum control of electronic fluxes during adiabatic attosecond charge migration in degenerate superposition states of benzene”. *Chemical Physics* 482 (Jan. 2017), pp. 146–159.

[130] H. Mineo, S. H. Lin, and Y. Fujimura. “Coherent -electron dynamics of (P)-2,2-biphenol induced by ultrashort linearly polarized UV pulses: Angular momentum and ring current”. *The Journal of Chemical Physics* 138.7 (Feb. 2013), p. 074304.

[131] A. Picón et al. “Auger-induced charge migration”. *Physical Review A* 98.4 (Oct. 2018), p. 043433.

[132] Siqi Li et al. “Attosecond coherent electron motion in Auger-Meitner decay”. *Science* 375.6578 (Jan. 2022), pp. 285–290.

[133] Wojciech Skomorowski and Anna I. Krylov. “Feshbach–Fano approach for calculation of Auger decay rates using equation-of-motion coupled-cluster wave functions. I. Theory and implementation”. *The Journal of Chemical Physics* 154.8 (Feb. 2021), p. 084124.

[134] Nayanthara K. Jayadev et al. “The Auger spectrum of benzene”. *The Journal of Chemical Physics* 158.6 (Feb. 2023), p. 064109.

[135] Manuel Lara-Astiaso et al. "Decoherence, control and attosecond probing of XUV-induced charge migration in biomolecules. A theoretical outlook". *Faraday Discussions* 194 (2016), pp. 41–59.

[136] Morgane Vacher et al. "Electron dynamics following photoionization: Decoherence due to the nuclear-wave-packet width". *Physical Review A* 92.4 (Oct. 2015), p. 040502.

[137] Dustin K. James and James M. Tour. "Molecular Wires". *Molecular Wires and Electronics*. Berlin, Heidelberg: Springer Berlin Heidelberg, 2005, pp. 33–62.

[138] John E. Anthony. "Functionalized Acenes and Heteroacenes for Organic Electronics". *Chemical Reviews* 106.12 (Dec. 2006), pp. 5028–5048.

[139] Bryan Kudisch et al. "Ring currents modulate optoelectronic properties of aromatic chromophores at 25 T". *Proceedings of the National Academy of Sciences* 117.21 (May 2020), pp. 11289–11298.

[140] Gemma C. Solomon et al. "Exploring local currents in molecular junctions". *Nature Chemistry* 2.3 (Mar. 2010), pp. 223–228.

[141] Maximilian Hollstein and Nina Rohringer. "Stimulated resonant inelastic x-ray scattering with chirped, broadband pulses". *Physical Review A* 99.1 (Jan. 2019), p. 013425.

[142] Zhaoheng Guo et al. "Experimental demonstration of attosecond pump–probe spectroscopy with an X-ray free-electron laser". *Nature Photonics* 18.7 (July 2024), pp. 691–697.

[143] Daria Popova-Gorelova and Robin Santra. "Imaging instantaneous electron flow with ultrafast resonant x-ray scattering". *Physical Review B* 91.18 (May 2015), p. 184303.

[144] Mats Simmermacher et al. "Electronic Coherence in Ultrafast X-Ray Scattering from Molecular Wave Packets". *Physical Review Letters* 122.7 (Feb. 2019), p. 073003.

[145] Eleftherios Goulielmakis et al. "Real-time observation of valence electron motion". *Nature* 466.7307 (Aug. 2010), pp. 739–743.

[146] Song Bin Zhang and Nina Rohringer. "Quantum-beat Auger spectroscopy". *Physical Review A* 92.4 (Oct. 2015), p. 043420.

[147] Antonio Picón, Jordi Mompart, and Stephen H Southworth. "Stimulated Raman adiabatic passage with two-color x-ray pulses". *New Journal of Physics* 17.8 (Aug. 2015), p. 083038.

[148] Nikolay V. Vitanov et al. "Stimulated Raman adiabatic passage in physics, chemistry, and beyond". *Reviews of Modern Physics* 89.1 (Mar. 2017), p. 015006.

[149] Thierry Tran, Anthony Ferté, and Morgane Vacher. "Simulating Attochemistry: Which Dynamics Method to Use?" *The Journal of Physical Chemistry Letters* 15.13 (Apr. 2024), pp. 3646–3652.

[150] Morgane Vacher et al. "Electronic Control of Initial Nuclear Dynamics Adjacent to a Conical Intersection". *The Journal of Physical Chemistry A* 119.21 (May 2015), pp. 5165–5172.

[151] Caroline Arnold et al. "Control of Nuclear Dynamics through Conical Intersections and Electronic Coherences". *Physical Review Letters* 120.12 (Mar. 2018), p. 123001.

APPENDIX A

Perturbative theory

In this appendix, the complete derivations of the probability amplitudes associated with the WP expansion are presented. The derivation relative to probability amplitudes associated to the core-excited states, $a_c^{(1)}(t)$, is presented in section A.1. On the other hand, the derivation relative to probability amplitudes associated to the valence-excited and ground states, $a_v^{(2)}(t)$ and $a_g^{(2)}(t)$, is presented in section A.2.

A.1 Core-excited states

The derivation starts from the expression in eq. (2.67a)

$$a_c^{(1)}(t) = -i \int_{t_0}^{t} dt' \, \langle \psi_c | \, \hat{H}^L_{\text{int},I}(t') \, | \psi_g \rangle \, . \tag{A.1}$$

Applying the definition $\hat{H}^L_{\text{int},I}(t) = e^{i(\omega_n - i\frac{\Gamma_n}{2})t} \hat{H}^L_{\text{int}}(t) e^{-i(\omega_n - i\frac{\Gamma_n}{2})t}$ leads to

$$a_c^{(1)}(t) = -i \int_{t_0}^{t} dt' e^{i(\omega_{cg} - i\frac{\Gamma_{cg}}{2})t'} \, \langle \psi_c | \, \hat{H}^L_{\text{int}}(t') \, | \psi_g \rangle \, , \tag{A.2}$$

where $\omega_{cg} = \omega_c - \omega_g$ and $\Gamma_{cg} = \Gamma_c - \Gamma_g$. Since by definition of ground state $\Gamma_g = 0$, $\Gamma_{cg} \equiv \Gamma_c$ in the following. The substitution in eq. (A.2) of the definition of $\hat{H}^L_{\text{int}}(t')$ from eq. (2.22) leads to

$$a_c^{(1)}(t) = i \int_{t_0}^{t} dt' e^{i(\omega_{cg} - i\frac{\Gamma_c}{2})t'} E(t') \boldsymbol{\epsilon} \cdot \boldsymbol{\mu}_{cg}. \tag{A.3}$$

Here, $\boldsymbol{\mu}_{cg} = \langle \psi_c | \, \hat{\boldsymbol{\mu}} \, | \psi_g \rangle$ and the vector field $\boldsymbol{E}(t')$ is written as the product of its amplitude $E(t')$ and its polarisation $\boldsymbol{\epsilon}$. The Fourier transform of $E(t')$, i.e.

$$E(t') = \frac{1}{\sqrt{2\pi}} \int_0^{\infty} d\omega (E(\omega) e^{i\omega t'} + E^*(\omega) e^{-i\omega t'}), \tag{A.4}$$

is introduced in eq. (A.3) yielding

$$a_c^{(1)}(t) = \frac{i}{\sqrt{2\pi}} \int_{t_0}^{t} dt' e^{i(\omega_{cg} - i\frac{\Gamma_c}{2})t'} \Big[\int_0^{\infty} d\omega (E(\omega) e^{i\omega t'} + E^*(\omega) e^{-i\omega t'}) \Big] \boldsymbol{\epsilon} \cdot \boldsymbol{\mu}_{cg}, \quad \text{(A.5a)}$$

which after reorganising the terms leads to

$$a_c^{(1)}(t) = i \int_{t_0}^{t} \frac{dt'}{\sqrt{2\pi}} \int_0^{\infty} d\omega \Big(E(\omega) e^{i(\omega_{cg} + \omega - i\frac{\Gamma_c}{2})t'} + E^*(\omega) e^{i(\omega_{cg} - \omega - i\frac{\Gamma_c}{2})t'} \Big) \boldsymbol{\epsilon} \cdot \boldsymbol{\mu}_{cg}. \quad \text{(A.5b)}$$

At this point, the time-integral in eq. (A.5b) is evaluated in the limit $t_0 \to -\infty$ yielding

$$a_c^{(1)}(t) = \lim_{t_0 \to -\infty} \frac{\boldsymbol{\epsilon} \cdot \boldsymbol{\mu}_{cg}}{\sqrt{2\pi}} \int_0^{\infty} d\omega \times \\ \times \Big(E(\omega) \frac{e^{i(\omega_{cg} + \omega - i\frac{\Gamma_c}{2})t'}}{\omega_{cg} + \omega - i\frac{\Gamma_c}{2}} \Big|_{t_0}^{t} + E^*(\omega) \frac{e^{i(\omega_{cg} - \omega - i\frac{\Gamma_c}{2})t'}}{\omega_{cg} - \omega - i\frac{\Gamma_c}{2}} \Big|_{t_0}^{t} \Big), \quad \text{(A.6)}$$

which, since the t_0-dependent terms tend to 0 in the limit $t_0 \to -\infty$ [114], corresponds to

$$a_c^{(1)}(t) = \frac{\boldsymbol{\epsilon} \cdot \boldsymbol{\mu}_{cg}}{\sqrt{2\pi}} \int_0^{\infty} d\omega \Big(\underbrace{E(\omega) \frac{e^{i(\omega_{cg} + \omega - i\frac{\Gamma_c}{2})t}}{\omega_{cg} + \omega - i\frac{\Gamma_c}{2}}}_{\text{one-photon emission}} + \underbrace{E^*(\omega) \frac{e^{i(\omega_{cg} - \omega - i\frac{\Gamma_c}{2})t}}{\omega_{cg} - \omega - i\frac{\Gamma_c}{2}}}_{\text{one-photon absorption}} \Big), \quad \text{(A.7)}$$

Finally, considering only the 'one-photon absorption' term in eq. (A.7) leads to the final expression

$$a_c^{(1)}(t) = \frac{1}{\sqrt{2\pi}} \int_0^{\infty} d\omega \frac{e^{i(\omega_{cg} - \omega - i\frac{\Gamma_c}{2})t}}{\omega_{cg} - \omega - i\frac{\Gamma_c}{2}} E^*(\omega) \boldsymbol{\epsilon} \cdot \boldsymbol{\mu}_{cg}. \quad \text{(A.8)}$$

A.2 Valence-excited and ground states

The derivation starts from the insertion in eq. (2.67b), i.e.

$$a_v^{(2)}(t) = (-i)^2 \sum_m \int_{t_0}^{t} dt' \int_{t_0}^{t'} dt'' \langle \psi_v | \hat{H}_{\text{int,I}}^L(t') | \psi_m \rangle \langle \psi_m | \hat{H}_{\text{int,I}}^L(t'') | \psi_g \rangle, \quad \text{(A.9)}$$

of the definition $\hat{H}_{\text{int},I}^L(t) = e^{i(\omega_n - i\frac{\Gamma_n}{2})t} \hat{H}_{\text{int}}^L(t) e^{-i(\omega_n - i\frac{\Gamma_n}{2})t}$, while considering $\Gamma_g = 0$. This leads to the expression

$$a_v^{(2)}(t) = -\sum_m \int_{t_0}^{t} dt' e^{i(\omega_{vm} - i\frac{\Gamma_{vm}}{2})t'} \langle \psi_v | \hat{H}_{\text{int}}^L(t') | \psi_m \rangle \times \\ \times \int_{t_0}^{t'} dt'' \langle \psi_m | \hat{H}_{\text{int}}^L(t'') | \psi_g \rangle e^{i(\omega_{mg} - i\frac{\Gamma_m}{2})t''}. \quad \text{(A.10)}$$

The substitution of the definition of $\hat{H}^L_{\rm int}(t)$ from eq. (2.22), with $\boldsymbol{E}(t) = E(t)\boldsymbol{\epsilon}$, leads to

$$a_v^{(2)}(t) = -\sum_m \int_{t_0}^{t} dt' e^{i(\omega_{vm} - i\frac{\Gamma_{vm}}{2})t'} \langle\psi_v| \left(-E(t')\boldsymbol{\epsilon}' \cdot \hat{\boldsymbol{\mu}}\right) |\psi_m\rangle \times \\ \times \int_{t_0}^{t'} dt'' \langle\psi_m| \left(-E(t'')\boldsymbol{\epsilon}'' \cdot \hat{\boldsymbol{\mu}}\right) |\psi_g\rangle e^{i(\omega_{mg} - i\frac{\Gamma_m}{2})t''}, \quad \text{(A.11a)}$$

which, upon introducing of the compact notation for the dipole moments, becomes

$$a_v^{(2)}(t) = -\sum_m \int_{t_0}^{t} dt' e^{i(\omega_{vm} - i\frac{\Gamma_{vm}}{2})t'} E(t')\boldsymbol{\epsilon}' \cdot \boldsymbol{\mu}_{vm} \times \\ \times \int_{t_0}^{t'} dt'' E(t'')\boldsymbol{\epsilon}'' \cdot \boldsymbol{\mu}_{mg} e^{i(\omega_{mg} - i\frac{\Gamma_m}{2})t''}. \quad \text{(A.11b)}$$

The introduction of the Fourier expansion of the $E(t')$ and $E(t'')$ from eq. (A.4), together with some trivial algebraic passages, leads to

$$a_v^{(2)}(t) = -\frac{1}{2\pi}\sum_m \int_0^\infty d\omega' \int_0^\infty d\omega'' \times \\ \times \int_{t_0}^{t} dt' \left[E(\omega') e^{i(\omega_{vm} + \omega' - i\frac{\Gamma_{vm}}{2})t'} + E^*(\omega') e^{i(\omega_{vm} - \omega' - i\frac{\Gamma_{vm}}{2})t'}\right] \boldsymbol{\epsilon}' \cdot \boldsymbol{\mu}_{vm} \times \quad \text{(A.12)} \\ \times \int_{t_0}^{t'} dt'' \left[E(\omega'') e^{i(\omega_{mg} + \omega'' - i\frac{\Gamma_m}{2})t''} + E^*(\omega'') e^{i(\omega_{mg} - \omega'' - i\frac{\Gamma_m}{2})t''}\right] \boldsymbol{\epsilon}'' \cdot \boldsymbol{\mu}_{mg}.$$

The evaluation of the innermost time-integral with respect to t'', in the limit $t_0 \to -\infty$, leads to the expression

$$a_v^{(2)}(t) = -\frac{1}{2\pi}\sum_m \int_0^\infty d\omega' \int_0^\infty d\omega'' \times \\ \times \int_{t_0}^{t} dt' \left[E(\omega') e^{i(\omega_{vm} + \omega' - i\frac{\Gamma_{vm}}{2})t'} + E^*(\omega') e^{i(\omega_{vm} - \omega' - i\frac{\Gamma_{vm}}{2})t'}\right] \boldsymbol{\epsilon}' \cdot \boldsymbol{\mu}_{vm} \times \quad \text{(A.13)} \\ \times \left[E(\omega'') \frac{e^{i(\omega_{mg} + \omega'' - i\frac{\Gamma_m}{2})t'}}{i(\omega_{mg} + \omega'' - i\frac{\Gamma_m}{2})} + E^*(\omega'') \frac{e^{i(\omega_{mg} - \omega'' - i\frac{\Gamma_m}{2})t'}}{i(\omega_{mg} - \omega'' - i\frac{\Gamma_m}{2})}\right] \boldsymbol{\epsilon}'' \cdot \boldsymbol{\mu}_{mg},$$

which, upon multiplication of the two couples of terms enclosed in squared brackets, can be written as

$$a_v^{(2)}(t) = -\frac{1}{2\pi}\sum_m \int_0^\infty d\omega' \int_0^\infty d\omega'' (\boldsymbol{\epsilon}' \cdot \boldsymbol{\mu}_{vm})(\boldsymbol{\epsilon}'' \cdot \boldsymbol{\mu}_{mg}) \int_{t_0}^{t} dt' \times \\ \times \left[E(\omega')E(\omega'') \frac{e^{i(\omega_{vg} + \omega' + \omega'' - i\frac{\Gamma_v}{2})t'}}{i(\omega_{mg} + \omega'' - i\frac{\Gamma_m}{2})} + E^*(\omega')E(\omega'') \frac{e^{i(\omega_{vg} - \omega' + \omega'' - i\frac{\Gamma_v}{2})t'}}{i(\omega_{mg} + \omega'' - i\frac{\Gamma_m}{2})} + \right. \quad \text{(A.14)} \\ \left. + E(\omega')E^*(\omega'') \frac{e^{i(\omega_{vg} + \omega' - \omega'' - i\frac{\Gamma_v}{2})t'}}{i(\omega_{mg} - \omega'' - i\frac{\Gamma_m}{2})} + E^*(\omega')E^*(\omega'') \frac{e^{i(\omega_{vg} - \omega' - \omega'' - i\frac{\Gamma_v}{2})t'}}{i(\omega_{mg} - \omega'' - i\frac{\Gamma_m}{2})}\right],$$

where $\omega_{vg} = \omega_{vm} + \omega_{mg}$ and $\Gamma_v = \Gamma_{vm} + \Gamma_m$. Performing the four time-integrals in eq. (A.14) in the limit $t_0 \to -\infty$ leads to

$$\begin{aligned} a_v^{(2)}(t) = \frac{1}{2\pi}\sum_m \int_0^\infty d\omega' \int_0^\infty d\omega''(\boldsymbol{\epsilon}' \cdot \boldsymbol{\mu}_{vm})(\boldsymbol{\epsilon}'' \cdot \boldsymbol{\mu}_{mg}) \times \\ \times \Big[\underbrace{\frac{E(\omega')E(\omega'')e^{i(\omega_{vg}+\omega'+\omega''-i\frac{\Gamma_v}{2})t}}{(\omega_{mg}+\omega''-i\frac{\Gamma_m}{2})(\omega_{vg}+\omega'+\omega''-i\frac{\Gamma_v}{2})}}_{\text{two-photon emission}} + \\ + \underbrace{\frac{E^*(\omega')E^*(\omega'')e^{i(\omega_{vg}-\omega'-\omega''-i\frac{\Gamma_v}{2})t}}{(\omega_{mg}-\omega''-i\frac{\Gamma_m}{2})(\omega_{vg}-\omega'-\omega''-i\frac{\Gamma_v}{2})}}_{\text{two-photon absorption}} + \\ + \underbrace{\frac{E^*(\omega')E(\omega'')e^{i(\omega_{vg}-\omega'+\omega''-i\frac{\Gamma_v}{2})t}}{(\omega_{mg}+\omega''-i\frac{\Gamma_m}{2})(\omega_{vg}-\omega'+\omega''-i\frac{\Gamma_v}{2})}}_{\text{Raman}} + \\ + \underbrace{\frac{E(\omega')E^*(\omega'')e^{i(\omega_{vg}+\omega'-\omega''-i\frac{\Gamma_v}{2})t}}{(\omega_{mg}-\omega''-i\frac{\Gamma_m}{2})(\omega_{vg}+\omega'-\omega''-i\frac{\Gamma_v}{2})}}_{\text{Raman}} \Big], \end{aligned} \tag{A.15}$$

which, when considering only the 'Raman' terms, reduces to

$$\begin{aligned} a_v^{(2)}(t) = \frac{1}{2\pi}\sum_m \int_0^\infty d\omega' \int_0^\infty d\omega''(\boldsymbol{\epsilon}' \cdot \boldsymbol{\mu}_{vm})(\boldsymbol{\epsilon}'' \cdot \boldsymbol{\mu}_{mg}) \times \\ \times \Big[\frac{E^*(\omega')E(\omega'')e^{i(\omega_{vg}-\omega'+\omega''-i\frac{\Gamma_v}{2})t}}{(\omega_{mg}+\omega''-i\frac{\Gamma_m}{2})(\omega_{vg}-\omega'+\omega''-i\frac{\Gamma_v}{2})} + \\ + \frac{E(\omega')E^*(\omega'')e^{i(\omega_{vg}+\omega'-\omega''-i\frac{\Gamma_v}{2})t}}{(\omega_{mg}-\omega''-i\frac{\Gamma_m}{2})(\omega_{vg}+\omega'-\omega''-i\frac{\Gamma_v}{2})} \Big]. \end{aligned} \tag{A.16}$$

As a next step, in correspondence to ω' and ω'' being preceded by a $-$ or $+$ sign, these terms are substituted by ω_p or ω_d, respectively. This leads to the expression

$$\begin{aligned} a_v^{(2)}(t) = \frac{1}{2\pi}\sum_m \int_0^\infty d\omega_p \int_0^\infty d\omega_d \times \\ \times \Big[\frac{e^{i(\omega_{vg}-\omega_p+\omega_d-i\frac{\Gamma_v}{2})t}}{\omega_{vg}-\omega_p+\omega_d-i\frac{\Gamma_v}{2}} E^*(\omega_p)E(\omega_d) \frac{(\boldsymbol{\epsilon}_p \cdot \boldsymbol{\mu}_{vm})(\boldsymbol{\epsilon}_d \cdot \boldsymbol{\mu}_{mg})}{\omega_{mg}+\omega_d-i\frac{\Gamma_m}{2}} + \\ + \frac{e^{i(\omega_{vg}+\omega_d-\omega_p-i\frac{\Gamma_v}{2})t}}{\omega_{vg}+\omega_d-\omega_p-i\frac{\Gamma_v}{2}} E(\omega_d)E^*(\omega_p) \frac{(\boldsymbol{\epsilon}_d \cdot \boldsymbol{\mu}_{vm})(\boldsymbol{\epsilon}_p \cdot \boldsymbol{\mu}_{mg})}{\omega_{mg}-\omega_p-i\frac{\Gamma_m}{2}} \Big], \end{aligned} \tag{A.17}$$

which, upon gathering the terms with respect to the common factor, leads to the final expression

$$\begin{aligned} a_v^{(2)}(t) = \frac{1}{2\pi}\int_0^\infty d\omega_p \int_0^\infty d\omega_d \frac{e^{i(\omega_{vg}-\omega_p+\omega_d-i\frac{\Gamma_v}{2})t}}{\omega_{vg}-\omega_p+\omega_d-i\frac{\Gamma_v}{2}} \times \\ \times E^*(\omega_p)E(\omega_d) \sum_m \Big(\frac{(\boldsymbol{\epsilon}_p \cdot \boldsymbol{\mu}_{vm})(\boldsymbol{\epsilon}_d \cdot \boldsymbol{\mu}_{mg})}{\omega_{mg}+\omega_d-i\frac{\Gamma_m}{2}} + \frac{(\boldsymbol{\epsilon}_d \cdot \boldsymbol{\mu}_{vm})(\boldsymbol{\epsilon}_p \cdot \boldsymbol{\mu}_{mg})}{\omega_{mg}-\omega_p-i\frac{\Gamma_m}{2}} \Big). \end{aligned} \tag{A.18}$$

The expression for $a_g^{(2)}(t)$ is obtained from eq. (A.18) by considering $v = g$.

APPENDIX B

Properties of the 1PDM

The aim of this section is to discuss the properties of the state and transition 1PDM. The general definition of a 1PDM $\gamma_{pq}^{nn'}$ in second quantization is given by

$$\gamma_{pq}^{nn'} = \langle \psi_{n'} | \, \hat{c}_q^\dagger \hat{c}_p \, | \psi_n \rangle \, . \tag{B.1}$$

In the case of a state 1PDM $n = n'$ in eq. (B.1), which leads the 1PDM to behave upon conjugate transposition as

$$(\gamma_{pq}^{nn})^\dagger = (\langle \psi_n | \, \hat{c}_q^\dagger \hat{c}_p \, | \psi_n \rangle)^\dagger = \langle \psi_n | \, (\hat{c}_q^\dagger \hat{c}_p)^\dagger \, | \psi_n \rangle = \langle \psi_n | \, \hat{c}_p^\dagger \hat{c}_q \, | \psi_n \rangle = \gamma_{qp}^{nn}. \tag{B.2}$$

It follows that, when the state 1PDM is real, the matrix is symmetric. A similar analysis can be extended to the transition density matrix $\gamma_{pq}^{nn'}$, i.e.

$$(\gamma_{pq}^{nn'})^\dagger = (\langle \psi_{n'} | \, \hat{c}_q^\dagger \hat{c}_p \, | \psi_n \rangle)^\dagger = \langle \psi_n | \, (\hat{c}_q^\dagger \hat{c}_p)^\dagger \, | \psi_{n'} \rangle = \langle \psi_n | \, \hat{c}_p^\dagger \hat{c}_q \, | \psi_{n'} \rangle = \gamma_{qp}^{n'n}. \tag{B.3}$$

From this it follows that, in the case of a real transition 1PDM, the matrix is symmetric under simultaneous state- and orbital-index swap. On the other hand, differently from the state 1PDM, a transition 1PDM is not symmetric, i.e. $\gamma_{pq}^{nn'} \neq \gamma_{qp}^{nn'}$.

APPENDIX C

Analytical form of second order integral on strip element

The derivation starts from the definition of the double integral in eq. (3.35) over the domain of frequencies corresponding to the 'strip element', i.e.

$$a_k^{S_e}(t) = \lim_{\Gamma\to 0} \int_{\omega_0-\delta}^{\omega_0+\delta} d\omega_s \frac{e^{i(\omega_s-\omega_0-i\frac{\Gamma}{2})t}}{\omega_s-\omega_0-i\frac{\Gamma}{2}} f(\omega_s). \tag{C.1}$$

Here, ω_s runs over the strip element, while ω_0 corresponds to the centre of the element, which divides it in two parts of width δ. The $f(\omega_s)$ factor represents the values of $f_{kg}(\omega_p, \omega_d)$ evaluated on the points of the frequency grid corresponding to the strip element. The limit in eq. (C.1) can be written as

$$a_k^{S_e}(t) = \underbrace{\Big(\lim_{\Gamma\to 0} e^{\frac{\Gamma}{2}t}\Big)}_{=1} \Big(\lim_{\Gamma\to 0} \int_{\omega_0-\delta}^{\omega_0+\delta} d\omega_s \frac{e^{i(\omega_s-\omega_0)t}}{\omega_s-\omega_0-i\frac{\Gamma}{2}} f(\omega_s)\Big), \tag{C.2}$$

which, upon insertion of the Taylor expansion of $f(\omega_s)$ at ω_0 up to first order, is approximated as

$$a_k^{S_e}(t) \approx S = \lim_{\Gamma\to 0} \int_{\omega_0-\delta}^{\omega_0+\delta} d\omega_s \frac{e^{i(\omega_s-\omega_0)t}}{\omega_s-\omega_0-i\frac{\Gamma}{2}} [f(\omega_0) + f'(\omega_0)(\omega_s-\omega_0)]. \tag{C.3}$$

Taking the limit in the second term leads to

$$S = f(\omega_0) \lim_{\Gamma\to 0} \int_{\omega_0-\delta}^{\omega_0+\delta} d\omega_s \frac{e^{i(\omega_s-\omega_0)t}}{\omega_s-\omega_0-i\frac{\Gamma}{2}} + f'(\omega_0) \int_{\omega_0-\delta}^{\omega_0+\delta} d\omega_s \frac{e^{i(\omega_s-\omega_0)t}}{\omega_s-\omega_0} (\omega_s-\omega_0), \tag{C.4}$$

which upon simplification in the second term becomes

$$S = f(\omega_0) \lim_{\Gamma\to 0} \int_{\omega_0-\delta}^{\omega_0+\delta} d\omega_s \frac{e^{i(\omega_s-\omega_0)t}}{\omega_s-\omega_0-i\frac{\Gamma}{2}} + f'(\omega_0) \int_{\omega_0-\delta}^{\omega_0+\delta} d\omega_s e^{i(\omega_s-\omega_0)t}. \tag{C.5}$$

At this point, the limits of integration can be shifted in order to obtain the simpler form

$$S = \underbrace{f(\omega_0) \lim_{\Gamma\to 0} \int_{-\delta}^{\delta} d\omega_s \frac{e^{i\omega_s t}}{\omega_s - i\frac{\Gamma}{2}}}_{S_A} + \underbrace{f'(\omega_0) \int_{-\delta}^{\delta} d\omega_s e^{i\omega_s t}}_{S_B}, \tag{C.6}$$

where two different components, S_A and S_B, are highlighted for the purposes of their separate discussion in the following sections.

C.1 S_A component

The solution of the integral makes use of the following equality

$$\lim_{\epsilon\to 0} \int dx \frac{f(x)}{x \pm i\epsilon} = \mp i\pi f(0) + p.v. \int dx \frac{f(x)}{x}, \tag{C.7}$$

where $p.v.$ symbolises the Cauchy principal value. The definition in eq. (C.7) can be applied to the S_A component of eq. (C.6) to obtain

$$S_A = f(\omega_0) \lim_{\Gamma\to 0} \int_{-\delta}^{\delta} d\omega_s \frac{e^{i\omega_s t}}{\omega_s - i\frac{\Gamma}{2}} = f(\omega_0)\Big(i\pi + p.v. \int_{-\delta}^{\delta} d\omega_s \frac{e^{i\omega_s t}}{\omega_s}\Big), \tag{C.8}$$

Applying the explicit definition of the Cauchy principal value in eq. (C.8) leads to

$$S_A = f(\omega_0)\Big[i\pi + \lim_{\Gamma\to 0}\Big(\int_{-\delta}^{-\frac{\Gamma}{2}} \frac{d\omega_s}{\omega_s} e^{i\omega_s t} + \int_{\frac{\Gamma}{2}}^{\delta} \frac{d\omega_s}{\omega_s} e^{i\omega_s t}\Big)\Big], \tag{C.9}$$

which is further developed according to the following passages:

$$S_A = f(\omega_0)\Big[i\pi + \lim_{\Gamma\to 0}\Big(\int_{-\delta}^{-\frac{\Gamma}{2}} \frac{d\omega_s}{\omega_s} e^{i\omega_s t} + \int_{\frac{\Gamma}{2}}^{\delta} \frac{d\omega_s}{\omega_s} e^{i\omega_s t}\Big)\Big] = \tag{C.10a}$$

$$= f(\omega_0)\Big[i\pi + \lim_{\Gamma\to 0}\Big(-\int_{-\frac{\Gamma}{2}}^{-\delta} \frac{d\omega_s}{\omega_s} e^{i\omega_s t} + \int_{\frac{\Gamma}{2}}^{\delta} \frac{d\omega_s}{\omega_s} e^{i\omega_s t}\Big)\Big] = \tag{C.10b}$$

$$= f(\omega_0)\Big[i\pi + \lim_{\Gamma\to 0}\Big(-\int_{\frac{\Gamma}{2}}^{\delta} \frac{d(-\omega_s)}{-\omega_s} e^{-i\omega_s t} + \int_{\frac{\Gamma}{2}}^{\delta} \frac{d\omega_s}{\omega_s} e^{i\omega_s t}\Big)\Big] = \tag{C.10c}$$

$$= f(\omega_0)\Big[i\pi + \lim_{\Gamma\to 0}\Big(-\int_{\frac{\Gamma}{2}}^{\delta} \frac{d\omega_s}{\omega_s} e^{-i\omega_s t} + \int_{\frac{\Gamma}{2}}^{\delta} \frac{d\omega_s}{\omega_s} e^{i\omega_s t}\Big)\Big] = \tag{C.10d}$$

$$= f(\omega_0)\Big[i\pi + \lim_{\Gamma\to 0}\int_{\frac{\Gamma}{2}}^{\delta} \frac{d\omega_s}{\omega_s}(e^{i\omega_s t} - e^{-i\omega_s t})\Big] \tag{C.10e}$$

considering $\sin\omega_s t = \frac{e^{i\omega_s t} - e^{-i\omega_s t}}{2i}$ and taking the limit leads to

$$S_A = f(\omega_0)\Big(i\pi + 2i\int_0^{\delta} d\omega_s \frac{\sin\omega_s t}{\omega_s}\Big) \tag{C.11}$$

At this point, the integration variable is changed from ω_s to $\omega_s t$, leading to

$$S_A = f(\omega_0)\Big(i\pi + 2i\underbrace{\int_0^{\delta t} d(\omega_s t)\frac{\sin\omega_s t}{\omega_s t}}_{\mathrm{Si}(\delta t)}\Big), \tag{C.12}$$

where $\mathrm{Si}(\delta t)$ represents the Sine integral.

C.2 S_B component

The integral can be trivially solved as

$$S_B = f'(\omega_0)\int_{-\delta}^{\delta} d\omega_s e^{i\omega_s t} = f'(\omega_0)\frac{e^{i\delta t} - e^{-i\delta t}}{it} = f'(\omega_0)\frac{2\sin\delta t}{t}, \tag{C.13}$$

where the definition $\sin\delta t = \frac{e^{i\delta t}-e^{-i\delta t}}{2i}$ has been used.

C.3 Final expression of the integral

By assembling the results from eqs. (C.12) and (C.13) in eq. (C.6), the final expression for S is obtained, i.e.

$$S = S_A + S_B = f(\omega_0)\Big(i\pi + 2i\mathrm{Si}(\delta t)\Big) + f'(\omega_0)\frac{2\sin\delta t}{t}, \tag{C.14}$$

which, according to eq. (C.3), corresponds to the approximate evaluation of $a_k^{S_e}(t)$.